UNIVERSITÉ DU QUÉBEC

THÈSE PRÉSENTÉE À
L'UNIVERSITÉ DU QUÉBEC À CHICOUTIMI
COMME EXIGENCE PARTIELLE
DU DOCTORAT EN INGÉNIERIE

PAR

GUVENC ERGIN

ÉTUDE DE LA MOUILLABILITÉ DES PARTICULES GRANULAIRES PAR LES ALLIAGES D'ALUMINIUM DURANT LA FILTRATION D'ALUMINIUM

MAI 2006

Bibliothèque
Paul-Émile-Boulet

UQAC
Université du Québec
à Chicoutimi

Mise en garde/Advice

Afin de rendre accessible au plus grand nombre le résultat des travaux de recherche menés par ses étudiants gradués et dans l'esprit des règles qui régissent le dépôt et la diffusion des mémoires et thèses produits dans cette Institution, **l'Université du Québec à Chicoutimi (UQAC)** est fière de rendre accessible une version complète et gratuite de cette œuvre.

Motivated by a desire to make the results of its graduate students' research accessible to all, and in accordance with the rules governing the acceptation and diffusion of dissertations and theses in this Institution, the **Université du Québec à Chicoutimi (UQAC)** is proud to make a complete version of this work available at no cost to the reader.

L'auteur conserve néanmoins la propriété du droit d'auteur qui protège ce mémoire ou cette thèse. Ni le mémoire ou la thèse ni des extraits substantiels de ceux-ci ne peuvent être imprimés ou autrement reproduits sans son autorisation.

The author retains ownership of the copyright of this dissertation or thesis. Neither the dissertation or thesis, nor substantial extracts from it, may be printed or otherwise reproduced without the author's permission.

UNIVERSITY OF QUEBEC AT CHICOUTIMI

A THESIS SUBMITTED TO
THE UNIVERSITY OF QUEBEC AT CHICOUTIMI
IN PARTIAL FULFILLMENT OF THE REQUIREMENTS
FOR THE DOCTOR OF PHILOSOPHY DEGREE
IN THE DEPARTMENT OF APPLIED SCIENCES

BY
GUVENC ERGIN

THE WETTABILITY OF THE FILTER MEDIA BY ALUMINUM ALLOYS DURING ALUMINUM FILTRATION

MAY 2006

RÉSUMÉ

Cette thèse a été entreprise pour étudier le mouillage entre des particules granulaires (les particules d'alumine) et des alliages d'aluminium avec le magnésium. L'objectif était de développer une méthode pour caractériser les différentes particules d'alumine granulaires et les différencier les unes des autres en utilisant le concept du mouillage. Deux types de méthodes expérimentales ont été utilisés pour caractériser le mouillage: la goutte sessile (goutte posée) et l'infiltration.

Le système de goutte sessile qui a été construit est possiblement le seul disponible au Canada avec lequel les mesures d'angle de contact peuvent être effectuées en injectant une goutte de métal liquide directement sur la surface solide. Cependant, les résultats ont indiqué que cette méthode n'est pas appropriée pour différencier des différentes particules d'alumine granulaires par rapport à leur mouillabilité parce que la rugosité de la surface empêche les gouttes de prendre leurs propres formes.

L'évaluation de la mouillabilité des particules d'alumine diverses a été effectuée en utilisant le système d'infiltration. Les données expérimentales obtenues ont été analysées en employant trois méthodes capillaires basées sur (i) le bilan d'énergie pour les pores à taille moyenne, (ii) le bilan d'énergie pour les pores à des tailles distribuées et (iii) le bilan de forces dans les pores qui ont été constituées des capillaires dont le rayon change périodiquement. Les deux premiers modèles ont été développés essentiellement pour les expériences d'infiltration et le dernier a était tiré de la littérature. Les résultats étaient cohérents et ils ont démontré qu'il est possible de différencier les échantillons d'alumine de diverses sources avec la méthode d'infiltration. Les réactions ayant lieu entre les alliages d'aluminium (avec magnésium) et les particules d'alumine ont été aussi étudiées en utilisant la technique d'infiltration. Les analyses par microscopie électronique à balayage (MEB) et microscopie électronique à transmission (MET) ont montré que le spinelle s'est formé indépendamment de la durée d'expérience et du type des particules d'alumine utilisées à 1000 K sous une atmosphère d'argon. L'analyse thermodynamique a indiqué la même tendance.

SUMMARY

This thesis was undertaken to study the wetting between granular media (alumina) and Al-Mg alloys. The objective was to develop a test method to characterize different granular alumina particles and differentiate one from the other by using the wettability concept. Two types of experimental methods were used to measure the wetting: sessile drop and infiltration methods.

The sessile drop system constructed is one of the few, if not the only one, available in Canada in which the contact angle measurements can be carried out with a liquid metal drop injected directly onto the solid surface. However, the results indicated that this method is not appropriate to differentiate different granular alumina particles due to prevention, by the rough surface, of the droplets taking their proper form.

Using the infiltration system, various alumina particles were tested. The data obtained from these tests were analyzed using three capillary models based on: (i) an energy balance with an average pore size, (ii) an energy balance with a pore size distribution, and (iii) a force balance with periodically changing pore radius. The two models based on the energy balance were developed especially for infiltration experiments, and the third one was taken from the literature. The results were consistent and showed that it was possible to differentiate different alumina samples with the infiltration method. The reactions taking place between Al-Mg alloys and different alumina particles were also investigated by using the infiltration technique. SEM and TEM analyses showed that spinel was formed independent of the experiment duration and the type of alumina particles used in the experiments at 1000 K under argon atmosphere. The thermodynamic analysis indicated the same tendency.

ACKNOWLEDGEMENTS

The author would like to express his gratitude to Prof. Duygu Kocaefe and Dr. Yasar Kocaefe for their inspiring guidance and valuable help throughout the progress of this thesis.

The author would like to acknowledge ALCAN Inc. and National Science and Engineering Research Council (NSERC) of Canada for financial support. He would also thank to Mr. Andris Innus, Consultant in Alcan International Limited, for his contributions to the project, Mr. Patrice Paquet and Mr. Julien Tremblay for their technical supports, Ms.Hélène Grégoire of CTA for SEM analyses, and Dr. Daryoush Emadi, Valery Y. Gertsman, Dr. Jian Li and Ms. Cathy Bibby of CANMET-Materials Technology Laboratory for their help in TEM analysis.

The author would particularly thank to his parents for their precious support in all respects; without them it would be difficult to imagine all these. The author also wishes to acknowledge the help provided, in various aspects, by the staff of Engineering Department of UQAC. Thanks to all colleagues and friends working in Engineering Department of UQAC for their kindness and availability.

LIST OF SYMBOLS

Abbreviations

CFF	ceramic foam filter
displ.	displacement
EDS	energy dispersive x-ray spectrometry
EDX	energy dispersive x-ray
ICP-MS	induction coupled plasma mass spectrometry
MMC	metal matrix composite
NA	not applicable
OES	arc optical emission spectroscopy
RG	research grade
RMS	root mean square
SEM	scanning electron microscope
TEM	transmission electron microscopy
THC	total hydrocarbon
UHP	ultra high purity
UV	ultra violet
WDS	wave dispersive x-ray spectroscopy

WHO	world health organization
wt%	weight percent

Latin Symbols

A	area	m^2
A′	Helmholtz free energy	Nm
c	constant	-
C	principal radius of curvature	m
D	average particle diameter	m
e	surface stress	N/m
E	energy	J
F	force	N
g	gravitational acceleration	m/s^2
G°	standard Gibbs free energy	J/mol
h	height	m
l	height of capillary	m
m	mass of the metal	kg
n	number	-
P	pressure	N/m^2
Per	perimeter	m
r	radius	m
R	RMS surface height	m

t	time	s
T	temperature	K
V	volume	m^3
W	Wenzel's ratio	-
W	work	Nm
X	area fraction	-

Greek Symbols

α	maximum hysteresis angle	degree
ε	porosity of alumina bed	-
γ	surface tension	N/m
θ	contact angle	degree
λ	average distance between surface asperities	m
μ	chemical potential	J/mol
η	viscosity	poise
ρ	density	kg/m^3
ϕ	shape factor	-

Subscripts

appl	applied
bed	alumina bed

c	composite surface
cap	capillary
grav	gravitation
h	hydraulic
i	component index
j	component index
K	Kelvin
liq	liquid
mat	material
max	maximum
min	minimum
par	particle
r	rough surface
s	smooth surface
st	surface tension
vis	viscous

Superscripts

lv	surface tension of liquid/vapor interface
sl	surface tension of solid/liquid interface
sv	surface tension of solid/vapor interface

TABLE OF CONTENTS

LIST OF FIGURES

LIST OF TABLES

CHAPTER 1

INTRODUCTION

Aluminum is the third most abundant element in the Earth's crust after oxygen and silicon and constitutes 7.3% by mass in about 250 different minerals. In nature, however, it only exists in compounds in an oxidized state (particularly as silicates and oxides) because of its strong affinity for oxygen.

Alum was a familiar aluminum compound in ancient times. Although it was known to the Egyptians, the Greeks, and the Romans and was used as a mordant at those times, its existence was first established at the beginning of the 19th century. The first person, who at least had partial success in trying to liberate this metal, was H. Davy. In 1808, he isolated, by an electrothermic-electrochemical method, small amounts of an Al-Fe alloy, which he called aluminum.

It took many years of research to "unlock" the metal from its ore. For reaching a large scale production of aluminum, many more years had passed because a cheap source of electrical energy with large capacity had to be available. The invention of dynamo came in 1867, and by 1880 the dynamo was improved to such an extent that it could be employed in industrial scale commercial production processes [1]. On April 23rd, 1886, P. L. T. Héroult in France, and independently C. M. Hall in the U.S.A. on July 9th of the same year, applied for the registration of a patent for aluminum production by electrolysis of a molten solution of alumina in cryolite [2].

Measured either in quantity or value, mankind has been using copper, lead, and tin for thousands of years and yet today more aluminum is produced than all other non-ferrous metals combined[1]; and it is important in some fields such as transportation (automobiles, airplanes, trucks, railcars, marine vessels, etc.), packaging (cans, foil, etc.), construction (windows, doors, siding, etc.), consumer durables (appliances, cooking utensils, etc.), electrical transmission lines, and machinery. This strong demand for aluminum can be attributed to its favorable properties. For instance, aluminum weighs about one-third of steel or copper. It is malleable, ductile, and easily machined and cast; and it has high conductivity, excellent corrosion resistance and durability [3].

1.1 Occurrence of Aluminum

Traditionally, aluminum extraction starts with bauxite mining. Bauxite is a naturally occurring, heterogeneous material consisting of primarily one or more hydrated aluminum oxide minerals such as gibbsite, bayerite, boehmite, and diaspore[2] as well as various mixtures of silica (SiO_2), iron oxide (Fe_2O_3), titania (TiO_2), aluminosilicates (clay, etc.), and other impurities in trace amounts [4]. Hydrated aluminum oxide minerals in bauxite are recovered for alumina production by the Bayer process which was invented almost 100 years ago. It is still the most economical way of manufacturing aluminum hydroxide

---

[1] World annual primary aluminum production in 1999 was about 24 million tonnes and secondary - recycled - production some 7 million tonnes. The total of some 31 million tonnes compares with 14.1 million tonnes of copper, 6.0 million tonnes of lead and 0.2 million tonnes of tin.

commercially, but not the only one[3]. After Bayer process, the recovered aluminum hydroxide is calcined to produce alumina, most of which is smelted using the Hall-Héroult process to produce aluminum metal by electrolytic reduction in a molten bath of natural or synthetic cryolite ($NaAlF_6$). Today, on average, it takes about 5 t of bauxite to obtain 2 t of alumina, which in turn yields 1 t of metal.

In 2004, 41 countries accounted for 29.8 million metric tons of primary aluminum production all over the world [5]. China, Russia, Canada, and the United States accounted for more than one-half of total world production. China produced almost 22% of the world total, followed by Russia with 12%. Canada and United States each accounted for about 8.5% of the total world primary production.World primary metal production increased by more than 7% compared with that of 2003.

1.2 The Statement of Problem

In this study, the wettability of different kinds of tabular alumina by the molten aluminum or Al-Mg alloys was investigated, and a method was developed in order to pre-select the bed media based on its wetting characteristics.

---

[2] Detailed information on various hydrated aluminum oxides can be found in reference [6].

[3] If needed, bauxite can be substituted with clay, anorthosite, alunite, coal wastes, and oil shales for production of alumina. It will require new plants using new technology, but these nonbauxitic materials can satisfy the alumina demand for primary metal, refractories, aluminum chemicals, and abrasives. However, total reported reserves of bauxite are sufficient to meet cumulative world primary aluminum metal demand well into the 21st century [4].

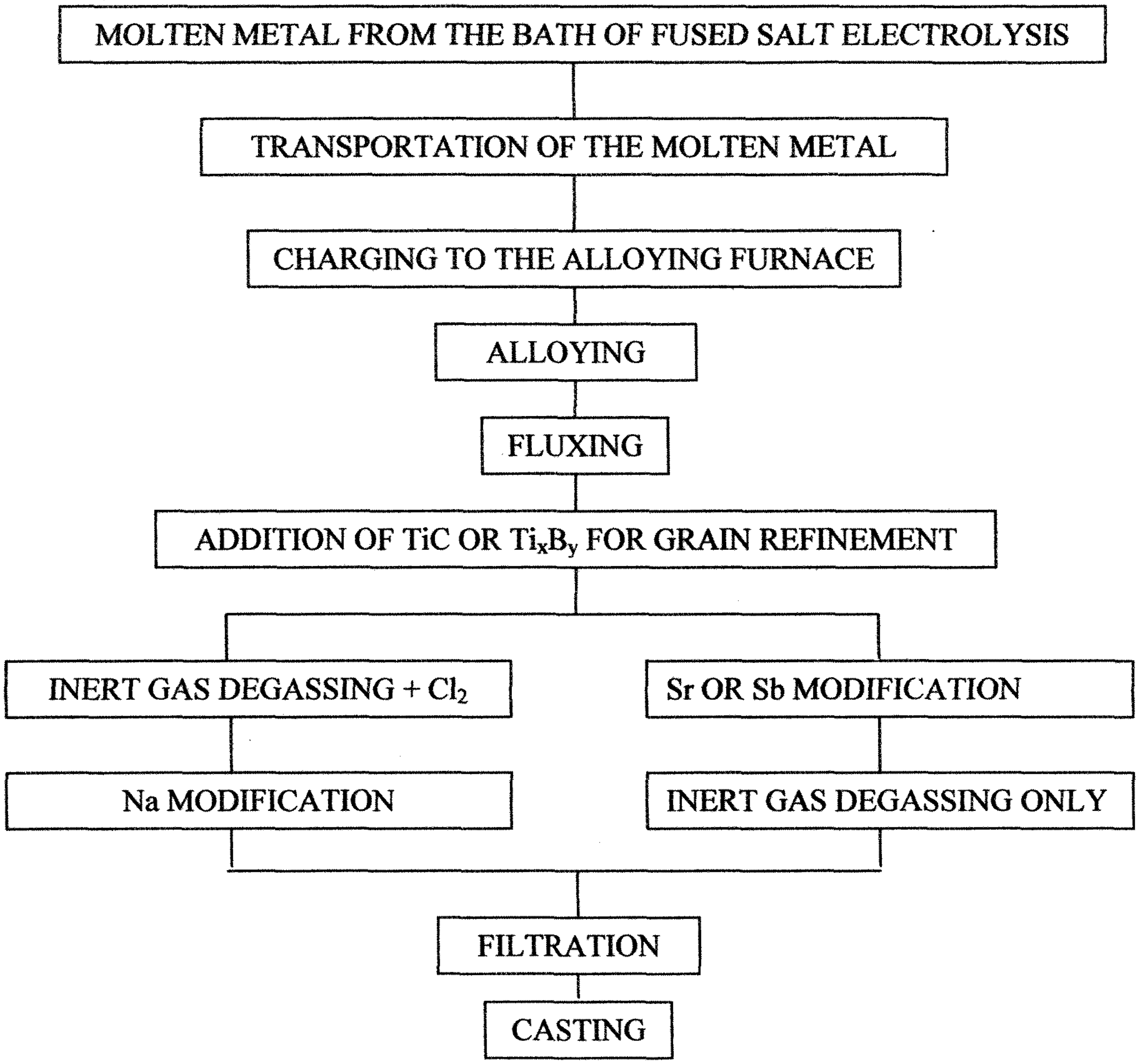

Figure 1.1. Molten Metal Treatment Stages Before Casting

Before the molten aluminum is cast into ingots, it passes through certain treatments summarized in Figure 1.1. The last step of these treatments is the filtration of molten aluminum. During filtration, the liquid aluminum passes through a filtering bed composed of superposed layers of tabular alumina particles with different sizes, and the interactions between solid and liquid phases start.

Filtration is particularly important both for the ingots, which are rolled to form aluminum metal sheets for can manufacture, and for the wires, which are used for the fabrication of cables, because undesired inclusions are removed from the aluminum alloy at this stage. An efficient filtration not only improves the filtration capacity of the aluminum plant and hence increases its productivity, but also makes the further metal forming steps less cumbersome. If the filtration step is by-passed or if the filtration efficiency is low, an inclusion left in the metal, for example during can manufacturing, can create a hole in the thinnest sections of the sheet metal, where the thickness goes down to 0.36 mm. Or, in the case of cable fabrication, an inclusion in the metal matrix can generate a crack during the formation processes, and the rupture of the material will occur.

Therefore, it is important to have an efficient filtration; and for reaching high efficiencies, good quality bed media is needed. However, the quality of the bed media changes from supplier to supplier as well as from shipment to shipment coming from the same supplier. At this point, the industry needs an index which can assure the efficiency of the filtration. In this project, the objective was to develop a method in order to compare the quality of different bed particles based on their wettabilities.

Wettability of different types of alumina particles depends mainly on physical (initial) and/or chemical (reactive) wetting [7]. In physical wetting, the reversible physical forces such as the Van der Waals and dispersion forces provide the energy required for wetting. In chemical wetting, a chemical reaction takes place on the liquid/solid interface, and chemical bonds which are responsible for wetting are formed.

In fact, the efficiency of the filtering bed depends on both modes of wetting. The filter bed forms the tortuous path for the molten aluminum, which increases the probability of the inclusions in the metal to attach the surface of the alumina particles in the bed by means of physical wetting, and prepares the necessary reactive media for the chemical wetting. However, since the filter bed is not as rigid as some other porous preformed materials, which are also used as the filtering medium in industry, it is more sensitive to vibrations. This limits the efficiency of filter bed to some extent to remove inclusions from the liquid metal due to physical wetting. Therefore, the contribution of reactive wetting may become more significant. Al-Mg alloy/alumina system is a good example for this kind of wetting. For this system, although it is known that wettability is increased because of the chemical reactions occurring on the Al-Mg alloy/alumina interface, the scientists cannot agree on the reaction mechanisms. Many scientists think that $MgAl_2O_4$ formation is responsible for improved wettability [8, 9, 10, 11, 12] whereas some scientists believe $MgAl_2O_4$ is not the key for enhanced wetting [13].

Since this project is related to filtration of aluminum and Al-Mg alloys through a bed of alumina particles, the results found from the analysis of samples will also contribute to a better understanding of the mechanism of the formation of spinel, which is not clear in the literature even today.

1.3 Objective

In this project, the objectives are: to investigate the interactions between different types of granular alumina particles and Al-Mg alloys by using sessile drop and infiltration techniques; and to develop a test method in order to characterize the granular alumina particles for their effectiveness as filter media by using their wettabilities.

1.4 Scope

In this study, to measure the wettability of the molten aluminum or Al-Mg alloys on different sorts of alumina particles at elevated temperatures two experimental methods were used, namely sessile drop and infiltration methods.

The sessile drop system developed is one of the few, if not the only one, available in Canada in which the contact angle measurements can be carried out with a liquid metal drop injected directly onto the solid surface. However, it was found out that, using this method, it is not possible to differentiate between the measured wettability values of the alumina particles concerned due to the pinning effect of the rough surface. Then, an infiltration set-up was constructed for testing the wettability of the alumina particles by molten aluminum and Al-Mg alloys.

In the infiltration system, various alumina samples were tested using industrial grade pure aluminum (1020) and Al-Mg alloys containing different magnesium contents for different durations. The samples obtained were analyzed by using scanning electron microscope (SEM) and transmission electron microscope (TEM). According to the results of these analyses, a thermodynamic analysis of the possible chemical reactions was conducted and a reaction mechanism was suggested. The results showed that it is possible to differentiate different alumina particles by using the infiltration system.

For the infiltration set-up, a capillary model was developed based on an energy balance, and it was shown that this model could be used to pre-select the bed media based on its wetting characteristics. In this capillary model, the pore space between the alumina particles in a cross-section of an experimental alumina bed was represented by a number of capillaries with an average radius. Upon the application of an external force, the molten metal infiltrates the bed through. Making an energy balance for this infiltration, the wetting characteristics of different (rough) alumina particles were found. The same model was used considering a pore size distribution. Similar results were found.

In this study, the data from the experimental work were also compared with the predictions of a model from the literature representing the penetration of liquid metals into porous refractories [14]. This model modifies certain aspects of classical capillary theory. The pore spaces are represented by vertical cylindrical capillaries with changing radii according to the porosity distribution which is measured experimentally. The maximum height of the metal in the capillaries is found by calculating the pressure difference according to Laplace's equation for cylindrical capillaries and inserting the known contact angle values. In this work, the metal penetration height in the capillaries is already available. Thus, the contact angles were calculated using the capillary radii determined experimentally from image analysis. The results obtained from the above two models were compared with the result of this model, and a good agreement was found.

CHAPTER 2

THEORY

In this study, the physicochemical interactions between different interfaces were investigated. This necessitates the quantitative definition of an interface, which may be defined by one of three related quantities, namely surface tension, surface free energy, and surface stress.

2.1 Surface Tension, Surface Free Energy, and Surface Stress

For a better understanding of surface tension, surface free energy, and surface stress, the key concept is equilibrium, and it is best described in terms of a thermodynamic quantity called the free energy. In brief, free energy is a function of the internal energy of a system, and also the randomness or disorder of the atoms or molecules (or entropy). A system is at equilibrium if its free energy is at a minimum under some specified combination of temperature, pressure, and composition. In a macroscopic sense, this means that the characteristics of the system do not change with time but persist indefinitely; that is, the system is stable. A change in temperature, pressure, and/or composition for a system in equilibrium will result in an increase in the free energy and in a possible spontaneous change to another state whereby the free energy is lowered.

Either Gibbs free energy or Helmholtz free energy can be used to measure free energy quantitatively. If the process takes place under constant temperature and pressure conditions, then by using Gibbs free energy, the equilibrium conditions can be predicted. On the other hand, Helmholtz free energy is used if the process occurs at constant temperature and volume conditions. Between these two thermodynamic quantities Gibbs free energy is generally more convenient because around us many processes occur isothermally at atmospheric pressure, i.e. at constant temperature and pressure.

Interfacial tension, γ, is defined as the contractile force of an interface between two phases [15]. Thermodynamically, it can be defined as the work (W) required for creation of an additional unit area (A) at constant temperature, volume, and chemical potential between two phases.

$$\gamma = \left(\frac{dW}{dA}\right)_{T,V,\mu_i} \tag{2.1}$$

By definition, interfacial tension between two phases, one of which is a gas, is called surface tension [15]. In high temperature metallurgical applications, usually three phases (solid, liquid, and vapor) coexist in a system. As a convention, only the interfacial tension values between liquid and vapor phases are called as surface tension. Unless otherwise specified, in this text, surface tension will refer to the interfacial tension between liquid and vapor phase.

Creation of an additional unit area is possible by either breaking chemical bonds at constant strain or by applying elastic strain. If the additional unit area is generated at constant strain by breaking chemical bonds, the value of surface tension can be approximated if the energy associated with the chemical bonds and the number of the chemical bonds per unit area of the surface formed is known. Considering the atom density is going to be different on different crystallographic planes, it can be stated that the surface tension in a solid crystal is anisotropic, and generally the highest atom density planes have the lowest values of surface tension. Cleavage achieved without any plastic or elastic deformation of a solid is a good example for this kind of surface creation.

Sometimes, for example in some metallurgical calculations, it is more convenient to replace the work term defined at constant temperature and volume with a dimensionally equivalent term. For this purpose *surface free energy* is defined. It is the change in the Helmholtz free energy (A') of the system per unit area of interface generated between liquid and vapor phases. The relationship between surface tension and surface free energy for pure metals is given as [16, 17]:

$$\gamma = \frac{dA'}{dA} \tag{2.2}$$

and for alloys as:

$$\gamma = \frac{dA'}{dA} - \sum_{i=1}^{m} \mu_i \left(\frac{dn_i}{dA} \right) \tag{2.3}$$

From these equations it is seen that surface tension is equal to the surface free energy in pure metals but not in alloys.

Second way to create an additional unit area without increasing the number of surface atoms is application of purely elastic strain. As explained by N. Eusthathopoulos et al. [18], the extra stress due to the surface, called by Gibbs (1961) "surface tension" or by other authors "surface stress" (Mullins 1963, Cahn 1989). In this text, Mullin's or Cahn's definition is used, and the extra stress due to the surface is called the surface stress.

Surface stress is the work required to deform a surface. To describe the state of stress in a material, one must specify three normal stress components. Similarly, to describe the state of stress on a surface in general, one must specify two normal stress components, e_{xx} and e_{yy}, and one shear stress component, e_{xy}. It is shown [16, 17] that the relationship between these surface stress components and the surface tension is given as $e_{xx} = \gamma + \frac{d\gamma}{de_{xx}}, e_{yy} = \gamma + \frac{d\gamma}{de_{yy}}$, and $e_{xy} = \frac{d\gamma}{de_{xy}}$, where e_{xx} and e_{yy} are normal strain components and e_{xy} is the shear strain component. If the surface atoms can maintain their same configuration via migration as the surface is stretched, $\frac{d\gamma}{de_{ij}}$ term will be zero, then surface stress will be equal to surface tension. This equality of surface tension and surface stress generally holds in liquids, but it holds in solids only for processes occurring at high temperatures and relatively slow rates.

2.1.1 Contact Angle and Wettability Parameter

Most of the interfaces observed during critical natural or artificial (man made) interactions are complex. During these interactions, there exist generally three phases (solid, liquid, vapor) which create three interfaces: solid/vapor, solid/liquid, and liquid/vapor. These phases meet at a point which is called triple point. A force balance conducted at the triple point determines the *wettability* of the solid phase by the liquid phase in the existence of vapor phase. The wettability can be determined by using optical methods directly. In this case, the angle between the tangents drawn to solid/vapor and liquid/vapor interfaces is defined as *contact angle* and denoted by θ. *Goniometry* is the branch of science interested in this kind of optical measurements and there exits a number of goniometric measurement methods in literature. These measurement methods are more detailed in the following chapter.

In this study, the objective was to measure the wettability of granular media. For this purpose two different methods were used. First one is the sessile drop method. The second one is the infiltration method.

2.1.1.1 Sessile Drop Method

In sessile drop method, a liquid drop rests on a smooth, rigid, insoluble, and homogenous solid substrate in a gaseous atmosphere. Liquid and vapor phases are in contact with the solid at triple point. In this case, it can be shown that equilibrium is possible only if the liquid/vapor interface forms a definite angle with solid. By convention, this angle is called the contact angle on a smooth surface, θ_s, as shown in Figure 2.1, and it characterizes the wetting of the substrate by the liquid.

A projection on the horizontal axis of the forces acting on the triple point eliminates the contribution of the gravity force and yields the following condition for equilibrium:

$$\cos\theta_s = \frac{\gamma^{sv} - \gamma^{sl}}{\gamma^{lv}} \tag{2.4}$$

where γ^{sv}, γ^{sl}, and γ^{lv} are the interfacial tension values of solid/vapor, and solid/liquid interfaces, and surface tension, respectively. This equation was first derived by Young [19], but it is often referred to as the Young-Dupré equation [20].

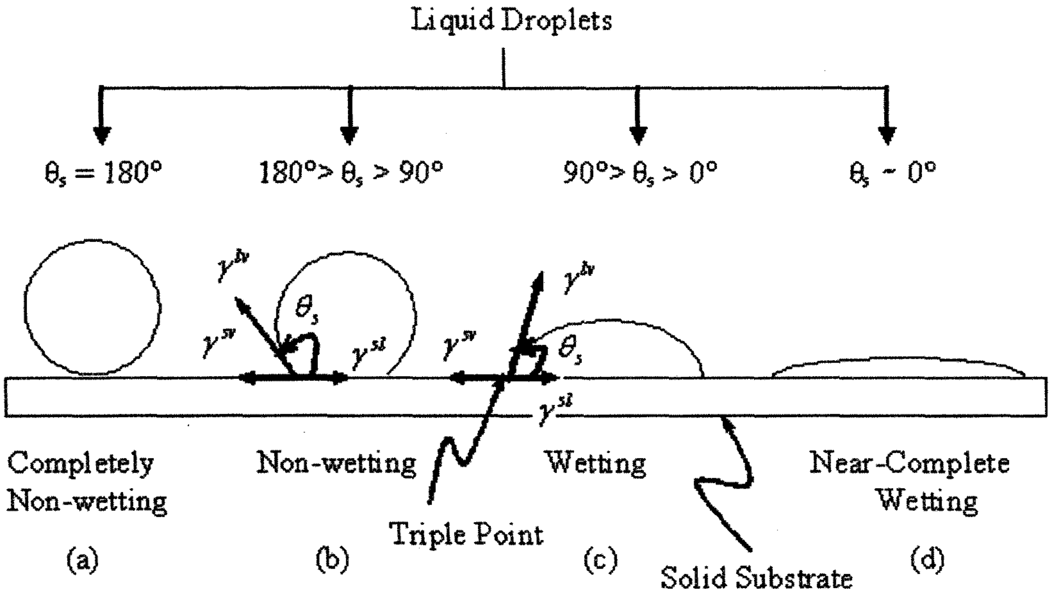

Figure 2.1 Determination of Wettability by Using θ_s Values

In literature, usually a liquid is considered to wet a solid when the *wettability parameter,* $\gamma^{lv}\cos\theta_s$, is greater than zero (a positive value) or the value of contact angle, θ_s, is between 0° and 90°. In this case, the degree of wetting increases as θ_s approaches 0. When non-wetting conditions apply, the wettability parameter becomes negative. Then, the degree of wetting decreases as the value of θ_s approaches to 180. In short, the wettability parameter and/or the contact angle can be used as the measure(s) of wettability.

When the contact angle term, θ_s, is used, it refers to a stable system as described above, and the overall condition of the system is called as static. Handling the system in this state is relatively easier than handling it before the equilibrium conditions are attained. When the system is dynamic, the situation is a lot more complicated, and a phenomenon that is called contact angle hysteresis is observed.

2.1.1.2 Infiltration Method

As an alternative to the direct measurement methods, the wettability of porous media can be measured indirectly by the infiltration method. The results are analyzed using capillary models.

Capillarity and Capillary Models

Leonardo da Vinci [21] (1452-1519) is believed to have been the first to observe capillarity phenomenon [22] which is closely related to the development of the concepts of surface tension that was revised briefly above. The phenomenon became known as capillarity because the tubes that were used possessed a bore as fine as a hair (in Latin: capillus = hair). After da Vinci, Isaac Newton [23] (1642-1727) referred to the forces of cohesion and adhesion that produce the rise of liquid in a capillary tube. He recognized that the forces were intermolecular in origin and that the mutual attraction gave rise to a pressure inside the liquid. At the end of 17th century, Hawksbee [24] performed the first accurate observations of the ascent of liquids in capillary tubes and between glasses. A half century later von Segner [25] brought together Newton's concept of cohesive forces and Hawksbee's idea of surface matter and proposed the first theory of capillarity. According to his theory, cohesive forces created a pressure which was resisted by a uniform tension in the surface. This tension was called the surface tension and was thought to explain capillarity. Following von Segner, in their simultaneous publications, Thomas Young [19] and Viscompte Pierre S. de Laplace [26], have shown that the pressure across a curved surface (Figure 2.2) was a consequence of two radii of curvature and not just one radius as suggested by von Segner. Their equation was:

$$\Delta P = \gamma^{lv}\left(\frac{1}{C_1}+\frac{1}{C_2}\right) \tag{2.5}$$

where ΔP is the pressure difference between any two sides of a curved surface element with principal radii C_1 and C_2, as shown in Figure 2.2 below.

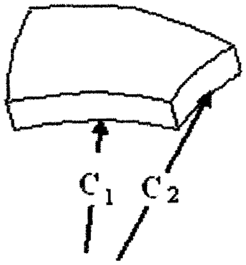

Figure 2.2 A Curved Surface Element with Principal Radii C_1 and C_2

For the specific case of a spherical meniscus inside a cylindrical capillary of radius r_{cap}, where the contact angle is θ, Equation (2.5) becomes:

$$\Delta P = \frac{2\gamma^{lv}\cos\theta}{r_{cap}} \tag{2.6}$$

Equation (2.5) is the fundamental equation governing the shape of all macroscopic menisci. The shape of menisci is important because it gives an idea about the wettability of the material under consideration and spontaneity of the process. For example, when a cylindrical glass capillary is immersed vertically in an infinite reservoir of water, it is observed that the water climbs through the capillary spontaneously, and the contact angle, θ, is smaller than 90°; however, this effect does not occur when the same capillary tube is immersed into mercury [27]. The motion of the liquid in the capillary in upwards direction is not spontaneous, and contact angle, θ, is larger than 90° [28]. This results in capillary depression. Figure 2.3 shows spontaneous capillary penetration and capillary depression as described above for water and mercury, respectively.

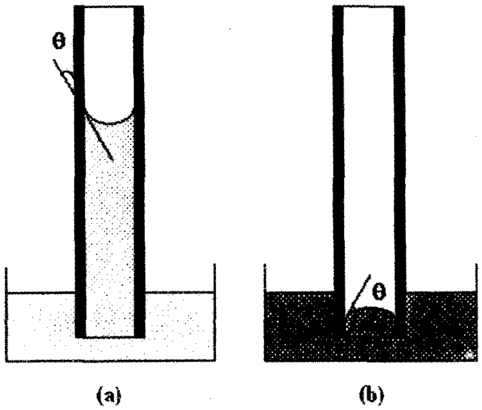

Figure 2.3 (a) Capillary Rise for Water, $\theta<90°$
(b)Capillary Depression for Mercury, $\theta>90°$.

Capillary models for porous medium are constructed by visualizing the porous medium as consisting of an assembly of capillaries. There exists a variety of capillary models such as straight, parallel type, serial type, branching type or network.

Models Used in This Study

Capillary Model Based on Energy Balance

a) Model I: With an Average Pore Size

In this model, a capillary model with straight vertical capillaries with a uniform size is used to represent the infiltration of liquid aluminum into a packed bed of alumina particles and to analyze the experimental data. It is known that aluminum does not wet alumina, so aluminum does not enter between the particles in the compacted bed spontaneously. A force has to be applied which will balance the surface tension, viscous and gravitational forces. When the magnitude of applied force increases sufficiently to overcome all the counteracting forces, the metal will infiltrate into the bed (Figure 2.4).

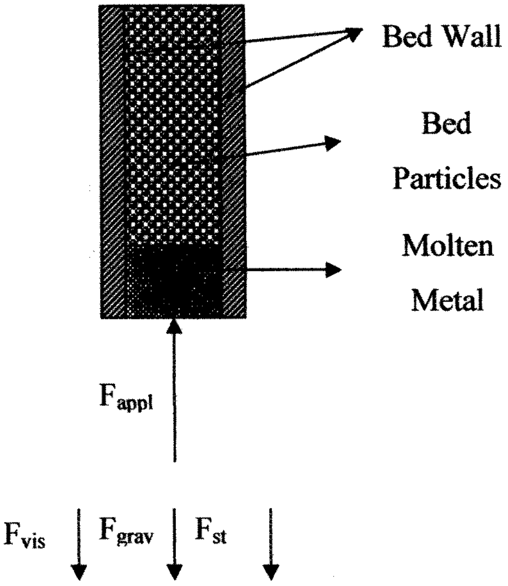

Figure 2.4 The Schematical Representation of the Forces Acting During Infiltration

F_{appl}: Applied Force
F_{vis}: Viscous Force
F_{grav}: Gravitational Force
F_{st} : Surface Tension Force

The period between the starting time and the time at which the penetration takes place is called the incubation period. During this period, the contribution of viscous force is very small compared to the contributions of others. Therefore, it can be neglected, and an energy balance for a capillary during this incubation period can be written as:

$$\Delta E_{appl} + \Delta E_{grav} + \Delta E_{st} = 0 \tag{2.7}$$

where ΔE_{appl} is the amount of energy given to the system externally per capillary during the incubation period, ΔE_{grav} is the change in the potential energy of the metal infiltrated through the alumina per capillary during the same period, and ΔE_{st} is the energy change due to surface tension forces along the length of the alumina bed during incubation. The energy given to the system can be calculated as:

$$\Delta E_{appl} = \int_0^l \left(F_{appl} / n_{cap}\right) dl \tag{2.8}$$

where F_{appl} is the force applied to push the aluminum into the alumina bed, l is the height of the capillary and n_{cap} is the number of capillaries present in the bed which is calculated from:

$$n_{cap} = \frac{\pi\, r_{bed}^2\, \varepsilon_{bed}}{\pi\, r_{cap.}^2} \tag{2.9}$$

where r_{bed} is the radius of the alumina bed, ε_{bed} is the porosity of the bed, and r_{cap} is the radius of the capillary. The hydraulic radius of the capillary, r_h, can be found using [29]:

$$r_h = \frac{\pi\, r_{cap}^2}{2\,\pi\, r_{cap}} = \frac{r_{cap}}{2} \tag{2.10}$$

Also, it can be shown that:

$$r_h = \frac{D\,\phi\,\varepsilon_{bed}}{6\,(1-\varepsilon_{bed})} \tag{2.11}$$

where D is average particle diameter, and ϕ is shape factor, which is defined as:

$$\phi = \frac{4\,\pi\,A_{par}}{Per_{par}^{2}} \tag{2.12}$$

where A_{par} is the area of the particle, and Per_{par} is the perimeter of the particle. ϕ and r_h are found from image analysis using optical microscopy. Then, r_{cap} and n_{cap} are calculated using Equations (2.9) and (2.10).

The energy due to gravitational force can be written as:

$$\Delta E_{grav} = \frac{1}{n_{cap}} \int_0^l (m\,g)\,dl \tag{2.13}$$

where m is the mass of the molten metal, g is the gravitational acceleration.

The energy due to surface tension force is given as:

$$\Delta E_{st} = \int_0^l 2\,\pi\,r_{cap}\,\gamma^{lv}\cos\theta_r\,dl \tag{2.14}$$

where γ^{lv} is the surface tension of liquid/vapour interface, and θ_r is the contact angle on the rough surface which is more detailed in the next chapter.

b) Model II: With Pore Size Distribution

This model is similar to the first model; however, a pore size distribution is used instead of an average pore size representing the whole bed. The pore size distribution curve is divided into a number of sections. Every capillary radius of each section, r_{cap_i}, and the number of capillaries in each section, n_{cap_i}, are given by Equations (2.9) and (2.10), respectively. The total energy balance is given in Equation (2.7). The components of the energy balance are determined using the following equations:

$$\Delta E_{appl} = \int_0^l (F_{appl})dl \tag{2.15}$$

$$\Delta E_{grav} = \int_0^l (mg)dl \tag{2.16}$$

$$\Delta E_{st} = \int_0^l 2\pi\left[\sum_i (r_{cap_i})(n_{cap_i})\right](\cos\theta)dl \tag{2.17}$$

Capillary Model Based on Force Balance

c) Model III: With Periodically Changing Pore Radius

This model was developed by Kaptay et al. [14]. The pore spaces were represented as cylindrical capillaries with periodically changing radii as shown in Figure 2.5. The force balance explained in the previous section is the same for the capillary model of cylindrical pores with periodically changing radii (see Figure 2.4). The contribution of viscous force is too small; thus, it is neglected. When penetration in the capillaries is less than 1 mm, the gravitational force is small compared to the surface tension force; therefore, gravitational force is also neglected. Since the total bed cross-sectional area is constant, the force balance for the incubation period, which is defined in the previous section, can be reduced to:

$$\Delta P_{appl} + \Delta P_{st} = 0 \tag{2.18}$$

where ΔP_{appl} is the pressure difference due to applied force to push the liquid metal into the capillaries, and ΔP_{st} is the capillary pressure difference due to surface tension force.

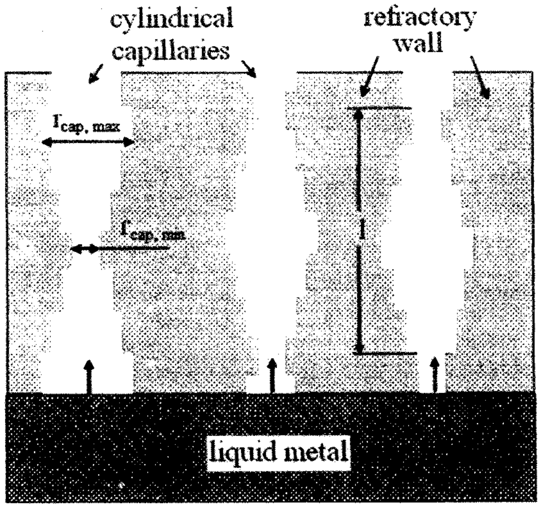

Figure 2.5. Schematical Representation of Capillary Penetration Model with different Radii. The Arrows Indicate the Direction of Molten Metal Penetration. (Figure is Taken from Reference [14]).

The height of the molten metal penetration in the refractory is calculated according to Equation (2.19) given below:

$$h_{penetration} = l\left(\frac{\Delta P_{appl} - \Delta P_{st,\min}}{\Delta P_{st,\max} - \Delta P_{st,\min}}\right)\frac{\Delta P_{st,\min}}{\Delta P_{appl}} \tag{2.19}$$

where $h_{penetration}$ is the height of the molten metal penetrated into porous refractory, l is the height of the capillaries having the same radii, ΔP_{appl}, is the pressure difference due to applied force to push the liquid metal into the capillaries, and $\Delta P_{st,\min}$ and $\Delta P_{st,\max}$ are the capillary pressure differences due to surface tension force at the beginning and the end of the incubation period. The capillary pressures are defined as follows:

$$\Delta P_{st,\min} = \frac{2(\gamma^{lv})\cos\theta_r}{r_{cap,\max}} \tag{2.20}$$

$$\Delta P_{st,\max} = \frac{2(\gamma^{lv})\cos\theta_r}{r_{cap,\min}} \tag{2.21}$$

where $r_{cap,\min}$ and $r_{cap,\max}$ are the minimum and maximum radius of capillaries, respectively, θ_r is contact angle on rough surface, and γ^{lv} is surface tension.

In the original model, $r_{cap,\min}$ and $r_{cap,\max}$ are determined from the pore size distribution which is measured by mercury porosimetry. ΔP_{st} values are calculated by inserting the appropriate radii values as well as the known contact angle, θ_r, and surface tension, γ^{lv} values for the materials used into Equations (2.20) and (2.21). The pressure applied, ΔP_{appl}, to force the metal for infiltration into the refractory is measured experimentally. Finally, using appropriate l values, molten metal penetration height, $h_{penetration}$, is calculated for different applied pressures.

In this study, this model is used: a) to predict penetration height as a function of time and applied pressure. This is compared with the experimental data of this study; b) to calculate the contact angle values. These angles are compared with those found from the previous two models.

The pressure applied on the system is calculated as:

$$\Delta P_{appl} = \Delta F_{appl} / \pi r_{bed}^2 \tag{2.22}$$

where ΔF_{appl} is the force applied to push the aluminum into the alumina bed, r_{bed} is the radius of the alumina bed.

The minimum and maximum of these ΔP_{appl} values in the incubation region give $\Delta P_{st,\min}$ and $\Delta P_{st,\max}$ values, respectively (see Equation (2.18)). Inserting the minimum and maximum radius of capillaries, $r_{cap,\min}$ and $r_{cap,\max}$, found from the image analysis, corresponding contact angle values are calculated by using Equations (2.20) and (2.21).

The height of the molten metal penetration according to this capillary model of cylindrical pores with periodically changing radii is calculated from Equation (2.19).

CHAPTER 3

LITERATURE SURVEY

3.1 Brief History of Wetting

For more than 400 years, well-known scientists like Leonardo da Vinci, Isaac Newton, Pierre Simon Laplace, Thomas Young, Siméon Denis Poisson, Josiah Willard Gibbs, Frederick M. Fowkes, and many others have conducted valuable pioneering work for the explanation of the basic concepts like surface tension, capillarity, and wetting phenomena. The maturity in many aspects is attained in late 19th century, and all of the accumulated information on wettability (mostly qualitative) started to be quantified rapidly. This transformation had impacts in various domains like pharmaceutics, painting, adhesive and textile industries, environmental and biological issues, and medicine.

The developments in aluminum industry started at the beginning of the 20th century. It was discovered that the properties of certain aluminum alloys could be improved by heat treatment. This stimulated the studies on aluminum alloys. As a result of 1st and 2nd World Wars, the production and application of high strength and low weight materials were favored. The increasing demand on novel joining or coating techniques of these kinds of materials increased the significance of wetting phenomena in the metallurgy, especially for aluminum. Then, the years of cold war shaped mostly the horizons of wettability studies and created new strategic fields like semi-conductors and optics.

Today's all known high technologies with a promising future, like wafer and chip production, composite materials, advanced joining and coating techniques, biochemistry and gene technology as well as micro-system technology benefit from the increasing understanding of the physicochemical nature of wetting.

3.2 Surface Tension and Contact Angle Measurement Methods

Surface tension and contact angle are the major parameters used for measuring wettability of materials. A summary of the existing methods for measuring surface tension and contact angle in literature is given in Table 3.1. They can be grouped into three main groups such as *tensiometric* methods, *goniometric* methods, and *infiltration* methods.

Table 3.1 Methods of Measuring Surface Tension and Contact Angle

Name of Method	**Kind of Method**	**Parameter(s) Measured**
Wilhelmy plate	Tensiometric	Surface tension / Contact angle
Single fiber Wilhelmy	Tensiometric	Surface tension / Contact angle
Du Noüy ring	Tensiometric	Surface tension / Contact angle
Metal rod	Tensiometric	Surface tension / Contact angle
Spinning drop	Goniometric	Surface tension
Maximum bubble pressure	Goniometric	Surface tension
Drop weight	Goniometric	Surface tension / Contact angle
Pendant drop	Goniometric	Surface tension / Contact angle
Sessile drop	Goniometric	Surface tension / Contact angle
Liquid intrusion	Infiltration	Surface tension / Contact angle
Direct measurement	Infiltration	Surface tension / Contact angle
Pressure of displacement	Infiltration	Contact angle
Modified pressure of displacement	Infiltration	Contact angle
Ultrasonic vibration	Infiltration	Contact angle
Rate of capillary penetration	Infiltration	Contact angle

3.2.1 Tensiometric Methods

Tensiometric methods listed in Table 2.1 take their names from the name of the probes used during experimental work, e.g. Wilhelmy plate, DuNoüuy ring, metal rod. The experimental set-up for these methods consists of a probe which is suspended from a sensitive force balance above a testing liquid stored in a reservoir. The probe is brought into contact with the testing liquid. Then, it is submerged into the liquid. After reaching the desired depth, the probe is taken out of the liquid. Starting from the moment that the probe touches the surface of the liquid, it experiences a certain force. The magnitude of this force is measured and recorded. Then, the compiled data is used to calculate the surface tension or contact angle.

There are three main advantages of these tensiometric methods. First, since the contact angles are determined from the forces measured, there is no possibility of subjective error. Second, they allow the user to analyze contact angles produced from wetting over an entire range of velocities throughout the static to dynamic wetting conditions. Therefore, the data compiled are very useful in studying hysteresis. It is possible to visualize the variations of the contact angles, both advancing and receding, through the entire length of the sample. Third, the analyses of fibers can be handled easier by a tensiometer.

There are three major limitations for the application of these techniques. First, the user must have enough of the liquid being tested so that a portion of the solid can be immersed in it. Second, the solid sample should meet certain requirements: (i) The solid sample must be formed or cut in a regular geometry such that it has a constant perimeter over a portion of its length. Rods, plates or fibers of known perimeter are ideal. (ii) The sample must have the same surface on all sides which contact the liquid. (iii) The sample must also be small enough so that it can be hung on a microbalance. Third, it is more difficult to use these techniques for high temperature systems.

3.2.2 Goniometric Methods

As it was mentioned before, the analyses of the shape of a liquid drop and/or assessing directly the contact angle values enter the application field of *goniometry*. If only the surface tension at the surface of a liquid is required, the spinning drop method [30] or the maximum bubble pressure method [30] is chosen. In the spinning drop method, the size and shape of a droplet profile, which has been deformed by a centrifugal field or force, are observed. In the maximum bubble pressure method, the size and shape of an air bubble which is pushed by means of a pressure through a vertical tube immersed into a liquid is investigated. The drop weight method [30] is one of the techniques which can be adapted to high temperatures. In this method, a relation between the weight of a drop formed and surface tension is obtained, and the contact angle is found from this data. Surface tension and contact angle can also be determined by using pendant drop method [30, 31, 32]. This method is well suited for high temperature and pressure applications. Contact angle and other parameters necessary for the calculation of surface tension are obtained from optical observations of the shape and size of the pendant drop. Another goniometric method reported in the literature is sessile drop [18, 30, 31]. Since this is one of the methods used in this study, more detailed information will be given on this method in the following section.

3.2.2.1 Sessile Drop Method

More than 80% of wetting studies at high temperatures are conducted by using different variants of the classic sessile drop method [18, 30, 33], such as in situ formation of alloy, dispensed drop, transferred drop, double substrate, tilted plate.

A classic sessile drop experimental set-up mainly consists of a closed-end, horizontal quartz [34, 35] or metal tube heated externally by an appropriate resistance furnace. Generally, a quartz window is fitted to one end of the tube in order to be able to capture the images of sessile drops. After the substrate and metal sample are prepared, metal sample is put onto the substrate and they are placed into the furnace. When the atmosphere inside the furnace is taken under control, the sample and the substrate are heated up to the desired temperature. The experiments are finished after a series of images of the sessile drop are taken at previously determined time intervals [36]. Value of contact angle, θ_s, is assessed directly from the captured images of the liquid drop's profile on the solid substrate.

Many scientists used aluminum [36, 37, 38, 39] or aluminum alloys [34, 39, 40, 41] for testing the wettability of certain substrates. Among the alloys tested there are binary alloys like Al-Si [34, 39, 40], Al-Cu [40], Al-Ni [40], and Al-Mg [34], ternary alloys like Al-Mg-Si [34] and Al-Cu-Mg [39], and four-component alloys like Al-Cu-Mg-Mn [41]. Other pure metals and alloys are also tested by sessile drop experiments. For instance, Saiz et al. [42] studied Ni, Cu, and Au metals, Wen Shi et al. [43] worked with Mg, Landry et al. [44] focused on Cu-Si and Cu-Cr alloys, Raraz et al. [45] studied the behavior of Cu-Cu_2O system.

Different researchers investigated the wettability of various polished substrates [36, 37, 44] like SiC [36, 39], AlN [37], alumina [34, 42, 43], polycor (99.7% alumina, 0.3% MgO) [40], corundum (94.87% alumina) [40], sapphire [38], copper oxide coated alumina [45], carbon coated sapphire [38], vitreous carbon [44], graphite [38], TiC [41], zirconia [34], titania [34], silica [34], silicon nitride bonded silicon carbide (Refrax) [39].

There are three important advantages of this method. First, various solid substrates with different surface characteristics can be tested. Although this method is designed basically for testing the wettability of rigid, insoluble, homogenous, and smooth solid substrates, it is also possible to investigate the effect of surface roughness, chemical reactions taking place along the metal alloy/substrate interface, and temperature [38, 40, 41] on the wettability of the substrate. Second, testing can be done using small quantities of liquid, and finally it is possible to conduct tests at elevated temperatures with acceptable accuracy and good repeatability.

On the other hand, there are some shortcomings of this method. First of all, the experimental results with sessile drop systems show that the oxidation of the metal at elevated temperatures is the most common problem in wetting studies. Because of oxidation problems, some scientists found sessile drop technique unreliable for measuring contact angles [46]. The control of the atmosphere has a key role to achieve practically sound results [42]. For this purpose, generally a diffusion pump is integrated into the system, and the oxygen partial pressure is dropped down to 10^{-7}-10^{-9} atm [34, 37, 38, 40, 41, 44], and the experiments are conducted under an inert atmosphere. Most of the scientists used an inert Ar [37, 41, 42] atmosphere; however, some of them tried different gas atmospheres. For instance, Nowok [36] maintained an atmosphere of purified argon gas together with 2% hydrogen gas, Foister et al. [39] used nitrogen gas during the experiments, Landry et al. [44] utilized helium. Sometimes titanium particles [34, 41, 47] and/or copper [37] are also placed in the vicinity of the samples in order to reduce the oxygen potential around the metal sample further [34].

Second shortcoming of this method is the assignment of the tangent line which will define the contact angle. In literature, the contact angles are measured from the image of the drop using different techniques. For example, a group of scientists measured the contact angles by projecting the image onto a screen in magnified formats [36, 44]. Some scientists [41, 47] treated the digital images manually with commercial software; however, this kind of treatment can lead easily to significant error in contact angle measurements, especially subjective error between multiple users, because conventional goniometry relies on the consistency of the operator in the assignment of the tangent line. Some scientists tried to overcome these difficulties encountered in measuring the contact angles by using computer programs to analyze the shape of the sessile drop. Some of the techniques applied to analyze the shape of the drop are based on the drop outlines obtained using singular points [18]. Others fit different functions to the drop profiles such as polynomial [48, 49] or ellipsoid [50]; or a least square fit is carried out [50]. The intersections of the baseline and drop profiles (liquid-solid-vapor intersection) are found from the simultaneous solution of the corresponding equations. The contact angle is calculated from the slope of these equations at the intersection points. Others use the theoretical knowledge of drop shape (Laplacian axisymmetric drop) which involves the solution of capillary equations [43, 50, 51, 52]. Then, the contact angles from these profiles are calculated using numerical solutions of differential equations. Some of these researchers use image analysis to obtain the drop profiles [50, 53, 54], then fit an expression to the drop profile to calculate contact angle and surface tension.

Other than the shortcomings mentioned above, three other disadvantages can be stated. First, the amount of surface sampled at each measurement is limited. Second, the fibers cannot be easily studied by using this method. Third, if the experiments are conducted under dynamic conditions, the conditions which produce advanced and receded angles are sometimes difficult to reproduce (hysteresis).

3.2.2.1.1 Effect of Roughness on Wettability

Sessile drop method is designed to measure the contact angles on smooth substrates. If surface is rough, the contact angle values measured on smooth surfaces are no longer valid. In other words, roughness of the substrate affects its wettability. Theoretically, if the liquid is wetting, the roughness is expected to increase the strength of the interface since a rough surface area is larger than the corresponding projected flat surface area [18, 55]. Therefore, by controlling the roughness of the surface, materials with higher strength and better performance can be developed. However, some studies show that the rough surfaces might not be completely wetted because of unfavorable wetting conditions between the solid and liquid and/or pinning effect of sharp edges of the triple line [18]; therefore, roughness itself can be a factor which affects material properties adversely [56, 57, 58].

In the literature, Wenzel [59] was the first to try to formulate the effect of surface roughness on the thermodynamic equilibrium contact angle (θ_s) between a liquid and a solid substrate. He claimed that if a smooth surface of a certain substrate wets well ($\theta_s < 90^0$), it will even wet better if the surface is rougher. Controversially, he predicted that if the smooth surface of a substrate does not wet well ($\theta_s > 90^0$), on the rougher surface a worse wetting behavior will be observed. He expressed this behavior mathematically as follows:

$$\cos\theta_r = W_r \cos\theta_s \qquad \textbf{(3.1)}$$

where W_r is the ratio of the actual wetted surface area to the geometric or projected area ($W_r > 1$), θ_r is the contact angle on a surface with roughness ratio "W_r", and θ_s is the thermodynamic equilibrium contact angle.

Wenzel's contribution to the literature led to definition of composite surfaces. It is explained that the lack of penetration is not due to the pressure of the air or the gaseous media trapped in the voids but is caused by the surface forces [60, 61]. For composite surfaces, Cassie and Baxter [62] derived an equation analogous to Wenzel's equation:

$$\cos\theta_c = X_1 \cos\theta_1 + X_2 \cos\theta_2 \qquad \textbf{(3.2)}$$

where X_1 and X_2 are the area fractions occupied by the two types of patches, and θ_1 and θ_2 are the corresponding intrinsic contact angles. In spite of the fact that Cassie and Baxter's approach is conceptually more complete than Wenzel's approach, it is not used frequently because it is very difficult to measure the identified terms practically [28].

Later on, Shuttleworth and Bailey [63] reported that a wide range of contact angles are observed instead of a single contact angle value predicted by Young's equation. To explain this phenomenon, they proposed the following relationship:

$$\theta_r = \theta_s \mp \alpha \tag{3.3}$$

where θ_r is the contact angle on a surface with roughness ratio "W_r", θ_s is the thermodynamic equilibrium contact angle, and α is the maximum angle (+ or -) of the local surface: contact angle hysteresis. In contrast to Wenzel's equation, Equation 3.3 predicts that the apparent contact angle will increase as roughness increases. Afterwards, most of the experimental studies conducted at low temperatures concentrated on either explaining the interaction between the contact angle hysteresis and surface roughness [64, 65, 66-68] or testing the validity of Equations 3.1 and 3.2. It can be concluded from these works that hysteresis topic remains still not well-understood and Wenzel's equation (Equation 3.1) explains the fundamental observation that roughening of the surface improves wettability for well-wetting systems [69-72]. However, for non-wetting systems, controversial points of views still exist [69, 65, 73].

In literature, there exist numerous attempts for predicting the wettability of the substrates by modeling the rough surfaces, and the triple line of the rough surfaces [73-76]. Although most of these studies are purely mathematical efforts [77-81], there are also a number of works which compare the numerical results of the mathematical models with the experimental data [72]. As explained above, although there is no consensus on Wenzel's equation, it is still the most commonly accepted theory to explain the effect of roughness.

Therefore, mathematical models which fit the experimental data are generally based on estimating the roughness ratio value, W_r, in Wenzel's equation (Equation 3.1).

In the recent studies, the scientists mostly accepted that "roughness" is defined as the root-mean-square (RMS) deviation from an arbitrary datum because roughness ratio value, W_r, in Wenzel's equation (Equation 3.1) is related to the RMS slope of a surface rather than any direct measure of amplitude. Originating from surface metrology context, RMS slope of a surface, is a function of RMS surface height, R, and the average distance between surface asperities, λ. It is a physical measure of surface irregularities and related to roughness ratio, W_r, by Hitchcock [69] as given below:

$$W_r = 1 + c_1\left(\frac{R}{\lambda}\right)^2 \qquad \textbf{(3.4)}$$

where c_1 is a constant.

In some of the high temperature roughness studies, randomly rough surfaces are also investigated [82]. The hysteresis is again one of the serious problems to determine the contact angle. The parameters necessary to calculate RMS slope of a surface are measured by profilometer [55, 58]. Usually, it is reported that the models which use RMS slope of a surface provide a good estimate for defining the roughness of the substrates [55, 73, 83].

3.2.2.1.2 Effect of Chemical Reactions on Wettability

In sessile drop experiments, as mentioned in previous sections, most of the time there are three phases. At elevated temperatures, molecular interactions between these phases gain importance. The interactions between solid/liquid and liquid/vapor phases are more pronounced and play an important role in determining the wettability of the system. These interactions are chemically governed most of the time and strongly depend on temperature. In literature, it is stated that the chemical interactions between solid and liquid phases can improve significantly the wetting on the liquid/solid interface, e.g. metal/ceramic interfaces. This phenomenon is called chemical wetting, and it is promoted by either introducing certain alloying elements into the metal [40, 46, 84-86] or coating the substrate surface with a substance chemically preferred by the metal [87, 88].

When alloying elements are added into a liquid metal, the alloying element that has a higher affinity for oxygen tends to migrate to the oxygen rich interface in order to produce an interfacial bond. Upon the reaction between the alloying element and the substrate, a continuous layer of solid, which is better wetted by the metal with respect to the original substrate, is created. The creation of this additional layer causes an increase in the surface energy and/or a fall in the metal/ceramic interfacial tension value.

In literature, the studies related to Al-Mg alloy/alumina interfaces can be found in the field of composite materials and refractories. The works on oxidation of Al-Mg alloys are also helpful for understanding the possible reactions taking place along the Al-Mg alloy/alumina interfaces. In these studies, it is reported that some chemical reactions take place on the Al-Mg alloy/alumina interface resulting in the formation of MgO (magnesia) and/or $MgO.Al_2O_3$ (spinel) [89, 90].

In the field of composite materials, magnesium is one of the common alloying elements added to the majority of alumina-reinforced aluminum metal matrix composites (MMCs). It adds strength to the composites and improves wettability of molten aluminum. Many authors think that spinel formation is responsible from improved wettability [87, 88, 91-93].

The studies in the field of refractories show that magnesium as an alloying element in aluminum contributes to an aggravated chemical attack on the refractories due to its reducing nature [94]. However, it is not the only problem. Calcium as an alloying element behaves also the same manner. Another important problem is the attack of aluminum to the silica in the refractories and the formation of spinel on the refractory surface. While spinel is forming, there is a volume reduction about 26% associated to this reaction. Hence, spalling of the refractories is observed. This causes many operational problems and generally increases the cost of the process. On the other hand, since spinel is a mechanically and thermodynamically stable phase at the operating temperatures, if the diffusion of aluminum can be blocked on the surface of the refractories and the formation of spinel can be favoured, this can serve as a barrier to inhibit further undesired interactions mentioned above. This idea inspired Moya et al. [88] to find a mechanism for using the spinel in prolonging the lifetime of refractories used in aluminum industry.

The works on the oxidation of Al-Mg alloys conclude that magnesium increases the oxidation potential of Al-Mg alloys because of its high affinity for oxygen [95, 96]. The analysis of the oxides formed on the surface shows strong evidence of extensive magnesia and spinel formation.

In the literature, different statements are found on the formation of spinel and/or magnesia based on the chemical reactions between Al-Mg alloys and alumina. It is usually reported that the liquid magnesium will react with alumina to form spinel or magnesia according to reaction given in Equations 3.5 and 3.6, respectively [87]:

$$Mg(l) + 4/3\,Al_2O_3(s) \rightarrow MgAl_2O_4(s) + 2/3\,Al(l) \tag{3.5}$$

$$Mg(l) + 1/3\,Al_2O_3(s) \rightarrow MgO(s) + 2/3\,Al(l) \tag{3.6}$$

Sometimes, it is suggested for spinel formation that first magnesia will form according to the reaction:

$$Mg(l) + 1/2\,O_2(g) \rightarrow MgO \tag{3.7}$$

Then, spinel particles will appear due to the reaction [97]:

$$MgO(s) + 2Al(l) + 3/2\,O_2(g) \rightarrow MgAl_2O_4(s) \tag{3.8}$$

In fact, the formation of spinel and/or magnesia phase(s) is a function of the gas surrounding the samples, alloy compositions, type of substrate, and experimental procedure. Therefore, the differences in type and composition of products arise mainly from these parameters. When the formation of these two phases was investigated, it was also observed that sometimes thermodynamically favorable reactions between the metal and the alumina do not take place. Then, the chemical kinetics gains importance [85].

3.2.3 Infiltration Methods

Wettability of particles forming a porous media can be measured by using one of the following infiltration methods:

(a) Liquid intrusion method

(b) Direct measurement method

(c) Pressure of displacement method

(d) Modified pressure of displacement methods

(e) Ultrasonic vibration method

(f) Rate of capillary penetration method

Liquid intrusion method is developed using the fundamental aspects of porosimetry [98]. This method is based on pressure-volume curves and specific area of powders.

Direct measurement method is a modified form of sessile drop technique [98]. In this method, rigid, solid, homogenous, and simple-piece substrates are replaced by a compressed cake of powders.

All the other methods, pressure of displacement, pressureless displacement, ultrasonic vibration, and rate of capillary penetration, use the concept of capillarity for modeling a porous media and calculating the wettability of a porous media by a liquid. The concept of capillarity is a very broad subject. In this literature search, the concept of capillarity was limited to the penetration and displacement [99, 100] in capillary systems [28, 67]. Some aspects of capillary penetration at low temperatures such as viscous fingering [101], penetration into mesoporous media [102], the existence of thin films in very narrow capillaries [103] or percolation theory approach [104] are not considered in detail since they are not used in the interpolation of the data in this project.

Historically, the quantitative measurement of particle wettability has been a challenge for scientists. Chronologically, first, Bartell [105-107] gave quantitative measurements of wettability in his works using capillarity concept. He measured quite reproducible pressure values. In the beginning of 1940's, Carman [108] introduced the concept of hydraulic radius. This concept was used to combine the capillary pressure and work of immersion (the work done by replacing the solid/gas interface with a solid/liquid interface) together by Oh et al [109] successfully. Thus, using the capillarity concept, the work of immersion was transformed into a quantitative measure of wettability. The advantage of this method is that the work of immersion is independent of particle size as well as shape and void fraction. It is only a function of threshold (minimum) pressure which is used to force the liquid metal into a porous structure.

The pressure of displacement method for high temperature applications is first proposed by Oh et al. [110]. Garcia-Cordovilla et al. [111], Jonas et al. [112], Mortensen [33], and others [113-124] followed him with some modifications in their systems. In this method, generally the molten metal is stationary in a chamber under a controlled atmosphere at elevated temperature. Pressurized inert nitrogen [113, 116, 117, 122, 123] or argon [115, 119, 121] gas is applied up to a previously determined pressure. Sometimes different atmospheres such as air [114, 115, 120, 124], argon/hydrogen [115], and nitrogen/hydrogen [115] are used. After the chamber is pressurized the porous structure is immersed into the molten metal.

Modified pressure of displacement methods can be grouped into two main categories: pressure of improved displacement method and pressureless displacement method.

In the pressure of improved displacement method, the surface characteristics of the non-wetting particles are modified by applying coatings [47, 113, 117, 122]. As a result of this treatment, the wettability of the particle surfaces enhances and the liquid metal infiltrates more easily.

Pressureless displacement method is developed as a novel approach for the manufacture of composites by some scientists [41, 125-127]. This method is based on using chemical interactions for driving the liquid into a porous structure.

Ultrasonic vibration is the only physical infiltration method. In this method, the necessary energy for infiltration is given to the system by ultrasonic vibration. It was applied to molten aluminum infiltration by a group a scientists [128, 129]. It was stated that full infiltration of molten aluminum through alumina particles and fibers was achieved without applying any external pressure. Short processing time and inhibition of non-infiltrated defects appearing at the contact points of the particles can be counted as the advantages of this method.

Rate of capillary penetration method is based on Washburn-type fluid flow equations [28, 35, 64, 67, 130, 131]. According to this theory when a porous solid is brought into contact with a liquid metal, infiltration of the liquid metal into the pores of the solid will obey the following relationship:

$$t = \left(\eta / c_{mat} \rho_{liq}^{2} \gamma^{lv} \cos\theta\right) m_{liq}^{2} \tag{3.9}$$

where t is the time after contact, η is the viscosity of the liquid metal, c_{mat} is the material constant (characteristic of solid sample), ρ_{liq} is the density of the liquid metal, γ^{lv} is the surface tension, θ is the contact angle, and m_{liq} is the mass of the liquid metal adsorbed on solid.

If an experiment is performed where the mass of the adsorbed liquid is measured with respect to time and if a graph of t versus m_{liq}^{2} is drawn by using this data, it should yield a straight line whose slope is $\eta / c_{mat} \rho_{liq}^2 \gamma^{lv} \cos\theta$. If viscosity, density and surface tension (which can be found using the same tensiometer) are known from separate experiments, there are only two unknowns left in this term, contact angle, θ, and the material constant for the solid, c_{mat}. To resolve this situation, an experiment is performed in which the contact angle may be assumed zero, i.e. during this experiment a liquid with very low surface tension is used. When such an experiment is performed, and the graph of t versus m_{liq}^2 is drawn fro the data obtained, the material constant for the solid may be solved from the slope of that graph (slope=$\eta / c_{mat} \rho_{liq}^2 \gamma^{lv}$). It is then possible to carry out experiments with any test liquid and calculate the contact angle for that system from Equation (3.9).

Many scientists contributed to a better understanding of the infiltration process by conducting kinetic studies. A theoretical review on the kinetics of capillary penetration can be found on a paper by Marmur [28]. Experimental works on the kinetics of capillary penetration are presented usually as infiltration kinetics in literature. The infiltration kinetics of various interfaces is studied by different scientists, e.g. Al/SiC [111, 115, 118, 123, 132], Al/TiC [35, 41, 133], Al-Ti alloys/SiC [118], Al/Al_2O_3 [111, 112], Al/ALTEX (85% Al_2O_3, 15% SiO_2) [119], Al/C [119], Al//α-Al_2O_3 [121], Al-Mg alloys/α-Al_2O_3 [112], Al-Mg alloys/SiC [118], Al-Pb alloys/Al_2O_3 [114], Al-Pb alloys/SiC [114, 124], Al-Si alloy/C-fiber performs [120], Al-Si alloy/SiC particulates [123], Al-Sn alloys/Al_2O_3 [114], Al-Sn alloys/SiC [114], Al-Si-Mg alloy/SiC particulates [124], Sn/SiC [118], Cu/Cu_2O coated alumina preforms [45].

There are also attempts in the literature for the modeling of infiltration [35, 112, 120, 132, 133]. Muscat and Drew [35] developed a mathematical model starting from Washburn equation. They considered the kinetic effect on the contact angle and incorporated into the model the effect of turtuosity. However, the notion of turtuosity was described as “somewhat doubtful” by Scheidegger [134]. Jonas et al. [112] proposed a model for the infiltration of Al-Mg alloys and α-alumina preforms. Edwards et al. [132] developed a model in order to explain the infiltration kinetics by using the technique of capillary rise for aluminum matrix SiC composite materials.

CHAPTER 4

EXPERIMENTAL SET-UP AND PROCEDURE

In this project, two different types of experimental methods were used to measure the wetting between molten aluminum and granular media. The first one is the "sessile drop" method and the second one is the "infiltration" method. In the following sections, the experimental set-up and procedures for both methods will be given.

4.1 Sessile Drop Experimental Set-Up

The experimental system for the sessile-drop measurements is shown in Figure 4.1. The experimental system consists of a tube furnace (Thermolyne F21135), a digital video camcorder (Canon, XL-1), a secondary, rotary vacuum pump (GE, Precision Vacuum Pump, Model D25), and an inconel tube which contains a metal injection system and a graphite sample crucible with three compartments (Figure 4.2). The sample to be tested is placed in the middle compartment. The other two compartments contain titanium particles which are used for the removal of residual oxygen. The graphite injection chamber holds the solid aluminum sample. This chamber has a small hole at the bottom and is placed just above the sample.

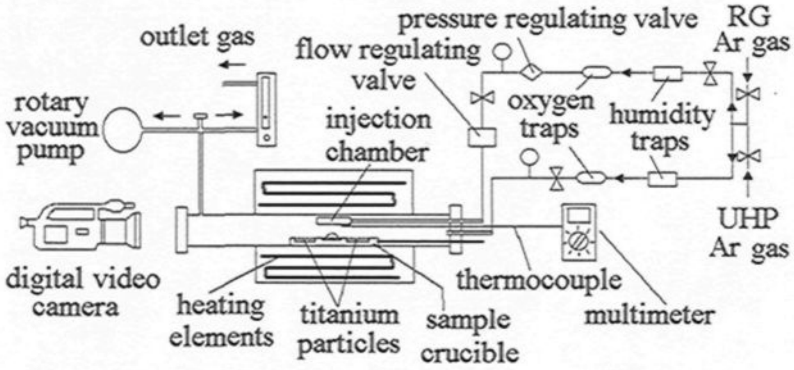

Figure 4.1 Schematical Drawing of Sessile Drop Experimental Set-up

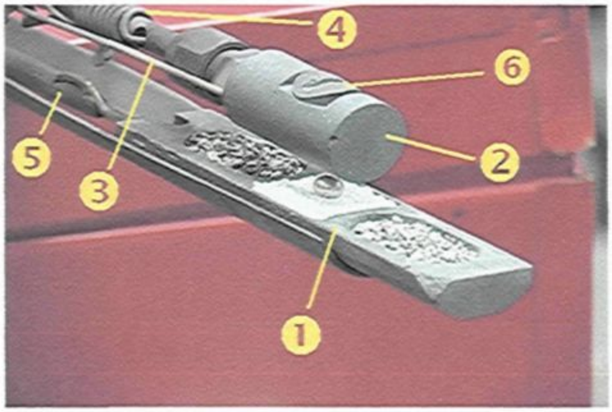

Figure 4.2 A General View of Metal Injection System and Graphite Crucible

1. Sample Crucible with Three Compartments
2. Injection Chamber Charged with Solid Aluminum
3. Thermocouple
4. Argon Supplying Line for Pushing the Metal
5. Sample Removing Mechanism
6. Cap of Injection Chamber Charging Hole

The atmosphere inside the furnace is controlled. The experiments are conducted under argon atmosphere. There are two entry lines for argon. The main line is directly connected to the inconel tube to maintain the inert atmosphere inside. The other line, which connects the injection chamber to inert gas supply, carries the necessary argon for pushing the liquid metal out of the injection chamber. Ultra high purity (UHP) and research grade (RG) argon gases with 99.999% and 99.9999% argon, respectively, are used during the experiments. The impurities certified by the supplier (Praxair) for each kind of argon gas are given below in Table 4.1. In order to decrease the oxygen and humidity content of the argon, it is passed through oxygen (Chromatographic Specialties, Oxygen Trap, C36060) and humidity traps (Chromatographic Specialties, Glass Moisture Trap, C36150) before it enters the system. Pressure of argon is measured on each of these two lines by manometers (Winter's Economy Gauge, 0-15 psi) with 0.1 psi accuracy. A simple system is installed on the secondary line, which is connected to the injection chamber, for generating a higher pressure with respect to the main line and depressurizing it when necessary. A compressed gas regulator which can regulate a maximum supply of 250 psi up to 140°F is used to pressurize the secondary line. The pressure range was 0-10 psi. In order to prevent the liquid metal to overflow over the particles and damage the furnace, the formation of the sessile drop is carried out in a controlled manner by relieving the pressure gently with a desired flow rate by means of a flow regulator (Nupro Company, Cleveland, Ohio).

Table 4.1 Summary of Impurities Reported by the Supplier of Argon Gas

Argon Gas Type	O_2 [ppm]	H_2O [ppm]	CO_2 [ppm]	CO [ppm]	THC[4] [ppm]	N_2 [ppm]	H_2 [ppm]
Research Grade	< 0.2	< 1	< 0.1	< 0.1	< 0.1	< 1	< 1
Ultra High Purity	< 1	< 3	< 1	N.A.	< 0.5	< 4	< 1

---

[4] THC stands for total hydrocarbon

4.2 Experimental Procedure of Sessile Drop Experiments

4.2.1 Master Alloy Preparation

The schematical drawing of the master Al-Mg alloy preparation system for sessile drop experiments is given below in Figure 4.3.

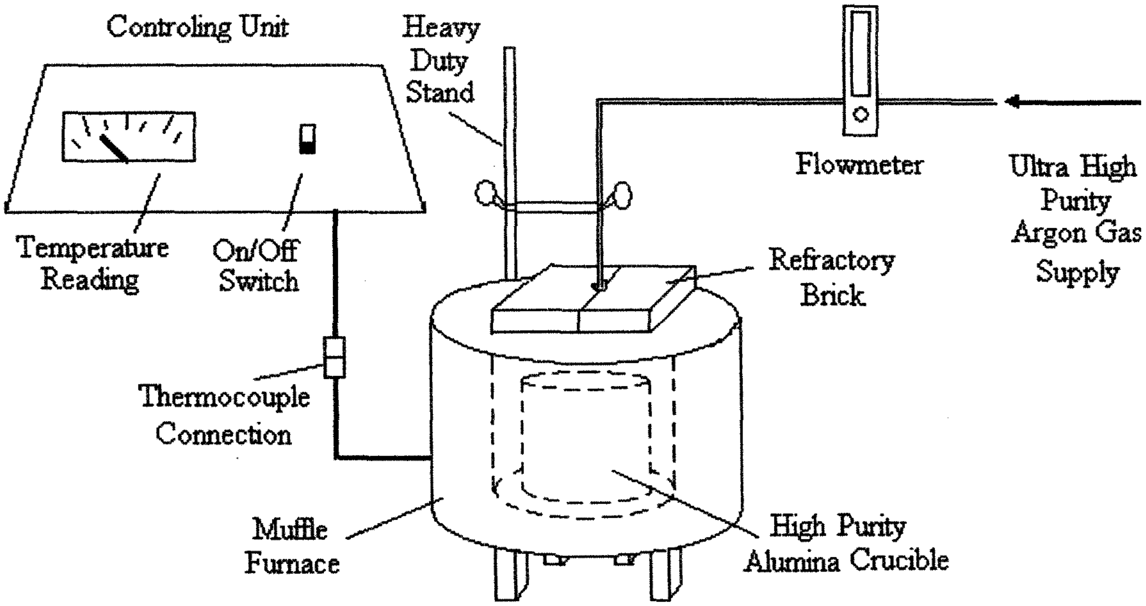

Figure 4.3 Primary Alloy Preparation System for Sessile Drop Experiments

Preparation of Al-Mg alloy was problematic at the beginning because magnesium has a high vapor pressure, thus, it tends to evaporate during alloying additions. This could cause magnesium levels significantly lower than theoretically calculated ones in the prepared alloys. This problem is resolved by developing a method for alloying. In this method, first the necessary amounts of scientific grade pure aluminum and pure magnesium

(NorskHydro, Noranda) are cut into pieces from their ingots in calculated amounts and are cleaned.

Pure magnesium is cut into rectangular prism shaped pieces. These pieces are machined into the form of cylinders each of which can enter into specially prepared high purity alumina tubes (CoorsTek, 99.8%-pure alumina, AD-998 Labware) 200-300 mm long with dimensions of 12mm (outer diameter, OD) X 8 mm (inner diameter, ID). 3-4 oval holes of 1 cm in height are opened on these tubes (see Figure 4.4). The upper ends of these high purity alumina tubes are isolated by applying a 2-5 cm thick BN paste starting from approximately 1 cm above the farthest hole from the bottom of these tubes, and they are left to dry in air. After the pastes are completely dry, the prepared magnesium cylinders are placed into them.

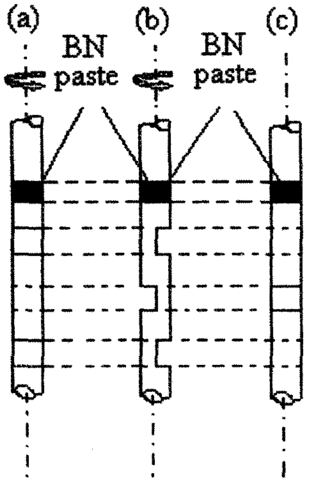

Figure 4.4 Schematically Drawn Specially Prepared High Purity Alumina Tubes (a) Original Position, (b) 90° Rotation with Respect to Original Position in the Direction Shown on the Figure Around Symmetry Axis, (c) 180° Rotation with Respect to Original Position in the Direction Shown on the Figure Around Symmetry Axis

Pure aluminum is cleaned by simply removing a thin layer from the exterior surface of the metal pieces by grinding with 120 grid emery paper. After these cleaned pieces of pure aluminum are put into a high purity alumina crucible (CoorsTek, 99.8%-pure alumina, AD-998 Labware), which has a height of 97 mm with 36.5 mm (OD) X 32.5 mm (ID), the crucible is placed into the muffle furnace (Welmet Industries Limited, 1.2 kW). The top of the furnace is covered with a refractory brick as shown in Figure 4.3, and UHP argon is supplied via a copper tube at a flow rate of 400 cm^3/min. The specially prepared high purity alumina tubes charged with pure magnesium are put on the brick horizontally to evaporate any entrapped water while the furnace is heating up. The furnace (Lindberg Hevi-Duty) is turned on. When the furnace reaches to the desired temperature, the temperature inside the melted aluminum is controlled by using a portable thermocouple. The thin slag layer on the metal is cleaned and magnesium is added into the molten metal by plunging the high purity alumina tubes vertically. The liquid alloy is stirred immediately after the magnesium addition with the tubes for 10-15 seconds. Then, the top of the furnace is closed again. After a predetermined time required for the dissolution of all of the magnesium, the high purity alumina tubes are taken away. Then, the slag is cleaned once more, and the bricks are again closed. The furnace is shut down and the metal is left to cool down while argon is still passing through the system. As soon as the metal is solidified and the temperature fall to about 250°C, the argon flow is interrupted.

The solidified master alloys are machined to obtain metal rods (see Figure 4.5 below) which can pass through the injection chamber charging hole shown in Figure 4.2.

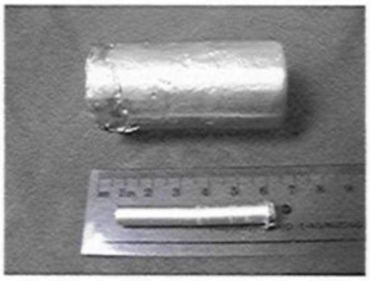

Figure 4.5 A Machined Metal Rod and a Cast Al-Mg Master Alloy

The chemical compositions of the alloys produced are obtained by analyzing the sections that are cut from the solidified master alloy in ALCAN.

4.2.2 Sample Preparation

The sessile drops are formed on the alumina particles by using two techniques as explained below:

a) Packed Particles

In the first technique, the alumina particles are packed in the sample crucible, and the sessile drop is formed directly on them. The sample crucible is filled with alumina particles and the particles are tapped with an aluminum weight. The size ranges of particles used in these experiments are 1.7 mm – 2.8 mm (Figure 4.6 (a)) or 1.0 mm – 1.7 mm (Figure 4.6 (b)). To reduce the oxidation of the drop, two other graphite crucibles, which are filled with titanium, are placed behind and in front of the sample crucible.

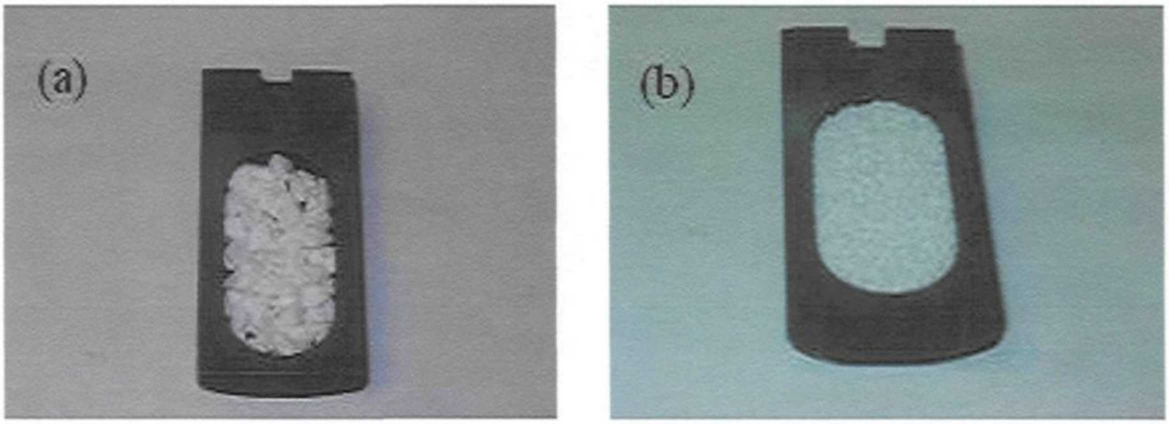

Figure 4.6 Sample Crucible Used with Packed Particles
(a) View of packed particles in the size range of 1.7 mm – 2.8 mm
(b) View of packed particles in the size range of 1.0 mm – 1.7 mm

b) Particles Fixed with a Binder

In the second technique developed, the alumina particles are cemented onto an alumina plate by using a binder, and the drop is formed on this layer of particles supported by the plate (Figure 4.7). In this case, smaller size alumina particles are utilized (0.3 mm – 0.5 mm, 0.5 mm – 0.7 mm, and 0.7 mm – 1.0 mm). The particles are crushed down by using a direct driven pulverizer (Braun, UD32). In order to prevent any contamination during crushing, the lining of the milling discs is specially chosen. They are made of alumina (Bico Inc, Burbank, California, Serial No. 54652). In addition, the impurities which can contaminate the crushed alumina particles are removed from the lining surface by grinding the surfaces of the linings using diamond points before the discs are utilized.

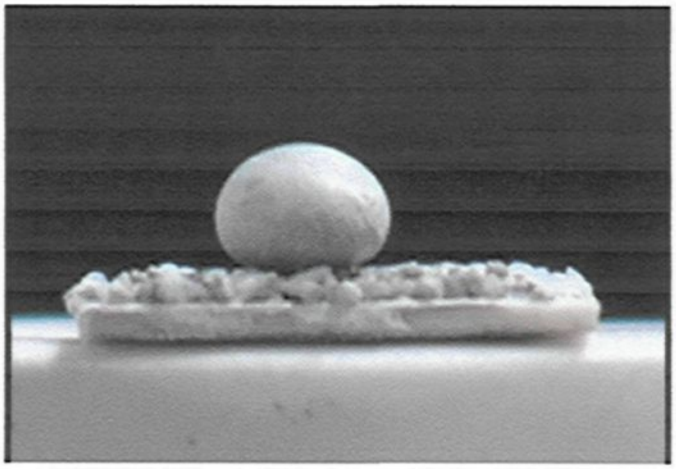

Figure 4.7 A Sessile Drop Formed on Alumina Particles Cemented onto an Alumina Plate

For the second case, a different sample crucible is designed (see Figure 4.8). This crucible has three compartments. The compartments in front and back of the middle compartment are filled with titanium particles to reduce the oxidation potential around the drop. The middle compartment has a large enough shallow space into which the prepared sample is placed during experiments. This space envelops the sample tight enough to prevent it from moving in any directions. The base of the sample is a 1 mm thick tabular alumina plate. It fits into the middle compartment firmly. It is cut from a larger alumina plate by using a diamond-tipped pencil (Agilent, catalog no: 420-1000) and cleaned neatly with distilled water. After it is dried on a hot plate (Scientific Products, TekPlate, Cat No. H2151), the binder is spread onto it.

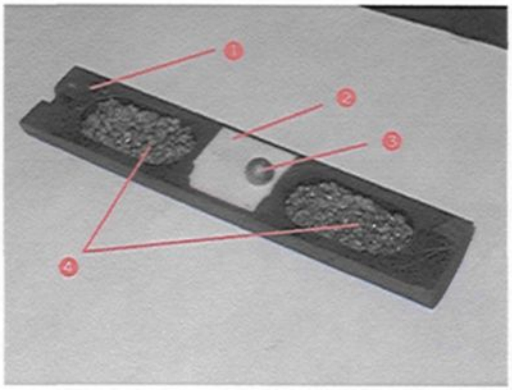

Figure 4.8 Photograph of the Sample Crucible with Three Compartments
(1) Sample Crucible
(2) Tabular Alumina Plate
(3) Sessile Drop
(4) Titanium Particles

Three kinds of binders are used (QF150, Alphabond100, and pure alumina). Their chemical compositions are given in Table 4.2. QF150 is a coating cement (Sohio Carborundum, Fiberfrax, Type QF150) in the form of a white paste. It is applied as thin as possible on the alumina plate. Then, the alumina particles with the desired size are sprinkled onto the alumina plate and tapped. If pure alumina (Buehler Micropolish II, 0.05 μ, 40-6325-016) or Alphabond100 (Almatis, former Alcoa) is used as a binder, a small amount of the alumina powder is added into distilled water and mixed to form a suspension of alumina particles. A few drops of this suspension are placed onto the alumina plate and they are spread over the surface with a capillary tube. When a very thin layer of suspension on the alumina plate is formed, the alumina particles to be tested are sprinkled onto the alumina plate and tapped.

After the alumina particles are cemented onto the alumina plate with a binder, the alumina plate is placed into a horizontal muffle furnace (Blue M, Electric Company, Mode no: RG-2090A-1, Serial no: GFV 770) which is preheated to 400°C. After it is baked there for 30 minutes, the temperature of the furnace is increased to 800°C. The alumina plate is baked for another 30 minutes at this temperature before the furnace is shut down. Then, the plate is left in the furnace to cool down slowly.

Table 4.2 Chemical Compositions of the Binders Used to Cement the Alumina Particles on the Alumina Plates

Ingredients	**Chemical Compositions of Different Binders [wt%]**		
	QF150	**Alphabond 100**	**Pure Alumina**
Al_2O_3	38.2	90.4	100
SiO_2	57.5	0.2	-
Na_2O	0.7	0.4	-
MgO	0.3	-	-
Fe_2O_3	0.7	-	-
TiO_2	1.5	-	-

4.2.3 Experimental Procedure

Before starting the experiments, UHP argon was passed through the furnace for 15 min. Then, all of the argon in the lines and inside the tube furnace is evacuated and the system is purged with UHP argon for another 15minutes. Vacuum is applied a second time for about 10 minutes and RG argon is filled into the furnace. After a steady RG argon flow is maintained, the set-up is heated to the desired temperature. When the temperature is stabilized at 730°C, the liquid aluminum in the injection chamber is pushed down gently by applying a small pressure to the line leading to the injection chamber. A sessile drop is formed, and the experiment started. The images of the drop are captured during for a desired time interval. Then, the furnace is shut down, and the sample crucible is pulled back by using a specially designed sample removing mechanism from the hot region of the furnace. This way, the sample is quenched for further analysis and the experiment is finished.

4.2.4 Titanium Recycling

When the industrially pure grade titanium particles are used once in an experiment, their exterior surfaces are oxidized. It is not economical to discard these oxidized titanium particles and use fresh titanium particles for each experiment because below the oxidized layer there is still considerable amount of titanium. Therefore, the oxidized titanium particles are cleaned and recycled by means of a particle cleaning procedure which was optimized by trial and error. The cleaning procedure is a long but efficient one. In this procedure, 75 ml 10% NaOH solution (by volume) is poured into a 100 ml conical flask into which a batch of oxidized titanium particles is added. The level of the liquid in the flask is marked. After the flask is placed onto a hot magnetic stirring plate (Fisher Thermix, Model 210T), the flask is closed by a rubber bung, and the solution is slightly heated and magnetically stirred for two days. During these two days, if it is observed that the level of the liquid is decreased, distilled water is added to keep the level of the liquid as marked. After hot leaching, the solution is decanted and the titanium particles are washed with fresh cold distilled water until the distilled water stays clean when added onto the particles.

4.3 Infiltration Experimental Set-up

Infiltration set-up basically consists of an inconnel tube placed into the heating zone of a single set point, vertical, electric tube furnace (Figure 4.9). Both ends of the inconnel tube are closed with specially designed, water cooled stainless steel screw-caps. The challenge of this design is that the alumina tubes with 11.4 mm outer diameter can be moved vertically within certain limits without causing a change in the controlled, inner atmosphere of the furnace or disturbing the steady temperature profile at the central zone of the furnace (up to 101.6 mm). Two alumina tubes were used in the construction of the experimental set-up. The one that can be fixed to the top screw-cap was called upper alumina tube while the other one supported by the bottom screw-cap was called lower alumina tube. Lower alumina tube supports the graphite crucible which holds the alumina particles and the aluminum alloy inside the inconnel tube during the experiments. A small CFF (ceramic foam filter) is placed between the particle bed and aluminum alloy in order to support the particles. A graphite piston, which blocks the motion of the graphite sleeve and alumina particles in the graphite crucible during the experiments, is fixed to the lower end of the upper alumina tube.

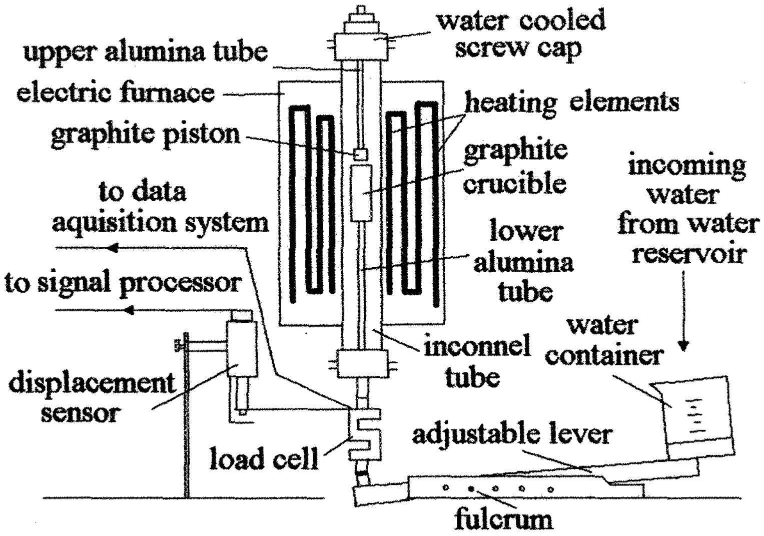

Figure 4.9 Schematical Sketch of Infiltration Set-up

The force required for the infiltration of molten metal through the alumina bed is applied by the mechanism shown in Figure 4.9. It consists of an adjustable lever which can be adjusted by changing the fulcrum of the lever before starting the experiment. A water container is placed on one end of the adjustable lever. During the infiltration experiment, distilled water flows from a reservoir into this container at a predetermined constant flowrate. The weight of the distilled water, which fills the water container, exerts a certain force on the adjustable lever at that point. This force is transferred to the other end of the lever and used to push the graphite crucible upwards (Figure 4.10). Since the upper alumina tube is fixed, the piston blocks the motion of the graphite sleeve and the alumina bed. This first squeezes the molten metal; and then, as the force applied increases linearly with time, the liquid metal infiltrates first through the CFF and then through the porous bed.

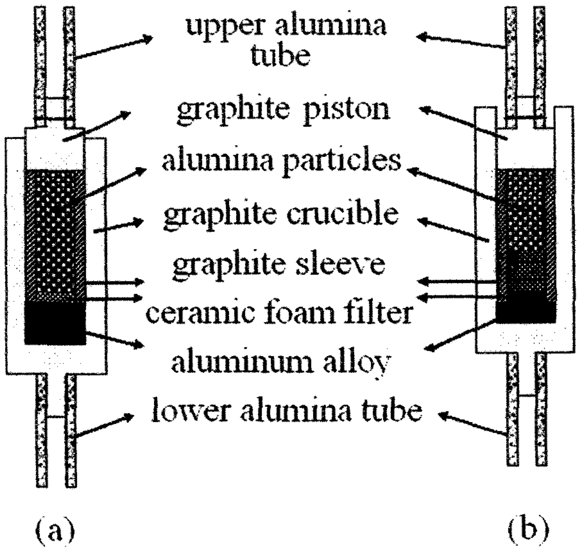

Figure 4.10 Schematic Illustration of the Elements (a) Before Infiltration (b) After Infiltration

The objective of the infiltration experiments was to determine the change in the height of the molten metal as a function of time and to measure the force necessary for this change in position within this time interval. For this purpose, a data acquisition system was installed to measure the displacement of the metal and the force applied as a function of time (Figure 4.9). In this data acquisition system, the displacement sensor (Omega, LD-100) detects the displacement and sends the information to a signal conditioner (Omega, Signal Processor, SP200A) which then sends the processed information to the module of instruNet (Omega, Model 100). A load cell (Omega, LCCA-25) is also placed onto the adjustable lever conveniently to gather the applied force information in situ as a function of time. Once the load cell starts to measure the applied force values, it sends also the information to instruNet module through another channel. The instruNet module sends the output of the incoming data in real time to a compatible data acquisition card which communicates with a computer by means of an interface so that the gathered data could be saved as a text file on the hard disk of the computer.

4.4 Physical Characterization of Granular Alumina Particles

All types of granular alumina particles used in the infiltration experiments have been sieved to have a size range of 1.19 – 1.41 mm. They were crushed by using the direct-driven pulverizer with alumina discs mentioned before. Although they were all in the same size range, their surface properties were not physically similar. Wenzel's approach for rough surfaces is used to express the degree of roughness of alumina surfaces, and a roughness ratio value for each type of granular alumina particles is found.

Roughness ratio values, W_r, are calculated from Equation 3.4. In this equation, there are three unknowns: c_1, R, and λ. Hitchcock [69] gives c_1 as an arithmetic factor with a value of about 50; but he adds that for surfaces consisting of close packed arrays of uniform cones, square based pyramids or spherical domes, c_1 is 56.5, 64.6, and 45.4, respectively. In this work, taking into consideration the three dimensional surface patterns of the alumina particles, c_1 was assigned a value of 60. Investigation of the three dimensional surface patterns of alumina particles showed that there were not spherical dome shapes on the surface. Therefore, c_1 value was calculated as an average of values corresponding to uniform cone or square based pyramid patterns only, i.e. 60.55~60. The other two unknowns, R and λ, are determined by using a profilometer equipped with a MicroXAM surface mapping microscope whose stage is controlled in two axes by a motor.

A profilometer determines the shape of the surface irregularities in three dimensions. Some sample images are given in Appendix A. It is possible to scan the surface more than once. In this project, the surface is scanned three times and their average is used for further analysis. An image analysis software[5] is also installed on the profilometer (MapVue-EX Surface Mapping Software ver.6-51). A short program (its code is given in Appendix B) is developed using the commands of this image analysis software. It fits to the surface irregularities a series of mathematical functions using the advanced profile analysis module of the software; and as a result, statistical parameters of the surface irregularities are recorded as MS Excel file. Then, these statistical analyses are processed using programs developed in Visual Basic for MS Excel to calculate R and λ values in transverse (horizontal) and longitudinal directions. The average of these calculated values are taken, and R/λ values for each type of particles are found. Then, taking c_1 as 60, corresponding surface roughness values, W_r, are calculated.

4.5 Chemical Characterization of Granular Alumina Particles

Eight types of alumina particles were tested using the infiltration system. The chemical analyses of these alumina particles are given in Table 4.3.

Table 4.3 Chemical Analysis of Alumina Particles Used in Infiltration Experiments

Element	Aluchem [wt%]	Alcoa [wt%]	Itochu [wt%]	Russian [wt%]	Naigai [wt%]	Alufin [wt%]	New Alufin [wt%]	Fused Alumina [wt%]
Ca	0.0289	0.0063	0.0193	0.0173	0.0142	0.0159	0.0339	0.0285
Cu	NA	NA	NA	NA	NA	NA	0.0018	0.0048
Fe	0.0153	0.0439	0.0143	0.0445	0.0099	0.0148	0.0150	0.0081
Ga	NA	NA	NA	NA	NA	NA	0.0037	0.0043
K	0.0000	0.0000	0.0000	0.0000	0.0000	0.0000	0.0074	0.0053
Mg	0.0042	0.0005	0.0013	0.0059	0.0016	0.0028	0.0099	0.0030
Mn	NA	NA	NA	NA	NA	NA	0.0024	0.0003
Na	0.0800	0.3139	0.2353	0.0214	0.0488	0.2260	0.3227	0.4518
Ni	NA	NA	NA	NA	NA	NA	0.0002	0.0001
Si	0.0956	0.0276	0.0285	0.1599	0.0593	0.0232	0.0150	0.0233
Ti	0.0028	0.0041	0.0043	0.0024	0.0041	0.213	0.3550	0.0051
V	NA	NA	NA	NA	NA	NA	0.0006	0.0013
Zn	NA	NA	NA	NA	NA	NA	0.0161	0.0241

In this table, for each type of alumina particles, the balance was taken as the pure alumina. The analyses were conducted by using induction-coupled plasma mass spectrometry (ICP-MS) in ALCAN's research facilities in Arvida, Saguenay.

---

[5] © Copyright 1985-2000 ADE/Phase Shift

4.6 Experimental Procedure of Infiltration Experiments

Experimental procedure of infiltration experiments can be divided into three main steps. First, the master alloys needed for the infiltration experiments are prepared. Second, the experiments are conducted, and then the samples obtained from the experiments are prepared metallurgically for optical microscope and scanning electron microscope (SEM) analyses.

4.6.1 Master Alloy Preparation

Pyradia™ resistance melting furnace and SiC graphite crucibles with 15 kg molten metal capacity are used to prepare Al-Mg master alloys for the infiltration experiments. The cover of the furnace is made of two Pyrotek™ B-3 rectangular refractory boards. When they are placed adjacently, they covered the top of the furnace. In order to prevent oxidation of the metal on the surface, the contact between the molten metal and air is prohibited by passing non-reactive CO_2 gas inside the furnace towards the top of the molten metal. For this purpose, a ¾ in. diameter hole was drilled in the middle of the refractory boards through which a copper gas pipe is inserted. This pipe is connected to a CO_2 gas source and carried the gas. The flowrate of CO_2 was 10 cubic feet per hour.

For the addition of magnesium, a special graphite plunger is designed. The handle of the plunger is screwed to the plunging head. Around the plunging head, there are circular holes to help the transfer of the melted magnesium into the liquid aluminum. At the bottom of the plunging head, there are two rectangular holes facing each other through which a graphite plate passes. This graphite plate serves to keep the magnesium pieces inside the plunging head. Before the furnace is turned on, the calculated amount of pure magnesium pieces are loaded into this plunging head. Then, it is placed onto the refractory boards to preheat the graphite. This prevents the fracture of graphite due to thermal shock which can dehydrate the magnesium pieces, consequently, prevents a possible explosion during alloying.

When the temperature of the pure molten aluminum reaches 740°C, the furnace is set to 720°C and the temperature in the furnace is decreased. When the temperature indicator of the furnace shows 725°C, the cover on the furnace is opened and the oxidized layer is removed with the help of a copper skimmer. Then, the plunger is submerged into the crucible towards the bottom. After it is left there for a certain time, to purge the metal and to attain a homogenous magnesium distribution in the molten metal, the plunger is started to be displaced up and down gently for a few minutes.

After all of the magnesium melted, the plunger is taken out of the liquid metal, and the cover of the furnace is closed. After a little while, the cover is opened again. The oxidized layer is skimmed away. The sample ladle is immersed in the molten metal sideways with a stirring action well below the surface for at least 15 seconds prior to sampling. Then, the ladle is turned upright and quickly withdrawn. The hot metal in the ladle is poured down inside the sprue cavity of the horizontal disk mold at an even rate to allow air to escape from the mold until the mold is filled appropriately. As soon as the butt is solidified, the sample is chilled immediately by dropping it into the water. After the chill, cast disks for analysis are produced, the surface of the metal is skimmed once more, and the crucible is taken out of the furnace by using 36 in. charging tongs. It is transferred to nearby stainless steel triangular prism molds, and Al-Mg alloy is cast. As soon as the exterior surfaces of the ingots are solidified, they are quenched in water. The crucible is replaced into the furnace. A certain amount of pure aluminum is put into the crucible. When the aluminum is melted, the inner surface of the crucible is cleaned with it. The resultant liquid metal is cast into another mold and recycled. After the crucible is cleaned before the subsequent use, the metal solidified around the plunger is also removed for further use by using line-man and needle-nose pliers.

The cast triangular shaped ingots are machined to obtain metal rods with the inner diameter of the graphite crucible as seen in Figure 4.11:

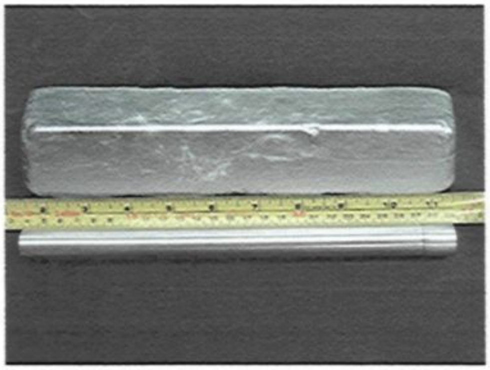

Figure 4.11 A Machined Metal Rod and a Cast Al-Mg Master Alloy

The chemical compositions of the Al-Mg alloys produced are obtained by analyzing the chill cast disks using arc optical emission spectroscopy (OES) in ALCAN.

4.6.2 Procedure for the Infiltration Experiments

The aluminum alloy necessary for the experiments is supplied by cutting the metal rods into cylindrical metal pieces. The surfaces of these metal pieces are ground roughly with 120 or 220 grit emery papers. After they are treated with a 15 vol% NaOH solution, they are washed with distilled water and brushed neatly to get rid of the basic solution completely. Then, they are dried with UHP argon. 30 pores per inches SIVEX® ceramic foam filter (CFF) blocks are machined appropriately to prepare CFF pieces that fit into the sleeve of the graphite crucible. These pieces are dried by heating them up to 150-200°C. For removing the tiny CFF particulates stuck on the CFF pieces during shaping, UHP argon is blown onto them. Before the metal piece is placed at the bottom of the graphite crucible, UHP argon is blown into the graphite crucible to remove any graphite dust. After the graphite sleeve is put onto the metal piece, CFF piece is placed into the sleeve onto the metal piece. The cross-section of the graphite crucible is shown in Figure 4.12.

Figure 4.12 Cross-section of the Graphite Crucible Before Addition of the Alumina Particles

The graphite crucible is placed on a metal support manufactured specially to be used with the vibrating table (FMC, Model VP-51-D1). Then, the metal support is fixed onto the vibrating table, with the help of the clamps on the vibrating table as shown on the image below (Figure 4.13):

Figure 4.13 The Metal Support Fixed onto the Vibrating Table

Alumina particles of desired type are weighed in a disposable aluminum weighing dish with handle (Fischer Scientific Cat. No. 08-732) by using a digital balance (Mettler PJ3000) to prepare a 1.00 g sample. They are poured into the graphite crucible by using a plastic funnel. Then, an aluminum rod, weighing 49.48 g. is placed onto the alumina particles, and the graphite crucible is vibrated for 1 minute.

While vibration takes place, another 1.00 g. sample of alumina particles of the same type is weighed in the empty aluminum weighing dish. When the vibration is finished, the aluminum rod is taken out and the recently weighed alumina particles are added into the graphite crucible. Then, the aluminum rod is reinserted into the graphite crucible. The vibrating table is restarted. The procedure described above is repeated until the level of the added alumina particles reaches the top of the graphite sleeve.

After the preparation of the alumina bed is completed, the graphite crucible is placed into the inconel tube, and vacuum is applied by using a primary vacuum pump. Then, the inside of the inconel tube is filled with UHP argon. Before the furnace is started, a continuous flow of UHP argon is assured. After the temperature inside the furnace reached the desired level (about 720°C), the furnace is kept at that temperature for five minutes. When the temperature is stabilized, the position of the upper alumina tube holding the piston is adjusted, fixed, and the experiment is carried out by applying force to the bottom of the crucible. The molten aluminum alloy passes through the CFF and the bed of alumina particles. The force applied and the change of the alloy height is recorded as a function of time.

When the infiltration is complete, the data are stored and compiled for further analyses. The results of these analyses determine the wettability of tested alumina particles by molten metal. Also, the infiltration experiments served to study the chemical interactions between alumina particles and various Al-Mg alloys. When the infiltration is complete, the alumina particles and molten metal are in contact and the chemical interaction starts between them. The completely infiltrated bed samples are held at constant temperature and pressure along the previously determined time intervals. When holding time is over, the furnace is shut down, and cooled down to ambient temperature. The bed samples were sectioned, mounted, and polished for investigating the reaction products by using optical and electron microscope analyses to study the reactions taking place.

4.6.3 Sample Preparation for Analyses

While the furnace is cooling down to ambient temperature, the liquid metal in the alumina bed is already solidified, and a solid sample is formed in the sleeve. The sample is taken out of the graphite crucible together with the sleeve. Generally, the sleeve enveloping the sample is broken to get the sample out. Then, the sample is prepared for optical microscope and SEM analyses.

4.6.3.1 Sectioning and Mounting

The first step in sample preparation is sectioning. Since the sample is a type of metal matrix composite material, it is not easy to cut. For this purpose, a sample cutting unit was built. This unit is composed of a lapidary blade (MK-303 Professional™) to cut the ceramic and/or composite materials, and a lapidary mill to grind ceramic pieces. The samples are cut vertically and horizontally (Figure 4.14 and 4.15).

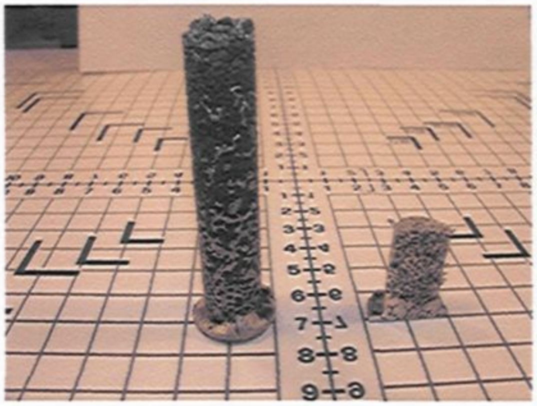

Figure 4.14 Vertical Cross-section of an Infiltration Sample

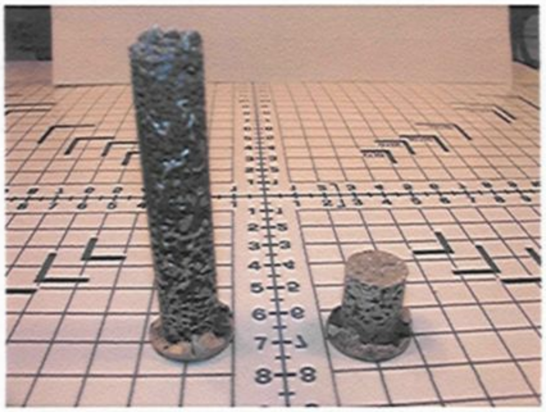

Figure 4.15 Horizontal Cross-section of an Infiltration Sample

When the sectioning is completed, piece(s) of the sample is/are mounted by using compression mounting method (Figure 4.16 and 4.17). For mounting, Struers Prontopress-2 mounting press is utilized. The piece(s) of sample is/are placed on the base plug, which is inserted in the mold cylinder made of hardened steel. The molding material in powder form (Buehler, short-glass fiber-filled blue diallylphtalate resin) is put on the sample until the sample piece is covered entirely. Onto the molding material, a preformed mold (Buehler, green phenolic premolds™, 38 mm. diameter) is placed. The plunger is inserted into the open end of the mold cylinder, and the mounting press is turned on. Mounting takes 13 minutes in average. During the first 10 minutes, a prescribed pressure of 25 kN is exerted, and the mold assembly is heated to 150°C. The following three-minute period is the cooling period. In this period, the mounted specimen and the mold assembly are cooled down at a known cooling rate.

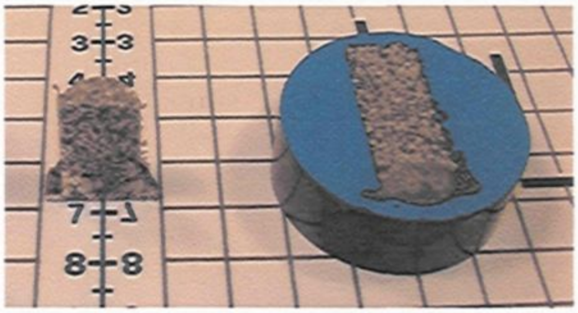

Figure 4.16 Mounted Infiltration Sample Sectioned Vertically

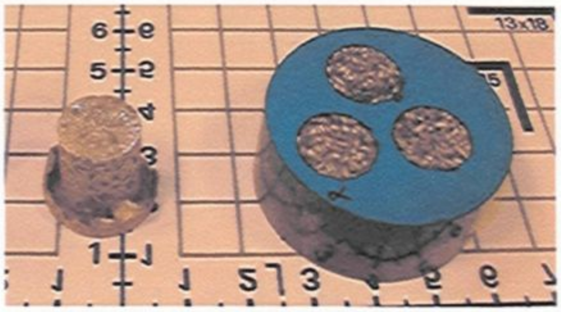

Figure 4.17 Mounted Infiltration Sample Sectioned Horizontally

4.6.3.2 Grinding and Polishing

After the samples are mounted, they are ground and polished using a variable speed grinder-polisher (Buehler, Ecomet 4 with Automet 2 Power Head assembly). Grinding and polishing are semi-automatic processes. Before starting grinding (or polishing), three or six mounted samples are placed into the specimen holder which is installed to the power head of the grinder-polisher. The desired type of platen is installed onto the deck of the grinder-polisher. Then, the force to be exerted by the power head, the rotation speed and direction of the platen, the type of the cooler to be used, and the process duration are entered to Automet 2 assembly. If a solution other than water will be used, it is added manually while grinder-polisher is running.

Before starting to grind, a 30.48 mm. diamond grinding disc, which is precision coated in a consistent diamond dot matrix to provide accuracy in cutting, is placed as platen, and the samples are ground until the entire surface area of the specimen fixed to the specimen holder is flattened. Water is used as cooler, and 11 kg force is exerted for all samples.

During either grinding or polishing, the rotation speed and direction of the platen remain unchanged as 120 RPM and clock-wise, respectively. The polishing procedure is summarized below in Table 4.4. When polishing is completed, the samples are treated in an ethyl alcohol bath for two minutes in an ultrasonic cleaner (Branson, 5200).

Table 4.4 Summary of Polishing Procedure

Platen	**Polishing Cloth**	**Polishing Suspension**	**Polishing Compound**	**Polishing Extender**	**Force for 3 Samples [kg]**	**Duration [min.]**
Metlap 10	-	15 μ, diamond Metadi	-	-	13.5	15
Plain	Textmet 1000	-	9 μ, diamond Metadi II	Metadi Fluid	9.5	12
Plain	Textmet 1000	-	6 μ, diamond Metadi II	Metadi Fluid	9.5	10
Plain	Textmet 1000	-	3 μ, diamond Metadi II	Metadi Fluid	9.5	5
Plain	Textmet 1000	-	1 μ, diamond Metadi II	Alcohol + glycerin	9.5	3

4.6.3.3 Analysis of Samples Prepared

As mentioned previously, the analyses conducted on the prepared samples can be grouped into three categories; optical microscope analysis, SEM analysis, and TEM analysis.

4.6.3.3.1 Optical Microscope Analysis

The optical microscope (Nikon Eclipse ME600 with 3-axis motorized stage controller, Model ST100) was utilized to determine certain parameters required for contact angle calculations with capillary model whose details are given in Chapter 2.

In the capillary model with average pore (capillary) radius, the hydraulic radius of a capillary, r_h, is used to calculate the radius of a capillary, r_{cap}, (see Equation 2.10). Hydraulic radius is a function of the mean diameter of particles and the porosity of the bed. Since the alumina particles are not perfect spheres, the mean radius should be corrected using a shape factor, ϕ. Therefore, the shape factor and the bed porosity are measured to calculate hydraulic radius, and hence the radius of a capillary. In the capillary model with pore size distribution, this distribution is also determined from bed porosity measurements. The minimum and maximum pore sizes are used also in Kaptay's model [14] based on the force balance. In the following sections, the procedures followed for measuring these two parameters are given.

4.6.3.3.1.1 Shape Factor Measurements

The image analysis software[6] (CLEMEX Vision™, Version 3.0, Build 036) of the optical microscope was utilized for measuring the shape factors of different types of particles. For this purpose, a short code was written by using the commands of this software. The code generated is given in Appendix C. It serves first to differentiate the alumina particles from the background for a given image and second to carry out some measurements on each alumina particle detected.

Alumina particles are generally whitish in color. To facilitate the work, the alumina particles are arranged on a black background with a ruler nearby and their photograph is taken (see Figure 4.18).

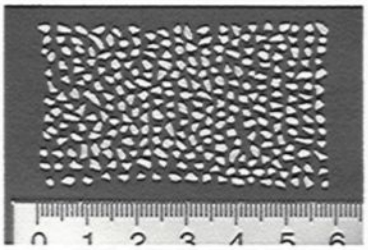

Figure 4.18 Alumina Particles Arranged for Shape Factor Measurements Next to a Ruler in SI Units.

At the beginning of the measuring process, the scale is entered correctly. Then, the processing zone is defined on the image with the help of the code. Making use of the color difference between alumina particles and the background, they are separated from one another. To eliminate the misinterpretation by the image analysis software, the perimeter of each alumina particle is smoothed following the most appropriate route (pruning). Then the analysis starts. Software determines the area and perimeter of each particle and calculates the shape factors for corresponding particles. Considering each particle as a feret, the

---

[6] © Copyright 1990-1999 Clemex Technologies Inc.

software finds the largest and smallest chords of a particle and calculates also the aspect ratio for each particle. Finally, the program counts the number of particles treated. Once all of the measures are taken, the data are compiled as an MS Excel file. The total number of counted particles is found, and the corresponding parameters are averaged.

4.6.3.3.1.2 Bed Porosity Measurements

The porosity values for horizontally and vertically sectioned samples are also obtained using the image analysis software of the optical microscope. Before the calculations, the photograph of a mounted and polished sample is taken (Figure 4.19(a) and 4.20(a)).

For vertically sectioned samples, the contours of alumina particles are drawn manually (Figure 4.19(b)). The inside of these figures are filled (Figure 4.19(c)) and alumina particles are determined (in blue). The spaces left after the experiment are filled with another color (green). The spaces filled with bacalite are also colored (brown). Then, the rectangular processing zone is defined for the computations. After the background, which represents the infiltrated metal, is colored (red), the image analysis software calculates the fraction of alumina particles in the selected area as well as the fraction of void spaces (porosity) (see Figure 4.19 (d)). The porosity values of a few sections of the same sample are found and their average is used in the calculations.

For horizontally sectioned samples, first the perimeter of the cross-section is determined and marked with a red circle. Using the image analysis software, the metal (bright areas in Figure 4.20(a) and 4.20(b)) is colored (blue), automatically. Then, the alumina particles (yellow) and holes (green) are colored, manually (Figure 4.20(c)). After the large metal and hole areas are divided into smaller ones (measuring not bigger than 1 mm^2) by red lines (Figure 4.20(d)), the area and perimeter of each metal, particle and hole area are calculated for three different cross-sections by the image analysis software. From this data calculated the distribution of porosity is obtained.

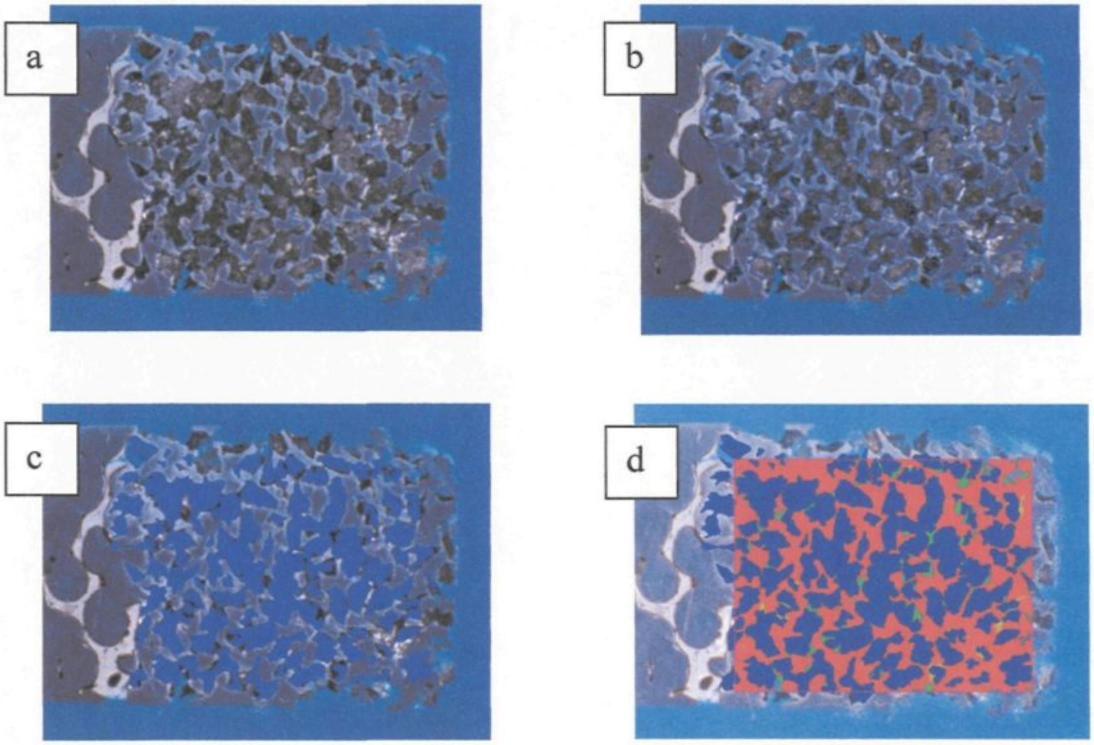

Figure 4.19 Porosity Calculations of a Vertically Sectioned Sample

a) Untreated Image of Alumina Bed with Infiltrated Aluminum

b) Image with Alumina Contours

c) Image with Identified Alumina Particles (Blue)

d) Image with Identified Alumina Particles (Blue) and Infiltrated Aluminum (Red)

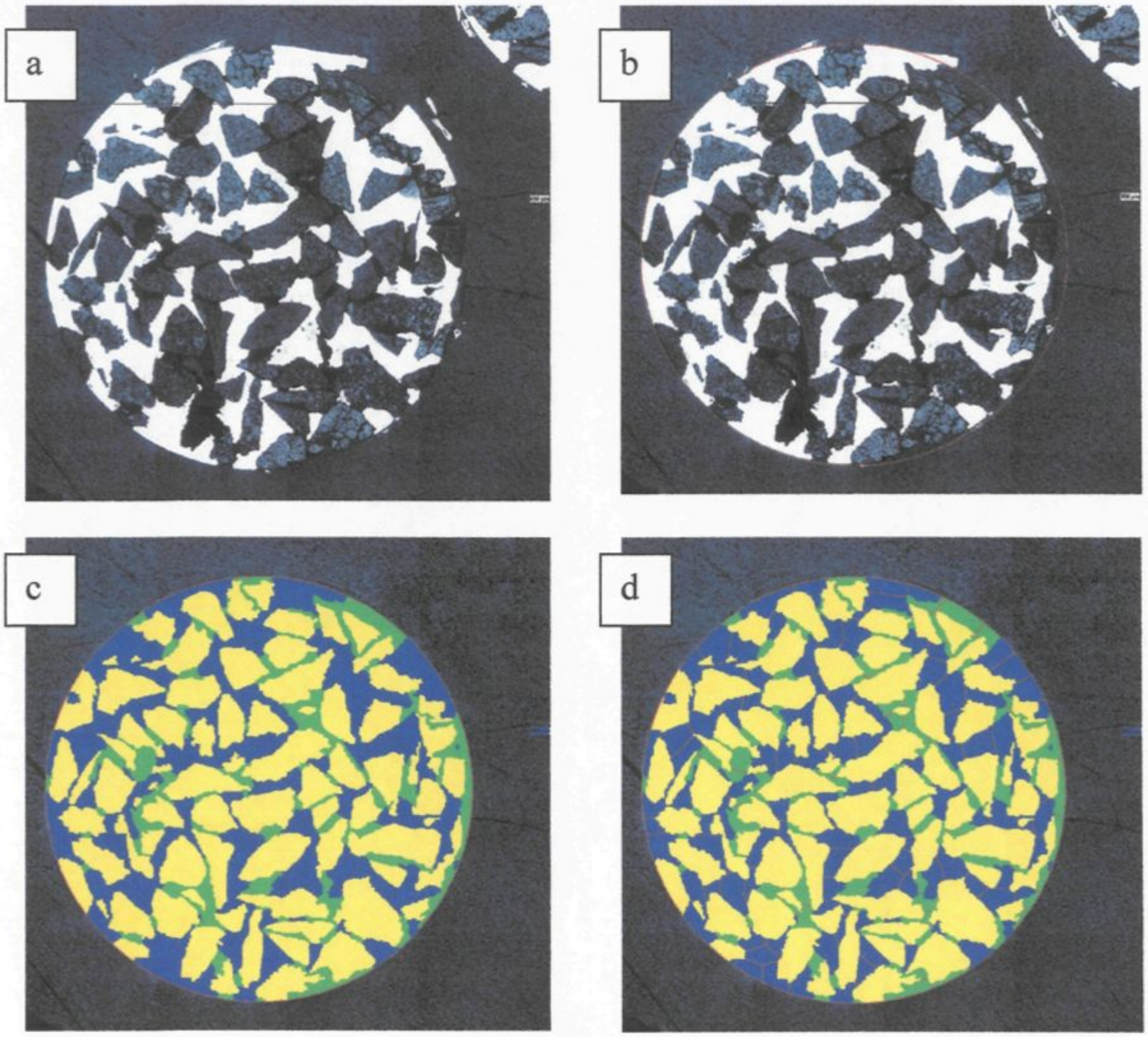

Figure 4.20 Porosity Distribution Calculations of a Horizontally Sectioned Sample

a) Untreated Image of Alumina Bed with Infiltrated Aluminum

b) Image with Marked Perimeter

c) Image with Identified elements (Metal: Blue; Holes: Green; Alumina Particles: Yellow)

d) Image with Divided Areas

4.6.3.3.2 SEM Analysis

A part of scanning electron microscopy was conducted in the Electron Microscope Laboratory of the Aluminum Technology Center of the National Research Council of Canada in Saguenay. The device used was a field-emission-gun Leo 1525 FEG-SEM equipped with an Oxford Instrument INCA 300 thin-window energy-dispersive x-ray (EDS) system analyzer. The operating voltage was 20kV. EDS examination were performed using 30 or 60 µm aperture diameters, which gave a probe size of approximately 20-25nm. EDS chemical maps with pixel resolution of 512x512 are acquired without automatic drift correction. Additional analyses were carried out in the Materials Technology Laboratories of the Natural Resources Canada (CANMET), Ottawa, on a field-emission-gun Philips CM20-FEG TEM equipped with an Oxford Instruments thin-window energy-dispersive x-ray (EDS) detector with INCA system analyzer. The operating voltage was 200 kV. EDS examinations were performed in the scanning mode (STEM) with apertures 15 µm or 50 µm, giving the nominal probe sizes of about 1 nm or 2 nm, respectively. EDS chemical maps with the pixel resolution of 512×352 were acquired in the automatic drift correction regime with the beam controlled by the INCA system.

In order to facilitate SEM analysis, a method was developed making use of different fluorescence characteristics of magnesia and spinel under the ultra-violet (UV) light. According to this method, in a dark room, long wave UV-light is applied onto the polished samples by using a portable UV light source (Model UVGL-25, Mineralight® Lamp, multi band 254/366 nm), and the sites where the spinel is formed are determined. The vicinities of the fluorescent regions were marked by using a diamond tipped pencil (Agilent, catalog no: 420-1000) so that the spinel formation sites are rapidly recognized during SEM analysis.

4.6.3.3.3 TEM Analysis

Analytical transmission electron microscopy was carried out in the Materials Technology Laboratories of Natural Resources Canada (CANMET) in Ottawa. The details of the machine utilized are specified above in the previous section.

CHAPTER 5

RESULTS AND DISCUSSIONS

In this chapter, some of the calculations related to sessile-drop and infiltration experiments are illustrated; and the results obtained are presented and discussed.

5.1 Calculations in the Sessile Drop Experiments

For measuring the contact angles and calculating the surface tension accurately, an image analysis program is developed. This program uses the images which are captured by a digital video and transferred to a computer. In addition, it measures the surface area of the drop, hence the volume of the drop as well as various geometric dimensions of the drop such as its height, width, and interface length between the drop and the bed media.

5.1.1 Measurement of Contact Angle and Geometric Dimensions of Sessile Drop

For carrying out all the measurements, the program first identifies the contour of the drop and fits a spline to this contour (see Appendix D). Then, it finds the tangent of this curve at the triple point (solid-liquid-gas interface). From the angle between the tangent and the line identifying the bed surface, it determines the contact angle as shown in Figure 5.1. The program has also the capability to follow the changes in contact angle (if there is any), drop volume and interface length with time. The details of the curve fitting are given elsewhere [135].

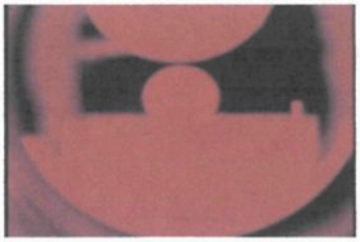

(a) Raw Image from the Experiment

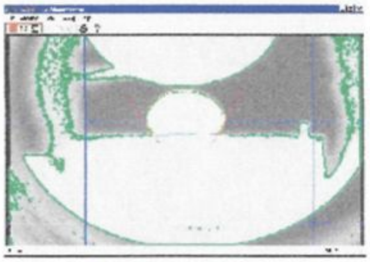

(b) Image Contours and Contact Angles Identified by the Image Analysis Program

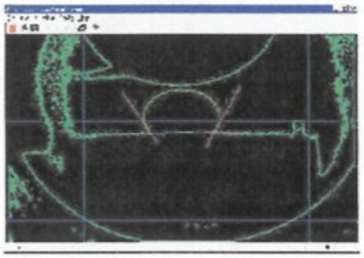

(c) Image Contours and the Contact Angles Identified by the Image Analysis Program

Figure 5.1 Example Images from Different Phases of Image Analysis Program

5.1.2 Surface Tension Calculations

The surface tension is calculated by the image analysis program developed. For this purpose, the empirical relationship proposed by Dorsey [136] is utilized:

$$\gamma^{lv} = \frac{g\rho_{liq} d_m^2}{4}\left(\frac{0.0520}{k} - 0.1227 + 0.0481k\right) \tag{5.1}$$

where $k = (2H' / d_m) - 0.4142$, ρ_{liq} is the density of the liquid. The parameters H' and d_m, are defined in Figure 5.2, are also measured by the image analysis program.

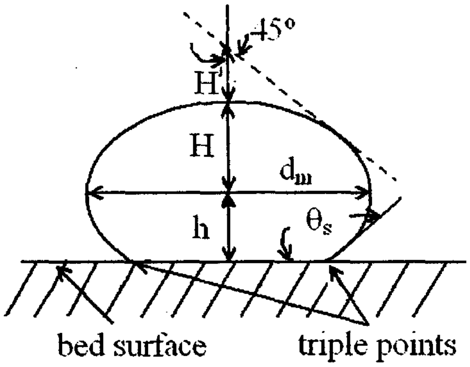

Figure 5.2 Identification of Geometric Parameters of a Sessile Drop

5.2 Results and Discussions of Sessile Drop Experiments

The results of sessile drop experiments can be divided into three main groups: the results of preliminary experiments, the results of experiments with granular alumina particles (Table 5.1), and the results of experiments with smooth crystals (Table 5.3).

5.2.1 Results of Preliminary Experiments

Numerous preliminary experiments are conducted to develop the experimentation technique and minimize the practical difficulties associated with the sessile drop method. As a result of these efforts, appropriate operating conditions were determined, a method for the preparation of Al-Mg alloys was developed, the magnesium loss during the experiments was determined in order to take necessary precautions, and the oxidation of the sessile drop was decreased to negligible levels.

5.2.1.1 Adjustment of Experimental Parameters

The experimental parameters adjusted can be grouped into two as the determination of the most appropriate injection chamber geometry and size of aluminum drop. Different injection chamber designs tested are shown in Figure 5.3.

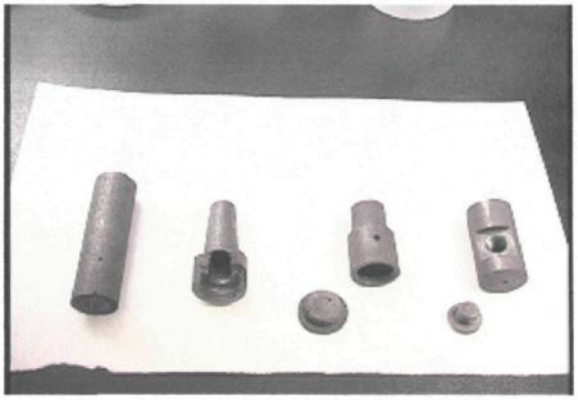

Figure 5.3 Different Injection Chamber Geometries Tested.

The size of the sessile drop should be between 1 and 4 cm so that the Equation 5.1 can be used for calculating the surface tension of the liquid metal [31]. For this range, the gravity effect is negligible. Due to the high pressure used during metal injection and sessile-drop formation, it was sometimes observed that the injected metal can bounce and roll on the alumina bed surface depending on the distance between the bed surface and the injection hole. Therefore taking into account these *theoretical* and *practical* factors mentioned above, the injection hole size, injection pressure, and the distance between the bed surface and the injection hole were optimized.

5.2.1.2 Developing an Al-Mg Master Alloy Preparation Technique

The developed technique is given in the previous chapter. While developing the preparation technique, it was found out that the thermocouples left in the metal caused contamination because of the small quantity of alloy prepared. Thus, the contact between the metal and the thermocouples was kept to minimum by immersing the thermocouple into the metal momentarily to measure the temperature. Continuous contact was avoided. Also the cutting tools, which were used for cutting the metal for the master alloy preparation, were cleaned carefully. The oxides, which can form on the surface of the metal, were removed by immersing the metal in 15% NaOH solution and washing with distilled water afterwards. With these measures, the contamination of the metal was almost eliminated.

5.2.1.3 Determination of Magnesium Loss

One of the fundamental problems encountered was the loss of magnesium. Due to high vapor pressure of magnesium at the temperatures studied (730°C), magnesium in the liquid alloy evaporates. Since the volume of the drop is also relatively small (a diameter of about 1 cm), the amount of magnesium lost changes the chemical composition of the liquid alloy considerably. Therefore, the change in the composition of the binary Al-Mg binary alloys under the experimental conditions should be measured. For this purpose, the magnesium contents of the initial alloy and the solidified metal droplet were measured. It was found that the magnesium content reduced from 5.3% to 4.2% in two hours. Initially, a number of experiments with seven to ten day durations were planned to study the wetting behaviour during a typical filtration cycle. This was abandoned since it is not very likely that the drop could be kept in the furnace for such extended times without affecting its composition.

5.2.1.4 Minimization of Aluminum Oxidation

The prevention of aluminum oxidation on the liquid metal droplet was the crucial part of the preliminary experiments. The installation of a vacuum system and the utilization of titanium oxide, various filters, and research grade Ar gas prevented the surface oxidation to a great extent. Figure 5.4 shows EDX Spectra of two droplet surfaces and corresponding surface structures (a) before and (b) after the measures were taken for oxidation prevention.

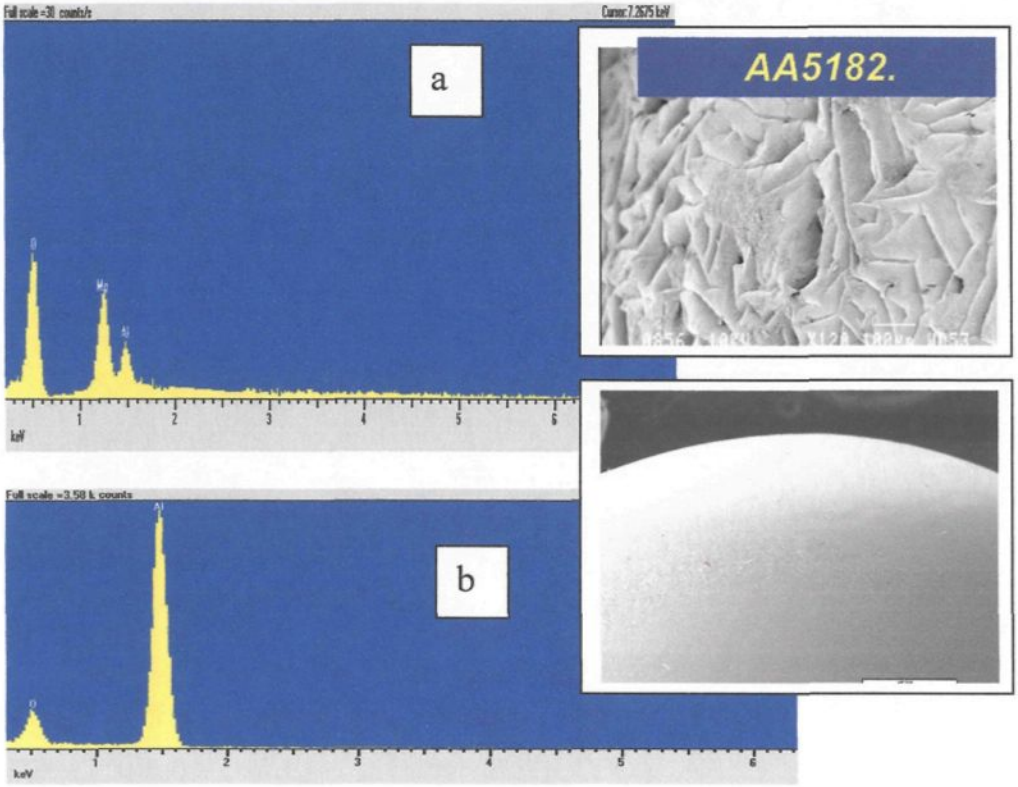

Figure 5.4 Structure and the EDX Spectra of the Drop Surface; a) Oxidized, b) Negligible Oxidation

5.2.2 Results of Experiments with Granular Alumina Particles

The experimental conditions for the experiments with granular alumina particles are summarized in Table 5.1. The parameters investigated during the sessile drop experiments are the size of particles, temperature, amount of magnesium in metal, experiment duration, and chemical reaction. This section summarizes the effects of these five experimental parameters on the wettability of granular alumina particles.

Table 5.1 Experimental Parameters for the Experiments with Granular Alumina Particles in Tabulated Form

Exp. No	Particle Size Range	Binder	Particles	Chemical Composition of Sample Metal	Atmosphere
1	-0.5mm +0.3mm	-	Alumina	Al-5.5wt%Mg	UHP Ar
2	-0.5mm +0.3mm	-	Alumina	Al-5.5wt%Mg	UHP Ar
3	-0.5mm +0.3mm	QF150	Alumina	Al-5.5wt%Mg	UHP Ar
4	-0.5mm +0.3mm	-	Alumina	Al-5.5wt%Mg	UHP Ar
5	-0.5mm +0.3mm	-	Alumina	Al-5.5wt%Mg	UHP Ar
6	-0.5mm +0.3mm	-	Alumina	Al-5.5wt%Mg	UHP Ar
7	-0.5mm +0.3mm	α-alumina powder	Alumina	Al-5.5wt%Mg	UHP Ar
8	-0.5mm +0.3mm	-	Alumina	Al-5.5wt%Mg	UHP Ar
9	-0.5mm +0.3mm	-	Alumina	Al-5.5wt%Mg	UHP Ar

Table 5.1 (Cont'd)

Exp. No	Particle Size Range	Binder	Particles	Chemical Composition of Sample Metal	Atmosphere
10	-0.5mm +0.3mm	-	Alumina	Al-5.5wt%Mg	UHP Ar
11	-1.7 mm +0.7 mm	α-alumina powder	Alumina	Al-5.5wt%Mg	UHP Ar
12	-0.5mm +0.3mm	α-alumina powder	Alumina	Al-5.5wt%Mg	UHP Ar
13	-0.5mm +0.3mm	α-alumina powder	Alumina	Al-5.5wt%Mg	UHP Ar
14	-0.5mm +0.3mm	Alpha Bond 100	Alumina	Al-5.5wt%Mg	UHP Ar
15	-1.7 mm +0.7 mm	-	Alumina	Al-5.5wt%Mg	UHP Ar
16	-0.5mm +0.3mm	α-alumina powder	Alumina	Al-5.5wt%Mg	UHP Ar
17	-0.7mm +0.5mm	α-alumina powder	Alumina	Al-5.5wt%Mg	UHP Ar
18	-0.7mm +0.5mm	α-alumina powder	Alumina	Al-5.5wt%Mg	UHP Ar
19	-0.7mm +0.5mm	Alpha Bond 100	Alumina	Al-5.5wt%Mg	UHP Ar
20	-0.7mm +0.5mm	Alpha Bond 100	Alumina	Al-5.5wt%Mg	UHP Ar
21	-0.7mm +0.5mm	-	Alumina	Al-5.5wt%Mg	UHP Ar
22	-0.7mm +0.5mm	α-alumina powder	Alumina	Al-5.5wt%Mg	RG Ar
23	-0.7mm +0.5mm	α-alumina powder	Alumina	Al-5.5wt%Mg	RG Ar
24	-0.7mm +0.5mm	α-alumina powder	Alumina	Al-5.5wt%Mg	RG Ar
25	-0.7mm +0.5mm	α-alumina powder	Alumina	Pure Mg	RG Ar
26	-1.0 mm +0.7 mm	α-alumina powder	Alumina	Al-5.3wt%Mg	RG Ar
27	-1.0 mm +0.7 mm	α-alumina powder	Alumina	Al-5.3wt%Mg	RG Ar

Table 5.1 (Cont'd)

Exp. No	Particle Size Range	Binder	Particles	Chemical Composition of Sample Metal	Atmosphere
28	-1.0 mm +0.7 mm	α-alumina powder	Alumina	Al-5.3wt%Mg	RG Ar
29	-1.0 mm +0.7 mm	α-alumina powder	Alumina	Al-5.3wt%Mg	RG Ar
30	-1.0 mm +0.7 mm	α-alumina powder	Alumina	Al-5.3wt%Mg	RG Ar
31	-1.0 mm +0.7 mm	α-alumina powder	Alumina	Al-5.3wt%Mg	RG Ar
32	-1.0 mm +0.7 mm	α-alumina powder	Alumina	Al-5.3wt%Mg	RG Ar
33	-1.0 mm +0.7 mm	α-alumina powder	Alumina	Al-5.3wt%Mg	RG Ar
34	-1.0 mm +0.7 mm	α-alumina powder	Alumina	Al-5.3wt%Mg	RG Ar
35	-1.0 mm +0.7 mm	α-alumina powder	Alumina	Al-5.3wt%Mg	RG Ar
36	-1.0 mm +0.7 mm	α-alumina powder	Alumina	Al-5.3wt%Mg	RG Ar
37	-1.0 mm +0.7 mm	α-alumina powder	Alumina	Al-5.3wt%Mg	RG Ar
38	-1.0 mm +0.7 mm	α-alumina powder	Alumina	Al-5.3wt%Mg	RG Ar
39	-1.0 mm +0.7 mm	α-alumina powder	Alumina	Al-5.3wt%Mg	RG Ar
40	-1.0 mm +0.7 mm	α-alumina powder	Alumina	Al-5.3wt%Mg	RG Ar
41	-1.0 mm +0.7 mm	α-alumina powder	Alumina	Al-5.3wt%Mg	RG Ar
42	-1.0 mm +0.7 mm	α-alumina powder	Alumina	Al-5.3wt%Mg	RG Ar
43	-1.0 mm +0.7 mm	α-alumina powder	Alumina	Al-5.3wt%Mg	RG Ar
44	-1.0 mm +0.7 mm	α-alumina powder	Alumina	Al-5.3wt%Mg	RG Ar
45	-1.0 mm +0.7 mm	α-alumina powder	Alumina	Al-5.3wt%Mg	RG Ar

Table 5.1 (Cont'd)

Exp. No	Particle Size Range	Binder	Particles	Sample Metal	Atmosphere
46	-0.7mm +0.5mm	α-alumina powder	Alumina	Al-5.3wt%Mg	RG Ar
47	-1.0 mm +0.7 mm	α-alumina powder	Alumina	Al-5.3wt%Mg	RG Ar
48	-1.0 mm +0.7 mm	α-alumina powder	Alumina	Al-5.3wt%Mg	RG Ar
49	-1.0 mm +0.7 mm	α-alumina powder	Mulcoa 60	Al-5.3wt%Mg	RG Ar
50	-1.0 mm +0.7 mm	α-alumina powder	Mulcoa 60	Al-5.3wt%Mg	RG Ar
51	-1.0 mm +0.7 mm	α-alumina powder	Alumina	Al-5.3wt%Mg	RG Ar
52	-0.7mm +0.5mm	α-alumina powder	Alumina	Al-5.3wt%Mg	RG Ar
53	-1.0 mm +0.7 mm	α-alumina powder	Mulcoa 60	Al-5.3wt%Mg	RG Ar
54	-1.0 mm +0.7 mm	α-alumina powder	Pure Silica	Al-5.5wt%Mg	RG Ar
55	-1.0 mm +0.7 mm	α-alumina powder	Mulcoa 60	Al-5.5wt%Mg	RG Ar
56	-1.0 mm +0.7 mm	α-alumina powder	Pure Silica	Al-5.5wt%Mg	RG Ar
57	-1.0 mm +0.7 mm	α-alumina powder	Pure Silica	Al-5.5wt%Mg	RG Ar

5.2.2.1 Effect of Particle Size on Wettability of Alumina Particles

The experiments with granular alumina (0.3 mm – 2.8 mm) can be separated into two major parts. In the first part, six kinds of tabular alumina particles from six different suppliers (Alcoa Chimie Nederland T-60, Itochu Ceratech, Naigai, AluFin GmbH, AluChem Grande-Baie, unknown Russian company) were tested. Their size range was between 1.0 mm and 2.8 mm. They were sieved and classified into two size groups (1.0

mm – 1.7 mm and 1.7 mm – 2.8 mm). During these experiments, the middle compartment of the sample crucible was filled with these classified alumina particles and the particles were tapped with an aluminum weight. The sessile drop was formed on these particles directly. The results showed that the drop was pinned down by the rough alumina particles. This pinning down effect prevented the drop to take its proper shape. Therefore, smaller particles were used.

In the second part, Alcoa T-60 grade alumina particles were chosen, among the six types of alumina particles, and the size of the particles were reduced down to 0.3 mm. These alumina particles were classified into three size groups (0.3 mm – 0.5 mm, 0.5 mm – 0.7 mm, and 0.7 mm – 1.0 mm). When the size of the particles was reduced, another problem arose. After the liquid metal was injected onto the bed surface, it contacted with the alumina particles. While the drop was spreading to take its final shape, some of the alumina particles detached from the surface and stuck to the droplet. This caused problems during the contact angle measurements (Figure 5.5).

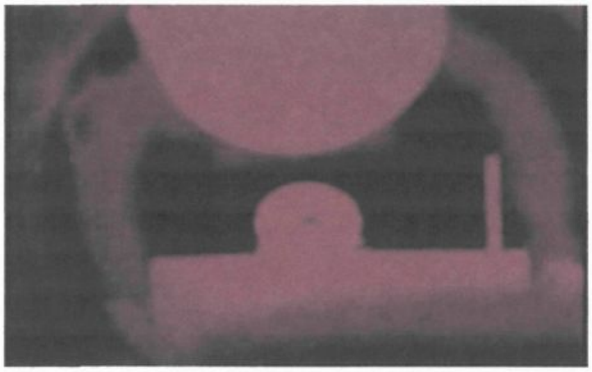

Figure 5.5 Adherence of Small Alumina Particles to the Surface of the Drop During Injection

To overcome this adherence problem, two sample preparation techniques were developed and tested. At first, particles were sintered while they were on an alumina plate so that they wouldn't stick to the liquid drop during the short period of instability immediately after injection. Sintering was carried out at 1550-1600°C for 2 to 6 hours. It was visually observed that the color of alumina changed from white to pink. Therefore, this technique was abandoned due to the changes observed in alumina. Second, a binder was used to hold the particles together. Ingredients of these binders and sample preparation procedures were given in the previous chapter in more detail in Section 4.2.2. In this case, the binder served to hold the particles and prevent their adhesion to the liquid metal drop during the injection. Although precautions were taken to prevent the contact between the binder and the liquid metal during the experiments, all of the binders except pure alumina powder interacted chemically with the liquid metal. The experiments conducted showed also that the samples prepared by using this technique prevented sticking of the bed particles to the droplet after injection. Therefore, the test samples used during the experiments were prepared by using the alumina powder suspension in distilled water as a binder.

The experiments were carried out at 730°C under argon atmosphere by using Al-5wt%Mg alloy. The only parameter changed was the size of particles. The tests were conducted on three different particle sizes as mentioned above. The results of these experiments showed that the contact angles measured are always around 120°. Therefore, it was concluded that even with smaller alumina particles, the effect of surface roughness, consequently, the pinning effect were very important. It was not possible to see the effect of particle size on the contact angle.

5.2.2.2 Effect of Temperature on Wettability of Alumina Particles

A few wetting experiments were also carried out at a higher temperature, 800°C, under argon atmosphere by using Al-5wt%Mg alloy. Three different particle sizes were tested (0.5 mm – 0.7 mm, 0.7 mm – 1.0 mm and 1.0 mm-1.7 mm).

At this temperature, there was a chemical interaction between the graphite and Al-Mg alloy. This caused problems while injecting Al-Mg alloy. Therefore, the graphite injection chamber was coated with pure BN, and the experiments were conducted.

No appreciable change was observed in contact angles (around 120°). The majority of the experiments were not carried out at higher temperatures because the filtration of aluminum is carried out around 730°C.

5.2.2.3 Effect of Amount of Magnesium in Metal on Wettability of Alumina Particles

Pure research grade aluminum and its alloys with 1wt%, 3wt% and 5%Mg were used for testing the effect of magnesium in aluminum alloy on the wettability of alumina particles. During the experiments conducted with different particle sizes at 730°C under argon atmosphere, it was not possible to measure the effect of magnesium content of the alloy on the contact angle. This is again probably due to lack of sensitivity caused by surface roughness and pinning effect.

5.2.2.4 Effect of Experiment Duration on Wettability of Alumina Particles

The images recorded at different time intervals indicated that the contact angles did not seem to change with time. Figure 5.6 shows the images captured at different time intervals during the experiments with Alcoa alumina particles within the particle size range and Al-5wt%Mg alloy at 730°C under argon atmosphere.

During the experiment, as explained before, the alloy was heated to 730°C in a graphite injection chamber. The alloy melts and a thin oxide forms around it during heating. Then, a slight pressure is applied to the line leading to injection chamber. This pressure breaks the thin oxide layer and forces part of the molten metal out of the chamber through the small hole. Therefore, the first moments that the sessile drop touches the bed, it is not oxidized and the contact angle can be measured (Figure 5.7). However, with the passing time, a thin oxide layer forms on the drop which prevents its spreading due to interfacial reactions (MgO, and spinel formation). Although the experimental procedure developed prevents the excessive oxidation, it is not possible to eliminate it entirely. Considering also the presence of roughness effect, it is not possible to follow the change in the drop shape of the aluminum alloy, i.e. contact angle values for this system (aluminum/alumina) do not change with time.

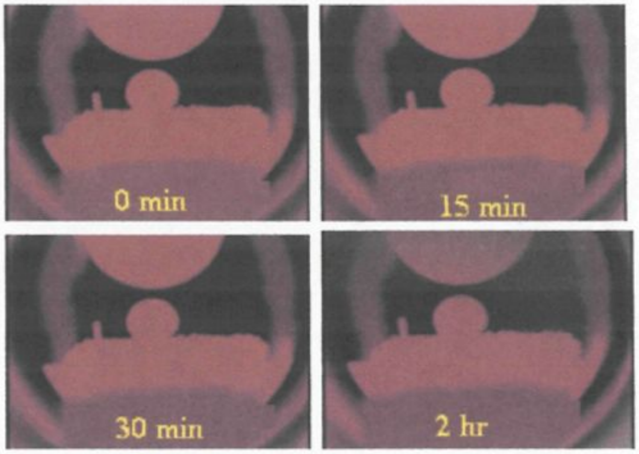

Figure 5.6 Images from the Sessile Drop Experiments at Different Time Intervals

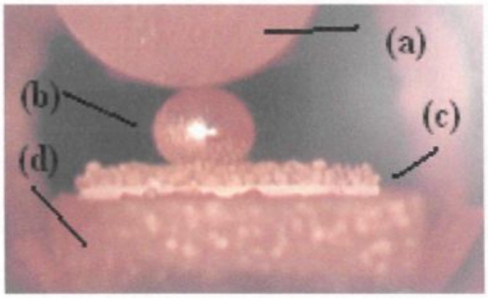

Figure 5.7 Image of a Sessile Drop Immediately After the Injection
(a) Injection Chamber
(b) Sessile Drop
(c) Binded Particles on an Alumina Plate
(d) Graphite Sample Crucible

5.2.2.5 Effect of Chemical Reactions on Wettability of Granular Particles

In the literature, it was stated that chemical reactions can enhance the wettability of granular particles [10, 12, 13, 14, 137]. To investigate the effect of chemical reactions on the wettability of granular particles, three different groups of tests were conducted with three different kinds of granular particles - alumina, mulcoa60, and pure silica.

5.2.2.5.1 Interactions Between Alumina Granular Particles and Al-Mg Alloy

In the literature, at the typical elevated working temperatures, two solid phases (spinel and magnesia) are observed to form due to the chemical reactions taking place between alumina and Al-Mg alloys. However, as it was mentioned in the previous sections of this chapter, it was not possible to keep the liquid metal in the furnace for extended time periods (up to 7 days) to study the chemical reactions taking place between alumina and Al-Mg alloys. Thus, to investigate the effect of thermodynamically stable phases like spinel or magnesia at the elevated working temperatures and extended time intervals, another method was developed. In this method, the stable phase was formed on the granular alumina particles by contacting alumina with the alloy before the sessile drop experiments. Then, these particles were used as bed particles during the experiments. This permitted to avoid the adverse effects of prolonged experimentation periods.

The same experimental set-up described in Section 4.2.1 was used to form a stable phase on the alumina particles. The alumina particles and Al-Mg alloy was brought into contact in a graphite crucible for twenty hours in the muffle furnace. The crucible had a lid to prevent the magnesium loss. The amount of magnesium in the alloy was measured before and after the experiment and it was found that the loss of magnesium was negligible. Figure 5.8 shows the alumina and Al-Mg alloy after the experiment.

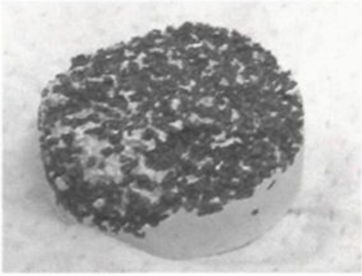

Figure 5.8 Alumina Particles After 20 Hours of Contact with Al-6.9wt% Mg Alloy

The color of alumina changed from white to black indicating deposition or formation of a different phase. In a dark room, using the UV method described in Section 4.4.3.3.2, long wave UV light is applied onto the alumina particles, and spinel formation was observed.

More quantitative discussions of this result can be found in the following sections of this chapter. These indicate that the spinel is the only stable phase which forms on the alumina particles as a product of chemical reactions under the conditions studied. After these alumina particles with spinel structure on the surface were separated mechanically from the alloy and they were used to prepare test samples. Then, the experiments were carried out to observe the effect of spinel (which was formed as a chemical reaction product after 20 hours) on the contact angle.

The result of these experiments showed no appreciable change in the contact angle (~120°). Since spinel was considered to enhance the wetting of aluminum on the granular alumina particles, this result also indicated that the sessile drop method may not be suitable for measuring the wettability of highly rough surfaces. Although in general it was believed that spinel formation makes it easier for the aluminum to wet the alumina particles, there are some conflicting studies in the literature. Therefore, to resolve this matter, two other granular particles (mulcoa60 and pure silica) were procured. They were specially chosen because they are known as well-wetted materials by Al-Mg alloys.

5.2.2.5.2 Interactions Between Mulcoa60 Granular Particles and Al-Mg Alloy

Mulcoa60 is composed of mainly three minerals, 77 % mullite ($3Al_2O_3.2SiO_2$), 23% glass, and trace amounts of cristobalite (polymorph quartz). A typical analysis of this refractory material is given below in Table 5.2. The experiments were conducted by using samples prepared with 0.7 mm – 1.0 mm size range particles. The particles were crushed by using a shatter box (Spex Industries Inc., Model No:8500) with WC carbide coated discs.

As it can be seen from Table 5.2, there is a considerable amount of silica in Mulcoa60 granular particles. In literature, it was found that Mg reacts extensively with SiO_2 to form MgO [138], and this reaction enhances the wettability of silica. Therefore, lower contact angle values are expected for the tests conducted using mulcoa60 granular particles; however, no change in contact angle values was observed.

Table 5.2 Chemical Analysis of Mulcoa60 Granular Particles

Ingredients	**Chemical Composition [wt%]**
Al_2O_3	58.6 (min. 58.0)
SiO_2	37.8
TiO_2	2.21
Fe_2O_3	1.13 (max. 1.35)
CaO	0.06
MgO	0.07
Na_2O	0.07
K_2O	0.04
P_2O_5	0.10

5.2.2.5.3 Interactions Between Granular Pure Silica Particles and Al-Mg Alloy

Although uniformity and high mullite content of Mulcoa60 particles are guaranteed by the company, a few experiments were carried out using granular pure silica particles within the 0.7 mm – 1.0 mm size range, but the contact angles were again similar to those of the previous experiments.

Therefore, as a result of the investigations carried out considering five experimental parameters, it was concluded that roughness of the surface is the dominant factor, and the sessile drop method is not suitable for measuring the wettability of highly rough surfaces formed by granular particles.

5.2.3 Results of Experiments with Smooth Substrates

In this part of the study, a number of experiments were carried out by using polished spinel ($MgO.Al_2O_3$), fused silica (SiO_2), and magnesia (MgO) single-grained crystal substrates in order to verify the conclusion reached. Some of the experimental parameters are tabulated in Table 5.3. The substrates were bought as polished (Commercial Crystal Laboratories). Spinel, fused silica, and magnesia crystals had been polished down to 7 Å, 4 Å, and 3.5 Å, respectively[7]. Since their effective roughness values are quite low for this study, they are considered to be smooth.

Table 5.3 Summary of Experiments with Smooth Substrates

Experiment No	Substrate	Sample Metal	Atmosphere
60	Polished fused silica	Al-6.87wt%Mg	RG Ar
61	Polished spinel	Al-6.87wt%Mg	RG Ar

---

[7] The related departments of Stanford University approve the polishing procedures and guarantee the final roughness of the substrates.

Table 5.3 (Cont'd)

Experiment No	Substrate	Sample Metal	Atmosphere
62	Polished fused silica	Pure Aluminum	RG Ar
63	Polished spinel	Pure Aluminum	RG Ar
64	Polished magnesia	Al-6.87wt%Mg	RG Ar
65	Polished spinel	Al-6.02wt%Mg	RG Ar
66	Polished magnesia	Pure Aluminum	RG Ar

In the experiments, industrial grade pure aluminum (AA1020), Al-6.0 wt% Mg, and Al-6.9 wt% Mg alloys were used. The contact angle values recorded were plotted against time. The results of the experiments conducted by using fused silica and magnesia substrates are given in Figure 5.9 and Figure 5.10, respectively. These two figures show that the wettability of fused silica and magnesia by aluminum is enhanced with magnesium additions into the aluminum metal. On the other hand, it was observed that the wettability of spinel is not affected by the magnesium content of the metal (see Figure 5.11). This might indicate that once a layer of spinel is formed on an alumina particle while it is in contact with aluminum alloy, the magnesium content of the alloy does not affect its wetting characteristics any further. As it can be seen from the figures (Figures 5.9 to11), it was also possible to follow the change of contact angle with time on smooth surfaces.

In the literature, the wettabilities of smooth magnesia and substrate by Al-5wt%Mg alloy were studied at 710°C [139]. In this study, the contact angles were measured two minutes after the drop was formed. The reported contact angle value is 94°. This is in very good agreement with the values presented in Figure 5.10. As it was stated before, as the magnesium content of the alloy increases, the wettability of magnesia substrate enhances.

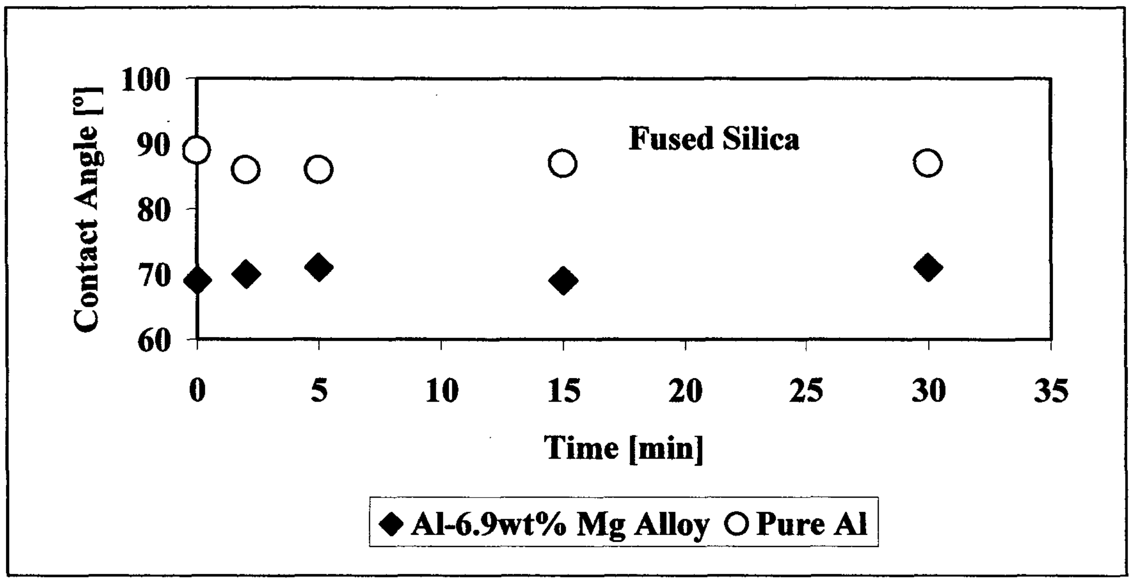

Figure 5.9 Effect of Magnesium Addition on the Wettability of Smooth Fused Silica Substrate

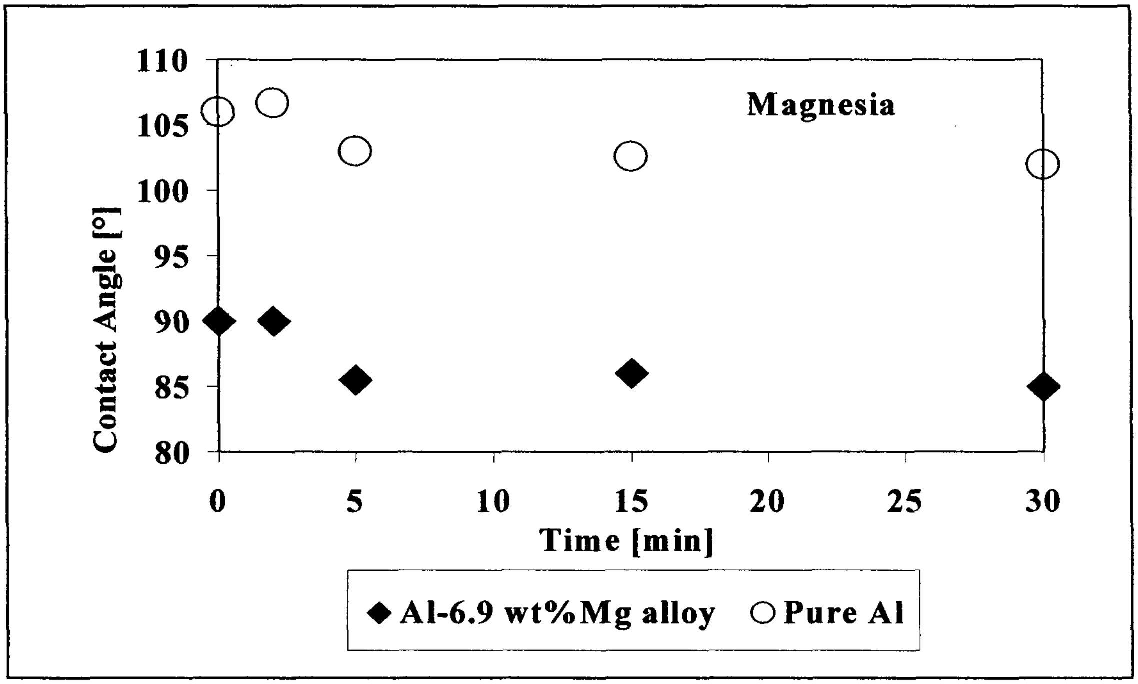

Figure 5.10 Effect of Magnesium Addition on the Wettability of Smooth Magnesia Substrate

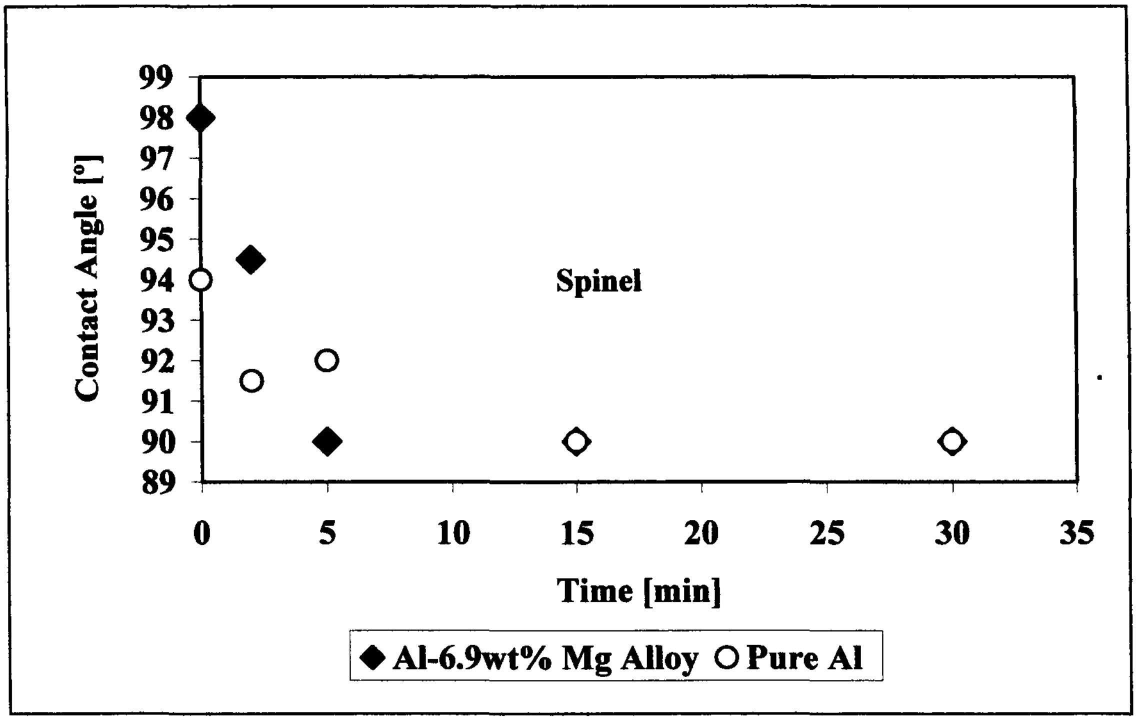

Figure 5.11 Effect of Magnesium Addition on the Wettability of Smooth Spinel Substrate

In this study, the surface tension values of Al-6.0 wt% Mg and Al-6.9 wt% Mg alloys (under argon atmosphere and 720°C) were also determined by using the image analysis program developed. In Figure 5.12, the calculated surface tension values are compared with those reported in the literature [140, 141] for various Al-Mg alloys under argon atmosphere between 700 and 740°C and a good agreement was found. As expected, the surface tension of the Al-Mg alloy decreases while the amount of added magnesium increases. It can also be stated that the values of surface tension show a sharper decrease as the magnesium content increases from 0 to 4.0 wt% Mg compared to those reported between 4.0 to 6.9 wt% Mg.

Both the contact angle and the surface tension results confirmed that the sessile drop experimental system is working properly for solids with smooth surfaces. However, another technique should be used to evaluate the wettability of rough solids.

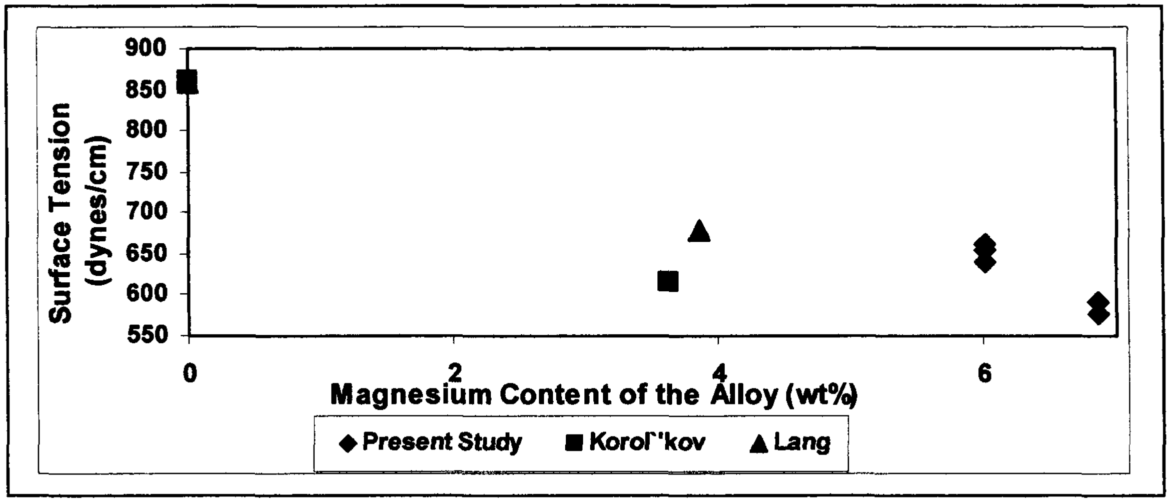

Figure 5.12 Effect of Magnesium Addition on the Surface Tension of Aluminum 700 to 740°C in Argon

5.3 Results and Discussions of Infiltration Experiments

The sessile drop experiments showed that this method is not suitable to study the effect of different parameters such as alumina type, contact time, particle size, temperature, etc. on the wettability characteristics of aluminum alloy and granular alumina system. It is not sensitive enough to be used as a tool in order to choose the type of alumina to be used in aluminum filtration.

Therefore, suitability of the infiltration method to characterize granular alumina was investigated. Six different types of alumina particles were tested in 1.4 mm – 1.2 mm size range. These are Alufin, Aluchem, Itochu, Alcoa, Russian and Naigai. Same compaction method was applied for all experiments. The experimental method is given in Section 4.3. The experimental conditions of infiltration experiments are given in Table 5.4 below:

Table 5.4 Summary of Experimental Parameters of Infiltration Experiments

Exp. No	Type of Alumina Particles	Weight Percent Magnesium in the Alloy	Duration [hours]	Duration [days]
1	Russian	Pure Aluminum	20.7	0.9
2	Russian	5.6	20.7	0.9
3	Naigai	Pure Aluminum	20.7	0.9
4	Aluchem	Pure Aluminum	20.7	0.9
5	Alufin	Pure Aluminum	21	0.9
6	Itochu	Pure Aluminum	20.7	0.9
7[8]	Russian	5.6	64	2.7
8	Alcoa	Pure Aluminum	20.7	0.9
9	Naigai	5.6	20.7	0.9
10	Aluchem	5.6	20.7	0.9
11	Alufin	5.6	21	0.9
12	Itochu	5.6	21	0.9
13	Alcoa	5.6	23	1
14[8]	Alcoa	6.9	72	3

---

[8] It indicates the samples analyzed with SEM and TEM. The results of these analyses were given in Sections 5.3.4.2 and 5.3.4.3. All of the analyses carried out were reported in Appendix E.

Table 5.4 (Cont'd)

Exp. No	**Type of Alumina Particles**	**Weight Percent Magnesium in the Alloy**	**Duration [hours]**	**[days]**
15[8]	Russian	6.9	72	3
16[8]	Naigai	6.9	72	3
17[8]	Aluchem	6.9	72	3
18	Alufin	6.9	72	3
19	Itochu	6.9	72	3
20	Fused Silica	6.9	72	3
21	Alcoa	6.9	24	1
22	Alcoa	3.3	72	3
23	Alcoa	5.4	72	3
24	Alcoa	5.4	24	1
25	Alcoa	3.3	24	1
26	Alcoa	6.7	0	0
27	Fused Alumina	6.7	0	0
28	New Alufin	6.7	0	0
29	Fused Alumina	6.7	72	3
30	New Alufin	6.7	72	3

5.3.1 Results of Preliminary Infiltration Experiments

Preliminary experiments were carried out to study the effect of crucible dimensions, particle size, alloy composition and medium used to apply the force.

It was found out that the size of the crucible had a major effect on the magnitude of force needed for infiltration of alloy into the bed. Small diameter bed and relatively large particles required the application of a large force just to overcome the friction between the components of the system. Sand was used to apply a force. When the bed diameter was increased to 11.3 mm and particle size was decreased to 1.41mm-1.19 mm, the applied force requirement was significantly reduced. Therefore, sand was replaced with water as medium to apply the force.

For the alloy preparation, a procedure was developed. The alloys used in the experiments were prepared in the foundries of UQAC (see Section 4.6.1).

It was determined that the infiltration results depend on how the bed was packed. If packing is not consistent, the bed porosity changes for each experiment. Therefore, a packing procedure was also developed for alumina particles (see Section 4.6.2). These changes improved the reproducibility of the experiments.

5.3.2 Results of a Typical Infiltration Experiment

After the infiltration experiments were completed, the crucible was kept at constant temperature for a predetermined holding time in order to study the chemical interactions between alumina bed and aluminum alloy. Then, the bed was sectioned, mounted, ground and polished. The samples were analyzed using different techniques such as SEM and TEM.

During each infiltration experiment, the data coming from the displacement sensor and the load cell were stored on the hard disk of a computer as a text file. After the experiment is finished, the text file was converted to an MS Excel file to be used in the calculation of contact angles. “Applied force versus Time” and “Displacement versus Time” graphics, which enable rapid visualization of the compiled data, were drawn. A typical, superimposed form of these graphics is given in Figure 5.13. From this figure, it appears that the infiltration is a three-step process. In the first step, the liquid metal penetrates through the ceramic foam filter, which supports the alumina bed. The second step is the incubation period, which is a function of the wettability of alumina particles. Normally, the molten aluminum or aluminum-magnesium alloys do not wet alumina within the range of temperatures studied. Therefore, it can be said that the surface tension forces are strong enough to prevent the infiltration of molten metal through the alumina particles. However, there is a limiting force equivalent to the resultant of surface tension forces, called threshold force. By applying an external force greater than the threshold force, the surface tension forces can be overcome and the liquid metal is forced to penetrate into the bed, wetting the alumina. That is, once the external force exceeds the threshold force, the third step starts and the infiltration takes place. Molten metal penetrates through the entire alumina bed rapidly.

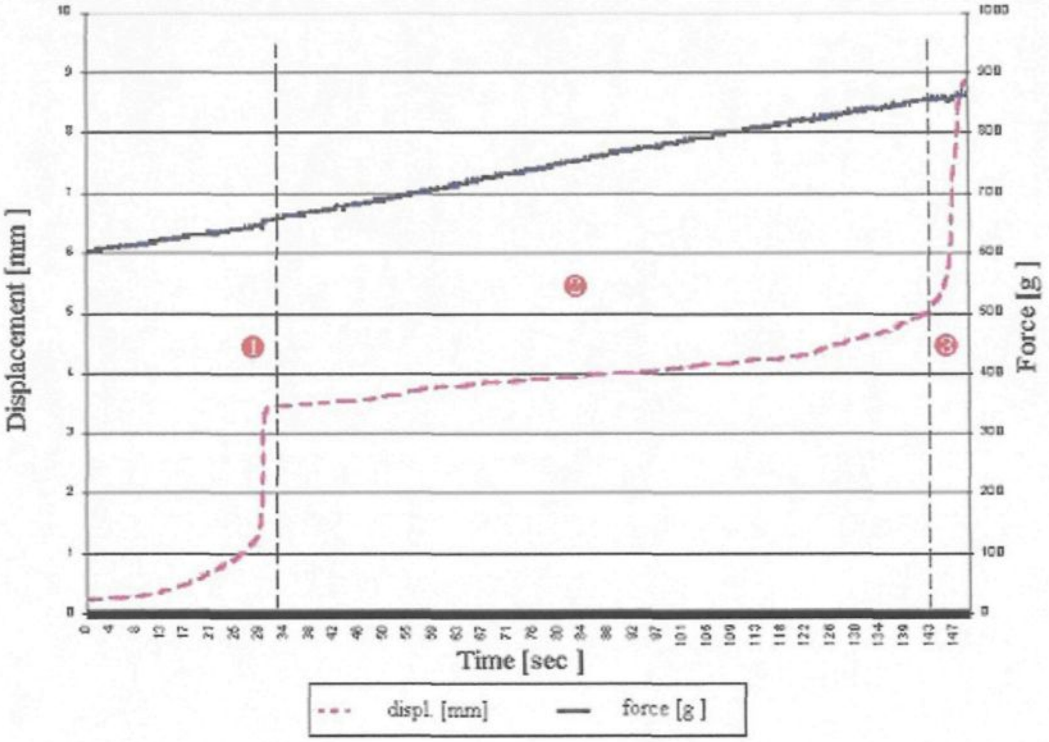

Figure 5.13 A Typical Visualization of the Data Obtained During Infiltration:

Region 1: Penetration of Molten Metal into CFF;

Region 2: Incubation Period;

Region 3: Penetration of the Molten Metal into the Alumina Bed.

The data compiled in the second region were used to calculate the contact angle values on rough surfaces by using the models described in Chapter 2.

For the capillary model developed which uses an average capillary radius and is based on energy balance, first optical microscopy measurements were carried out. The bed porosity (ε_{bed}), the sphericity (shape factor, ϕ) and pore hydraulic radius of different alumina particles were determined (see Table 5.8). From these measurements, the number of capillaries (n_{cap}, see Equation (2.9)) and the capillary radius (r_{cap}, see Equation (2.10)) were calculated. The height of the metal, l, was calculated from the quantity of metal infiltration and the bed porosity. After the amount of energy given to the system externally per capillary during the incubation period, ΔE_{appl}, (see Equation (2.8)), and the change in the potential energy of the metal infiltrated through the alumina per capillary during the same period, ΔE_{grav}, (see Equation (2.13)) were calculated, the contact angle value on rough surface, θ_r, was determined from Equations (2.7) and (2.14) and the results are presented in Table 5.6.

To illustrate the capillary model with a pore size distribution, model II, Alcoa alumina particles were chosen. The pore size distribution was divided into three sections. The sphericity of the particles did not change. Therefore, previously measured values of sphericity were used, l was taken as that of the first model. The average hydraulic radius and porosity of each section were determined using optical microscope image analysis for three different horizontal cross-sections. The porosity values were very similar at different cross-sections. An average value was used. From these results, the average capillary radius and the number of capillaries were determined for each section. Then, the rough surface contact angle was determined from Equation (2.17). Table 5.5 gives the capillary radius and number of pores found for each section. As a result of these calculations, the contact angle value on rough surface of Alcoa alumina particles by using the energy balance model with pore size distribution, model II, was found as 122°.

Table 5.5 Summary of Capillary Radius and Number of Pores For Each Section of Pore Size Distribution of Alcoa Alumina Particles

	Pore Size Distribution (Measured Pore Area, mm^2)		
	0-0.58	**0.58-0.75**	**0.75+**
Capillary Radius [μm]	71	452	523
Number of Pores	2936	12	2

For the third capillary model, which was based on a force balance, the bed porosity values (ε_{bed}) measured for the first model were utilized. From the porosity distribution measured with the help of an image analysis system from the horizontal cross-sections of the samples (see Section 4.6.3.3.1.2), the minimum and maximum radius of capillaries ($r_{cap,\min}$ and $r_{cap,\max}$) were determined. From Equation (2.22), ΔP_{appl} values were calculated. $\Delta P_{st,\min}$ and $\Delta P_{st,\max}$ were determined from the experimental data. The force values corresponding to them were the initial and final values of the incubation period. These values were corrected by subtracting the force required to push the metal through CFF and the force required to counteract the friction between the moving parts of the crucible. The net force was converted to pressure since the cross-section of the system was known. The height of the capillaries, l, was known since the bed height was known. From the experimental force versus time data, ΔP_{appl} versus time data was found by using Equation

(2.22). Substituting ΔP_{appl} values in Equation (2.19), metal penetration versus time was calculated and compared with the experimental data.

Again, with the same model, using Equations (2.20) and (2.21) the rough surface contact angles were calculated and compared with the results of the first model. In these equations the minimum and maximum capillary radii ($r_{cap,\min}$ and $r_{cap,\max}$) were determined from measured porosity distribution. Since γ^{lv}, $\Delta P_{st,\min}$ and $\Delta P_{st,\max}$ were known, the contact angle values on rough surfaces, θ_r, were determined, and these are presented in Table 5.7.

Figures 5.14 and 5.15 show the dependence of the height of the molten metal penetrated into porous refractory, $h_{penetration}$, on the externally applied pressure, ΔP_{appl}, schematically. The plotted points are the experimental data, and the lines are the model results. As it can be seen, the experimental data are in agreement with the model results. The penetration of liquid metal for different types of alumina particles can be found from this graph. Moreover, threshold pressure, $\Delta P_{st,\max}$, corresponding to threshold force for Region 2 in the discussion above can easily be determined from Equation (2.21). This helps determining quickly the wettability of the alumina particles. In this equation, there are two parameters which affect the value of threshold pressure: minimum radius of capillaries, $r_{cap,\min}$ and contact angle, θ. Although the distributions of porosities change for the analyzed bed samples, the minimum radii of capillaries forming these porosity distributions do not change significantly. Therefore, a pronounced increase in the threshold pressure indicates a considerable change in the contact angle values. As threshold pressure increases, contact angle increases according to Equations (2.18) and (2.21). Therefore, the lower the value of the threshold pressure, the better the wetting of alumina particles. However, it should be kept in mind that if the threshold pressure values are not very different from each other, the contribution due to the minimum radius of capillaries, $r_{cap,\min}$, to the threshold pressure value should also be taken into consideration for precise determination of contact angle.

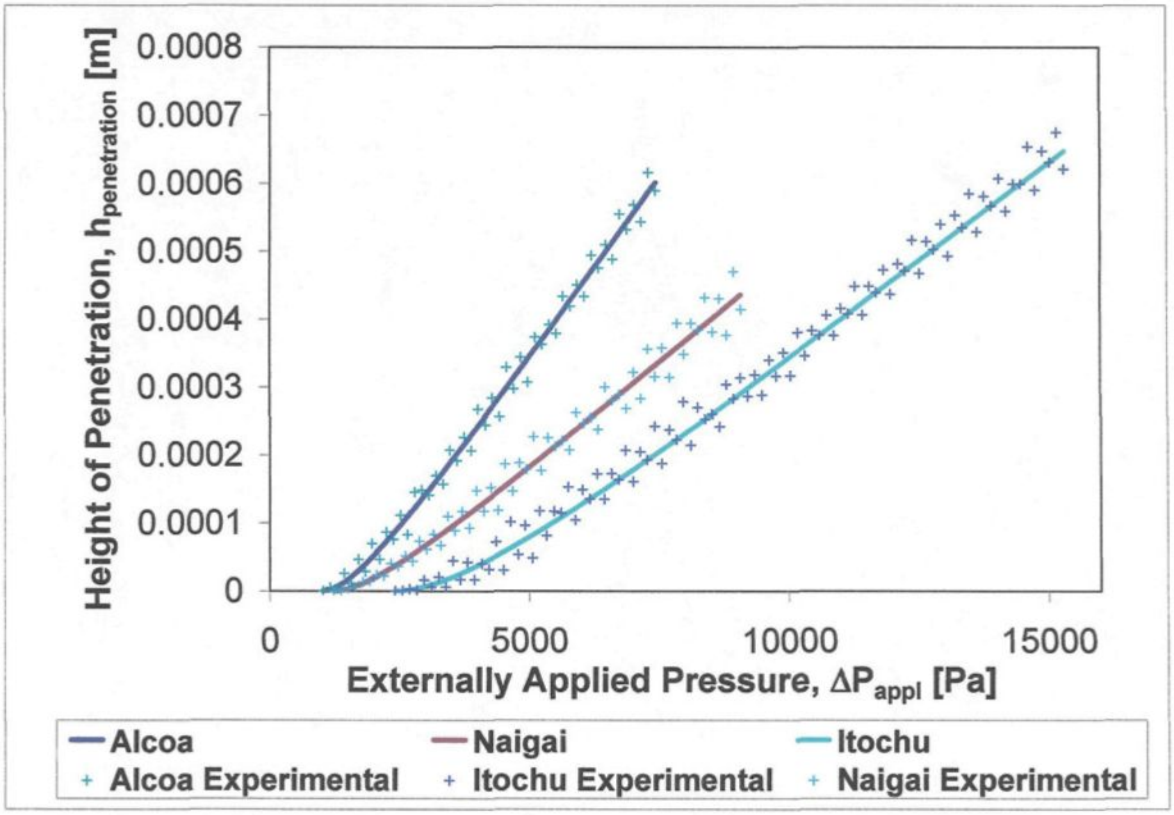

Figure 5.14 Height of Capillaries as a Function of Externally Applied Pressure for the Capillary Model of Cylindrical Pores with Periodically Changing Radii

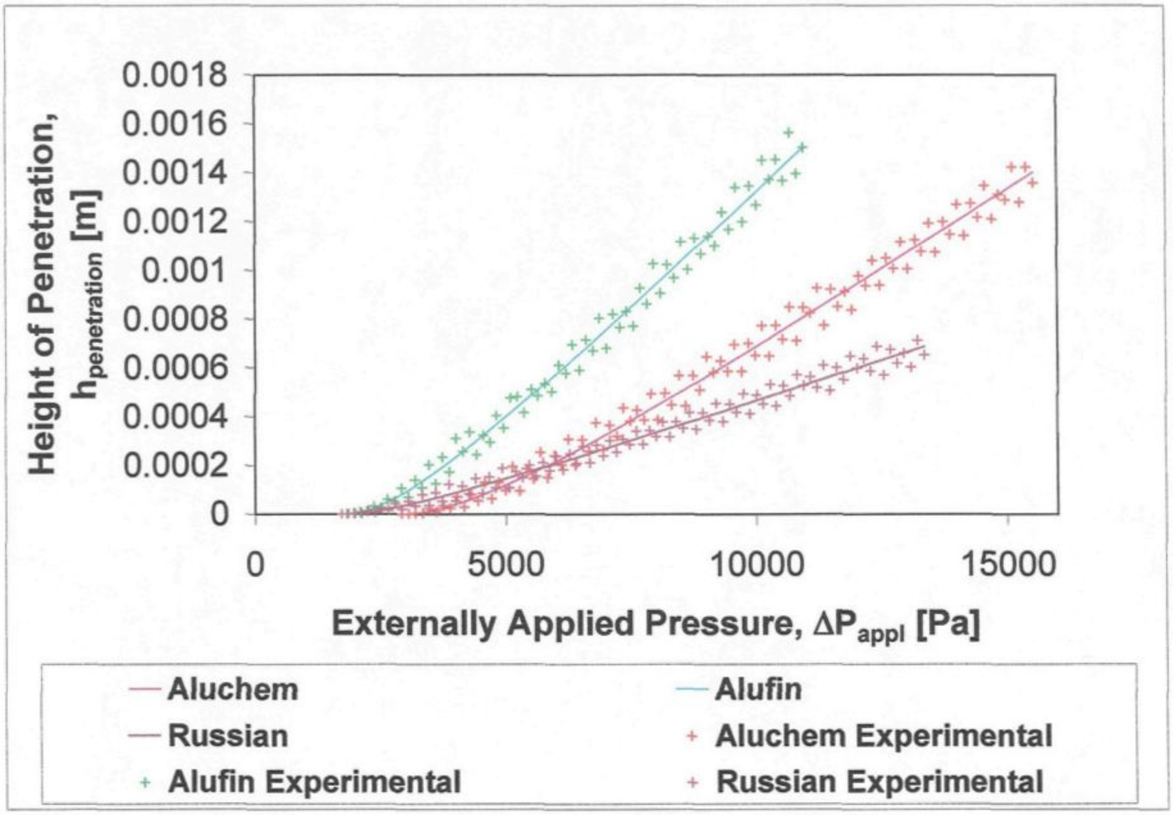

Figure 5.15 Height of Capillaries as a Function of Externally Applied Pressure for the Capillary Model of Cylindrical Pores with Periodically Changing Radii

5.3.3 Results of Contact Angle and Roughness Calculations

It is very important to determine the degree of surface roughness because, as it was discussed for the sessile drop experiments, roughness plays an important role on the wettability of particles. The experiments were conducted with rough particles, and it was desired to find a method to separate or classify the rough particles as they are. The contact angle values which were calculated by using Equation 2.14 are for rough particles. Therefore, the contact angle values calculated from this equation, θ_r, can be taken directly to compare the wettability of the particles. On the other hand, the contact angle values for smooth surfaces, θ_s, can be calculated by using Equation 3.1 if roughness ratio values, W_r, of that particular size range are known. In this equation, θ_r values are known and θ_s values are determined. θ_r and θ_s values can be compared to determine the effect of roughness on the wettability of smooth surfaces as well as to explain the effect of roughness on the wettability of a certain size range of alumina particles.

Another important use of θ_s is as follows. The roughness of alumina particles depends on the alumina production and the size reduction. Therefore, these factors can change the rough surface contact angle, θ_r, but it will not affect the smooth surface contact angle, θ_s. If the roughness of a given alumina can be measured using the θ_s determined for that alumina during this study θ_r which is the defining factor for wetting can be determined for that specific alumina. This will give a good idea about the wetting characteristics of that specific alumina. This can be compared with the contact angles of other alumina particles in order to decide whether it is suitable for filtration or not. Calculation of θ_s requires determination of accurate roughness ratio values, W_r.

In this study, roughness ratios, W_r, were determined from profilometer analyses as explained in Section 4.4. The total area scanned for each type of alumina particles and the corresponding values for roughness ratio values and contact angles calculated for two size ranges by using the capillary model with energy balance are given in Table 5.6.

Table 5.6 Summary of Contact Angle and Roughness Calculations

Type of Alumina Particles	**R/λ** ***1.2-1.4 mm**	**R/λ** ***3-6 mm**	**Total Area [μm²]**	**θ_r [°]** ***1.2-1.4 mm**	**W_r** ***1.2-1.4 mm**	**θ_s [°]**	**W_r** ***3-6 mm**	**θ_r [°]** ***3-6 mm**
Alcoa	0.1869	0.1080	29403	115	3.0964	98	1.6998	104
Russian	0.1744	-	20764	149	2.8250	108	-	-
Naigai	0.1691	0.1265	21275	122	2.7157	101	1.9602	112
Aluchem	0.1085	-	27259	165	1.7067	125	-	-
Alufin	0.1440	-	21901	129	2.2441	106	-	-
Itochu	0.1657	-	14010	164	2.6480	111	-	-
Fused Alumina	0.0256	0.0664	65577	124	1.0393	122	1.2644	132
New Alufin	0.1168	0.1324	21555	129	1.8189	110	2.0517	135

* Particle Size Range

Considering the θ_r values of alumina particles within 1.41-1.19 mm size range, it can be seen that Naigai alumina particles wet slightly better than Alufin and Russian particles; however, Alcoa particles wet better than all three of them. Aluchem and Itochu alumina particles wet the least among them. Although the infiltration experiments are conducted by using 1.41-1.19 mm size range alumina particles, according to Equation 3.1, the θ_s values calculated for each type of alumina particles can be utilized to calculate the wettability of the same type of alumina particles with the same chemical properties as long as their roughness ratios are known. Thus, the roughness ratios for four types of alumina particles within 3-6 mm size range were found by analyzing their surfaces using profilometer. Then using the θ_s values calculated for the corresponding type of alumina particles, the wettabilities of these four types of alumina particles within 3-6 mm size range were calculated and tabulated together with other results in Table 5.6. As far as 3-6 mm particles are concerned, it is observed that the order of wetting is not changed. Still Alcoa particles have best wettability followed by Naigai, fused alumina and New Alufin particles in the order of decreasing wettability. On the other hand, for these four types of alumina particles the contact angle values for rough particles change between 6-11° due to the changes in their respective roughness ratios. This shows once more the significant effect of roughness on the wettability.

In Table 5.7, the contact angle values calculated by using two of the models described in Chapter 2 are given for six different types of alumina particles. The tabulated results are for one size range of particles (1.2-1.4 mm). The model developed on energy balance with an average pore radius is presented as Model I. The contact angle value on rough surface of Alcoa alumina particles by using the energy balance model with pore size distribution, Model II, was found as 122°. The force balance model is called as Model III. It can be concluded that the results of all three models are consistent. Model I and III can be used to explain the wettability phenomenon of granular tabular alumina particles. However, the results of Model II can be enhanced by measuring the pore size distribution of the bed more precisely, for instance with the help of a mercury porosimeter.

Table 5.7 Comparison of Calculated Contact Angle Values by Two Capillary Models

Type of Alumina Particles	θ_r [°], from Model I	θ_r [°], from Model III
Alcoa	115	117
Russian	149	148
Naigai	122	124
Aluchem	165	168
Alufin	129	130
Itochu	164	163

5.3.4 Results of Sample Analysis

In this section, results obtained from the optical microscope, SEM, and TEM analyses are summarized. All of the analyses were given in Appendix E.

5.3.4.1 Results of Optical Microscope Analyses

Four different physical aspects of alumina particles were determined using optical microscope. These results were used in contact angle calculation as explained in Section 5.3.3. The results obtained are summarized in Table 5.8.

Table 5.8 Summary of Parameters Measured by the Image Analysis Software

Type of Alumina Particles	**Number of Particles**	**Aspect Ratio**	**Shape Factor ϕ**	**Bed Porosity ε**	**Hydraulic Radius of Capillary, r_h [mm]**
Alcoa	1008	1.5380	0.882039388	0.4093	0.13242
Russian	1378	1.3930	0.95751736	0.4147	0.146992
Naigai	1307	1.4525	0.93275612	0.3848	0.126409
Aluchem	1646	1.4269	0.93695162	0.4499	0.166029
Alufin	1802	1.4390	0.95041713	0.3756	0.123871
Itochu	1779	1.4564	0.929335519	0.4255	0.149133
Fused	1494	1.3871	0.945978754	0.4943	0.200342
New Alufin	1560	1.3373	0.976573402	0.4602	0.180389

The aspect ratio values given in Table 5.8 were found to correct some results of the image analysis. Sometimes, undesired but inevitable light contrasts are captured. These sharp differences in the contrast are detected by the software like perfectly circular tiny points and have been taken into consideration as alumina particles. This problem is avoided by applying a cross check between aspect ratio and area measurements taken. When very small area values having an aspect ratio very close to 1 were detected, they were discarded.

5.3.4.2 Results of SEM Analysis

In order to facilitate SEM analysis, a method was developed making use of different fluorescence characteristics of magnesia and spinel under UV light. The investigations showed that some minerals such as brucite [$Mg(OH)_2$], dolomite [$CaMg(CO_3)_2$], hydromagnesite [$XH_2O.MgCO_3$], magnesite [$MgCO_3$], spinel [$MgAl_2O_4$], chondrodite [$(Mg, Fe)_5(SiO_4)_2(F,OH)_2$], forsterite [$Mg_2SiO_4$] showed fluorescent behavior under UV light [142]. It was also stated that periclase [MgO>90%] was not fluorescent under UV light in a dark environment. It can be concluded that the magnesium including fluorescent minerals other than spinel are carbonates or hydrates of magnesium. Since it is not possible for the magnesium to form carbonates or hydrates in the alumina bed during the experiments, and it is known that alumina is not fluorescent under UV light, the fluorescent sites under UV light should be spinel. Therefore, in a dark room, long wave UV-light was applied onto the polished samples by using a portable UV light source, so that the newly formed spinel sites were rapidly recognized and marked before SEM analysis (see Figure 5.16).

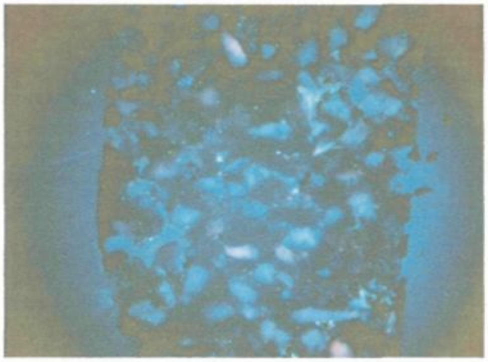

Figure 5.16 Newly Formed Spinel Sites (Dispersed Bright Dots) Detected Under UV light.

Figure 5.17 shows the SEM analysis of micron and sub-micron size spinel particulates which were previously identified using UV-light method.

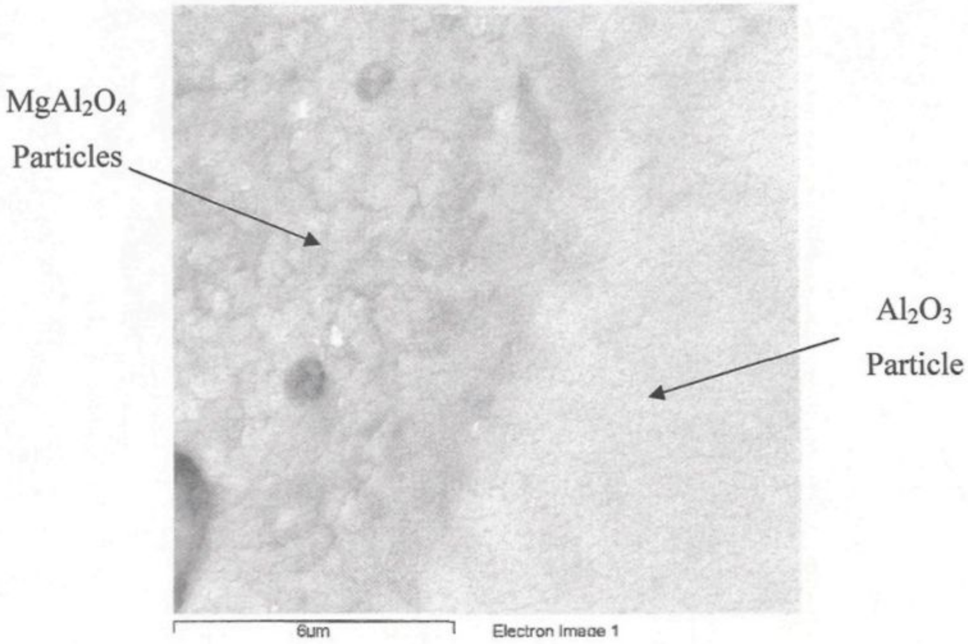

Figure 5.17 Image of Micron and Sub-micron Size Spinel Particulates Detected on the Alumina Particles

Although UV-light method helped facilitate SEM analysis, it has a disadvantage accompanied with it. All of the spinel particulates formed could not be observed by using this technique. Only the ones at preferred orientations could be observed. This makes UV-light method a semi-quantitative one.

The preliminary SEM analysis showed that the information obtained was not enough to prove the existence of spinel particulates. Theoretically, if EDS (energy dispersive x-ray spectroscopy) or WDS (wave dispersive x-ray spectroscopy) quant analysis conducted on a pure, stoichiometric, and thick enough spinel and magnesia samples, respectively, Al-Mg-O and Mg-O should be measured in corresponding stoichiometric amounts. Then, spinel and magnesia can be easily differentiated. However, this was not the case. Since the detected particulates were too small, when the electron beam coming from the field emission gun stroke one of them, for instance, the back-scattered electrons did not carry only the information coming from that tiny particulate, but also from the layer present under the detected particulate. In this work, this layer was always a part of an alumina particle. Consequently, the results of energy dispersive x-ray analysis obtained during SEM analysis always included aluminum and oxygen coming from the alumina particle (Figure 5.18). Depending on the size of the particle of interest, the amount of aluminum and oxygen coming from the alumina particle differed. Therefore, magnesia and spinel particulates that were analyzed could give similar results during SEM analysis. Thus, to determine the structures of these tiny particulates, TEM analysis was conducted.

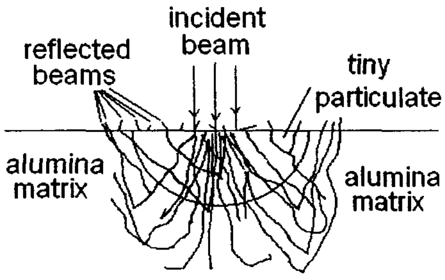

Figure 5.18 Schematical Sketch of the Problem Encountered During SEM Analyses

5.3.4.3 Results of TEM Analysis

The holding time for the samples, on which TEM studies were conducted, were one day or three days. Al-6.9 wt% Mg alloy was used during the experiments. The investigation focused on alumina/Al-Mg alloy interfaces in order to understand the type of chemical reactions taking place between alumina and Al-Mg alloy. In all of the examined samples, only spinel formation was observed. The existence of any magnesia was not detected. Figure 5.19 shows typical examples of TEM images of an interface between metal and alumina. In Figure 5.19, spinel layer on the interface is clearly visible. Bright particle on the left of the dark-field image is Al_2O_3, which is accidentally in a strong diffracting orientation simultaneously with the spinel layer. A theoretical [211] pattern for spinel is superimposed on the diffraction pattern. The corresponding EDS maps for Figure 5.19 are displayed in Figure 5.20. One can see that there is an oxide layer on the interface. It was identified as Al-Mg spinel using both the diffraction analysis and EDS data. Chemical composition of the spinel is somewhat variable. On this particular interface, individual measurements along the layer have shown the oxygen concentration from 52 to 56 at.%, while contents of Al and Mg are in the ranges 16-32 at.% and 13-31 at.%, respectively.

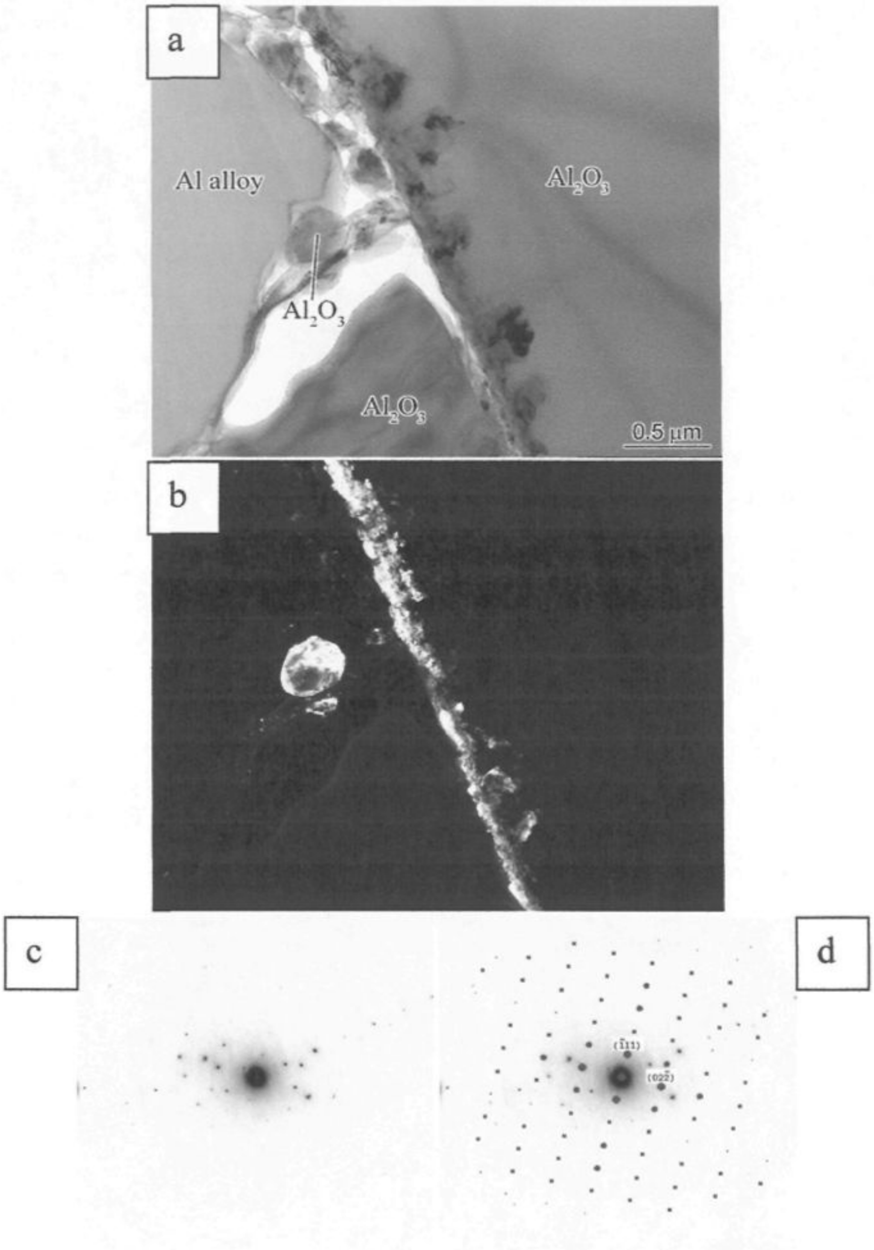

Figure 5.19 (a) Bright-Field Image, (b) Dark-Field Image in a Spinel Reflection, and (c) Selected Area Diffraction Pattern From Spinel (d) [211] pattern for spinel superimposed on the diffraction pattern

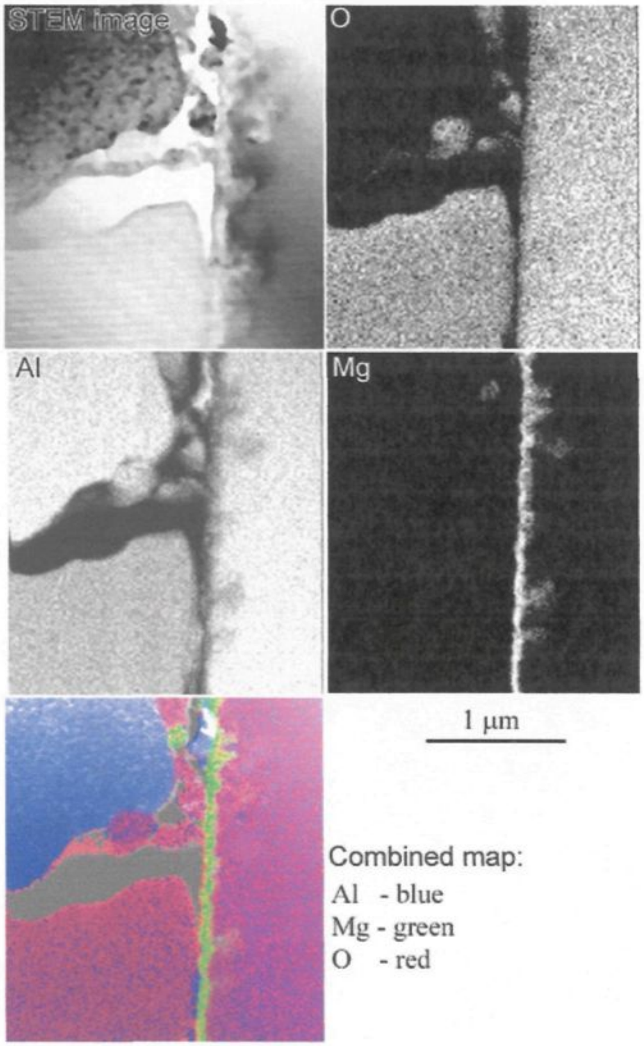

Figure 5.20 STEM-EDS Mapping of the Area Shown in Figure 5.19 (These Images Are Rotated with Respect to the Images in Figure 5.19)

Built-in standards provided by the software package of TEM were used for quantitative analysis. However, since the software usually underestimated the concentration of light elements, in this case O in Al-Mg spinel, the ratios of Al and Mg (i.e. Al/Mg or Mg/Al), which are neighboring elements in the periodic table, could be determined more accurately.

Since no experimental standards were available with different sample thickness and different chemical compositions containing three elements (Al, Mg and O), alumina particles present in the analyzed specimens were used for correcting the error coming from the software package, assuming that the alumina particles present in the sample were stoichiometric alumina particles. The complete results of TEM analyses are presented in Appendix E.

5.3.5 Thermodynamic Calculations and Results

The TEM results showed that only spinel was formed on the alumina surface under the conditions used. A thermodynamic analysis was carried out to determine the possible reactions for spinel formation. The standard Gibbs' free energy of formation for magnesia, spinel, and alumina are given in a report [95]:

$$Mg(l) + 1/2O_2(g) \rightarrow MgO(s) \tag{5.2}$$

$$\Delta G^{\circ}_{Rxn1} = -607{,}563 - T\log T + 112.65T \text{ J/mol} \tag{5.3}$$

$$Mg(l) + 2Al(l) + 2O_2(g) \rightarrow MgAl_2O_4(s) \tag{5.4}$$

$$\Delta G^{\circ}_{Rxn2} = -2{,}339{,}170 - 16.8T\log T + 491.2T \text{ J/mol} \tag{5.5}$$

$$2Al(l) + 3/2O_2(g) \rightarrow Al_2O_3(s) \tag{5.6}$$

$$\Delta G^{\circ}_{Rxn3} = -1{,}696{,}077 - 15.75T\log T + 385.5T \text{ J/mol} \tag{5.7}$$

The standard Gibbs' free energy of formation of reaction given in Equation 5.2 was verified using data from another source [143]:

$$\Delta G^{\circ}_{Rxn1} = -609{,}017 - 1.01T\log T + 112.92T \text{ J/mol} \tag{5.8}$$

These data are in good agreement, and data from reference [95] were used for the following reactions. During the experiments, vacuum was applied and the system was flushed with UHP Ar gas. Therefore, virtually very small quantity of oxygen is available, and the formation of spinel and magnesia through reactions given by Equations 5.9 and 5.11 is more probable; magnesia can react further giving spinel through reactions given by Equation 5.13 below:

$$Mg(l) + 4/3\,Al_2O_3(s) \rightarrow MgAl_2O_4(s) + 2/3\,Al(l) \tag{5.9}$$

$$\Delta G^{\circ}_{Rxn4} = \Delta G^{\circ}_{Rxn2} - 4/3\Delta G^{\circ}_{Rxn3} = -77{,}734 + 4.2T\log T - 22.8T \text{ J/mol} \tag{5.10}$$

$$Mg(l) + 1/3Al_2O_3(s) \rightarrow MgO(s) + 2/3Al(l) \tag{5.11}$$

$$\Delta G^{\circ}_{Rxn5} = \Delta G^{\circ}_{Rxn1} - 1/3\,\Delta G^{\circ}_{Rxn3} = -42{,}204 + 4.25T\log T - 15.85T \text{ J/mol} \tag{5.12}$$

$$MgO(s) + Al_2O_3(s) \rightarrow MgAl_2O_4(s) \tag{5.13}$$

$$\Delta G^{\circ}_{Rxn6} = \Delta G^{\circ}_{Rxn4} - \Delta G^{\circ}_{Rxn5} = -35{,}530 - 0.05T\log T - 6.95T \text{ J/mol} \tag{5.14}$$

Standard Gibbs free energies were calculated for the above reactions at 1000K and are given in Table 5.9. Reaction given in Equation 5.9 indicates the strong tendency of Al-Mg alloy to form spinel in the absence of any oxygen in gaseous form. Magnesia, which forms following the reaction shown in Equation 5.11, can be converted to spinel as well due to

Reaction 5.13. However, Reaction 5.13 is a solid phase reaction and such reactions are kinetically very slow. Therefore, the reaction given by Equation 5.9 is the most likely source of spinel formation. In the study reported in reference [12], only spinel formation was also observed. They also measured the variation of spinel thickness as a function of the Mg content of the alloy. Phase diagrams given by reference [10] indicate that spinel formation is favored under the experimental conditions used in the current study. These phase diagrams were reproduced by using ThermoCalc software and its available database. The results were the same. As an example, the calculated Al-Mg phase diagram was given in Figure 5.21 below:

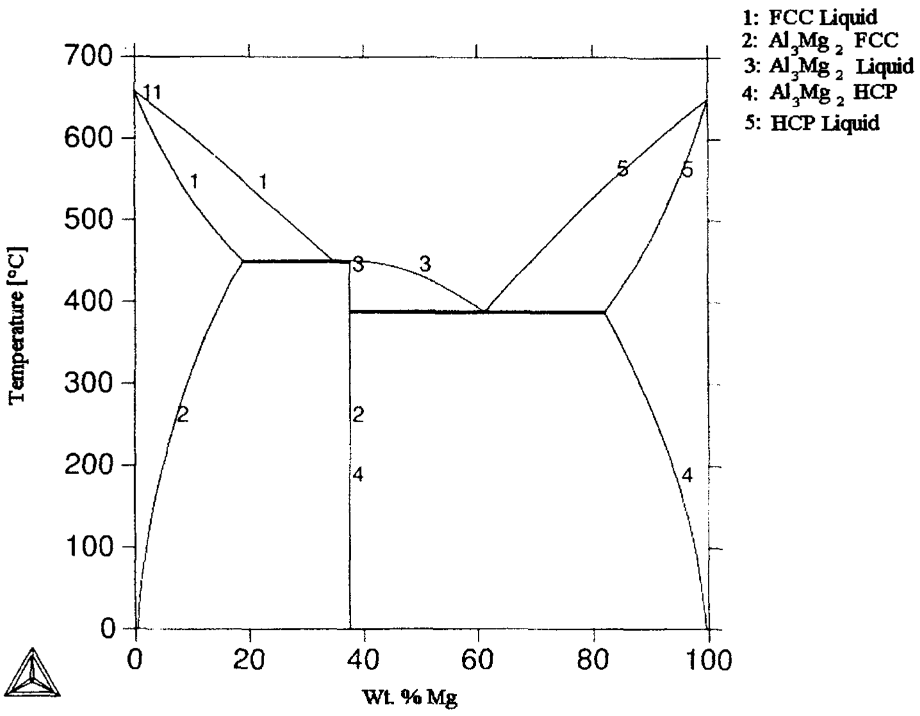

Figure 5.21 Al-Mg Phase Diagram Calculated by ThermoCalc Software[9]

---

[9] World wide web page can be reached in internet from http://www.thermocalc.com/

Table 5.9 Standard Gibbs free energies of the reactions calculated at 1000 K.

Reactions	**ΔG^0_{1000K} [kJ]**	**Equation No**
$Mg(l) + 1/2O_2(g) \rightarrow MgO(s)$	-495.9	**(5.2)**
$Mg(l) + 2Al(l) + 2O_2(g) \rightarrow MgAl_2O_4(s)$	-1,898.4	**(5.4)**
$2Al(l) + 3/2O_2(g) \rightarrow Al_2O_3(s)$	-1,357.8	**(5.6)**
$Mg(l) + 4/3\,Al_2O_3(s) \rightarrow MgAl_2O_4(s) + 2/3\,Al(l)$	-87.9	**(5.9)**
$Mg(l) + 1/3Al_2O_3(s) \rightarrow MgO(s) + 2/3Al(l)$	-45.3	**(5.11)**
$MgO(s) + Al_2O_3(s) \rightarrow MgAl_2O_4(s)$	-42.6	**(5.13)**

Very high Gibbs free energy values for reactions given in Equations 5.2, 5.4, and 5.6 show how stable the oxides are. Phase diagrams of reference [10] also show that spinel formation would take place at very low oxygen concentrations in the gas phase. After applying vacuum and flushing with UHP Ar gas, even if minute amounts of oxygen were left in the system, the most probable product that would form on alumina particle is spinel.

The TEM results in Figure 5.18 and 5.19 show that the infiltration of Al-6.9 wt% Mg alloy[10] into a bed of alumina particles resulted in the formation of spinel only. This is consistent with the thermodynamic analysis of the reactions that could take place under the conditions of the current study. In order to study the effect of holding time on the formation of spinel or magnesia, TEM studies were also carried out on the samples with one day

---

[10] The complete analysis of the Al-Mg alloy is 6.87 wt% Mg, 0.14 wt% Fe, 0.10 wt% Si, 0.009 wt% Ga, 0.007 wt% Mn, 0.006 wt% V, 0.002 wt% Cr, 0.002 wt% Cu, 0.002 wt% Ni, 0.002 wt% Zn, 0.001 wt% Pb, 0.001 wt% Zr, 0.0003 wt% B, 0.0001 wt% Cd.

holding time. Some results of the Al-6.9%Mg samples after one day holding are given in Figure 5.22. This result also showed that, only spinel was present and no magnesia was detected.

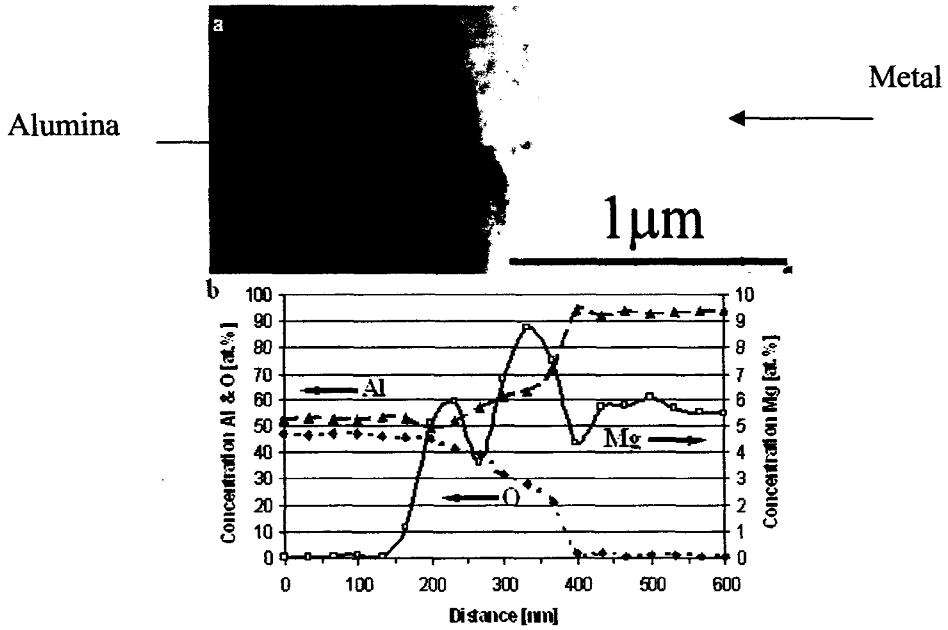

Figure 5.22 Interface Between Metal and Alumina: (a) STEM Image and (b) EDS Compositional Profile Across the Interface

CHAPTER 6

CONCLUSIONS AND RECOMMENDATIONS

Conclusions

Wetting between molten aluminum and granular media (alumina) was studied with the objective of developing a method to characterize the wetting of granular alumina in contact with Al-Mg alloys. Sessile-drop and infiltration methods were tested for their suitability for this characterization.

An experimental system with capabilities of a liquid metal injection and instantaneous quenching was set up for the sessile-drop method. After numerous trials with rough surfaces, it was concluded that this technique is not suitable for the wettability measurements using large alumina particles. During the experiments, the liquid droplet was pinned down by the sharp edges of the alumina particles. This prevents the droplet from taking its proper form. On the other hand, the trials with smooth surfaces showed that the sessile-drop experimental set-up is working properly. The contact angle and the surface tension values measured for different smooth substrates are in good agreement with the values found in the literature.

A second system was built for the infiltration experiments. The results show that it is possible to classify various alumina particles based on their wettability by aluminum alloys.

Different mathematical models were proposed to analyze the experimental data and to determine the actual contact angle of the alumina surfaces. The results of the models are in good agreement with each other. The angles determined from the experimental data are for the rough surfaces since the particles are never smooth.

A method was developed to evaluate the wettability of the alumina particles received by the industry without repeating the infiltration experiments each time. The contact angles for the smooth particles were determined from the measured contact angles of rough particles. This is carried out by measuring the surface roughness with profilometer and following the procedure given in Section 5.3.3 for different kinds of alumina particles used during this study. When a new batch of alumina particles is received by the industry, if the roughness of the particles are measured with a profilometer (which is a simple test), the actual contact angle can be calculated for the particles received by using the smooth contact angle determined during this study for that specific alumina type. This will facilitate the pre-evaluation of the alumina quality.

The chemical reactions taking place between Al-6.9wt%Mg alloy and different alumina particles were also investigated using the infiltration technique. SEM and TEM analyses showed that spinel was formed independent of the experiment duration and the type of alumina particles used in the experiments at 1000 K under argon atmosphere. The thermodynamic analysis indicated the same tendency.

Recommendations

In this study, the kinetics of the reactions were not measured. Measuring the kinetics of spinel formation would complement this study.

In model II, the porosity distribution curve was divided into three regions in order to demonstrate the model. If a more detailed porosity distribution can be measured, this might improve the accuracy of the results further.

During this study, an original method using the infiltration technique was proposed to determine the wetting characteristics of solid particles with rough surfaces for a given liquid. This method was tested for alumina/aluminum alloy systems and gave very good results. It would be interesting to apply this method to other solid-liquid systems.

REFERENCES

1. http://www.world-aluminum.org/history/index.html
2. K. Grjotheim, C. Krohn, M. Malinovsky, K. Matiasovsky, and J. Thonstad, Aluminium Electrolysis, The Chemistry of the Hall-Héroult Process, Aluminium-Verlag GmbH, Dusseldorf,1977.
3. P. A. Plunkert, *Annual Review of Aluminum*, U.S. Geological Survey, Mineral Industry Surveys, 2004.
4. P. A. Plunkert, *Annual Mineral Commodity Summaries: Bauxite and Alumina*, U.S. Geological Survey, January 2005.
5. P. A. Plunkert, *Minerals Year Book: Aluminum*, Aluminum-2004, U.S. Geological Survey, 2004.
6. K. Wefers, Nomenclature, Preparation, and Properties of Aluminum Oxides, Oxide Hydroxides, and Trihydroxides, Alumina Chemicals Science and Technology Handbook, pp.13-22, The American Ceramic Society Inc, 1990.
7. P. R. Chidambaram, G. R. Edwards and D. L. Olson, *A Thermodynamic Criterion to Predict Wettability at Metal-Alumina Interfaces*, Metallurgical Transactions B, Vol. 23B, pp. 215-222, 1992.

8. B. Hallstedt, Z. K. Liu and J. Agren, *Fibre-Matrix Interactions During Fabrication of Al_2O_3-Mg Metal Matrix Composites*, Materials Science and Engineering, Vol. A129, pp. 135-145, 1990.
9. A. Munitz, M. Metzger and R. Mehrabian, *The Interface Phase in Al-Mg/Al_2O_3 Composites*, Metallurgical Transactions A, Vol. 10A, pp.1491-1497, 1979.
10. I. Jin and D. J. Lloyd, *Control of Interfacial Chemical Reaction in Alumina-Reinforced Aluminum MMCs*, AFS Transactions, pp. 683-686, 1994.
11. J. S. Moya, H. P. Steier, J. Requena and R. Rezakhanlou, *Interfacial Reactions in Mg-Containing Aluminum Alloys/Mullite-Zirconia Reaction Sintered Composites*, Acta Materialia, Vol. 46, No. 7, p.2423-2429, 1998.
12. R. Mogilevsky, S. R. Bryan, W. S. Woolbach, T. W. Krucek, R. D. Maier, G. L. Shoemaker, J. M. Chabala, K. K. Soni and R. Levi-Setti, *Reactions at the Matrix/Reinforcement Interface in Aluminum Alloy Matrix Composites*, Materials Science and Engineering, Vol. A191, pp. 209-222, 1995.
13. D. G. Clark, J. A. Little and T. W. Clyne, *Ceramic/Metal Wetting in a Spontaneous Infiltration Process For Fabrication of Metal Matrix Composites*, The Minerals, Metals and Materials Society, pp.993-999, 1993.
14. G. Kaptay, T. Matsushita, K. Mukai and T. Ohuchi, *On Different Modifications of the Capillary Model of Penetration of Inert Liquid Metals into Porous Refractories and Their Connection to the Pore Size Distribution of the Refractories*, Metallurgical and Materials Transactions B, Vol. 35B, pp. 471-486, 2004.

15. Metals Handbook, 8th Edition, Vol. I, Properties and Selection of Metals, Edited by Taylor Lyman, ASM, 1961.

16. W. W. Mullins, *Solid Surface Morphologies Governed by Capillarity*, Metal Surfaces, W. D. Robertson and N. A. Gjostein, Eds., American Society of Metals, New York, Chapter 2, 1963.

17. R. K. Trivedi, *Theory of Capillarity*, Key Topics in the Theory of Phase Transformations, American Institute of Metallurgical Engineers, New York, Chapter 2, 1975.

18. N. Eusthathopoulos, M. G. Nicholas and B. Drevet, Wettability at High Temperatures, Pergamon Materials Series Volume 3, Series Editor: R. W. Cahn, Amsterdam, 1999.

19. T. Young, Phil. Trans. Roy. Soc., pp. 65, Vol. 95, London, 1805.

20. A. Dupré, Théorie Méchanique de la Chaleur, pp. 207, Paris, 1869.

21. Leonardo da Vinci, according to Pogg. Ann., 101, pp. 501, 1857. (the reference to da Vinci appears in a footnote)

22. J. F. Padday, in Surface and Colloid Science, Vol I, Ed. Egon Matijević, John Wiley and Sons, N.Y., pp. 39-99, 1969.

23. I. Newton, *Optiks*, 3rd Ed. 31st Query, Wand J. Innys, St.Pauls, London, 1721.

24. F. Hawksbee, *Physico-mechanical Experiments*, London, pp.139, 1709.

25. J. A. von Segner, Comment Soc. Reg. Göting., 1, pp.301, 1751.

26. P. S. de Laplace, *Mechanique Celeste, Suppl. au X Livre*, Courier, Paris, 1805.

27. R. de Boer, Theory of Porous Media, Highlights in the Development and Current State, Springer-Verlag, Berlin, 2000.

28. A. Marmur, *Penetration and Displacement in Capillary Systems*, in Modern Approach to Wettability : Theory and Applications, edited by M. E. Schrader and G. Loeb, Plenum Press, New York, 1992.
29. C. Garcia-Cordovilla, E. Louis and J. Narciso, *Pressure Infiltration of Packed Ceramic Particulates by Liquid Metals*, Acta Mater., Vol. 47, No. 18, pp. 4461-4479, 1999.
30. J. F. Padday, in Surface and Colloid Science, Vol I, Ed. Egon Matijević, John Wiley and Sons, N.Y., pp. 101-149, 1969.
31. L. E. Murr, Interfacial Phenomena in Metals and Alloys, London, 1975.
32. F. K. Hansen, G. Rodsrun, Journal of Colloid and Interface Science, Vol. 141, pp. 1-12, 1991.
33. A. Mortensen, *Interfacial Phenomena in the Solidification Processing of Metal Matrix Composites*, Materials Science and Engineering, A135, pp. 1-11, 1991.
34. T. Lebeau, J. O. Strom-Olsen, J. E. Gruzleski and R. A. L. Drew, *Aluminum Alloy/Alumina-Based Ceramic Interactions*, Materials Characterization, Vol. 35, pp. 11-22, 1995.
35. D. Muscat and D. A. L. Drew, *Modelling the Infiltration Kinetics of Molten Aluminum into Porous Titanium Carbide*, Metallurgical Transactions A, Vol. 25A, No. 11, pp.2357-2370, 1994.
36. J. W. Nowok, *Mass Transport Phenomena at the Liquid Metal/Substrate (Metal/Carbide) Interface*, Materials Science and Engineering, A232, pp. 157-162, 1997.

37. C. Toy and W. D. Scott, *Wetting and Spreading of Molten Aluminium Against AlN Surfaces*, Journal of Materials Science, Vol. 32, pp.3243-3248, 1997.
38. Jr. D. A. Weirauch and W. J. Krafick, *The Effect of Carbon on Wetting of Aluminum Oxide by Aluminum*, Metallurgical Transactions A., Vol. 21A, No. 6, pp. 1745-1751, 1990.
39. S. A. M. Foister, M. W. Johnston and J. A. Little, *The Interaction of Liquid Aluminum With Silicon Carbide and Nitride-Based Ceramics*, Journal of Materials Science Letters, Vol. 12, No. 4, pp. 209-211, 1993.
40. V. I. Nizhenko and L. I. Floka, *Wetting of* Al_2O_3*-Based Oxide Ceramics by Molten Aluminum*, Powder Metallurgy and Metal Ceramics, Vol. 40, No. 5-6, pp. 271-276, 2001.
41. A. Contreras, V. H. Lopez, C. A. Leon, R. A. L. Drew and E. Bedolla, *The Relation Between Wetting and Infiltration Behaviour in the Al-1010/TiC and Al-2024/TiC Systems*, Advances in Technology of Materials and Materials Processing Journal, Vol. 3, No. 1-2, pp. 27-34, 2001.
42. E. Saiz, R. M. Cannon and A. P. Tomsia, *Wetting and Diffusion Processes at Liquid Metal/Ceramic Interfaces*, Proc. 6th Japan International SAMPE Symposium, pp. 863-866, Oct. 26-29 1999.
43. W. Shi, M. Kobashi, and T. Choh, *Effect of Wettability and Powder Premixing on the Spontaneous Infiltration of Molten Mg into Alumina Fiber Preform*, Zeitschrift fur Metallkunde, vol. 90, 4, pp. 294-298, 1999.

44. K. Landry, C. Rado, R. Voitovich and N. Eustathopoulos, *Mechanisms of Reactive Wetting: The Question of Triple Line Configuration*, Acta Materialia, Vol. 45, No. 7, pp. 3079-3085, 1997.

45. A. G. Raraz, P. R. Chidambaram and G. R. Edwards, *Novel Wetting Technique for Metal-Ceramic Joining and Infiltration of Porous Ceramics by Liquid Metals*, Processing and Fabrication of Advanced Materials V, Cincinnati, Ohio, USA, 6-10 Oct. 1996, pp. 613-622, 1996.

46. P. J. Bunyan, *Liquid Phase Processing and Interfacial Behaviour of Metal Matrix Composites*, Australian Fracture Group Symposium, Sydney, Australia, pp. 120-125, 1990.

47. C. A. Leon and R. A. L. Drew, *Processing of Metal Matrix Composites by Wetting Assisted Infiltration Using Metal Coated Reinforcements*, Processing and Fabrication of Advanced Materials VII, p. 323-334, Edited by T.S. Srivatsan and K.A. Khor, The Minerals, Metals and Materials Society, 1998.

48. D. N. Stacopolus, *Computation of Surface Tension and of Contact Angle by the Sessile Drop Method*, Journal of Colloid and Interface Science, Vol. 23, pp. 453-456, 1967.

49. V. Leroux, J.C. Labbe, M.E.R. Shanahan, D. Tetard and J.F. Goujaud, *Contact Angle and Surface Tension Measurements on a Metal Drop by Image Processing and Numerical Calculations*, High Temperature Material Processes, Vol. 4, pp. 351-364, 2000.

50. O. I. Rio, D. Y. Kwok, R. Wu, J. M. Alvarez and A. W. Neumann, *Contact Angle Measurements by Axisymmetric Drop Shape Analysis and an Automated Polynomial Fit*

Program, Colloids and Surfaces A: Physicochemical and Engineering Aspects, Vol. 143, pp. 197-210, 1998.

51. A. Sklodowska, M. Wozniak and R. Matlakowska, *The Method of Contact Angle Measurements and Estimation of Work of Adhesion in Bioleaching of Metals*, Biological Procedures Online, Vol. 3, No 1, pp. 114-121, 1999. (http://www.biologicalprocedures.com)
52. M. E. R. Shanahan, *Profile and Contact Angle of Small Sessile Drops: A More General Approximate Solution*, Journal of Colloid Science Faraday I, Vol. 80, pp. 37-45, 1984.
53. S. B. G. M. O'Brian, *Some Surface Tension and Contact Angle Problems in Industry*, in Contact Angle, Wettability and Adhesion, Ed K.L.Mittal, VSP Publishers, pp. 937-951, 1993.
54. J. M. Alvarez, A. Amirfazli and A. W. Neumann, *Automation of Axysymmetric Drop Shape Analysis-Diameter for Contact Angle Measurements*, Colloid Surfaces A: Physical and Chemical Engineering Aspects, Vol. 156, pp. 163-176, 1999.
55. X. B. Zhou and J. Th. M. De Hosson, *Influence of Surface Roughness on the Wetting Angle*, Journal of Material Research, Vol. 10, pp. 1984-1992, 1984.
56. K. Grundke, T. Bogomil, T. Gietzelt, H. J. Jacobasch, D. Y. Kwok and A. W. Neumann, *Wetting Measurements on Smooth, Rough and Porous Solid Surfaces*, Progess in Colloid and Polymer Science, Vol. 101, pp. 58-68, 1996.
57. A. M. Cazabat and M. A. Cohen Stuart, *Dynamics of Wetting: Effect of Surface Roughness*, Journal of Physical Chemistry, Vol. 90, pp. 5845-5849, 1986.

58. C. Keisler and J. L. Lataillade, *The Effect of Substrate Roughness Characteristics on Wettability and on the Mechanical Properties of Adhesive Joints Loaded at High Strain Rates*, Journal of Adhesion Science and Technology, Vol. 9, pp. 395-411, 1995.
59. R. N. Wenzel, Industrial and Engineering Chemistry, Vol. 28, pp. 988, 1936.
60. C. L. F. Vigor, *Contact Angle Measurements on Roughened Surfaces*, M. S. Thesis, University of New Brunswick, 1972.
61. S. C.Colbeck, *Capillary Bonding of Wet Surfaces - The Effects of Contact Angle and Surface Roughness*, Journal of Adhesion Science and Technology, Vol. 11, pp. 359-371, 1997.
62. A. B. D. Cassie and S. Baxter, Transaction of the. Faraday Society, Vol. 40, pp.546, 1944.
63. R. Shuttleworth and G. L. J. Bailey, Discussions of the Faraday Society, Vol. 3, pp. 16, 1948.
64. A. Marmur, *Contact Angle Equilibrium: The Intrinsic Contact Angle*, Contact Angle, Wettability and Adhesion, pp. 125-137, 1993.
65. H. Nakae, R. Inui, Y. Hirata and H. Saito, *Effects of Surface Roughness on Wettability*, Proceeding of the Third International...Spain, September 1996/Proceeding edition, pp. 2313-2318, 1998.
66. R. D. Hazlett, *On Surface Roughness Effects in Wetting Phenomena*, Contact Angle, Wettability and Adhesion, p. 173-181, 1993.
67. D. Myers, Surfaces, Interfaces and Colloids Principles and Applications, 2nd ed., VCH Pub, N.Y., 1990.

68. R. E. Johnson and Jr, R. H. Dettre, *Wettability and Contact Angles*, in Surface and Colloid Science, Ed. Egon Matijevic, Wiley-Interscience, Vol. 2, pp. 85-153, 1969.

69. S. J. Hitchcock, N. T. Carroll and M. G. Nicholas, Journal of Materials Science, Vol. 16, pp. 714, 1981.

70. M. G. Nicholas and R. M. Crispin, Journal of Materials Science, Vol. 21, pp. 522, 1986.

71. B. M. Gallois, *Wetting in Nonreactive Liquid Metal-Oxide Systems*, Journal of Metals, No.6, 1997.

72. J. De Coninck, S. Miracle-Solé and J. Ruiz, *Is There an Optimal Substrate Geometry for Wetting?*, Journal of Statistical Physics, Vol. 100, pp. 981-997, 2000.

73. V. De Jonghe, D. Chatain, I. Rivollet and N. Eustathopoulos, *Contact Angle Hysteresis Due to Roughness in Four Metal/Sapphire Systems*, Journal de Chimie Physique et de Physico-Chimie Biologique, Vol. 87, pp. 1623-1645, 1990.

74. S. Semal, T. D. Blake, V. Geskin, M. J. de Ruijter, G. Castelein and J. de Coinck, *Influence of Surface Roughness on Wetting Dynamics*, The ACS Journal of Surfaces and Colloids, Vol. 15, pp. 8765-8770, 1999.

75. M. E. R. Shanahan, *Effects of Surface Flaws on the Wettability of Solids*, Contact Angle, Wettability and Adhesion, pp. 159-171, 1993.

76. Y. Y. Perng and S. Lichter, *Unsteady Wetting on a Rough Surface Due to Electrically Altered Surface Tension*, Journal of Colloid and Interface Science, Vol. 227, pp. 119-127, 1999.

77. K. Grabowski, A. Patrykiejew, S. Sokolowski, E. V. Albano and A. de Virgilis, *Substrate Roughness-Enhanced Wetting in a Two-Dimensional Ising Model with Boundary Fields*, Surface Science, Vol. 448, No. 1, pp. 11-22, 2000.

78. L. V. Mirantsev and A. V. Zakharov, *The Effect of Surface Roughness of a Solid Substrate on its Wetting by a Smectic-A Structure in the Nematic Phase of a Liquid Crystal*, Physics of the Solid State, Vol. 41, pp. 306-312, 1999.

79. P. A. Thompson, W. B. Brickerhoff and M. O. Robbins, *Microscopic Studies of Static and Dynamic Contact Angles*, Contact Angle, Wettability and Adhesion, pp. 139-158, 1993.

80. C. Borgs, J. De Coninck, R. Kotecky, and M. Zinque, *Does the Roughness of the Substrate Enhance Wetting?*, Physical Review Letters, Vol. 74, pp. 2292-2294, 1995.

81. A. O. Parry, P. S. Swain and J. A. Fox, *Fluid Adsorption at a Non-planar Wall: Roughness-Induced First-Order Wetting*, Journal of Physics, Vol. 8, pp. 659-666, 1996.

82. V. de Jonghe and D. Chatain, *Experimental Study of Wetting Hysteresis on Surfaces With Controlled Geometrical and/or Chemical Defects*, Acta Metallurgica et Materialia, Vol. 43, pp. 1505-1515, 1995.

83. I. Rivollet, D. Chatain and N. Eustathopoulos, *Simultaneous Measurement of Contact Angles and Work of Adhesion in Metal-Ceramic Systems by the Immersion-Emersion Technique*, Journal of Materials Science, Vol. 25, pp. 3179-3185, 1990.

84. F. Hodaj, J. N. Barbier, A. Mortensen, O. Dezellus and N. Eustathopoulos, *Modelling Kinetics of Diffusion Controlled Reactive Wetting: The Role of Reaction Behind the*

Triple Line, Diffusion and Defect Data Part B: Solid State Phenomena, Vol. 72, pp. 91-96, 2000.

85. A. Mortensen, B. Drevet and N. Eustathopoulos, *Kinetics of Diffusion-Limited Spreading of Sessile Drops in Reactive Wetting*, Scripta Materialia, Vol. 36, No. 6, pp. 645-651, 1997.
86. N. Eustathopoulos and L. Coudurier, *Influence of Alloying Elements on Wettability and Adhesion Energy in Liquid Metal-Ceramic Systems*, in Contact Angle, Wettability and Adhesion, Ed. K. L. Mittal, pp. 909-920, 1993.
87. I. Jin and D. J. Lloyd, *Control of Interfacial Chemical Reaction in Alumina-Reinforced Aluminum MMCs*, American Foundry Society Transactions, pp. 683-686, 1994.
88. J. S. Moya, H. P. Steier, J. Requena and R. Rezakhanlou, *Interfacial Reactions in Mg-Containing Aluminum Alloys/Mullite-Zirconia Reaction Sintered Composites*, Acta Materialia, Vol. 46, No. 7, pp. 2423-2429, 1998.
89. W. M. Zhong, G. L'Esperance and M. Suéry, *Effect of Current Mg Concentration on Interfacial Reactions During Remelting of Al-Mg(5083)/*Al_2O_3 *Composites*, Materials Characterization, Vol. 49, pp. 113-119, 2003.
90. A. D. McLeod and C. M. Gabryel, *Kinetics of the Growth of Spinel,* $MgAl_2O_4$*, on Alumina Particulate in Aluminum Alloys Containing Magnesium*, Metallurgical Transactions A, Vol. 23A, pp. 1279-1283, 1992.
91. B. Hallstedt, Z. K. Liu and J. Agren, *Fibre-Matrix Interactions During Fabrication of* Al_2O_3*-Mg Metal Matrix Composites*, Materials Science and Engineering, Vol. A129, pp. 135-145, 1990.

92. A. Munitz, M. Metzger and R. Mehrabian, *The Interface Phase in Al-Mg/Al_2O_3 Composites*, Metallurgical Transactions A, Vol. 10A, pp.1491-1497, 1979.

93. R. Mogilevsky, S. R. Bryan, W. S. Woolbach, T. W. Krucek, R. D. Maier, G. L. Shoemaker, J. M. Chabala, K. K. Soni and R. Levi-Setti, *Reactions at the Matrix/Reinforcement Interface in Aluminum Alloy Matrix Composites*, Materials Science and Engineering, Vol. A191, pp. 209-222, 1995.

94. O. J. Siljan, G. Rian, D. T. Pettersen, A. Solheim and C. Schøning, *Refractories for Molten Aluminum Contact Part I: Thermodynamics and Kinetics*, Refractories Applications and News, Vol. 7, No. 6, 2002.

95. D. Emadi, *Study of Oxide Film Formation and Fragmentation at the Liquid-Air Interface in Al and Al-Mg Alloys, Part A: Literature Review on the Melt Oxidation of Pure Al and Al-Mg Alloys*, CSMA-95-12, Arvida Research and Development Centre, Alcan International Limited, Jonquiére, Quebec, 1995.

96. S. P. Cashion, N. J. Ricketts, M. T. Frost and C. Korn, *The Protection of Molten Magnesium and Its Alloys During Die Casting*, CSIRO Queensland Centre for Advanced Technologies, Brisbane, Australia, 2000.

97. C. Allaire, *Mechanisms of Corundum Growth in Refractories Exposed to Al-Mg Alloys*, Aluminum Transactions, Vol. 3, No. 1, pp. 105-119, 2000.

98. A. W. Neumann and R. J. Good, in Surface and Colloid Science, Vol II, R. J. Good, R. R. Stromberg (eds), Plenum Press, New York, 1979.

99. A. Rimmer, J. Y. Parlange, T. S. Steenhuis, C. Darnault and W. Condit, *Wetting and Nonwetting Fluid Displacements in Porous Media*, Transport in Porous Media, Vol. 25, pp. 205-215, 1996.

100. A. Caruana and R. A. Dawe, *Flow Behaviour in the Presence of Wettability Heterogeneities*, Transport in Porous Media, Vol. 25, pp. 217-233, 1996.

101. G. M. Homsy, Annual Review of Fluid Mechanics, Vol. 19, pp. 271, 1987.

102. J. A. Wingrave, W. H. Wade and R. S. Schechter, in Wetting, Spreading and Adhesion, Ed. J. F. Padday, pp. 261, Academic Press, New York, 1978.

103. M. R. Moldover, R. W. Gammon, Journal of Chemical Physics, Vol. 80, pp. 528, 1984.

104. M. Sahimi, B. D. Hughes, L. E. Scriven and H. T. Davis, Chemical Engineering Science, Vol. 41, pp. 2103, 1986.

105. F. E. Bartell and H. T. Osterhof, Journal of Physical Chemistry, Vol. 130, pp. 715-723, 1927.

106. F. E. Bartell and H. T. Osterhof, Journal of Physical Chemistry, Vol. 32, pp. 1553-1571, 1928.

107. F. E. Bartell and C. E. Whitney, Journal of Physical Chemistry, Vol. 36, pp. 3115-3126, 1932.

108. P. C. Carman, Soil Science, Vol. 52, pp. 1-13, 1941.

109. S. Y. Oh, J. A. Cornie and K. C. Rusell, *Wetting of ceramic particulates with liquid aluminium alloys: Part I. Experimental Techniques*, Metallurgical Transactions A, Vol. 20A, pp. 527-532, 1987.

110. S. Y. Oh, J. A. Cornie and K. C. Rusell, *Wetting of ceramic particulates with liquid aluminium alloys: Part II. Study of Wettability*, Metallurgical Transactions A., Vol. 20A, pp. 533-541, 1987.

111. C. Garcia-Cordovilla, J. Goicoechea, E. Louis and A. Pamies, *Wetting of SiC and Al_2O_3 Particulates with Pure Liquid Aluminium*, Designing Ceramic Interfaces II: Understanding and Tailoring Interfaces, pp. 429-440, 1993.

112. T. R. Jonas, J. A. Cornie and K. C. Russell, *Infiltration and Wetting of Alumina Particulate Preforms by Aluminum and Aluminum-Magnesium Alloys*, Metallurgical Transactions A, Vol. 26A, pp.1491-1497, 1995.

113. R. Asthana and P. K. Rohatgi, *Melt Infiltration of Silicon Carbide Compacts I: Study of infiltration Dynamics*, Zietschrift fur Metallkunde, Vol. 83, No. 12, pp. 887-892, 1992.

114. A. Alonso, C. Garcia-Cordovilla, E. Louis, J. Narciso and A. Pamies, *Evaluation of the Wettability of Al-Pb and Al-Sn Alloys with SiC and Al_2O_3 Particulates by Means of Pressure Infiltration*, Journal of Materials Science, Vol. 29, No. 18, pp. 4729-4735, 1994.

115. J. Narciso, A. Pamies, C. Garcia-Cordovilla, E. Louis and A. Alonso, *Factors Effecting Pressure Infiltration of Packed SiC Particulates by Liquid Aluminum*, Metallurgical and Materials Transactions A. Physical Metallurgy and Materials, Vol. 26A, No.4, pp. 983-990, 1995.

116. V. J. Michaud, L. M. Compton and A. Mortensen, *Capillarity in Isothermal Infiltration of Alumina Fiber Preforms With Aluminum*, Metallurgical Transactions A, Vol. 25, No. 10, pp. 2145-2152, 1994.

117. R. Asthana and P. K. Rohatgi, *A Study of Metal-Ceramic Wettability in SiC-Al Using Dynamic Melt Infiltration of SiC*, Key Engineering Materials, Vol. 79, No. 80, pp. 47-62, 1993.

118. E. Candan, H. V. Atkinson and H. Jones, *Role of Surface Tension in Relation to Contact Angle in Determining Threshold Pressure for Melt Infiltration of Ceramic Powder Compacts*, Scripta Materialia, Vol. 38, No. 6, pp. 999-1002, 1998.

119. H. Kaufmann and P. Schulz, *Filling of Continuous Fiber Preforms During Isothermal Gas Pressure Infiltration*, Aluminium, Vol. 76, No. 1-2, pp. 75-79, 2000.

120. Z. Xia, Y. Zhou, Z. Mao and B. Shang, *Fabrication of Fiber-Reinforced Metal-Matrix Composites By Variable Pressure Infiltration*, Metallurgical Transactions B, Vol. 23B, No. 3, pp. 295-302, 1992.

121. H. Muellejans, W. D. Kaplan and M. Ruehle, *Interfaces Between Al and α-Al_2O_3 in Melt-Infiltrated Alumina*, Materials Science Forum, Vol. 207-209, pp. 405-408, 1996.

122. P. K. Rohatgi, R. Q. Guo, H. Iksan, E. J. Borchelt and R. Asthana, *Pressure Infiltration Technique for Synthesis of Aluminum-Fly Ash Particulate Composite*, Materials Science and Engineering A, Vol. 244, No. 1, pp. 22-30, 1998.

123. J. Goicoechea, C. Garcia-Cordovilla, E. Louis and A. Pamies, *Wetting and Reactivity of SiC Particulates With Liquid Aluminium Alloys*, European Materials

Research Society Symposia Proceedings, ICAM 91, Strasbourg, France, 27-29 May 1991, pp. 221-226, 1991.

124. A. Alonso, A. Pamies, J. Narciso, C. Garcia-Cordovilla and E. Louis, *Evaluation of the Wettability of Aluminum Alloys with SiC and* Al_2O_3 *Particulates by Means of Pressure Infiltration,* Proceedings of the 9th International Conference on Composite Materials, Vol. 1, pp. 187-194, 1993.

125. P. R. Chidambaram and G. R. Edwards, *Novel Approach for Processing Liquid Metal-Ceramic Composites*, Processing and Fabrication of Advanced Materials IV, Cleveland. Ohio, USA, 29 Oct. 1996, pp. 471-478, 1996.

126. M. R. Hanabe and P. B. Aswath, Al_2O_3/Al *Particle-Reinforced Aluminum Matrix Composite by Displacement Reaction*, Journal of Materials Research, Vol. 11, No. 6, pp. 1562-1569, 1996.

127. G. Arslan, F. Kara and S. Turan, *Phase Studies of Reactive Infiltrated Boron Carbide-Aluminum Composites by Quantitative XRD*, Key Engineering Materials, Vol. 206-213, No. 1, pp. 759-762, 2001.

128. Y. Tsunekawa, H. Nakanishi, M. Okumiya and N. Mohri, *Application of Ultrasonic Vibration to Molten Aluminum Infiltration*, Key Engineering Materials, Vol. 104-107, No. 1, pp. 215-223, 1995.

129. H. Nakanishi, Y. Tsunekawa, M. Okumiya and N. Mohri, *Ultrasound-Assisted Pressureless Infiltration of Molten Aluminum Into Alumina Capillaries*, Journal of Materials Science Letters, Vol. 12, No. 16, pp. 1313-1315, 1993.

130. E. W. Washburn, Physical Review, Vol. 17, pp. 374-382, 1921.

131. K. T. Hodgson and J. C. Berg, Journal of Colloid and Interface Science, Vol. 121, No. 1, pp. 22-31, 1988.

132. G. R. Edwards, D. L. Olson, G. P. Martins, B. R. Lanning and P. B. Maxwell, *Modeling of Infiltration Kinetics and Interfacial Bond Strength in Aluminum Matrix-Silicon Carbide Composites*, Annual Report, Center for Welding Research, Colorado School of Mines, Golden, Colorado, 80401, 1986.

133. D. Muscat, R. L. Harris, R. A. L. Drew, *The Effect of Pore Size on the Infiltration Kinetics of Aluminum in Titanium Carbide Preforms*, Acta Metallurgica et Materialia, Vol. 42, No. 12, pp. 4155-4163, 1994.

134. A. E. Scheidegger, Physics of Flow Through Porous Media, Univ. Toronto Press, 1960.

135. D. Kocaefe, G. Ergin, Y. Kocaefe, V. Villeneuve and D. Audet, "Investigation of Wetting Using Image Analysis", in preparation.

136. N. E. Dorsey, Journal of the Washington Academy of Sciences, Vol. 18, pp. 505, 1928.

137. N. Nagayama, *Metal-Filter Media Interface Conditions, Metallographic Results of ABF Core Samples with Alloy AA5182*, Alcan Inc, Arvida Research and Development Centre, APR-98/5.43.21,Progress Report No.6, 1998.

138. B. Hallstedt, in Thermodynamics and Reactions in Al-Ca-Mg-Si Alloy-Oxide Composites, pp.10, Royal Institute of Technology, Division of Physical Metallurgy, Stockholm, 1992.

139. Sai Wai Ip Technical Report on the Wettability of Different Solids by Aluminum, University of Toronto, Department of Metallurgy and Materials Science, 1997.

140. A.M. Korol'kov, Otdelenie Teknicheskik Nauk, Vol. 2, pp. 35-42, 1956.

141. G. Lang, "Gießeigenschaften und Oberflächenspannung von Aluminium und binären Aluminiumlegierungen", Aluminum-Verlag, Vol. 49, pp. 231-238, 1973.

142. M. Robbins, Fluorescence, Gems and Minerals Under Ultraviolet Light, Geoscience Press Inc., Phoenix, Arizona, 1994.

143. O. Kubaschewski and C. B. Alcock, Metallurgical Thermo-Chemistry, Revised and Enlarged 5th Edition, Editor: G. V. Raynor, International Series on Materials Science and Technology, Vol. 24, Pergamon Press, 1979.

APPENDICES

APPENDIX A

Example Images Obtained from Image Analysis Software of Profilometer

In this section, typical images that are obtained after a surface scan by the profilometer are given for Alcoa, Aluchem, Alufin and Naigai alumina particles.

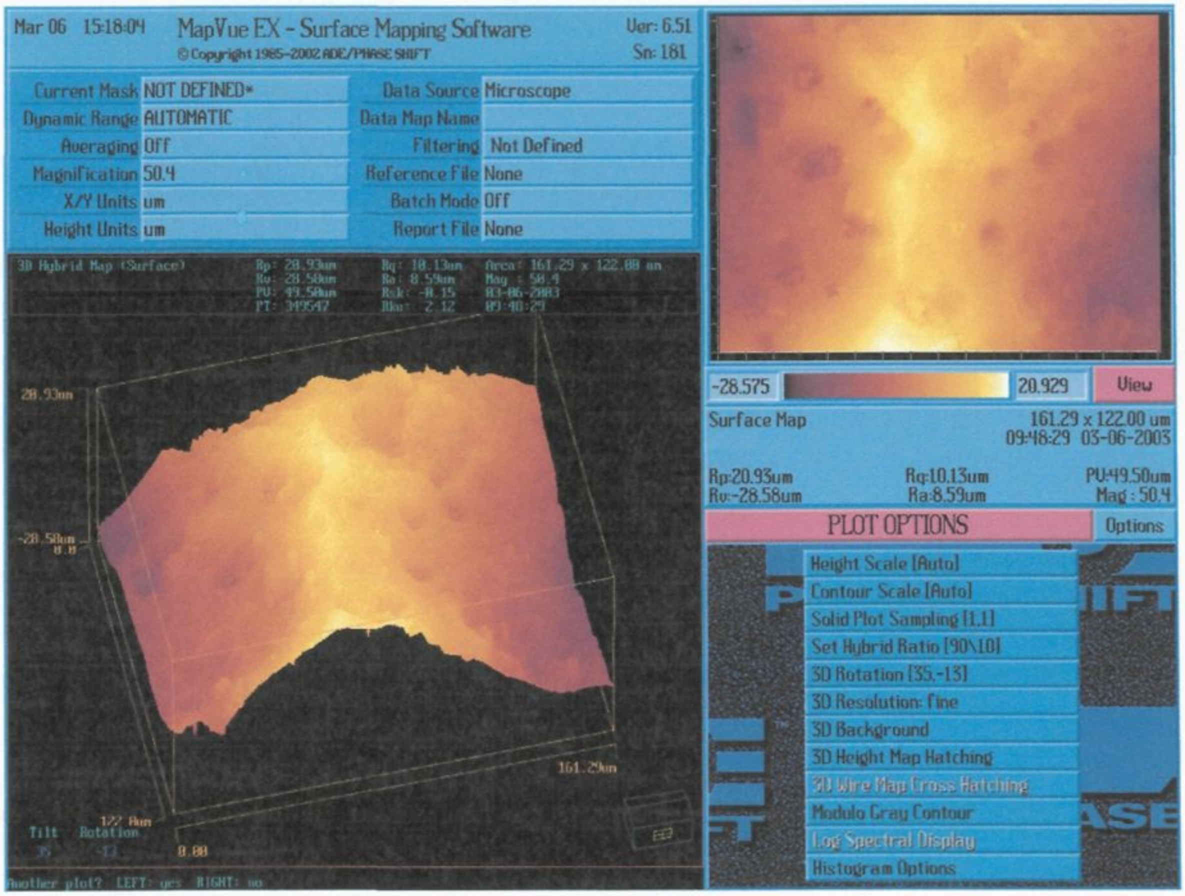

Mar 06 15:18:04 MapVue EX - Surface Mapping Software Ver: 6.51

© Copyright 1985-2002 ADE/PHASE SHIFT Sn: 181

Current Mask NOT DEFINED*
Dynamic Range AUTOMATIC
Averaging Off
Magnification 50.4
X/Y Units um
Height Units um
Data Source Microscope
Data Map Name
Filtering Not Defined
Reference File None
Batch Mode Off
Report File None

3D Hybrid Map (Surface)
Rp: 20.93um Rv: 28.58um PV: 49.50um PT: 349547
Rq: 10.13um Ra: 8.59um Rsk: -0.15 Rku: 2.12
Area: 161.29 x 122.00 um Mag : 50.4 03-06-2003 09:48:29

Another plot? LEFT: yes RIGHT: no

-28.575 20.929

Surface Map 161.29 x 122.00 um 09:48:29 03-06-2003

Rp:20.93um Rv:-28.58um Rq:10.13um Ra:8.59um PV:49.50um Mag : 50.4

Figure A.1 Three Dimensional Picture of an Alcoa Alumina Particle After the Analysis of its Surface by the Software

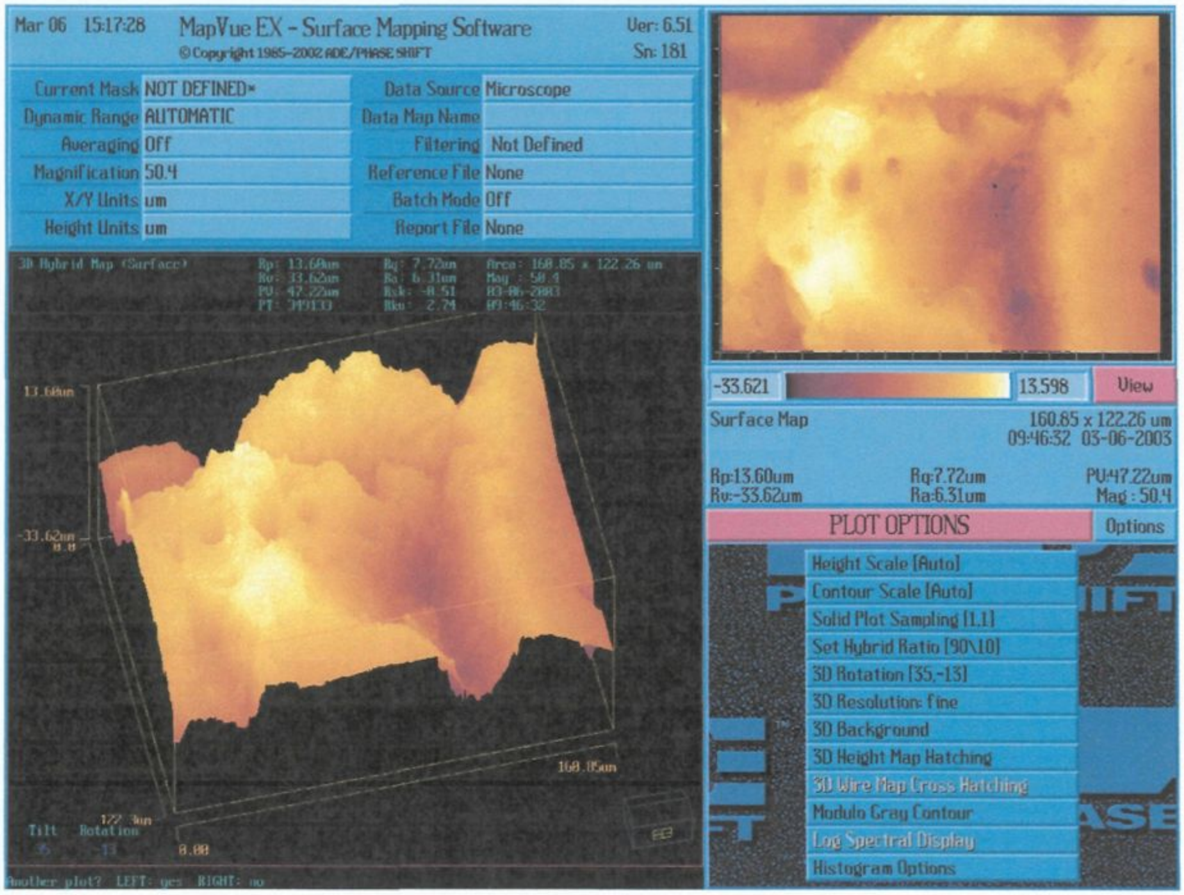
Mar 06 15:17:28 MapVue EX - Surface Mapping Software Ver: 6.51

© Copyright 1985-2002 ADE/PHASE SHIFT Sn: 181

Current Mask NOT DEFINED*
Dynamic Range AUTOMATIC
Averaging Off
Magnification 50.4
X/Y Units um
Height Units um
Data Source Microscope
Data Map Name
Filtering Not Defined
Reference File None
Batch Mode Off
Report File None

3D Hybrid Map (Surface)
Rp: 13.60um
Rv: 33.62um
PV: 47.22um
PT: 349133
Rq: 7.72um
Ra: 6.31um
Rsk: -0.51
Rku: 2.74
Area: 160.85 x 122.26 um
Mag : 50.4
03-06-2003
09:46:32

Surface Map
160.85 x 122.26 um
09:46:32 03-06-2003
Rp:13.60um
Rv:-33.62um
Rq:7.72um
Ra:6.31um
PV:47.22um
Mag : 50.4

Another plot? LEFT: yes RIGHT: no

Figure A.2 Three Dimensional Picture of an Aluchem Alumina Particle After the Analysis of its Surface by the Software

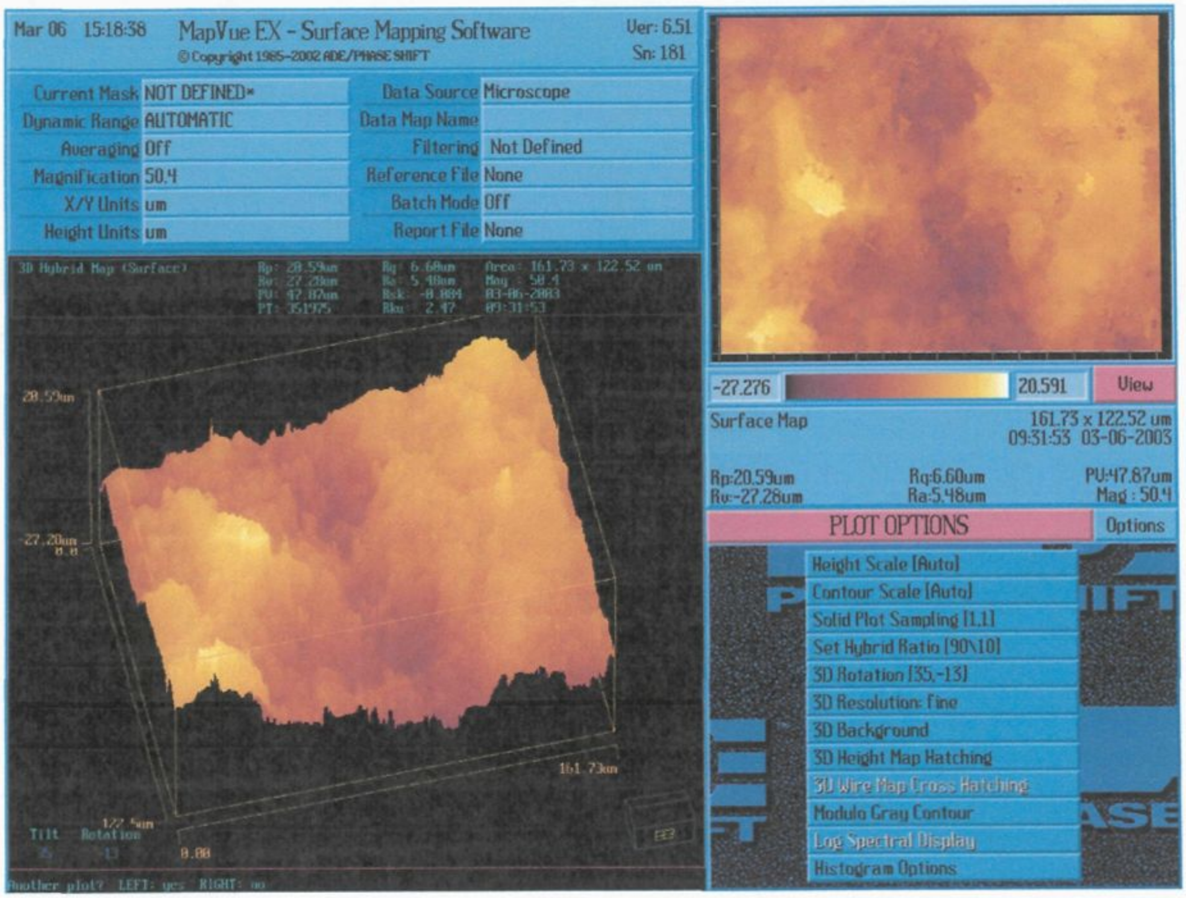

Mar 06 15:18:38 MapVue EX - Surface Mapping Software Ver: 6.51
© Copyright 1985-2002 ADE/PHASE SHIFT Sn: 181

Current Mask NOT DEFINED*
Dynamic Range AUTOMATIC
Averaging Off
Magnification 50.4
X/Y Units um
Height Units um
Data Source Microscope
Data Map Name
Filtering Not Defined
Reference File None
Batch Mode Off
Report File None

3D Hybrid Map (Surface)
Rp: 20.59um Rq: 6.60um Area: 161.73 x 122.52 um
Rv: 27.28um Ra: 5.48um Mag : 50.4
PV: 47.87um Rsk: -0.004 03-06-2003
PT: 351975 Rku: 2.47 09:31:53

Surface Map 161.73 x 122.52 um
09:31:53 03-06-2003
Rp:20.59um Rq:6.60um PV:47.87um
Rv:-27.28um Ra:5.48um Mag : 50.4

Another plot? LEFT: yes RIGHT: no

Figure A.3 Three Dimensional Picture of an Alufin Alumina Particle After the Analysis of its Surface by the Software

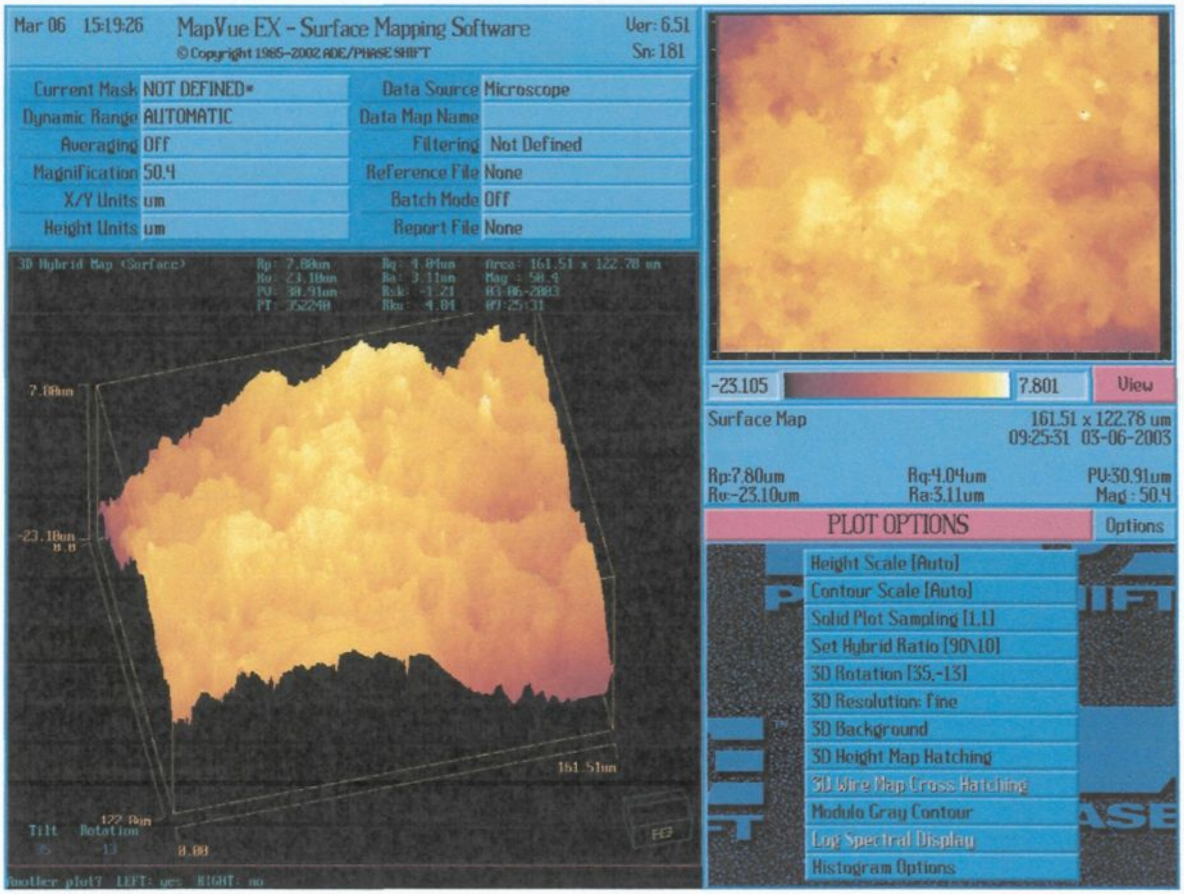

Mar 06 15:19:26 MapVue EX - Surface Mapping Software Ver: 6.51
© Copyright 1985-2002 ADE/PHASE SHIFT Sn: 181

Current Mask NOT DEFINED*
Dynamic Range AUTOMATIC
Averaging Off
Magnification 50.4
X/Y Units um
Height Units um
Data Source Microscope
Data Map Name
Filtering Not Defined
Reference File None
Batch Mode Off
Report File None

3D Hybrid Map (Surface)
Rp: 7.80um
Rv: 23.10um
PV: 30.91um
PT: 352240
Rq: 4.04um
Ra: 3.11um
Rsk: -1.21
Rku: 4.04
Area: 161.51 x 122.78 um
Mag : 50.4
03-06-2003
09:25:31

Tilt 35 Rotation -13

Another plot? LEFT: yes RIGHT: no

-23.105 7.801

Surface Map
161.51 x 122.78 um
09:25:31 03-06-2003
Rp:7.80um
Rv:-23.10um
Rq:4.04um
Ra:3.11um
PV:30.91um
Mag : 50.4

Figure A.4 Three Dimensional Picture of a Naigai Alumina Particle After the Analysis of its Surface by the Software

APPENDIX B

Program to Measure the Surface Characteristics of Alumina Using Profilometer and Image Analysis

```
RECIPE: C:\MapvueAE\Recipe\guvenc.rcp
  Recipe Status: MODIFIED
  Calibration Status: SAVED
  Processing Mode: EX

Sequence Options...
  » Sequence Mode: OFF

Units Settings...
  » Height Units: microns
  » Spatial Units: microns
  » Stage Units: microns

Ex Mode Options...
  » Scan Height: 150 µm
  » Scan Position: Center
  » Scan Mode: Normal

Acquire Options...
  » Noise Threshold: 0.10
  » Auto Coarse Focus, Range: 50.00 µm
  » Regular Average, Num: 3, "C:\...\guvenc\alcoa\alcoa18"
```

Post Processing Options...

» Tilt Removal

» Fill Bad Data

» Median Filter, Length X: 5, Length Y: 5

Application Options...

» Advanced Profile Analysis

» C1 Threshold: 0.1000 µm

» C2 Threshold: 0.0 µm

» Ctp Threshold: 0.0 µm

» High Pass Filter: Off

» Filter Cutoff: 0.0 cycles/µm

Analysis Options...

» Auto Save Statistics, "C:\...\guvenc\alcoa\alcoa18"

» Auto Save Map, "C:\...\guvenc\alcoa\alcoa18"

» Save Processed Map

» Save Raw Map

Labeling Options...

Video Gain/Offset Settings...

» Video Gain Level: -129

» Video Offset Level: -1

Data Area Specification...

» Horz offset: 1758 µm

» Vert offset: 1068 µm

» Horz Width: 3688 µm

» Vert Height: 2344 µm

Focus Area Specification...

» Using Data Area

Video Mask...

» Percent masked: 0.00

Remote Trigger Mode...

» COM Port: 1

» Baud Rate: 9600

» Byte Size: 8

» Parity: No parity

» Stop Bits: 1

» Flow Control: RTS/CTS Hardware

Calibration Settings...

» Height Correct Factor: 1.0000

» EX Calibration Slope - Pzt: 50.91

» EX Calibration Slope - Stage: 5000

Objective Settings...

» Combined Mag: 1.56

» Wheel Mag: 0.63

» Objective Mag: 2.50

» Objective Correction: 1.0000

» Objective Type: Interference

» Objective Ref Exists: No

APPENDIX C

Program for Image Analysis Software of Optical Microscope

```
End of Prolog
******
001 Set Process Frame to 148,69 484x454
002 Set Guard Frame to 168,96 496x389
003 Color Threshold -> BPL1
   Hue: start = 241°, delta = 0°
   Saturation: 99%..99%
   Intensity: 84..84
004 Color Threshold -> BPL2
   Hue: start = 0°, delta = 328°
   Saturation: 0%..44%
   Intensity: 51..254
006 Pruning HEX BPL1 x2
007 Chord Size BPL1 -> None 5x5
008 Fill BPL2
```

009 Object Measures (BPL1) -> OBJM2

Area

Perimeter

Sphericity

Aspect Ratio

010 Field Measures (BPL1) -> FLDM7

Count

******

001 Export Data FLDM7 OBJM2

File: exp57.xls

Path: F:\USERS\guvenc\bed porosity measurement

Info Header: Yes

End of Epilog

APPENDIX D

Configuration of the Drop Shape Analysis Software

In this section, the interface of the drop shape analysis software is described and the features of this interface are illustrated.

Principal Interface

Principal interface is divided into three sub-sections: Menu-bar, display zone and task bar (Figure D.1). Menu-bar is found at the top and the task-bar is placed at the bottom of the application window. The region application window, which stays in between menu-bar and task-bar, is called display zone. The image from an experiment can be seen in display zone. Menu-bar and task-bar are also identified. Sessile-drop and graphite sample crucible can also be identified from the image in the display zone.

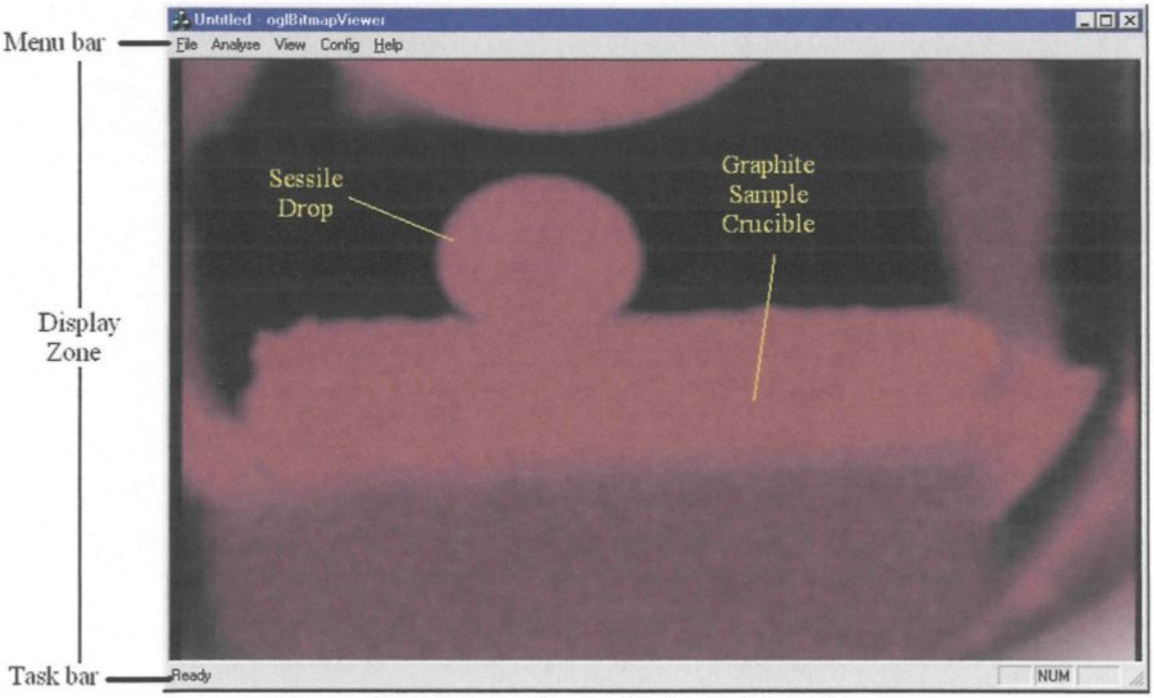

Figure D.1 Sub-sections of Principal Interface

The menu-bar allows the user to control various features of the application. The accessibility to these features is simplified by five drop down menus added to the menu-bar. *File* drop down menu allows the user to load and save the configurations. *Analyse* drop down menu permits the user to have a preview of an example analysis before the analysis or to launch the analysis of a series of images. *View* drop down menu gives access to options on the display of the image and *Config* drop down menu allows the user to open the windows of configuration by which the necessary adjustments for the analysis are carried out. *Help* drop down menu provides the user any help if needed.

The display zone allows the user to visualize the original and analyzed images. Using the display options, it is possible to determine which part(s) of the analyzed image will be visualized.

During the analyses, any particular information is not displayed on the task-bar for the version used. It is intended to display the name of the file that is being processed and the progress of the work for the updated versions.

Features of the Principal Interface

In this section, the features of the principal interface are illustrated with examples. Necessary explanations are given for operation of this interface as well.

Loading and Saving a Configuration

Although the original images are captured under almost the same conditions, the slight changes in some parameters like light contrast and sharpness make each image unique.

Therefore, the configuration of the software should be adjusted before the analysis to obtain the best results. If many images needed to be analyzed, this adjustment procedure can become time consuming. For this reason, the drop shape analyzing software is designed to minimize these efforts and facilitate the task of the user.

For loading a configuration, choose *Load Config* option from the *File* drop down menu as shown on Figure D.2. Then, the window shown on Figure D.3 will appear. Choose the desired configuration file. Double click or press on the OPEN button.

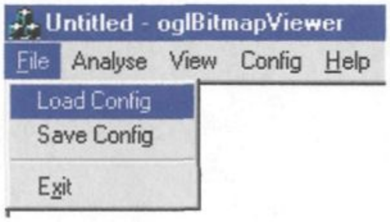

Figure D.2 The Placement of *Load Config* Option in the *File* Drop down Menu

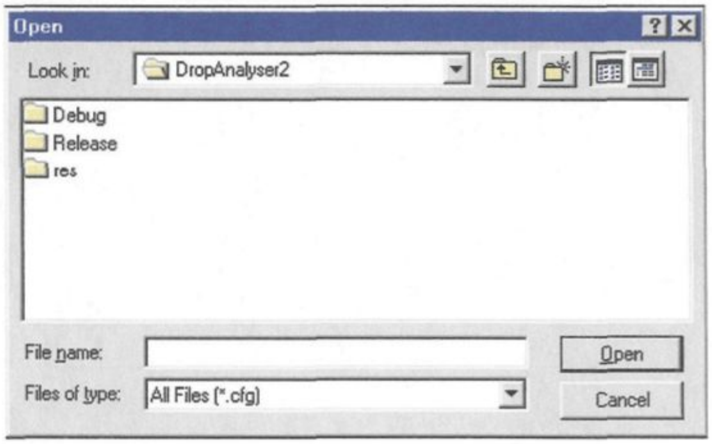

Look in: DropAnalyser2

File name:

Files of type: All Files (*.cfg)

Figure D.3 Opening a Desired Configuration File

To save a configuration, it is enough to go to the *File* menu and choose *Save Config* option as shown on Figure D.4. The window shown on Figure D.5 will appear. Enter the name of the configuration file and press on the SAVE button.

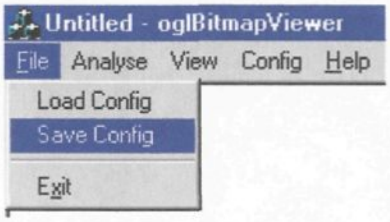

Figure D.4 The Placement of *Save Config* Option in the *File* Drop down Menu

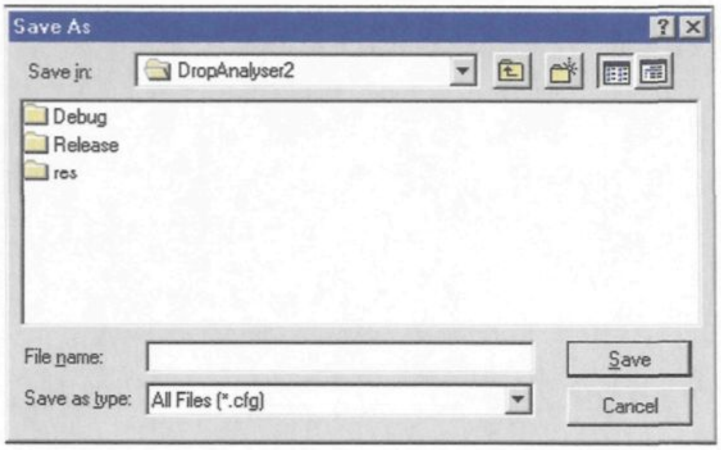

Save in: DropAnalyser2

File name:

Save as type: All Files (*.cfg)

Figure D.5 Saving a Configuration File

Analysis of a Series of Images

Analyse drop down menu serves to choose the images to be analyzed. There are two options in this menu: *Preview* and *Start* (see Figure D.6). *Preview* allows the user to pick up a typical image from a series of images and to display it on the display zone of the principal interface. This feature not only allows the user to see the image without going through all of the mechanisms of analysis; but also permits to carry out the necessary adjustments in the configuration files. *Start* option is utilized to choose a series of images and to conduct their analysis.

To preview the images before the analysis, first choose *Preview* option from *Analyse* drop down menu as shown on Figure D.6. Then, a window will appear (see Figure D.7). After choosing the desired image, press on OPEN button to have the preview of the desired image on the display zone.

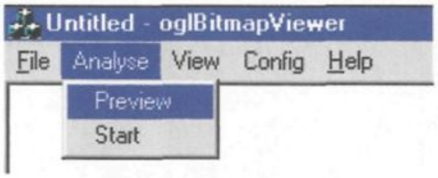

Figure D.6 The *Analyse* Drop down Menu (*Preview* Option)

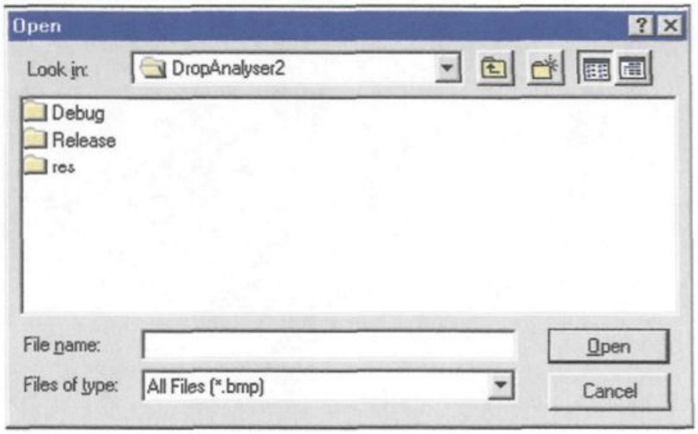

Figure D.7 Choosing an Image to Preview

To carry out the analysis of a series of images, choose *Start* option from *Analyse* drop down menu as shown on Figure D.8. Then, from the window appearing on the screen, choose a series of images (Figure D.9) and press on OPEN button.

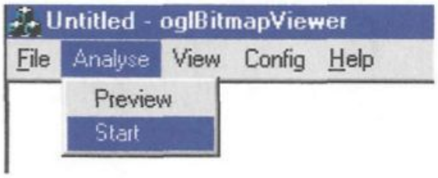

Figure D.8 The *Analyse* Drop down Menu (*Start* Option)

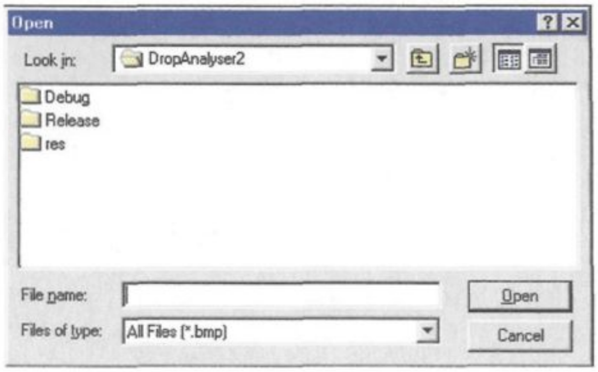

Figure D.9 Choosing a Series of Images to Analyze

Display of Images

The display tool is designed to increase the flexibility of the interface. The elements to display during the analysis can be preselected. To use this feature, click on the *View* drop down menu and choose *Elements* option as shown on Figure D.10. On the on coming window tick the boxes on the right hand side of the elements that are desired to be displayed (Figure D.11).

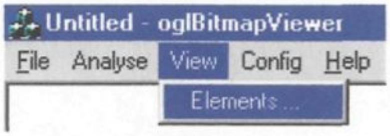

Figure D.10 *View* Drop down Menu

B&W Original picture ☑
Analysis Window ☑
Side detection ☑
Angles ☑
Crucible ☑
Drop ☑

Figure D.11 Options of *View* Drop down Menu

B&W Original Picture option allows visualizing the analyzed image on the display zone. If *Analysis Window* option is marked, a blue rectangle is superposed on the original image as well as the reference line (red). The blue rectangle specifies the analysis zone. The reference line is used for the conversion of pixels to SI units. If the box on the right hand side of *Side Detection* is ticked, green points will be plotted on the original image. These points show the outline detected on the whole image (injection chamber, support, sample crucible, and sessile drop). If *Angles* option is checked out, the angle calculated between the surface of the substrate and sessile drop will be drawn at left and right hand sides of the drop. If the boxes that are placed on the right of the options *Crucible* and *Drop* are ticked, the points forming the sample crucible and sessile-drop will be plotted in yellow, respectively.

Configuration

The optimum configuration to analyze the images is adjusted by using the *Config* drop down menu. The first element to adjust is the level of contrast. When the detection of outline is not precise enough, this option helps to enhance the analysis. To adjust the level of contrast, click on *Config* drop down menu and choose *Contrast Level* option as shown on Figure D.12. A box called "Config Contrast Level" will appear in another window (Figure D.13). Slide the button to change contrast as desired and press on the OK button to apply change or CANCEL to return to the menu without modification.

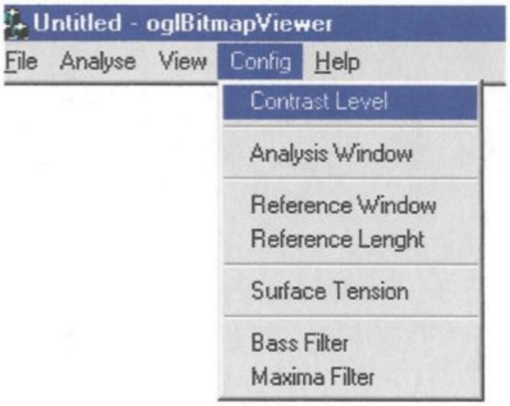

Figure D.12 *Config* Drop Down Menu Indicating *Contrast Level* Option

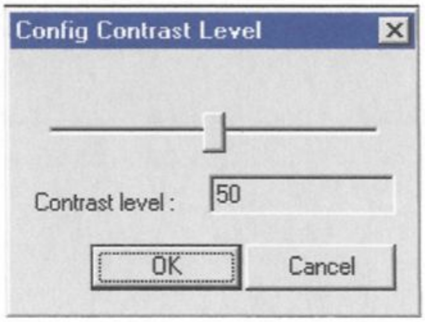

Contrast level : 50

Figure D.13 Contrast Level Adjustment Window

The image analysis is carried out inside a rectangular region predetermined by the user. To identify the exact location of this region *Analysis Window* option is chosen from the *Config* drop down menu (Figure D.14). Then, another window called "Config Analysis

Window" appears (Figure D.15). The position of the analysis window is determined by entering the coordinates of two corner points of this rectangular region to the software; for example, upper left and lower right corner points or upper left and lower right points of the rectangle. There two ways to assign these points. First, the coordinates of these points can be inserted into the appropriate boxes on the window named "Config Analysis Window", directly. Second, the mouse can be utilized. In this case, press SELECT button and click on two points on the display zone as mentioned above. Then, the software reads the ordinates and abscissas of these two points and draws a rectangle passing through them on the display zone. If the analysis window seems correct, press OK button to continue or press on SELECT button and repeat the procedure described above to select the two points identifying the location of analysis window.

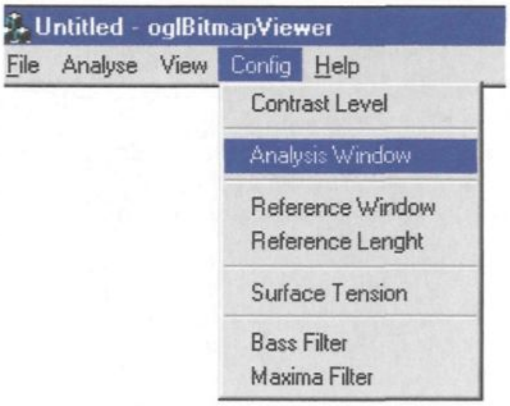

Figure D.14 *Config* Drop Down Menu Indicating *Analysis Window* Option

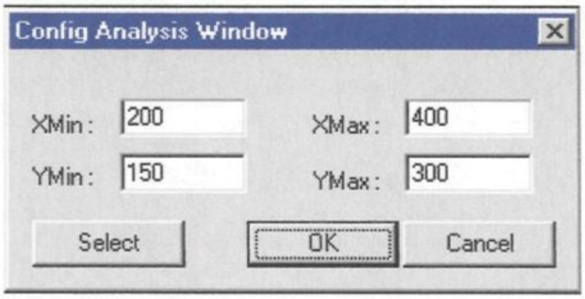

XMin: 200
XMax: 400
YMin: 150
YMax: 300

Figure D.15 Window of Config Analysis Window

The software determines the results of calculations in pixels. Therefore a conversion from pixels to SI units is required. For that purpose, the front view of the sample crucible is used. First, the length of this section (the width of the sample crucible) is defined on the display zone by means of a reference line. Second, the length of the reference line is assigned.

To define the reference line *Reference Window* option from *Config* drop down menu is chosen (Figure D.16). Then, "Config Crucible Width" window appears (see Figure D.17). The width of the sample crucible is determined by two points that are marked by the user. There two ways to assign these points. The first way is to insert the coordinates of these points into the appropriate boxes on the "Config Crucible Width" window, directly. The second way is to use the mouse. In this case, press SELECT button and click the appropriate locations on the display zone as described above. The ordinate of the first point clicked will be taken as the ordinate of the second one automatically. This helps to determine the reference line parallel to horizontal and eliminates a possible error source. Then, the software reads the ordinates and abscissas of these two points and draws a reference line passing through them on the display zone. If this reference line seems correct, press OK button to continue or press on SELECT button and repeat the procedure described above to select two points identifying the location of reference line.

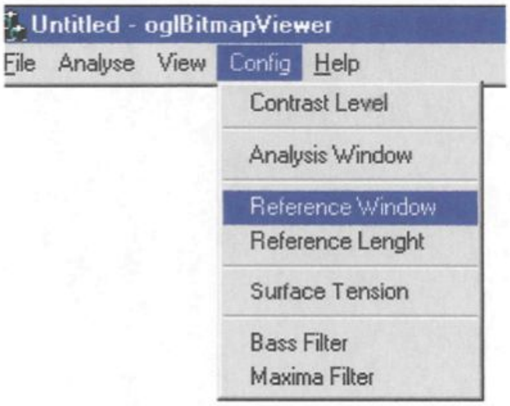

Figure D.16 *Config* Drop Down Menu Indicating *Reference Window* Option

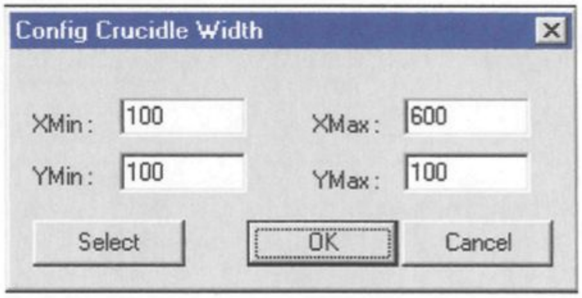

XMin : 100
XMax : 600
YMin : 100
YMax : 100

Figure D.17 Config Crucible Width Window

As mentioned above, the width of the sample crucible, which is measured by drawing a reference line superposed on the front view of the sample crucible, should be calibrated for unit conversion purposes. To calibrate the length of this reference line, choose *Reference Length* option from the *Config* drop down menu (Figure D.18). This will activate "Reference Length" window (Figure D.19). Insert the real length for the reference line in meters in the box and press OK button to save this information and continue.

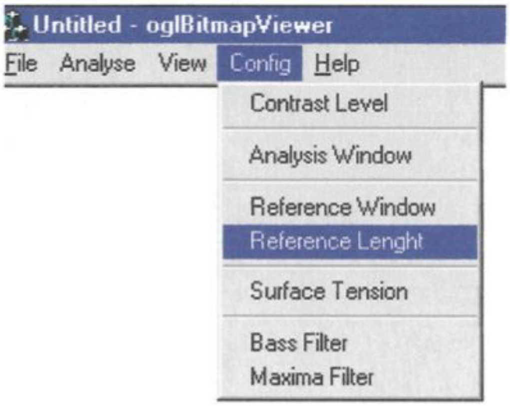

Figure D.18 *Config* Drop Down Menu Indicating *Reference Length* Option

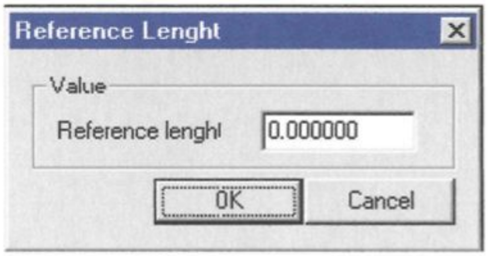

Reference lenght 0.000000

Figure D.19 Reference Legth Window

The software calculates also the surface tension of the molten metal from a couple of semi-empirical equations. The software is designed to allow the user to change the constants in these equations. If a change is desired, it can be carried out on the "Config Surface Tension" window (Figure D.21), which appears when *Surface Tension* option is chosen from the *Config* drop down menu (see Figure D.20). To accept the changes and continue, press on OK button.

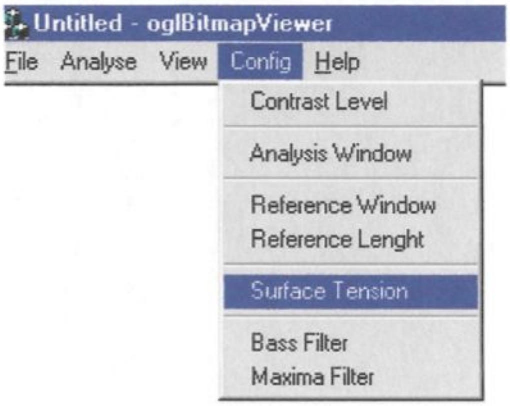

Figure D.20 *Config* Drop Down Menu Indicating *Surface Tension* Option

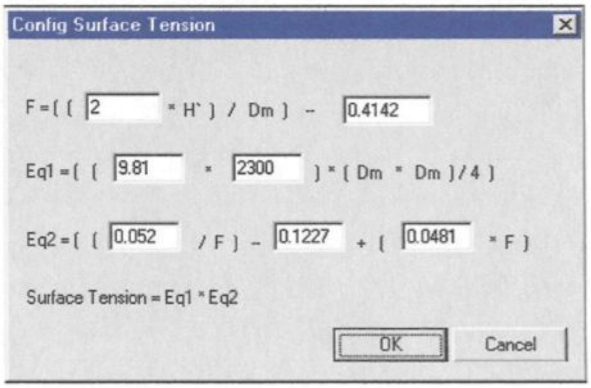

F = ((2 * H`) / Dm) – 0.4142

Eq1 = ((9.81 * 2300) * (Dm * Dm) / 4)

Eq2 = ((0.052 / F) – 0.1227 + (0.0481 * F)

Surface Tension = Eq1 * Eq2

Figure D.21 Config Surface Tension Window

If image is not clear enough, it is possible to decrease the noise, which can disturb the result of the analysis, by using the low and maximum filters. The effect of these filters on the image is measured by means of numbers changing between 1 and 20. Their effect increases from 1 to 20. If the values of these filters are equal to 1, it means that they are not active. To apply low filter to the image, choose *Bass Filter* option from *Config* drop down menu (Figure D.22). Then, "Config Bass Filter" window appears (Figure D.23). To change the value of the filter, slide the button as desired. To accept the value adjusted, press on OK button.

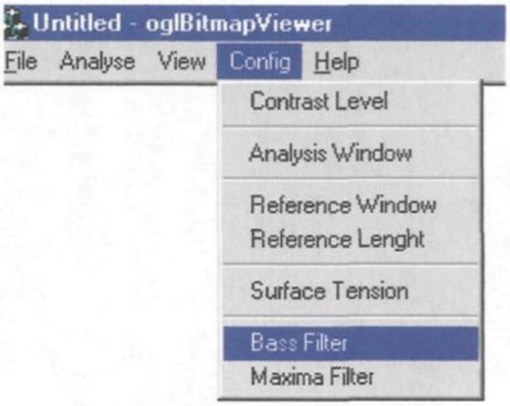

Figure D.22 *Config* Drop Down Menu Indicating *Bass Filter* Option

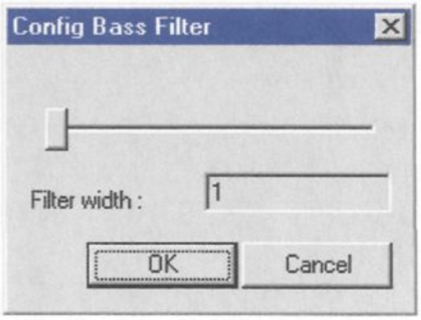

Filter width : 1

Figure D.23 Config Bass Filter Window

To change the value of the maximum filter, choose *Maxima Filter* option under the *Config* drop down menu (Figure D.24). Then, "Config Maxima Filter" window will appear (Figure D.25). To change the value of the filter, slide the button as desired. To accept the value adjusted, press on OK button.

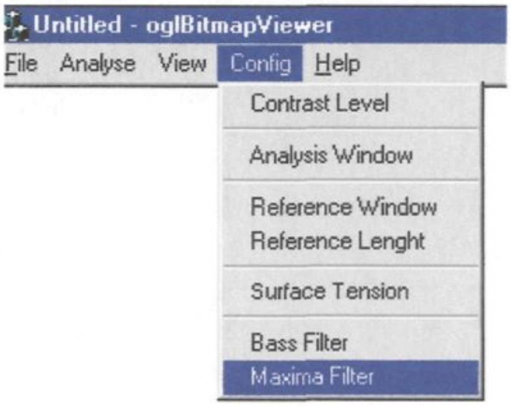

Figure D.24 *Config* Drop Down Menu Indicating *Maxima Filter* Option

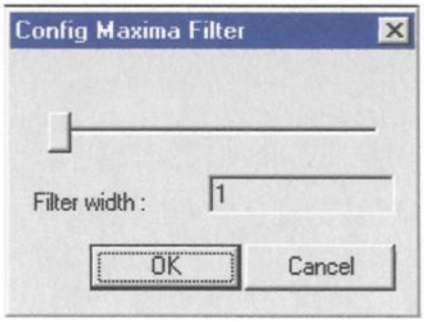

Filter width : 1

Figure D.25 Config Maxima Filter Window

APPENDIX E

Results of SEM and TEM Analyses of Infiltration Experiments

Appendix E summarizes the TEM results for samples numbered 14, 15, 16, and 17 in Table 5.4 in Section 5.3. The experimental conditions for these experiments are given in Table E.1 below:

Table E.1 Tabulation of Experimental Conditions for the Samples Investigated in TEM

Exp. No.	**Type of Alumina Particles**	**Particle Size Range [mm]**	**Alloy**	**Duration [min.]**
14	Alcoa	1.19-1.41	Al-6.9 wt %Mg	3
15	Russian	1.19-1.41	Al-6.9 wt %Mg	3
16	Naigai	1.19-1.41	Al-6.9 wt %Mg	3
17	Aluchem	1.19-1.41	Al-6.9 wt %Mg	3

Two techniques were used to prepare TEM samples (a) Focused Ion Beam (FIB), and (b) Ar Ion Milling process. A Micrion-2500 FIB system was used to prepare the TEM specimens. Standard FIB "H-bar lift-out" procedure using a biological micromanipulator tool was employed in order to minimize potential mechanical damage during sample preparation. The preparation technique used for each sample is given in Table E.2.

Table E.2 Summary of TEM Sample Preparation Technique for Each Sample

Preparation Technique	**EXP 14**		**EXP 15**	**EXP 16**	**EXP 17**
	Un-mounted	**Mounted**			
Focused Ion Beam	X	X	X		
Ar Ion Milling		X		X	X

The summary of the TEM results for EXP14-17 are given below.

UNMOUNTED SAMPLE OF EXP 14

1) Al alloy, 2) Al_2O_3 crystals, 3) fine-grained binder (Mg+O+P+Al+Si+…)

4) ultrafine-grained MgO + (amorphous) C + P +

5) amorphous Al-Mg-O, 6) Al_3Fe, 7) Al_2MgO_4

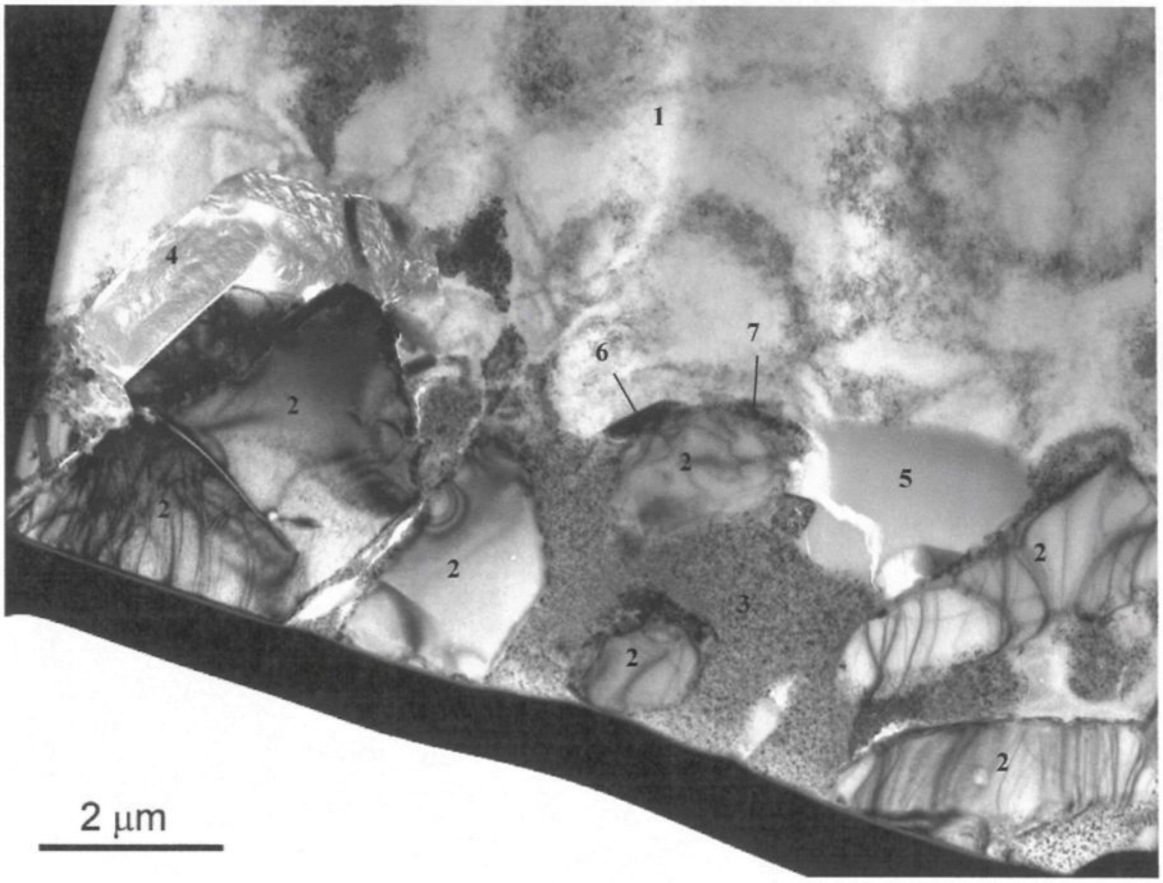

Figure E.1 General View of the Area Examined by TEM in the Unmounted EXP 14 Sample. Numbers Indicate Phases Revealed in the Sample.

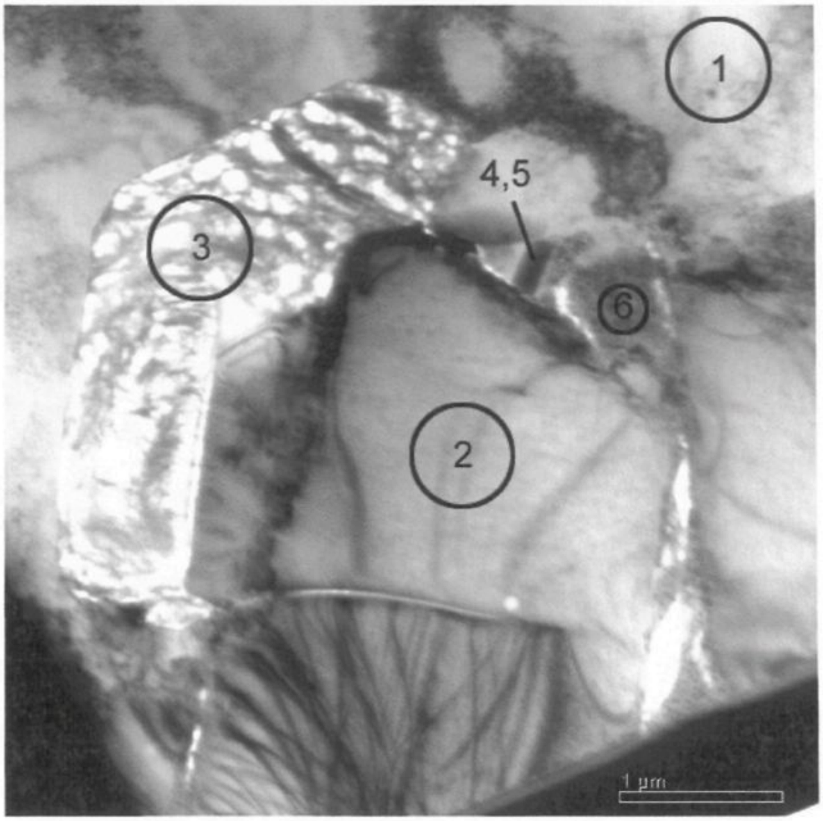

Figure E.2 Higher Magnification View #1 Indicating Locations of EDS Analyses

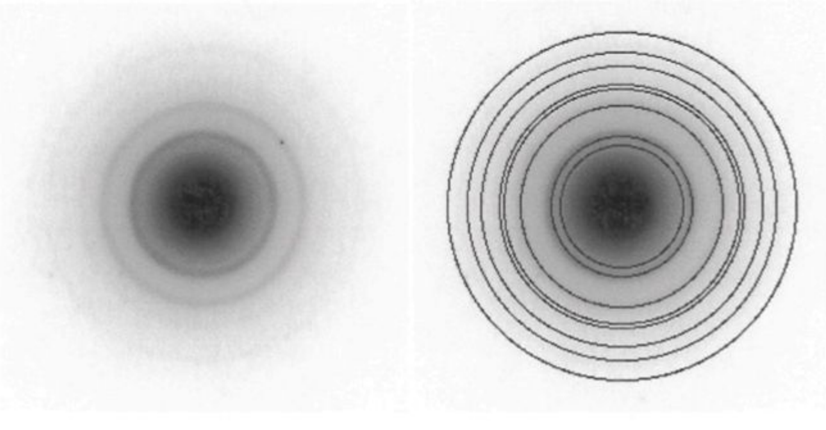

Figure E.3 Selected Area Electron Diffraction Pattern (SAEDP) Corresponding to Region 3 – Match MgO

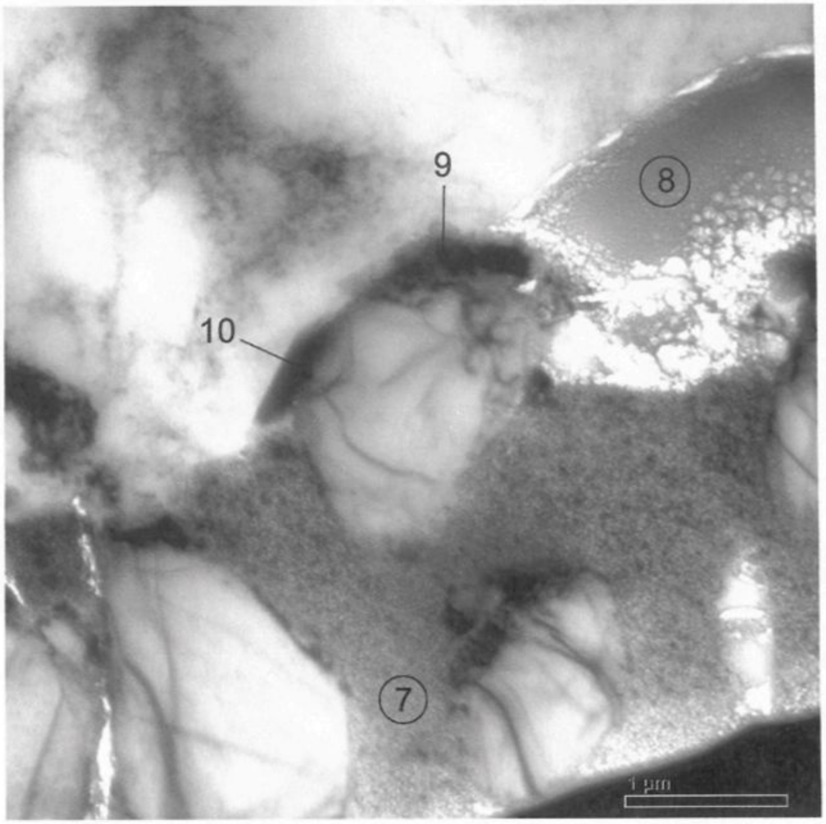

Figure E.4 Higher Magnification View #2 with Locations of EDS Analyses

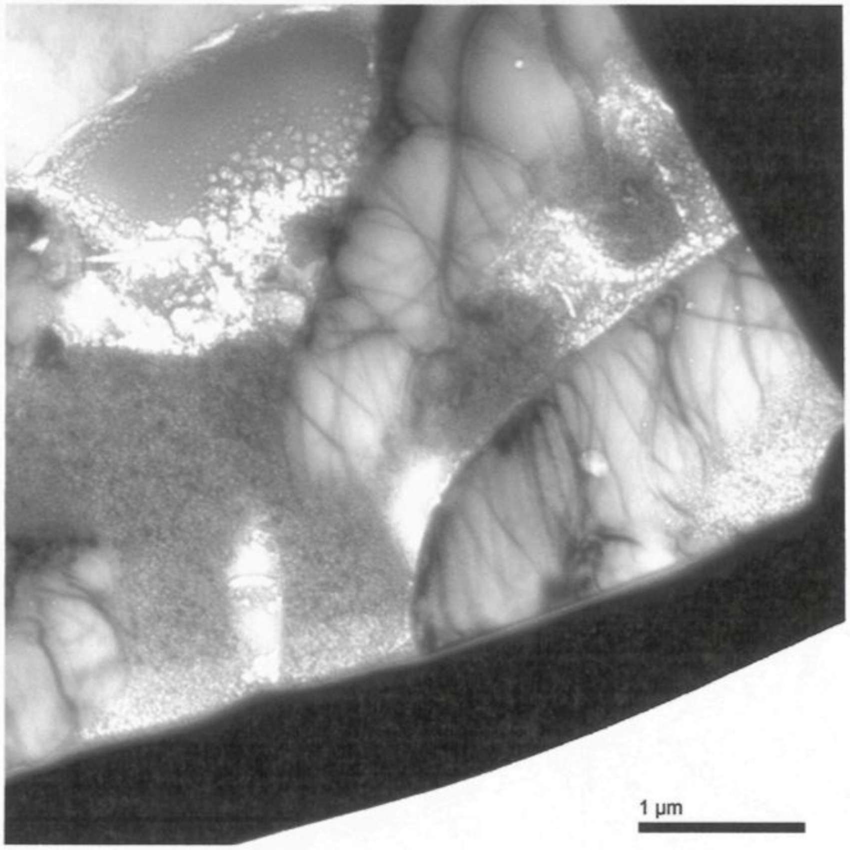

Figure E.5 Higher Magnification View #3

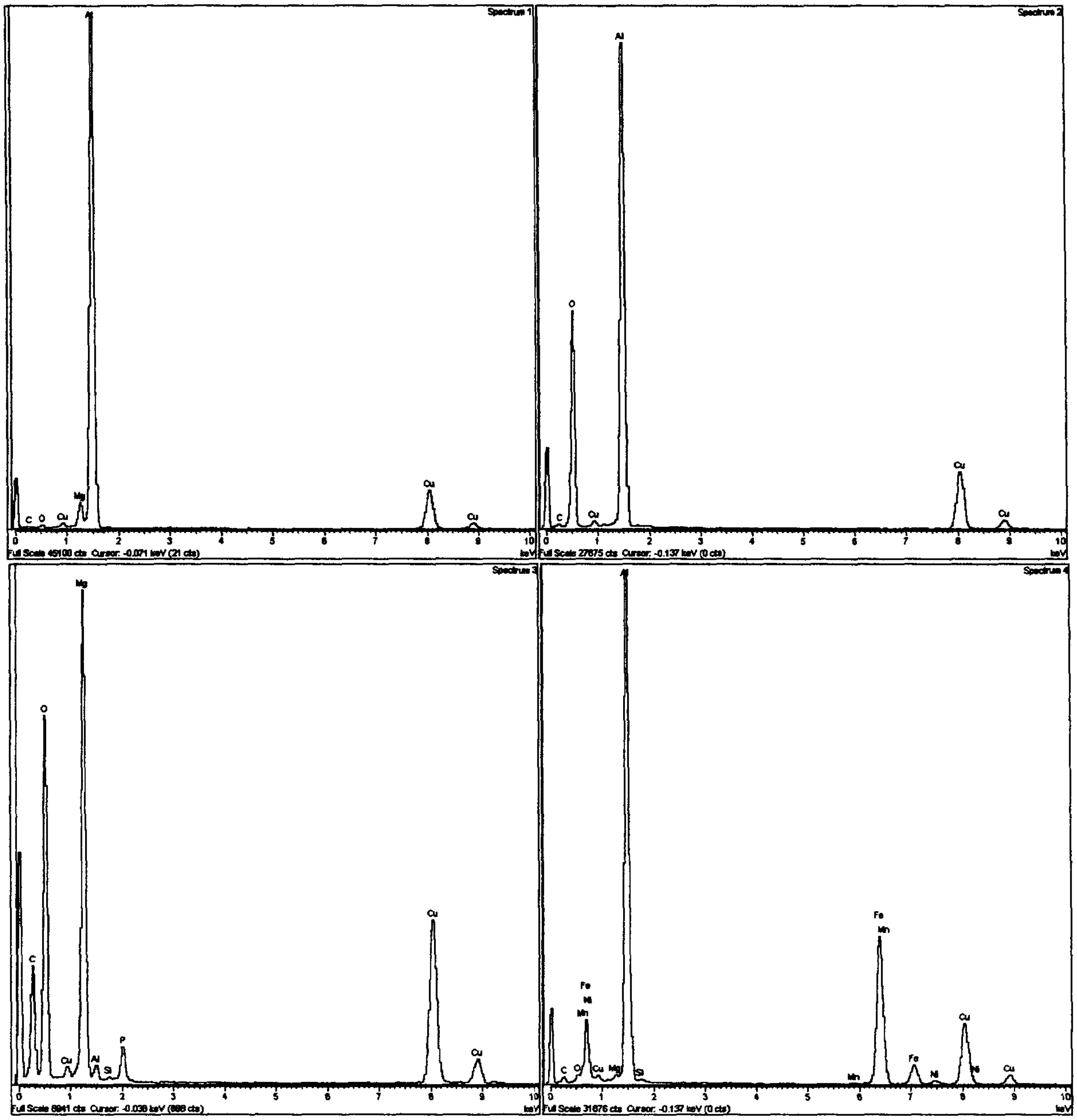

Figure E.6 EDS Spectra from Locations Indicated above in Figures 2 to 5 (Cu Signal on All Spectra Coming from the Sample Support Grid)

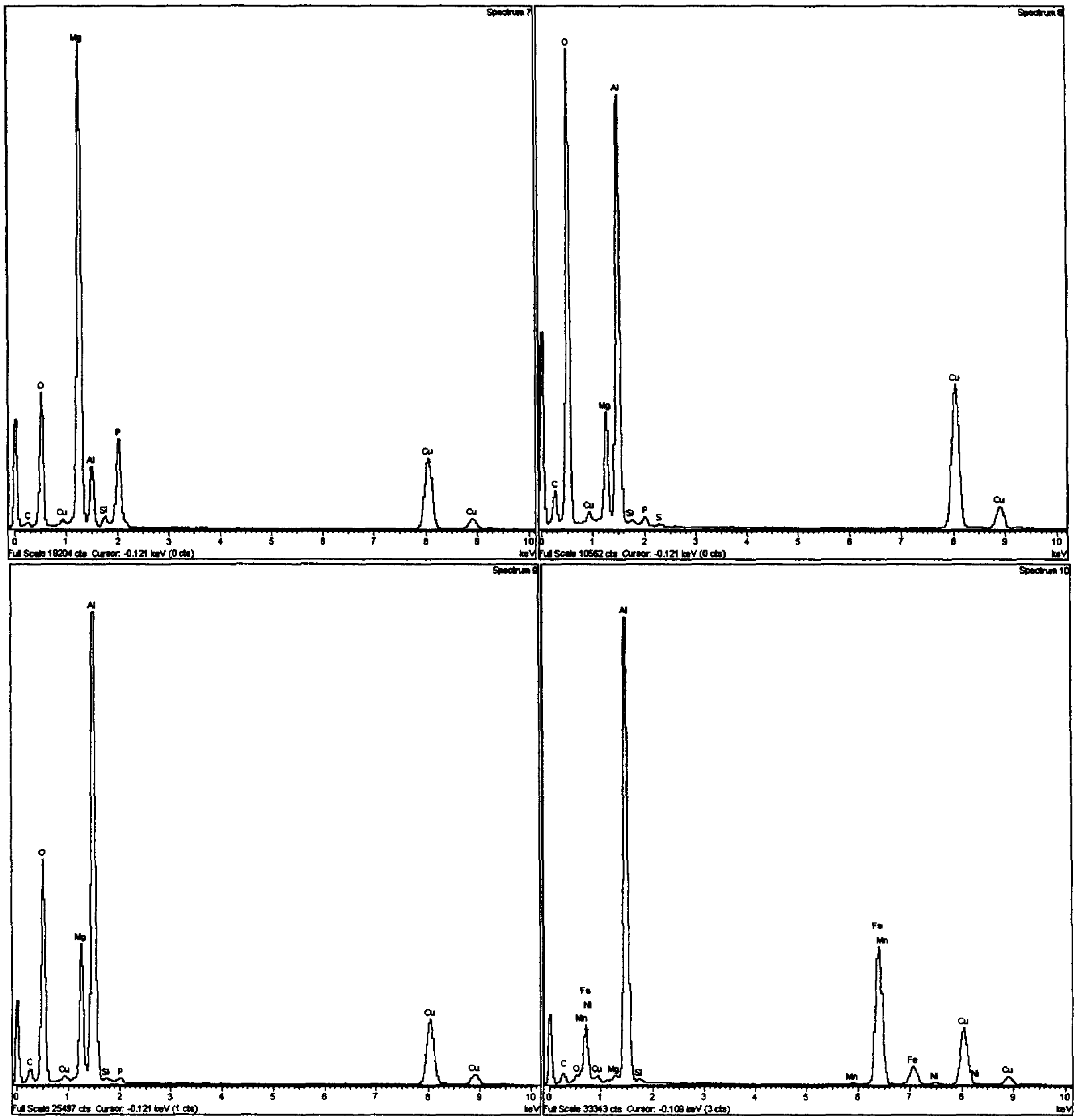

Figure E.6 (Cont'd)

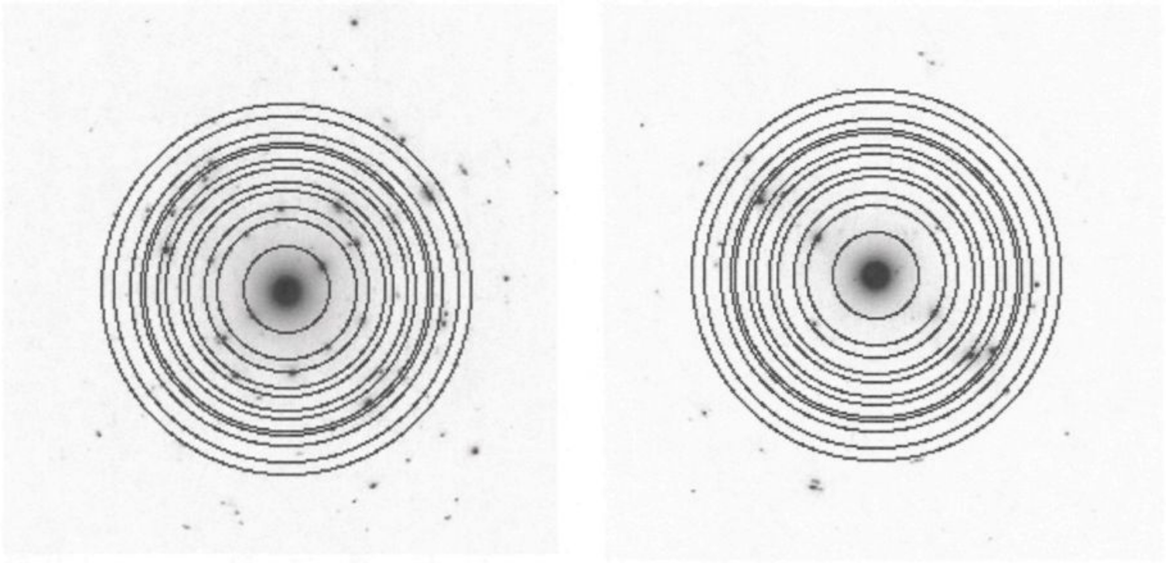

Figure E.7 SAEDPs from Small Crystals around Al_2O_3 Matching Al_2MgO_4 (There are Probably Al_3Fe Among These Small Crystals)

Table E.3 EDS Analysis Results as Given by the INCA System (All Results in Weight %)

SPECTRUM LABEL	O	Mg	Al	Si	P	Fe
Spectrum 1	0.6	4.1	95.3	0.0	0.0	0.0
Spectrum 2	38.7	0.0	61.1	0.1	0.1	0.0
Spectrum 3	49.7	44.9	1.3	0.3	3.9	0.0
Spectrum 4	2.0	0.5	62.3	0.2	0.0	35.1
Spectrum 5	2.0	0.4	61.3	0.4	0.0	35.9
Spectrum 6	23.3	56.5	10.0	0.9	9.2	0.1
Spectrum 7	22.8	56.5	7.3	1.2	12.2	0.1
Spectrum 8	55.1	8.6	35.1	0.3	0.9	0.0
Spectrum 9	34.4	13.9	50.7	0.3	0.5	0.1
Spectrum 10	2.0	0.5	61.8	0.3	0.0	35.4

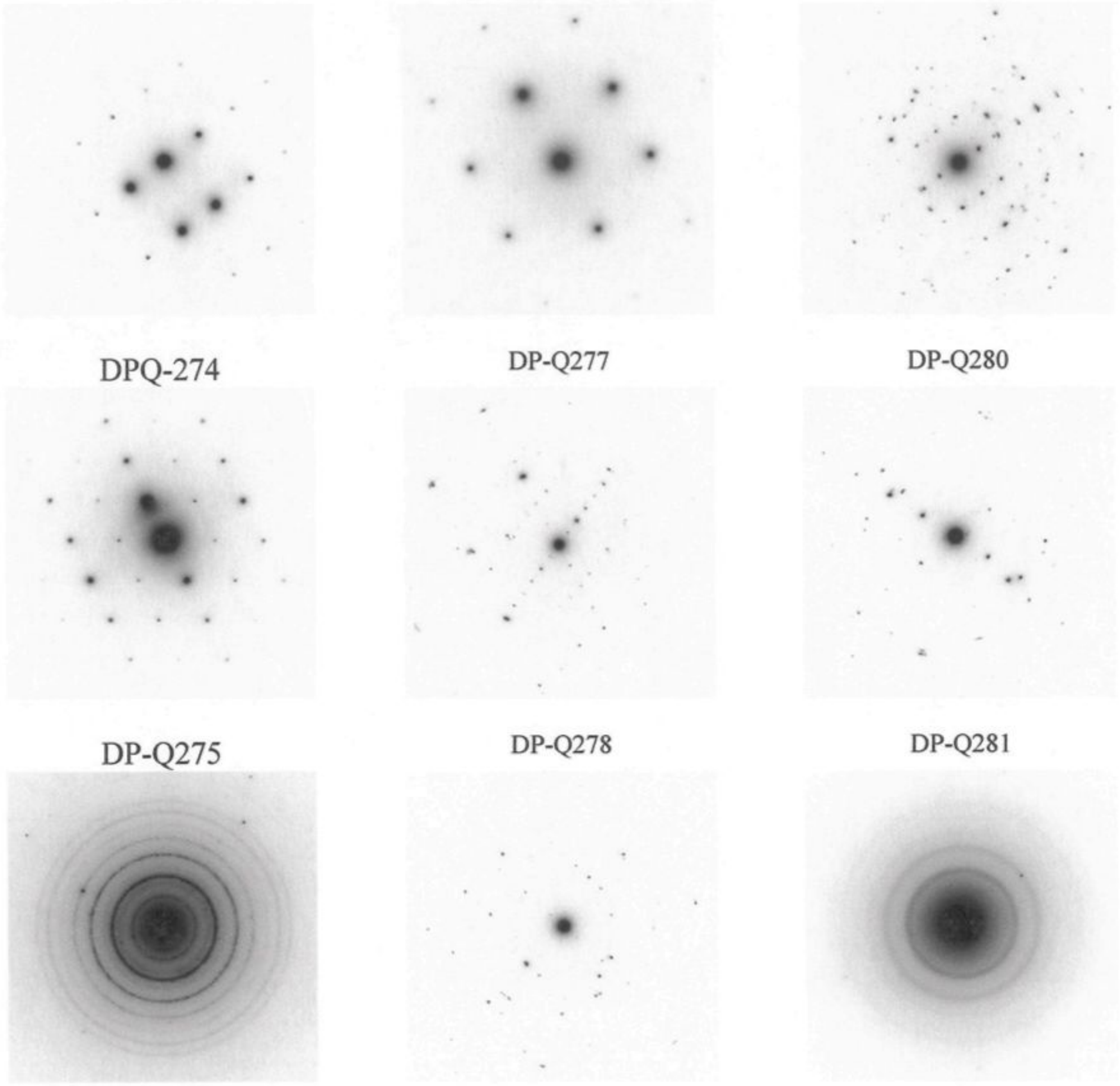

DPQ-274 DP-Q277 DP-Q280

DP-Q275 DP-Q278 DP-Q281

DP-Q276 DP-Q279 DP-Q291

Figure E.8 Selected Area Electron Diffraction Patterns:

DP-Q274: Al_2O_3 crystal
DP-Q275: another Al_2O_3 crystal
DP-Q276: binder
DP-Q277: Aluminum
DP-Q278: crystal "around" Al_2O_3
DP-Q279: another crystal "around" Al_2O_3
DP-Q280: another crystal "around" Al_2O_3
DP-Q281: another crystal "around" Al_2O_3
DP-Q291: from the area corresponding to EDS #3

MOUNTED SAMPLE OF EXP 14 (Ion Milled)

One region (Al/Al_2O_3 interface) in the samples prepared by Ar ion-milling contained spinel – a relatively large crystal and layer on the intephase boundary.

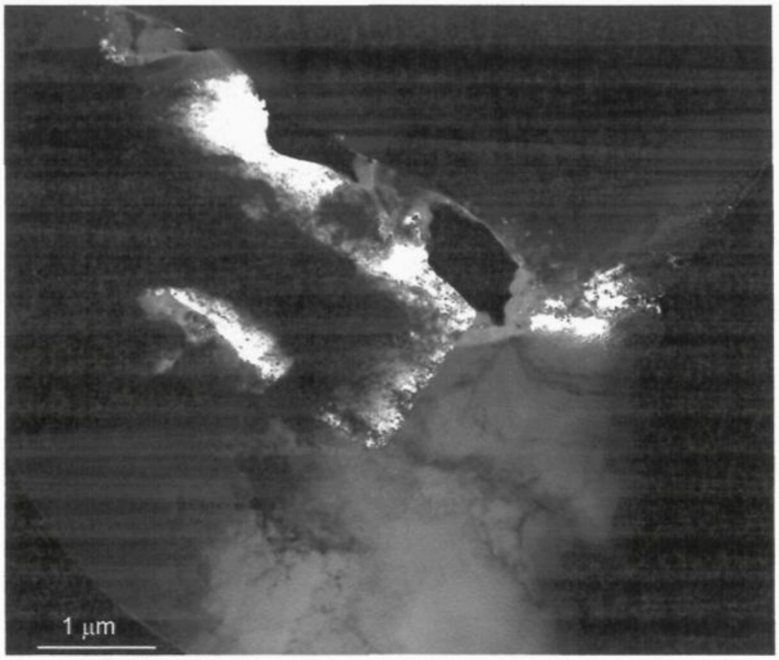

Figure E.9 Bright-field TEM Image

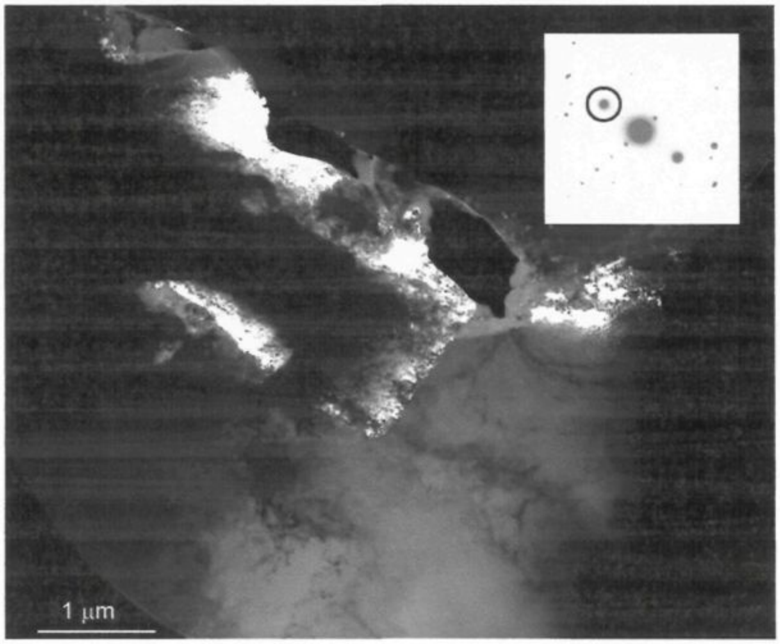

Figure E.10 Dark-field Image in Spinel Reflection (400). Only Edges of the Large Crystal are Lighted because the Middle is too Thick and not Electron-transparent

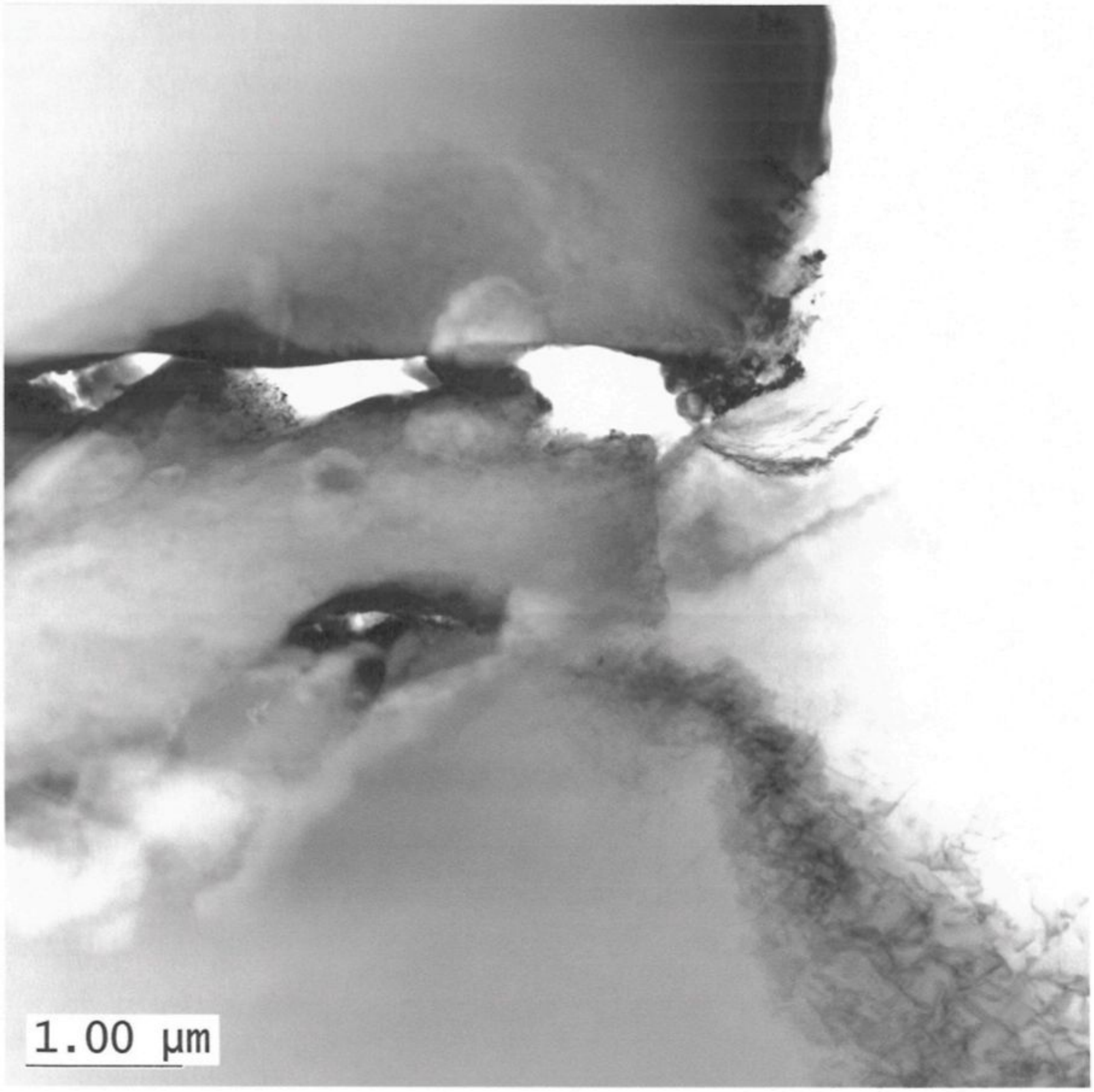

Figure E.11 Scanning TEM (STEM) Image of the Same Region

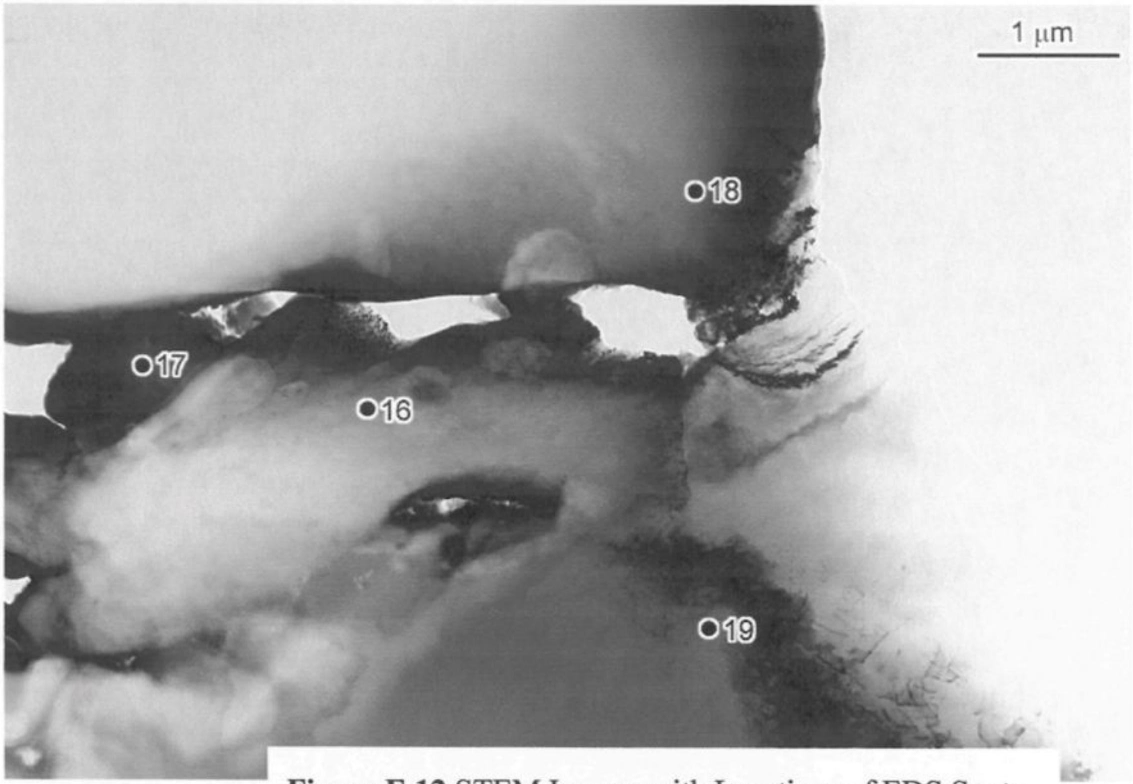

Figure E.12 STEM Images with Locations of EDS Spots

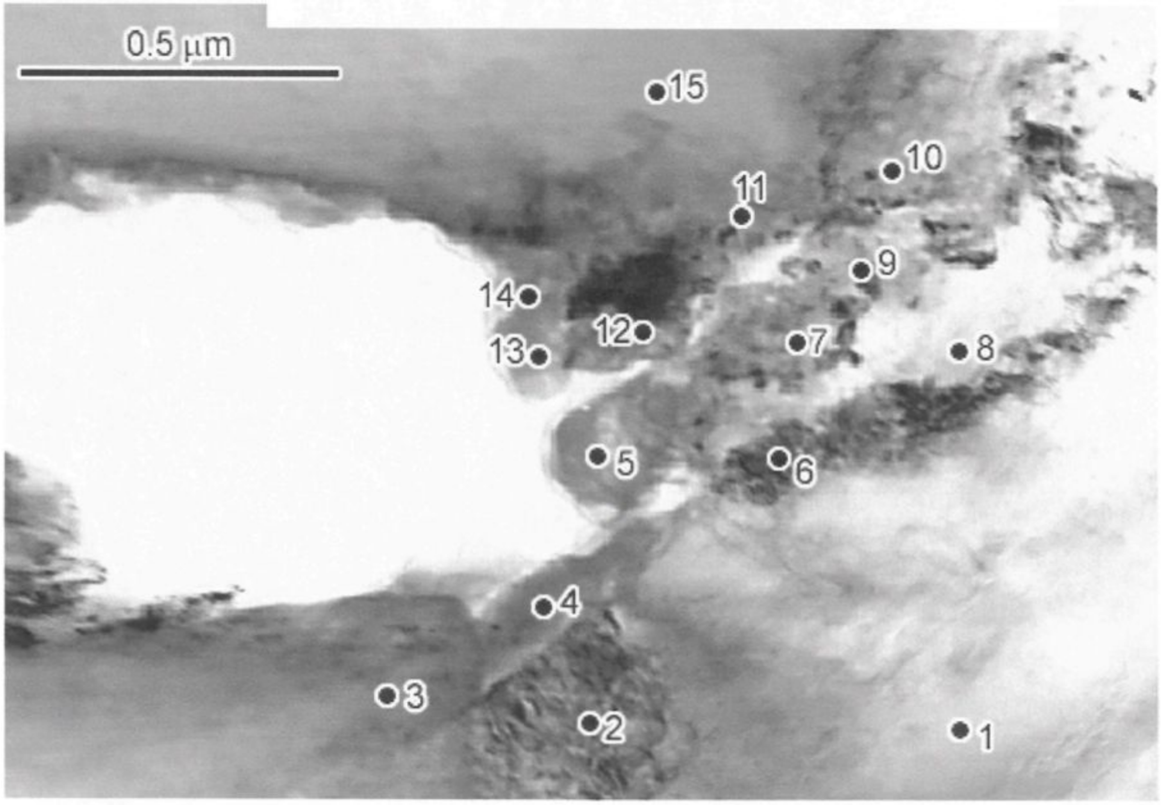

Table E.4 EDS Quant Results as Given by the INCA Software

	O [wt %]	O [at %]	Mg [wt %]	Mg [at %]	Al [wt %]	Al [at %]	Comments
Spectrum 1	0.4	0.7	4.7	5.2	94.9	94.2	Al alloy
Spectrum 2	0.7	1.1	5.0	5.5	94.3	93.4	Al alloy
Spectrum 3	24.9	35.4	15.7	14.7	59.4	49.9	Spinel*
Spectrum 4	36.8	49.1	9.8	8.6	53.4	42.3	Spinel[*]
Spectrum 5	29.8	41.2	14.1	12.8	56.2	46.0	Spinel*
Spectrum 6	0.6	1.0	4.7	5.2	94.7	93.8	Al alloy
Spectrum 7	17.8	25.6	48.6	45.9	33.6	28.5	Spinel*
Spectrum 8	0.7	1.2	4.6	5.1	94.6	93.7	Al alloy
Spectrum 9	23.1	32.6	35.3	32.7	41.6	34.8	Spinel*
Spectrum 10	33.5	45.8	3.5	3.2	63.0	51.1	Al_2O_3
Spectrum 11	30.6	41.8	24.4	21.9	45.0	36.4	Spinel*
Spectrum 12	25.2	35.7	16.7	15.5	58.1	48.8	Spinel*
Spectrum 13	19.7	29.0	11.3	10.9	69.0	60.1	Spinel*
Spectrum 14	18.7	27.6	9.5	9.2	71.9	63.1	Spinel*
Spectrum 15	26.2	37.5	0.2	0.2	73.6	62.4	Al_2O_3
Spectrum 16	14.9	22.6	9.9	9.9	75.2	67.5	Spinel*
Spectrum 17	3.8	6.2	4.1	4.5	92.1	89.4	Al alloy (oxidized)
Spectrum 18	24.4	35.3	0.1	0.1	75.5	64.6	Al_2O_3
Spectrum 19	0.3	0.5	4.9	5.3	94.8	94.1	Al alloy

---

[*] Certain scatter in measured composition may be due to the thickness effect – variable thickness of the foil at different locations.

Table E.5 EDS Results Corrected by Al_2O_3 Stoichiometry

	O [at %]	Mg [at %]	Al [at %]
Spectrum 1	2.06	5.17	92.77
Spectrum 2	3.07	5.49	91.44
Spectrum 3	49.66	11.4	38.93
Spectrum 4	61.32	6.85	31.83
Spectrum 5	54.66	10.01	35.33
Spectrum 6	2.91	5.14	91.95
Spectrum 7	37.53	34.95	27.52
Spectrum 8	3.56	5.07	91.36
Spectrum 9	44.96	24.78	30.26
Spectrum 10	60.08	2.57	37.35
Spectrum 11	53.73	16.81	29.47
Spectrum 12	49.82	12.02	38.16
Spectrum 13	44.62	8.87	46.51
Spectrum 14	43.62	7.38	49
Spectrum 15	54.4	0.16	45.44
Spectrum 16	45.46	7.32	47.22
Spectrum 17	21.47	4.01	74.53
Spectrum 18	59.48	0.09	40.43
Spectrum 19	2.55	5.36	92.09

Mounted EXP 14 Sample (FIB)

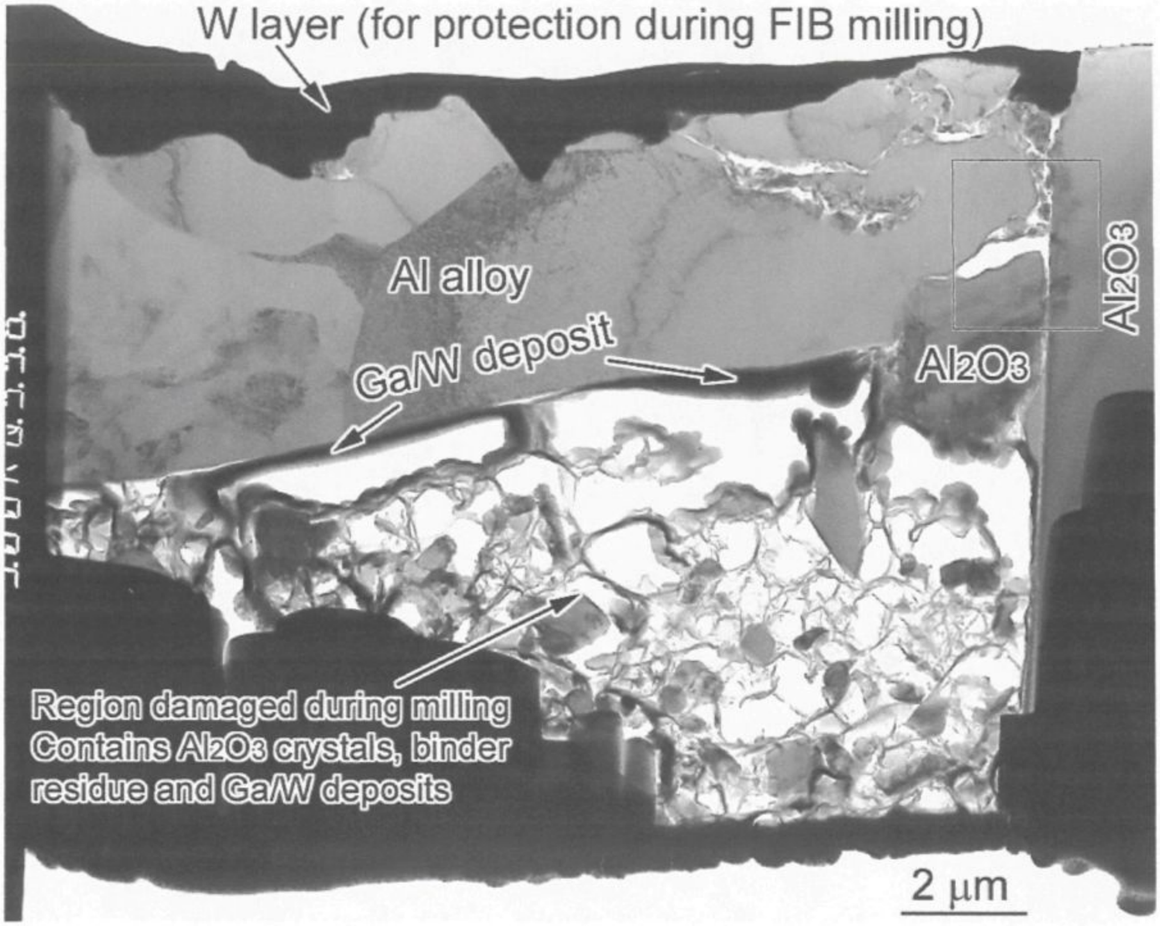

Figure E.13 General View of the Sample Prepared by the Focused Ion Beam (FIB)

Much of the sample was damaged during preparation – one can see a lot of voids as well as Ga and W re-deposits (Ga ions are used in the FIB microscope for milling, while W is used to protect the specimen surface). Only one area (marked by the rectangle on the photo above) was suitable for TEM examination in this FIB-prepared sample.

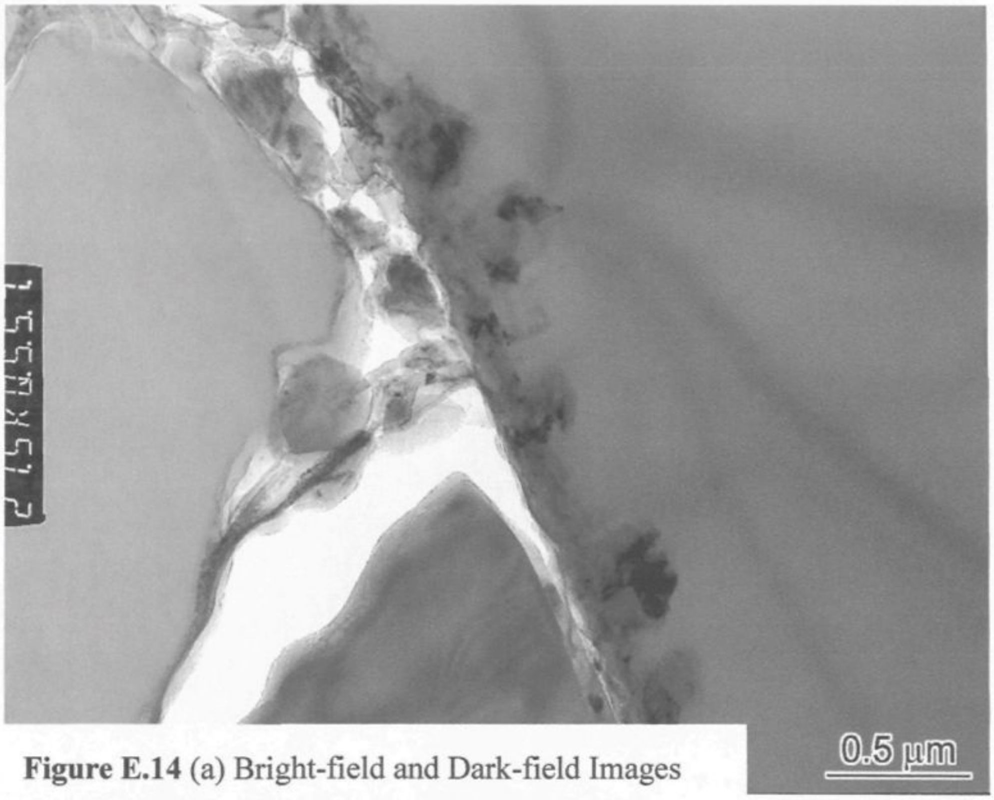

Figure E.14 (a) Bright-field and Dark-field Images

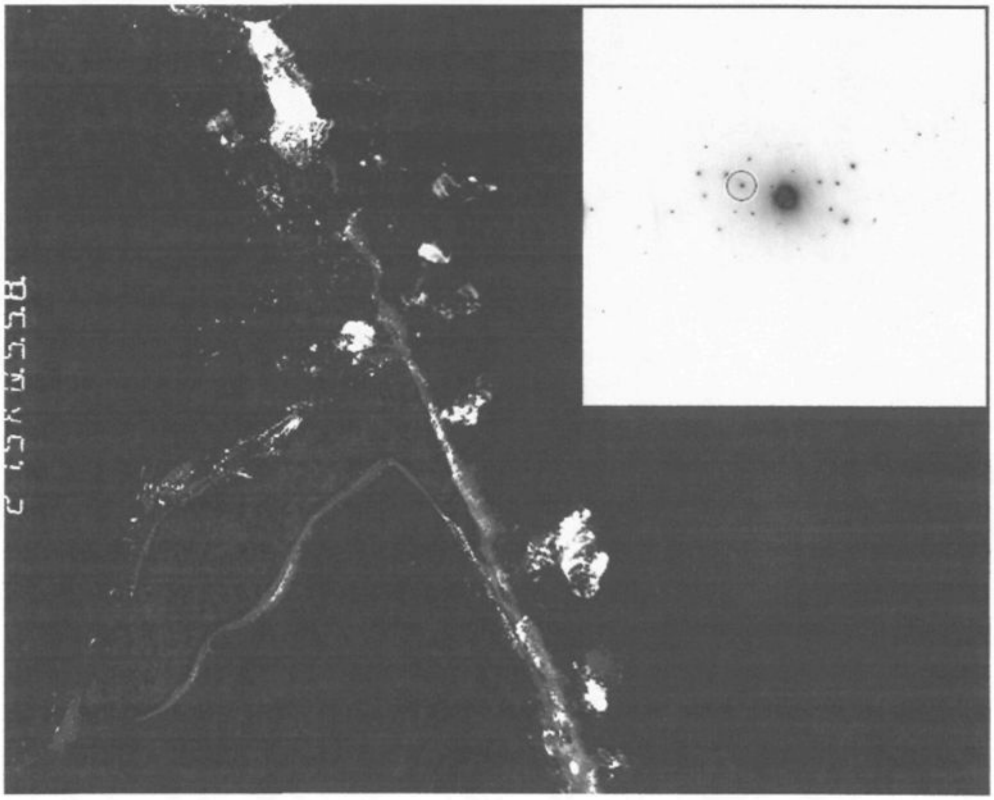

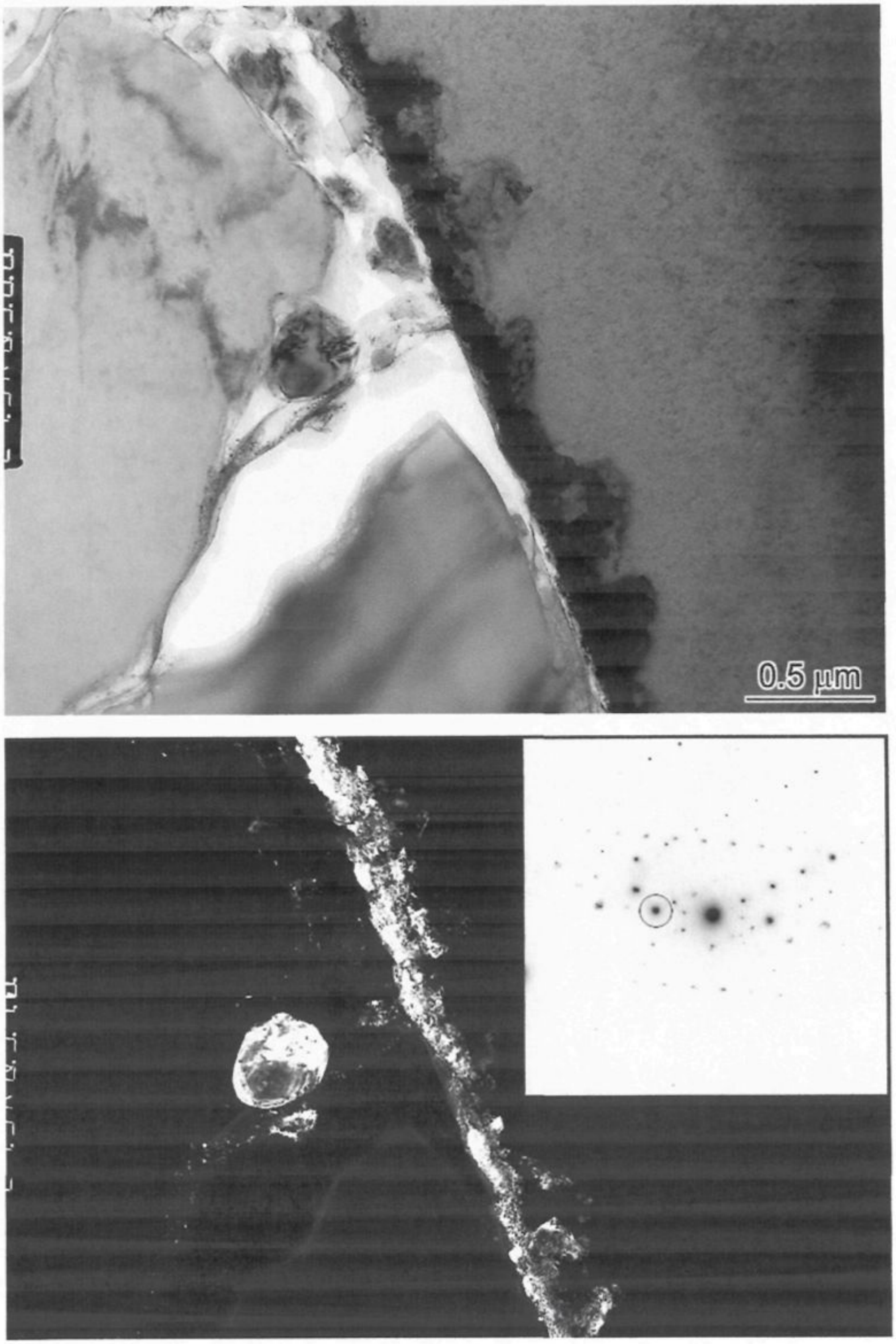

Figure E.14 (b) Bright Particle on the Left is Al_2O_3, which is Accidentally in a Strong Diffracting Orientation Simultaneously with the Spinel Layer.

[211] Spinel

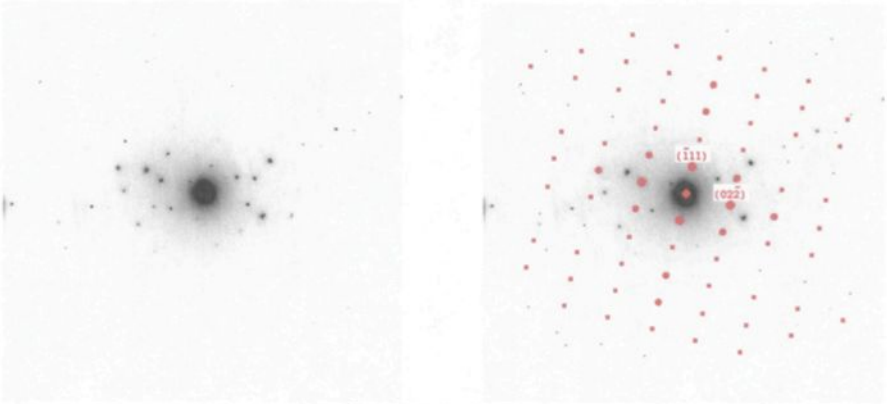

[310] Spinel

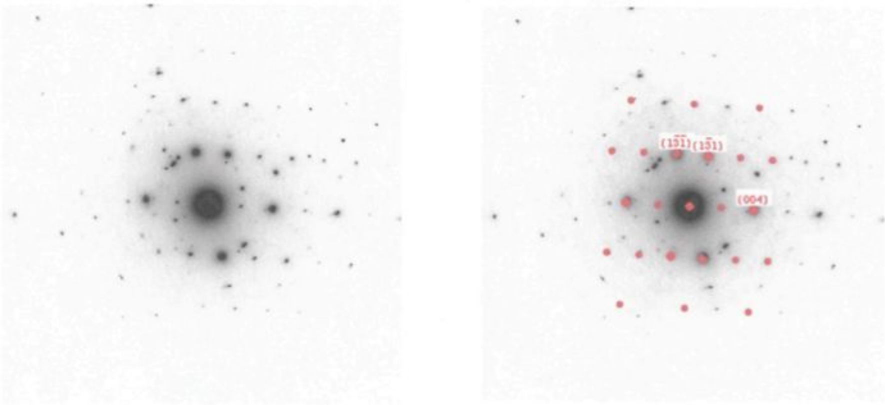

[410] Spinel

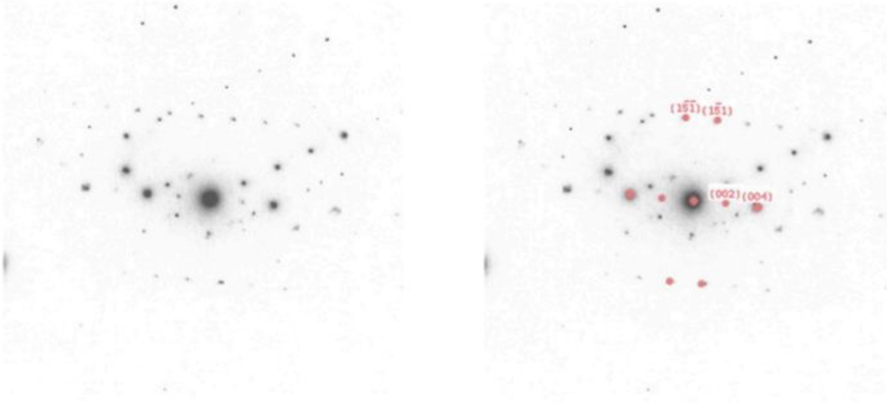

Figure E.15 Indexing of Selected Area Diffraction Patterns from Spinel. Superimposed are Diffraction Patterns from Al_2O_3 (See Next Page).

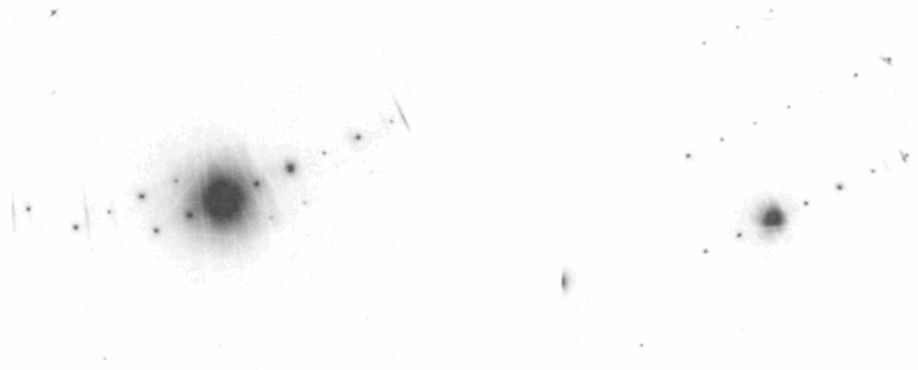

Figure E.16 Diffraction Patterns from Al_2O_3 (Superimposed onto the Spinel Patterns Shown on the Previous Page)

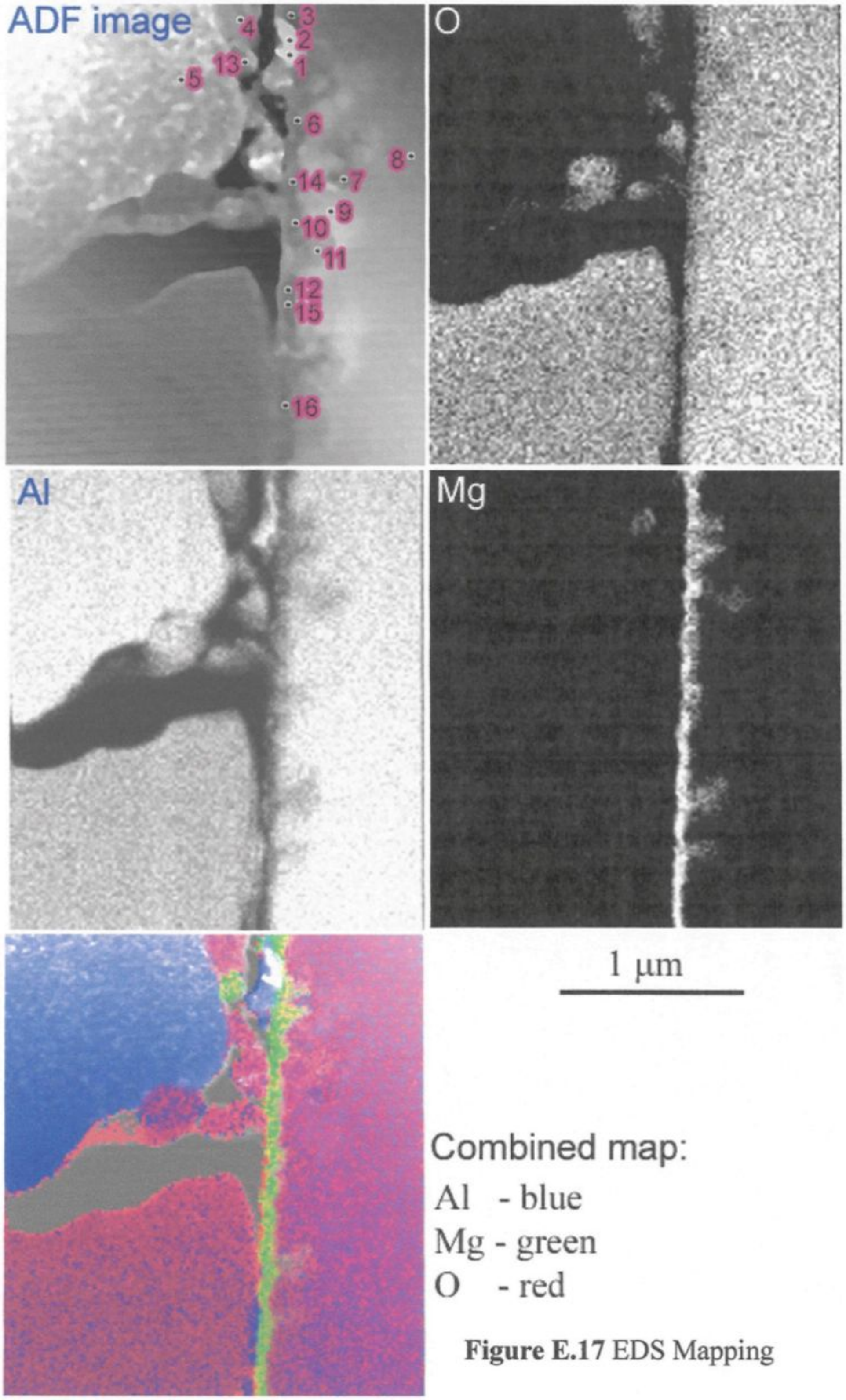

Figure E.17 EDS Mapping

Table E.6 EDS Quant Results as Given by the INCA Software

	O [wt%]	O [at %]	Mg [wt %]	Mg [at %]	Al [wt %]	Al [at %]	Comments
Spectrum 1	7.1	11.3	14.1	14.7	78.8	74.1	mix
Spectrum 2	21.8	30.8	37.1	34.6	41.2	34.6	mix?
Spectrum 3	29.0	38.9	52.0	45.9	19.1	15.2	mix?
Spectrum 4	35.2	47.7	1.4	1.2	63.5	51.1	~Al_2O_3
Spectrum 5	0.5	0.8	4.1	4.5	95.4	94.6	Al alloy
Spectrum 6	35.4	47.1	23.4	20.5	41.2	32.5	spinel?
Spectrum 7	36.6	49.1	4.1	3.6	59.3	47.2	mix?
Spectrum 8	35.2	47.8	0.0	0.0	64.8	52.2	Al_2O_3
Spectrum 9	36.2	48.8	0.2	0.1	63.7	51.0	Al_2O_3
Spectrum 10	34.2	45.2	37.2	32.3	28.7	22.5	spinel?
Spectrum 11	33.9	46.0	11.1	9.9	54.9	44.1	mix?
Spectrum 12	34.6	45.6	38.4	33.3	27.1	21.2	spinel?
Spectrum 13	33.9	44.6	44.2	38.3	21.9	17.1	spinel?
Spectrum 14	34.2	45.4	32.7	28.6	33.1	26.1	spinel?
Spectrum 15	35.3	46.7	29.0	25.2	35.8	28.1	spinel?
Spectrum 16	34.7	46.5	17.4	15.4	47.9	38.1	spinel?

Table E.7 EDS Results Corrected by Al_2O_3 Stoichiometry

	O [at %]	Mg [at %]	Al [at %]
Spectrum 1	19.9	12.9	67.2
Spectrum 2	40.6	27.9	31.6
Spectrum 3	47.2	37.7	15.1
Spectrum 4	59.2	1.0	39.8
Spectrum 5	2.0	4.5	93.5
Spectrum 6	55.7	16.7	27.6
Spectrum 7	59.9	3.1	37.1
Spectrum 8	59.5	0.0	40.5
Spectrum 9	60.3	0.1	39.6
Spectrum 10	53.1	26.4	20.5
Spectrum 11	56.3	8.2	35.6
Spectrum 12	53.4	27.2	19.4
Spectrum 13	52.3	31.4	16.3
Spectrum 14	53.6	23.3	23.2
Spectrum 15	54.9	20.6	24.5
Spectrum 16	55.9	12.6	31.5

Sample EXP 15

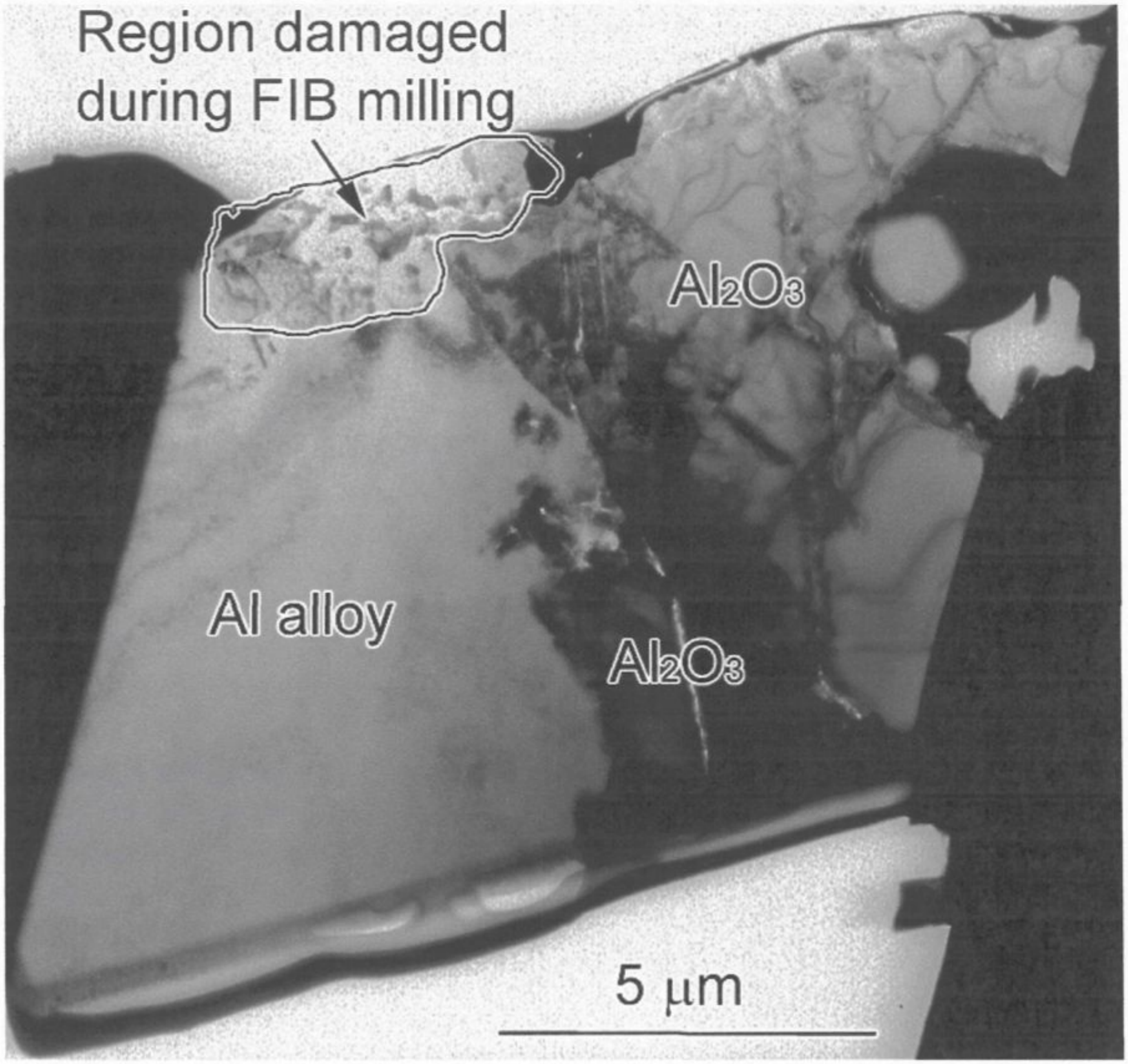

Figure E.18 Low-magnification View (TEM Bright-field Image) of Sample EXP 15 Prepared by FIB

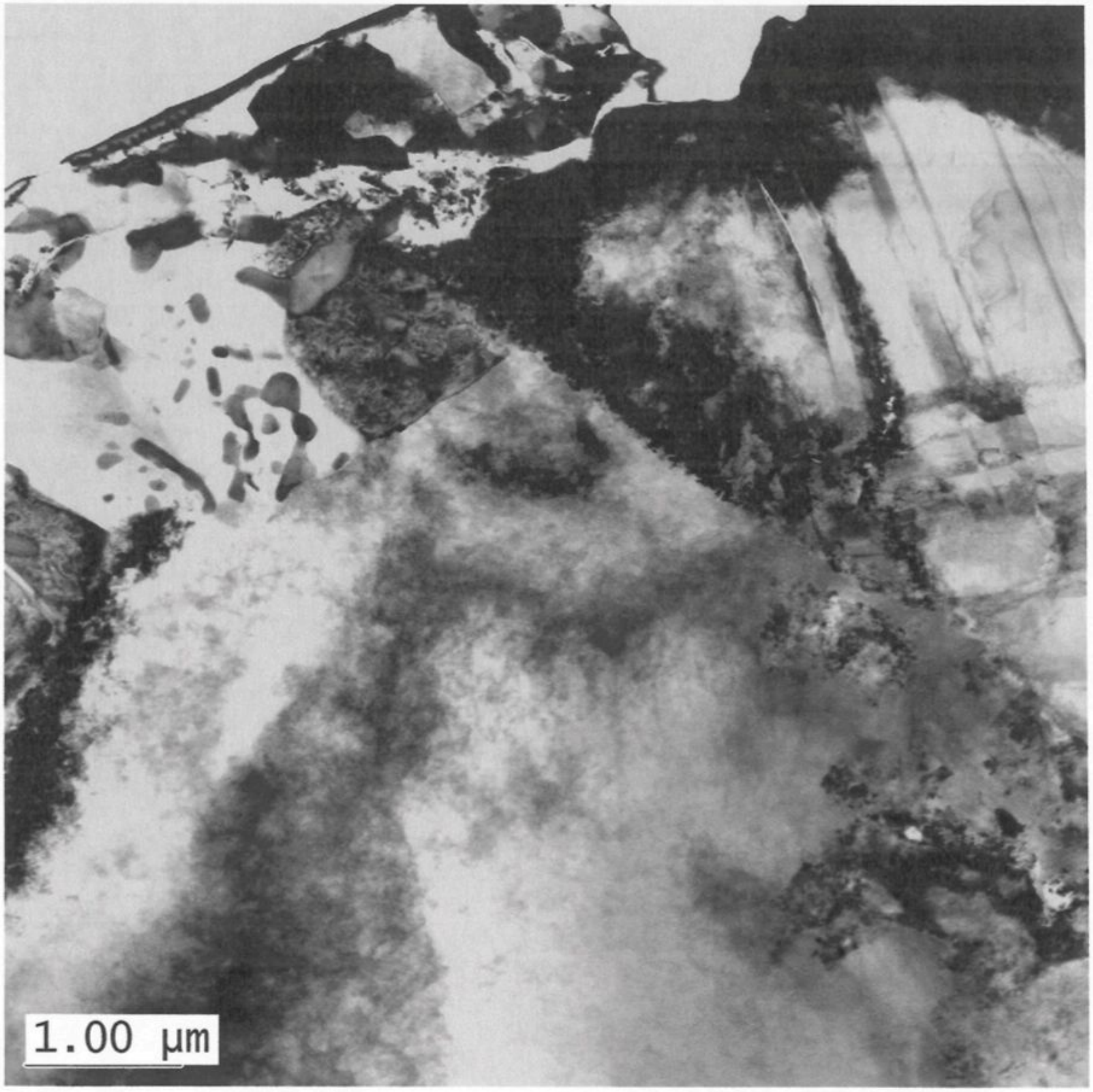

Figure E.19 STEM Image 1

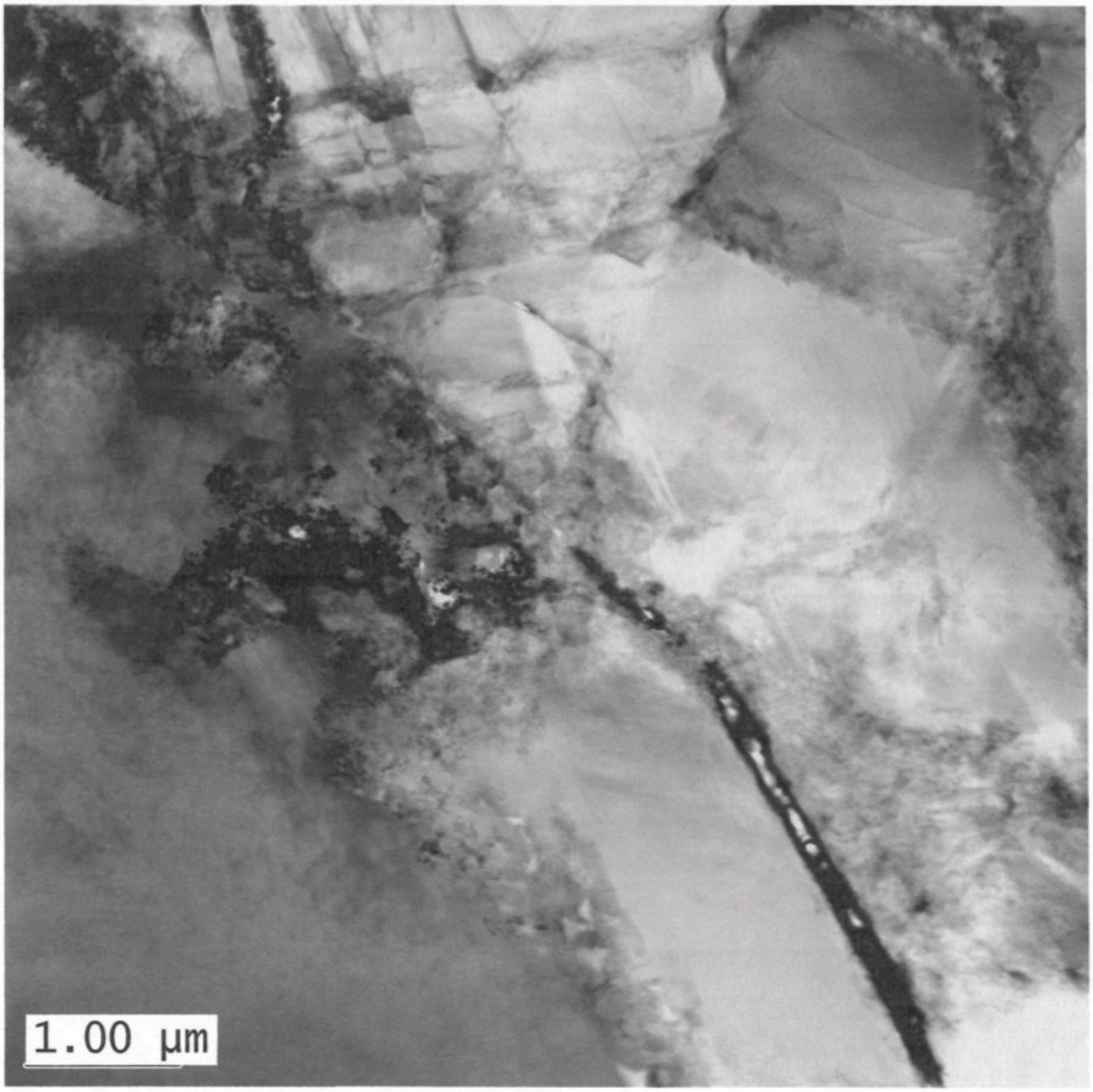

Figure E.20 STEM Image 2

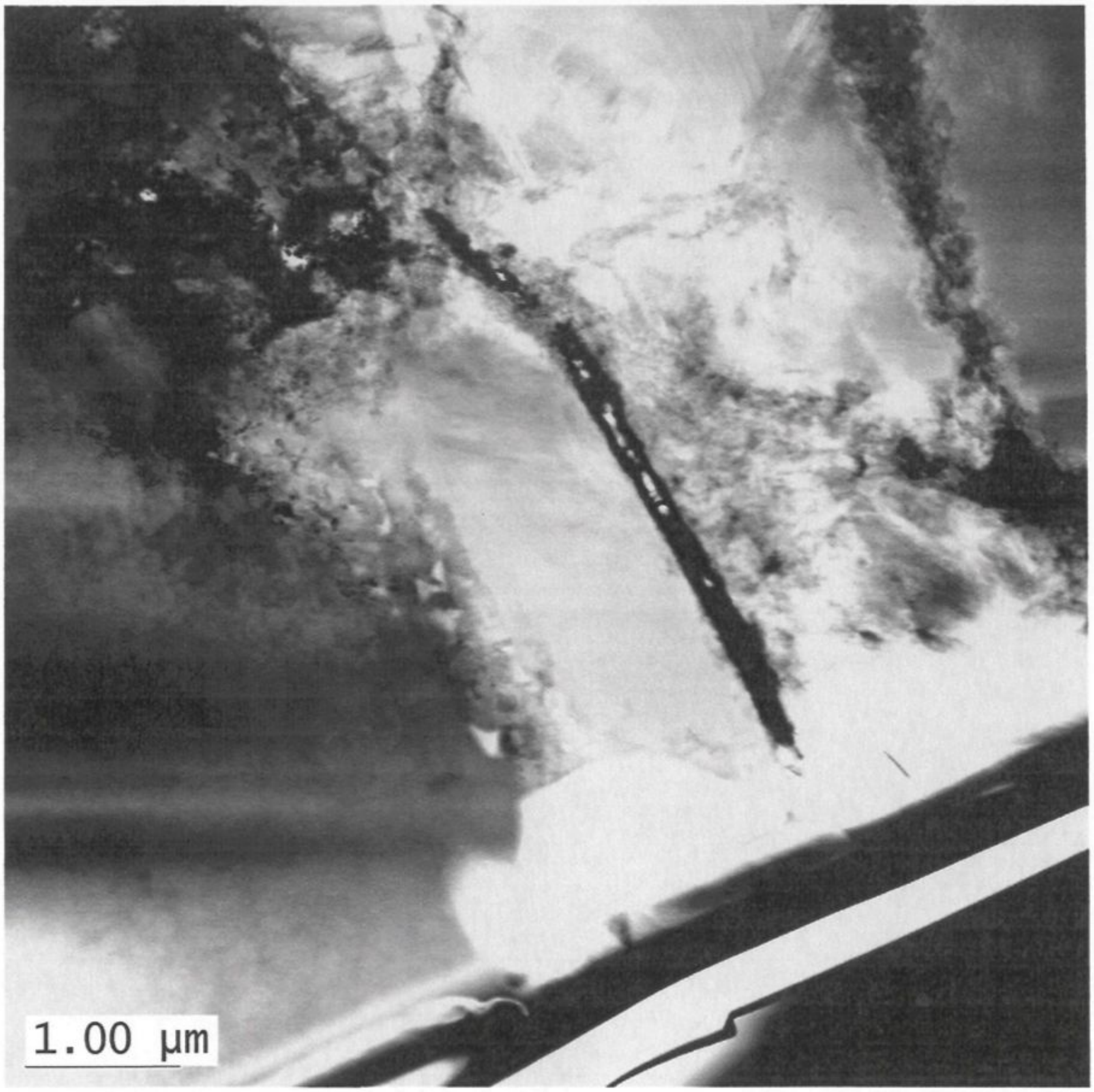

Figure E.21 STEM Image 3

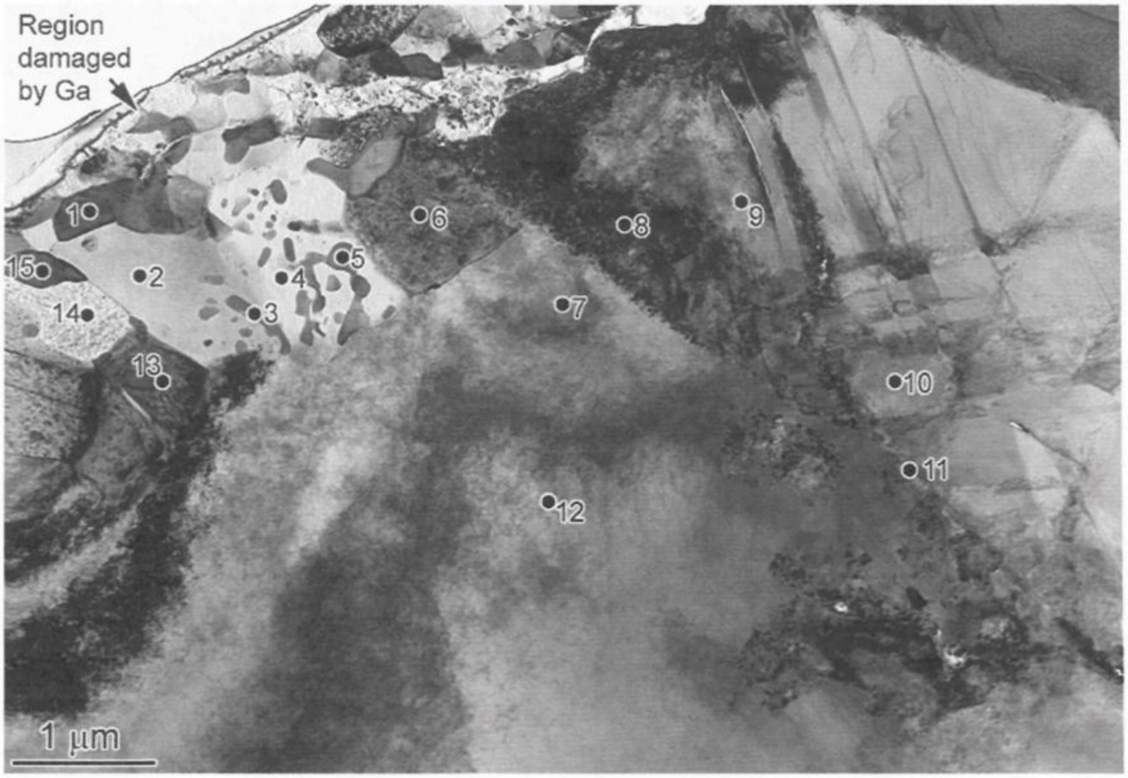

Figure E.22 STEM Image 4 with EDS Locations

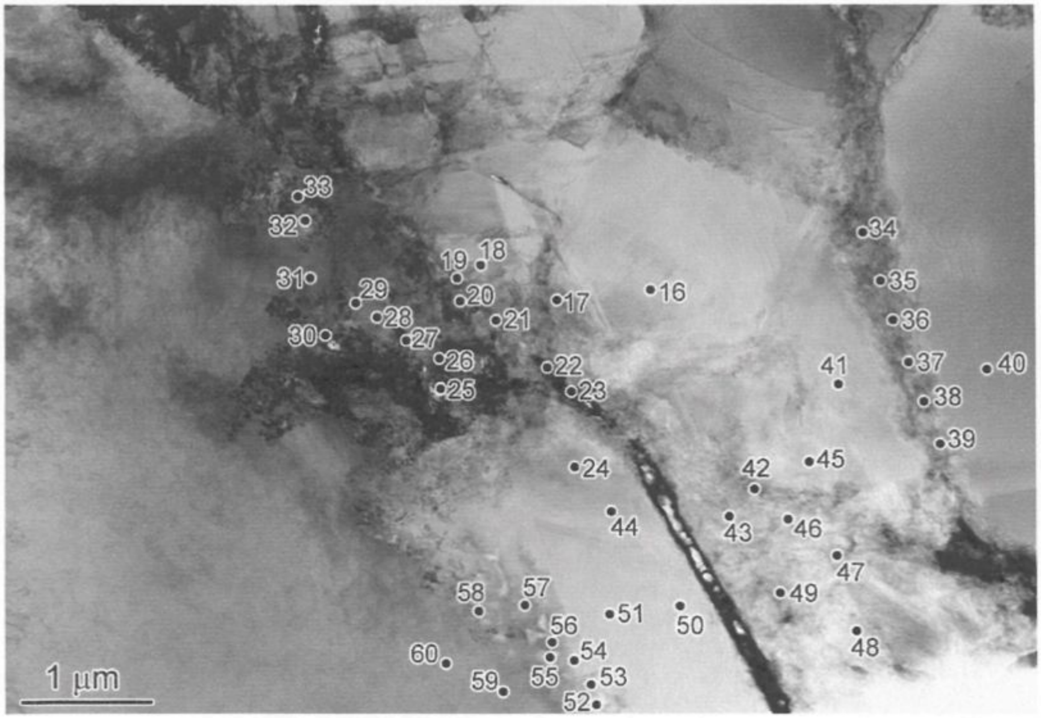

Figure E.23 STEM Image 5 with EDS Locations

Table E.8 EDS Quant Results as Given by the INCA Software

	O [wt %]	O [at %]	Mg [wt %]	Mg [at %]	Al [wt %]	Al [at %]	Ga [wt %]	Ga [at %]
Spectrum 1	1.0	3.4	10.2	23.3	2.1	4.4	86.7	68.9
Spectrum 2	0.8	1.4	0.0	0.0	88.6	94.3	10.7	4.4
Spectrum 3	0.6	1.5	6.7	10.1	46.9	64.2	45.8	24.2
Spectrum 4	0.3	0.5	0.0	0.0	91.0	96.0	8.7	3.6
Spectrum 5	0.4	1.0	4.4	6.4	54.7	72.0	40.5	20.6
Spectrum 6	0.5	0.8	0.3	0.4	90.4	95.2	8.9	3.6
Spectrum 7	0.4	0.7	5.9	6.5	93.0	92.5	0.7	0.3
Spectrum 8	36.1	48.9	0.0	0.0	63.6	51.1	0.3	0.1
Spectrum 9	36.1	48.9	0.1	0.1	63.5	50.9	0.2	0.1
Spectrum 10	33.9	46.4	0.2	0.2	65.6	53.3	0.3	0.1
Spectrum 11	17.2	24.9	44.6	42.5	37.8	32.4	0.4	0.1
Spectrum 12	0.6	0.9	5.9	6.5	93.2	92.5	0.4	0.1
Spectrum 13	0.7	1.4	5.6	7.9	56.9	72.5	36.8	18.1
Spectrum 14	0.9	1.5	0.0	0.0	88.0	93.9	11.3	4.7
Spectrum 15	1.1	2.0	0.6	0.7	85.1	91.8	13.3	5.5

(Ga was used for sample preparation and reacted with the material in one region, as seen from spectra 1-6 and 13-15)

Table E.9 EDS Results Corrected by Al_2O_3 Stoichiometry

	O [at %]	Mg [at %]	Al [at %]	Comments
Spectrum 8	59.2	0.0	40.7	Al_2O_3
Spectrum 9	59.2	0.1	40.7	Al_2O_3
Spectrum 10	57.2	0.2	42.6	Al_2O_3
Spectrum 11	33.1	35.4	31.4	Spinel ?

Table E.10 EDS Quant Results as Given by the INCA Software

	O	O	Mg	Mg	Al	Al	Comments
Spectrum 16	32.6	44.9	0.0	0.0	67.4	55.1	Al_2O_3
Spectrum 17	32.7	45.1	0.2	0.1	67.1	54.8	Al_2O_3
Spectrum 18	32.6	44.8	2.5	2.3	64.9	52.9	Al_2O_3 + Mg
Spectrum 19	27.6	38.0	30.4	27.6	42.0	34.4	spinel
Spectrum 20	26.7	37.6	13.9	12.8	59.4	49.6	spinel
Spectrum 21	29.9	41.1	18.9	17.1	51.2	41.7	spinel
Spectrum 22	33.2	44.8	17.6	15.7	49.2	39.5	spinel
Spectrum 23	30.1	39.8	61.1	53.3	8.8	6.9	spinel
Spectrum 24	33.3	45.7	0.3	0.3	66.5	54.1	Al_2O_3
Spectrum 25	35.6	46.2	50.9	43.5	13.5	10.3	spinel
Spectrum 26	3.0	5.0	9.1	9.8	87.8	85.2	mix
Spectrum 27	5.6	8.9	22.0	22.9	72.4	68.1	mix
Spectrum 28	0.6	1.1	6.3	6.9	93.1	92.0	mix
Spectrum 29	11.2	17.1	23.3	23.4	65.6	59.5	mix
Spectrum 30	17.8	25.8	35.7	34.1	46.6	40.1	spinel
Spectrum 31	0.7	1.1	6.0	6.6	93.3	92.3	Al alloy
Spectrum 32	21.3	30.1	42.4	39.4	36.3	30.4	spinel
Spectrum 33	29.2	39.7	38.2	34.1	32.6	26.2	spinel
Spectrum 34	30.1	40.9	32.7	29.2	37.2	29.9	spinel
Spectrum 35	31.0	41.3	48.6	42.6	20.4	16.1	spinel
Spectrum 36	29.8	40.1	43.7	38.7	26.5	21.2	spinel
Spectrum 37	27.3	36.7	60.7	53.7	12.0	9.5	spinel
Spectrum 38	28.3	37.7	65.9	57.7	5.8	4.6	spinel
Spectrum 39	21.3	30.1	42.5	39.6	36.1	30.3	spinel
Spectrum 40	32.1	44.3	0.1	0.1	67.8	55.6	Al_2O_3
Spectrum 41	33.1	45.4	0.8	0.7	66.2	53.9	Al_2O_3
Spectrum 42	21.3	30.8	21.6	20.5	53.7	46.0	Spinel + 3.3%S
Spectrum 43	23.5	33.8	11.9	11.3	64.6	55.0	spinel
Spectrum 44	32.7	45.0	0.3	0.3	67.0	54.7	Al_2O_3
Spectrum 45	31.4	43.6	0.2	0.1	68.4	56.3	Al_2O_3
Spectrum 46	30.2	41.8	8.9	8.1	60.9	50.1	spinel
Spectrum 47	31.2	43.0	8.2	7.5	60.6	49.5	spinel
Spectrum 48	30.1	41.9	5.0	4.6	64.9	53.5	spinel
Spectrum 49	19.3	28.2	20.0	19.2	60.7	52.6	spinel
Spectrum 50	32.2	44.5	0.2	0.2	67.6	55.3	Al_2O_3
Spectrum 51	31.4	43.5	0.1	0.1	68.5	56.3	Al_2O_3
Spectrum 52	14.4	21.7	19.6	19.4	66.0	58.9	mix
Spectrum 53	21.7	31.4	14.8	14.1	63.6	54.6	Spinel ?
Spectrum 54	22.3	32.3	9.5	9.1	68.2	58.6	Spinel
Spectrum 55	8.6	13.4	18.3	18.8	73.1	67.8	mix
Spectrum 56	12.3	18.7	19.7	19.8	68.0	61.5	mix
Spectrum 57	14.3	21.7	6.6	6.7	79.1	71.6	mix

Table E.10 (Cont'd)

	O	O	Mg	Mg	Al	Al	Comments
Spectrum 58	6.7	10.7	10.7	11.3	82.6	78.0	mix
Spectrum 59	0.4	0.7	5.9	6.4	93.7	92.9	Al alloy
Spectrum 60	0.4	0.6	6.0	6.6	93.7	92.9	Al alloy

Table E.11 EDS Results Corrected by Al_2O_3 Stoichiometry

	O [at %]	Mg [at %]	Al [at %]	Comments
Spectrum 16	59.4	0.0	40.6	Al_2O_3
Spectrum 17	59.4	0.1	40.5	Al_2O_3
Spectrum 18	58.8	1.9	39.4	Al_2O_3 + Mg
Spectrum 19	49.3	21.4	29.3	spinel
Spectrum 20	50.9	10.2	38.9	Spinel
Spectrum 21	53.1	13.5	33.4	Spinel
Spectrum 22	56.2	12.4	31.4	Spinel
Spectrum 23	49.5	43.1	7.5	Spinel ?
Spectrum 24	59.9	0.2	39.9	Al_2O_3
Spectrum 25	54.8	34.9	10.3	Spinel
Spectrum 26	11.4	9.1	79.5	mix
Spectrum 27	17.6	19.4	63.1	mix
Spectrum 28	2.8	6.8	90.4	mix
Spectrum 29	29.0	18.9	52.1	mix
Spectrum 30	37.7	26.5	35.9	spinel
Spectrum 31	2.8	6.5	90.7	Al alloy
Spectrum 32	41.5	30.5	28.1	spinel
Spectrum 33	50.1	26.5	23.4	spinel
Spectrum 34	51.5	22.7	25.8	spinel
Spectrum 35	50.9	33.6	15.5	spinel
Spectrum 36	50.1	30.2	19.7	spinel
Spectrum 37	46.8	43.1	10.2	spinel
Spectrum 38	47.6	47.2	5.2	spinel
Spectrum 39	41.5	30.6	28.0	spinel
Spectrum 40	58.9	0.1	41.0	Al_2O_3
Spectrum 41	59.6	0.6	39.9	Al_2O_3
Spectrum 42	43.9	16.0	37.5	spinel + 2.7% Si
Spectrum 43	47.9	9.0	43.1	spinel
Spectrum 44	59.4	0.2	40.4	Al_2O_3
Spectrum 45	59.3	0.1	40.6	Al_2O_3
Spectrum 46	56.1	6.4	37.5	spinel
Spectrum 47	57.1	5.9	37.0	spinel
Spectrum 48	56.8	3.7	39.5	spinel
Spectrum 49	42.6	14.9	42.5	spinel
Spectrum 50	59.9	0.2	39.9	Al_2O_3

Table 11 (Cont'd)

	O [at %]	Mg [at %]	Al [at %]	Comments
Spectrum 51	59.2	0.1	40.7	Al_2O_3
Spectrum 52	35.9	15.3	48.8	mix
Spectrum 53	46.3	11.0	42.7	spinel?
Spectrum 54	48.0	7.2	44.8	spinel?
Spectrum 55	25.6	15.4	58.9	mix
Spectrum 56	32.3	15.8	51.9	mix
Spectrum 57	37.9	5.5	56.6	mix
Spectrum 58	22.4	9.7	67.9	mix
Spectrum 59	2.0	6.4	91.6	Al alloy
Spectrum 60	1.7	6.5	91.8	Al alloy

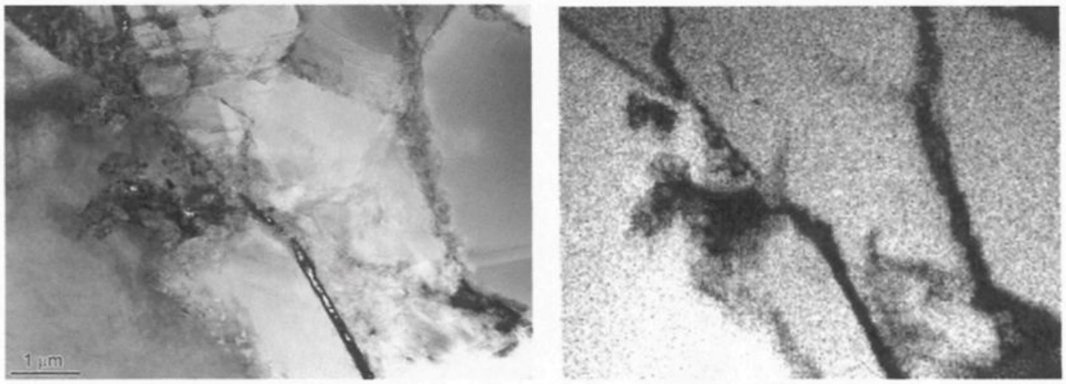

Al Ka1

STEM image

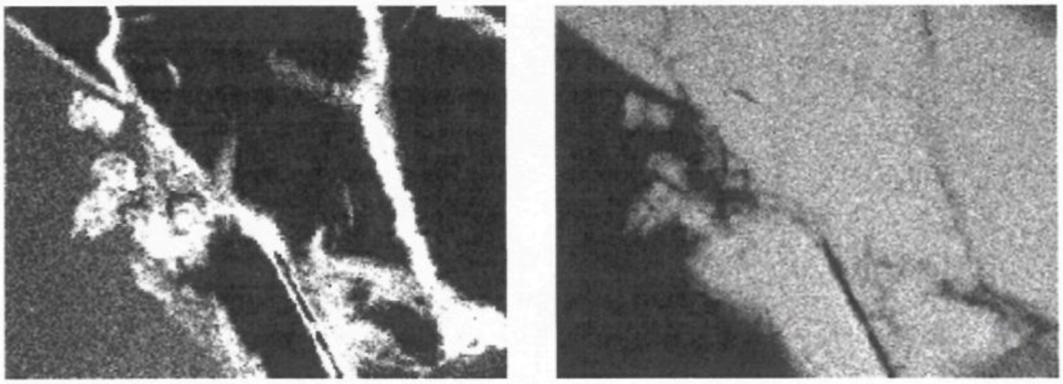

Mg Ka1 _2

O Ka1

Figure E.24 EDS Chemical Maps

Sample EXP 16

Al-Al_2O_3, sample EXP16 – prepared by Ar ion-milling.

Two regions on the Al alloy/ Al_2O_3 interface were examined.

Region 1:

Figure E.25 Bright-Field and Dark-Field Image of Region 1

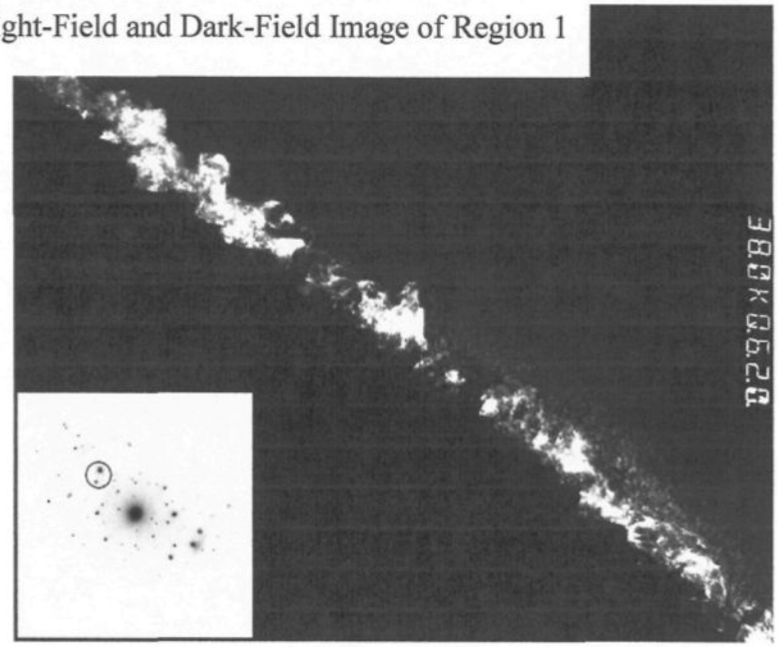

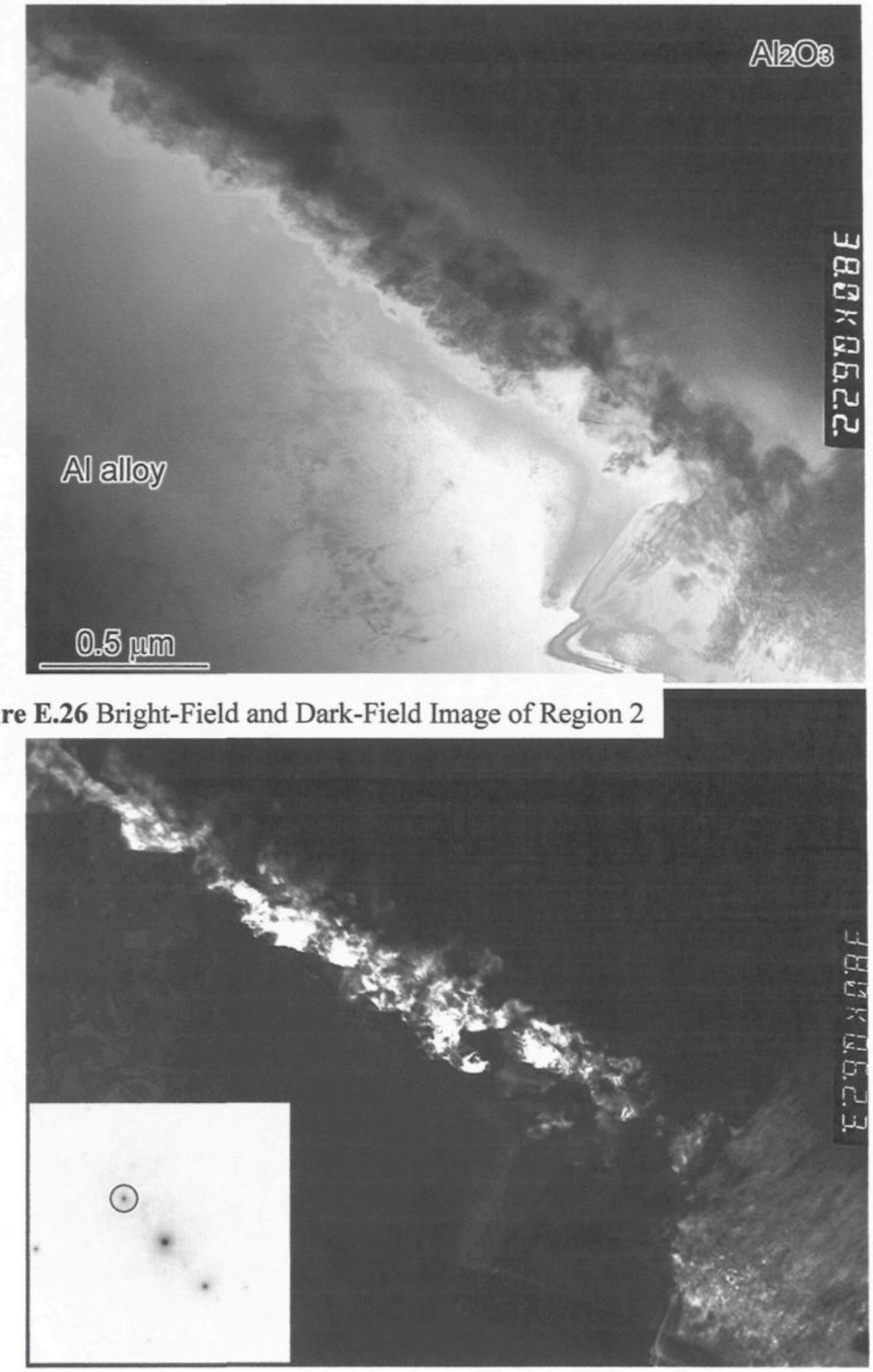

Figure E.26 Bright-Field and Dark-Field Image of Region 2

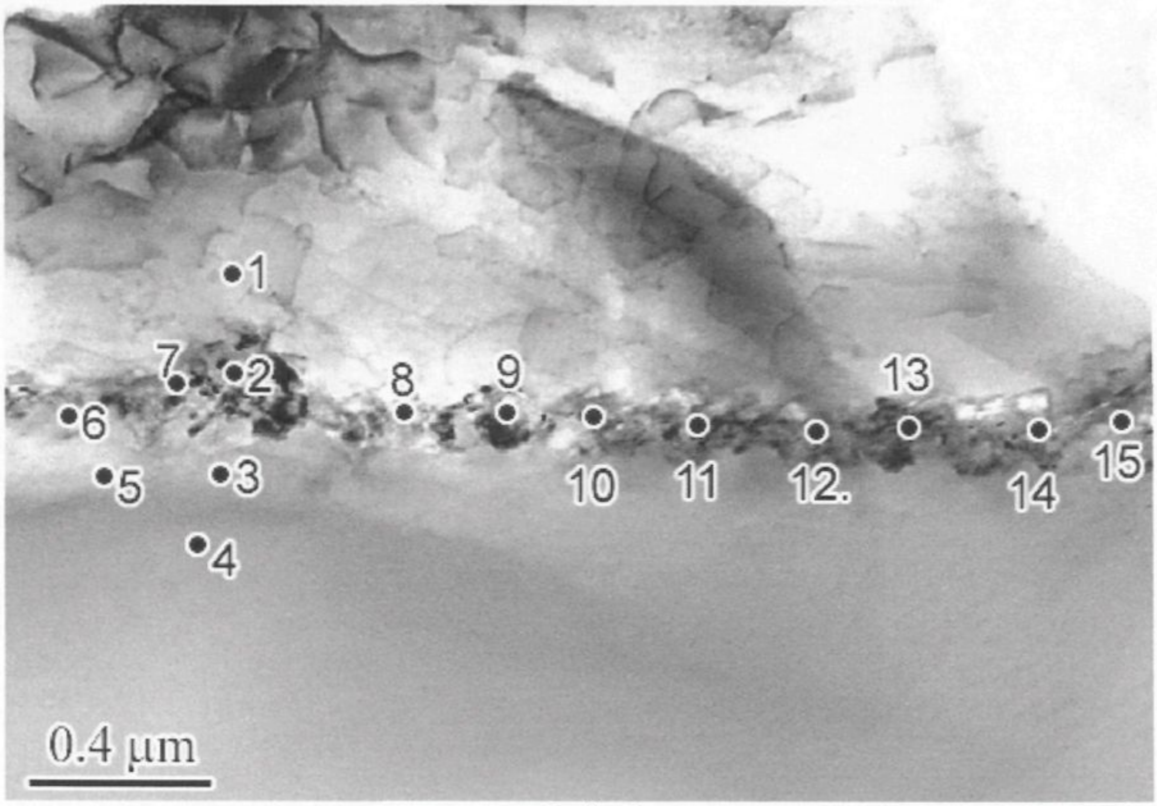

Region 1

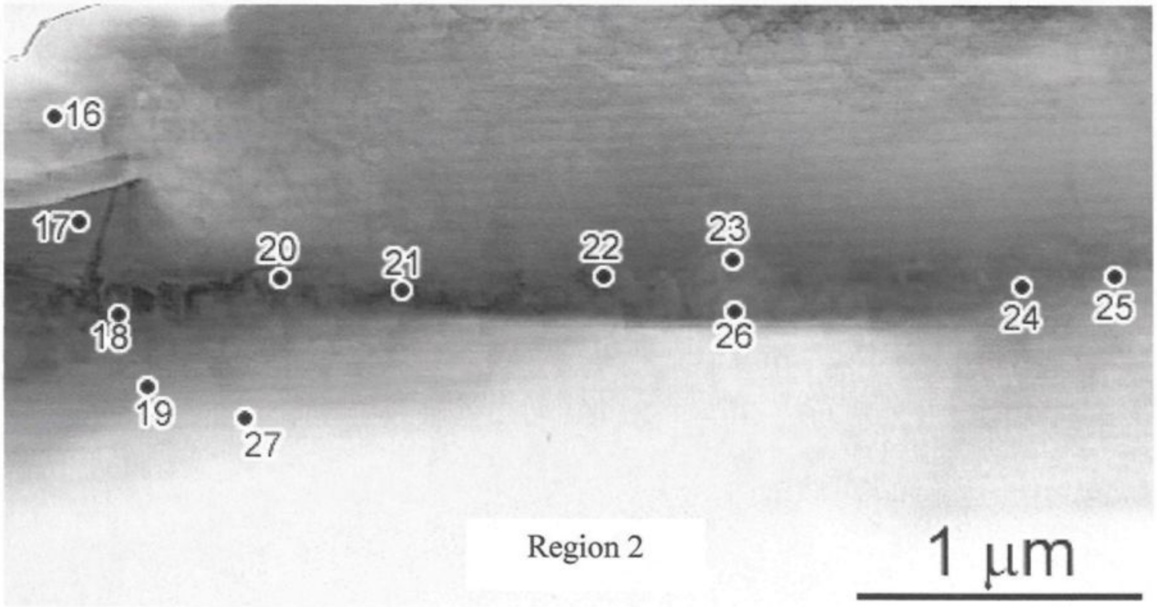

Figure E.27 STEM Images with Locations of EDS Analysis

Table E.12 EDS Quant Results as Given by the INCA Software

	O [wt %]	O [at %]	Mg [wt %]	Mg [at %]	Al [wt %]	Al [at %]
Spectrum 1	1.0	1.7	5.1	5.5	92.8	90.4
Spectrum 2	26.3	37.0	17.5	16.2	46.8	37.9
Spectrum 3	34.1	46.6	0.5	0.4	53.0	39.9
Spectrum 4	29.5	41.3	0.1	0.1	58.6	44.2
Spectrum 5	34.9	47.5	0.3	0.3	52.2	39.3
Spectrum 6	34.8	46.8	13.0	11.5	41.7	33.0
Spectrum 7	32.3	43.2	34.0	29.9	26.9	23.6
Spectrum 8	30.7	41.6	29.8	26.6	31.8	27.3
Spectrum 9	35.3	47.0	21.0	18.4	34.5	28.4
Spectrum 10	35.4	46.8	28.0	24.4	28.8	24.5
Spectrum 11	33.8	45.6	16.0	14.2	40.2	32.2
Spectrum 12	32.1	43.6	20.6	18.4	38.0	31.1
Spectrum 13	32.5	44.1	17.1	15.3	40.6	32.7
Spectrum 14	30.8	41.7	29.2	26.1	32.2	27.6
Spectrum 15	33.7	45.4	18.3	16.2	38.4	31.1
Spectrum 16	1.0	1.6	3.7	4.1	95.3	94.3
Spectrum 17	29.6	40.7	20.7	18.7	49.7	40.6
Spectrum 18	6.0	9.7	6.0	6.3	88.0	84.0
Spectrum 19	24.1	34.9	0.2	0.2	75.6	64.9
Spectrum 20	9.4	14.6	17.0	17.4	73.7	68.0
Spectrum 21	5.2	8.3	9.0	9.6	85.8	82.1
Spectrum 22	5.9	9.4	11.6	12.3	82.5	78.3
Spectrum 23	3.9	6.3	9.5	10.2	86.6	83.6
Spectrum 24	14.4	21.9	9.2	9.2	76.4	68.9
Spectrum 25	18.0	26.6	15.6	15.2	66.4	58.2
Spectrum 26	19.1	27.9	17.6	17.0	63.3	55.1
Spectrum 27	18.5	27.7	0.3	0.3	81.2	72.0

Table E.13 EDS Results Corrected by Al_2O_3 Stoichiometry

	O [at %]	Mg [at %]	Al [at %]	Comments
Spectrum 1	4.1	5.5	90.5	Al alloy
Spectrum 2	49.0	12.9	38.1	spinel
Spectrum 3	59.5	0.3	40.1	Al_2O_3
Spectrum 4	55.5	0.1	44.5	Al_2O_3
Spectrum 5	60.3	0.2	39.5	Al_2O_3
Spectrum 6	57.6	9.3	33.1	spinel
Spectrum 7	52.5	23.8	23.7	spinel
Spectrum 8	51.5	21.1	27.4	spinel
Spectrum 9	56.7	14.8	28.5	spinel
Spectrum 10	55.9	19.5	24.6	spinel
Spectrum 11	56.2	11.4	32.4	spinel
Spectrum 12	54.0	14.7	31.3	spinel
Spectrum 13	54.9	12.3	32.8	spinel
Spectrum 14	51.7	20.7	27.6	spinel
Spectrum 15	55.8	13.0	31.2	spinel
Spectrum 16	7.3	4.0	88.7	Al alloy
Spectrum 17	58.3	13.0	28.8	spinel
Spectrum 18	28.6	5.3	66.1	mix spinel + Al alloy
Spectrum 19	59.2	0.2	40.6	Al_2O_3
Spectrum 20	34.1	12.9	53.0	mix spinel + Al alloy
Spectrum 21	25.2	7.9	66.9	mix spinel + Al alloy
Spectrum 22	26.8	9.8	63.4	mix spinel + Al alloy
Spectrum 23	20.5	8.6	70.8	mix spinel + Al alloy
Spectrum 24	44.9	6.9	48.2	spinel
Spectrum 25	48.1	10.8	41.2	spinel
Spectrum 26	48.9	11.9	39.2	spinel
Spectrum 27	53.4	0.2	46.4	Al_2O_3

Sample EXP 17

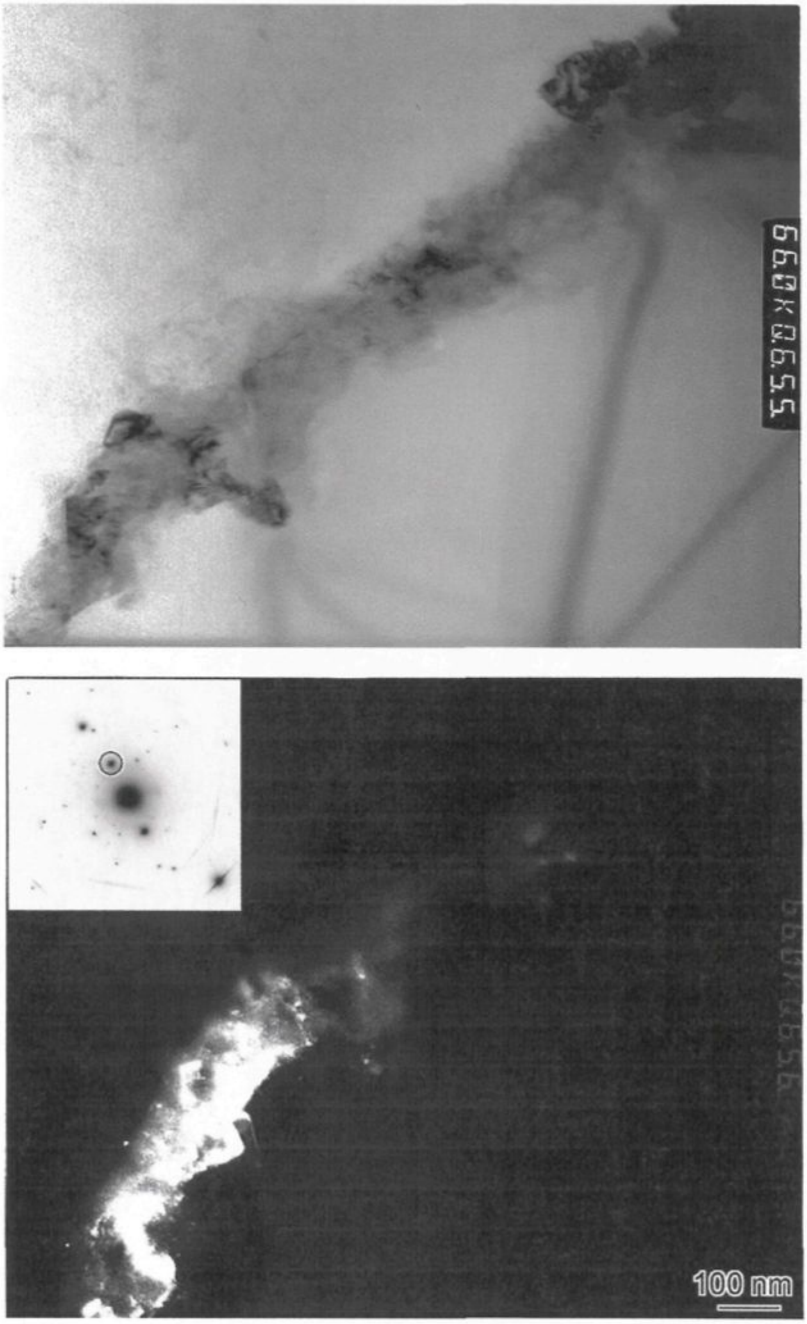

Figure E.28 Bright-field and Dark-field TEM Images of Spinel Layer on the Al/Al_2O_3 Interface (Region 1)

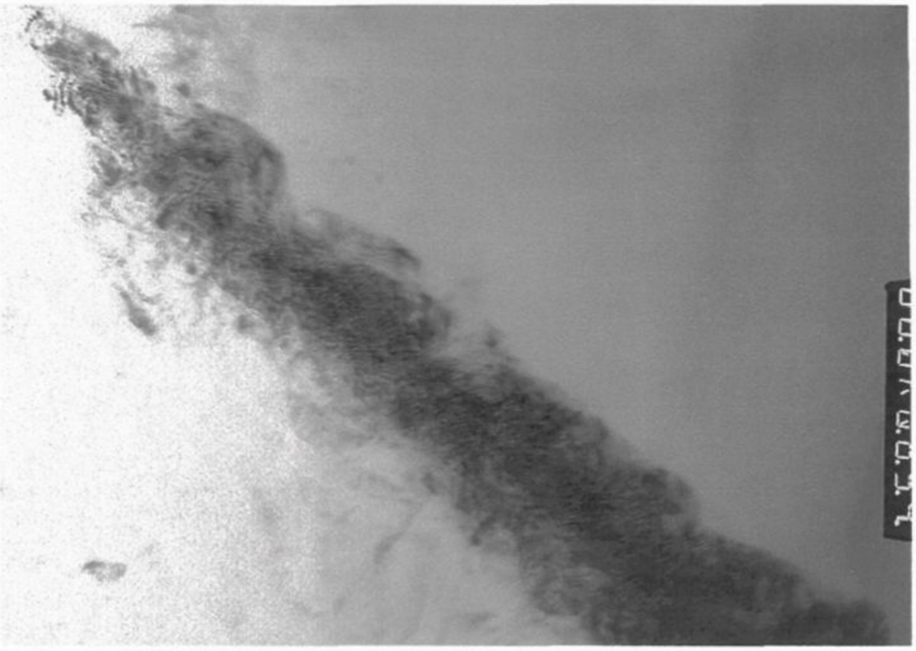

Figure E.29 Bright-field and Dark-field TEM Images of Spinel Layer on the Al/Al_2O_3 Interface (Region 2)

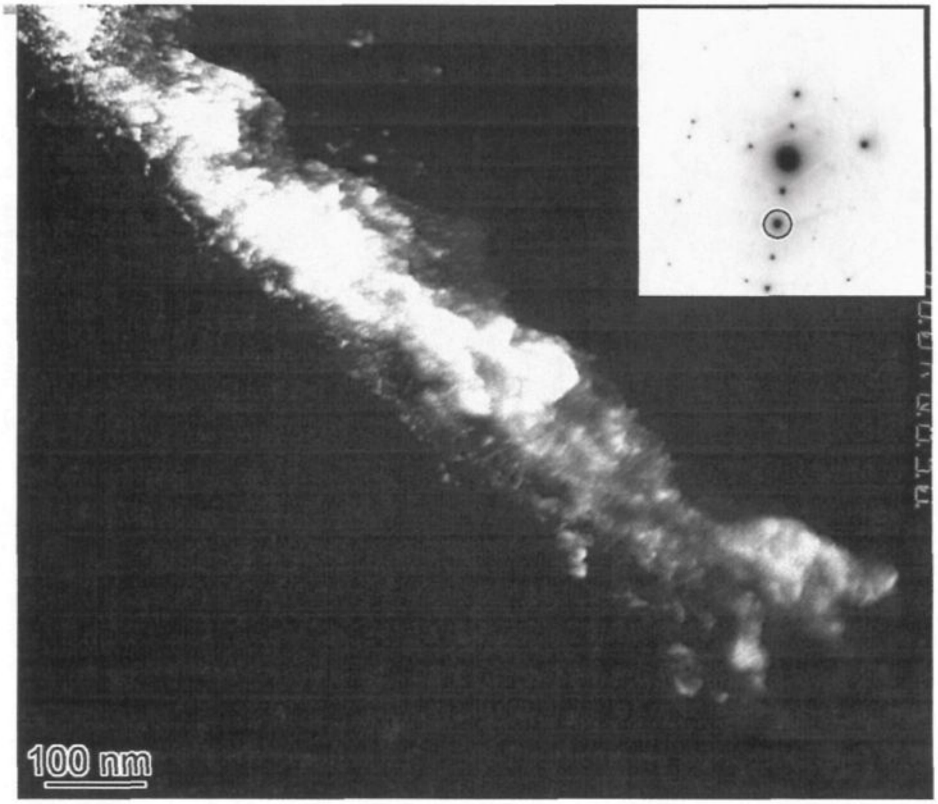

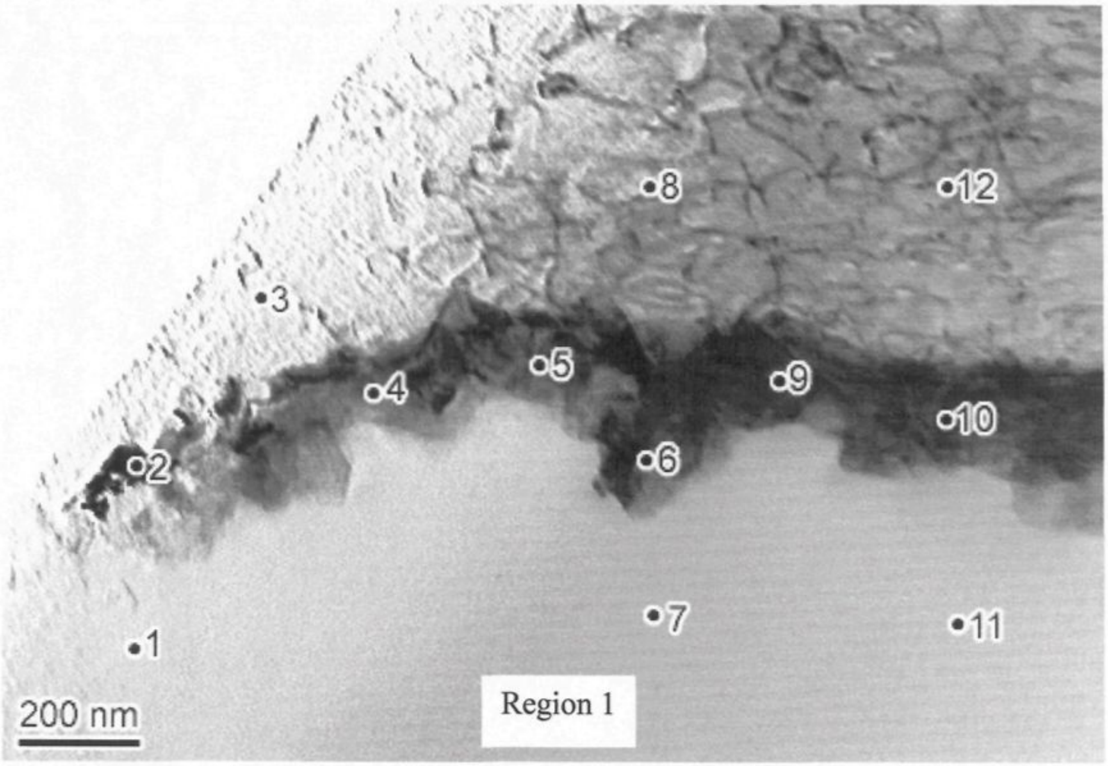

Figure E.30 STEM Images with EDS Locations

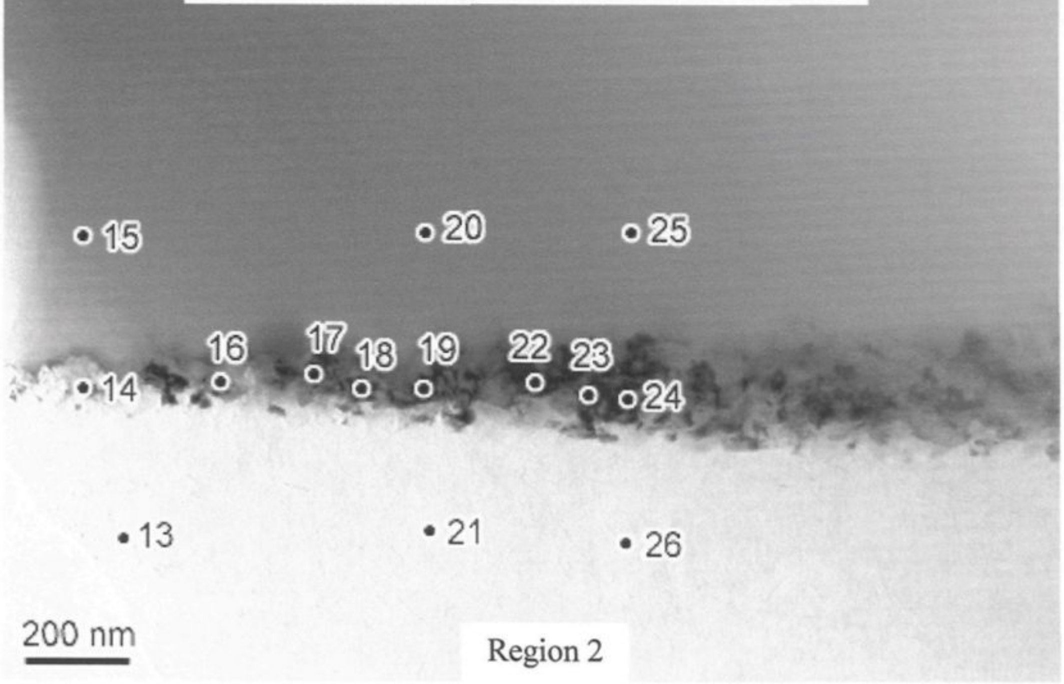

Table E.14 EDS Quant Results as Given by the INCA Software

	O [wt %]	O [at %]	Mg [wt %]	Mg [at %]	Al [wt %]	Al [at %]	Comments
Spectrum 1	41.9	54.9	0.1	0.1	58.0	45.0	Al_2O_3
Spectrum 2	31.9	42.6	39.7	34.9	28.4	22.5	spinel
Spectrum 3	1.2	1.9	5.3	5.9	93.5	92.2	Al alloy
Spectrum 4	36.0	46.8	43.7	37.5	20.3	15.7	spinel
Spectrum 5	35.9	47.3	30.2	26.2	33.9	26.5	spinel
Spectrum 6	36.5	48.2	25.9	22.5	37.5	29.4	spinel
Spectrum 7	37.9	50.7	0.1	0.1	62.0	49.2	Al_2O_3
Spectrum 8	0.9	1.4	5.7	6.3	93.4	92.3	Al alloy
Spectrum 9	35.1	46.6	26.4	23.0	38.5	30.3	spinel
Spectrum 10	35.2	46.6	29.6	25.8	35.2	27.7	spinel
Spectrum 11	36.5	49.2	0.2	0.2	63.3	50.6	Al_2O_3
Spectrum 12	0.8	1.3	5.3	5.8	93.9	92.9	Al alloy
Spectrum 13	1.7	2.7	5.3	5.7	93.1	91.5	Al alloy
Spectrum 14	37.2	48.5	33.5	28.8	29.4	22.7	spinel
Spectrum 15	38.4	51.2	0.1	0.0	61.6	48.8	Al_2O_3
Spectrum 16	36.0	47.5	26.2	22.8	37.9	29.7	spinel
Spectrum 17	34.3	45.9	21.3	18.7	44.5	35.3	spinel
Spectrum 18	27.6	37.9	33.7	30.5	38.7	31.6	spinel
Spectrum 19	28.5	39.7	14.3	13.1	57.2	47.3	spinel
Spectrum 20	0.7	1.2	5.0	5.5	94.3	93.3	Al alloy
Spectrum 21	34.9	47.5	0.1	0.1	65.1	52.5	Al_2O_3
Spectrum 22	31.5	42.4	33.6	29.8	34.9	27.8	spinel
Spectrum 23	23.5	33.1	29.6	27.5	46.9	39.3	spinel
Spectrum 24	20.5	29.7	19.5	18.7	60.0	51.7	spinel
Spectrum 25	0.7	1.1	5.2	5.7	94.1	93.2	Al alloy
Spectrum 26	32.9	45.3	0.1	0.1	67.0	54.7	Al_2O_3

Table E.15 EDS Results Corrected by Al_2O_3 Stoichiometry

	O [at %]	Mg [at %]	Al [at %]	Comments
Spectrum 1	62.8	0.1	37.1	Al_2O_3
Spectrum 2	49.0	29.8	21.2	spinel
Spectrum 3	3.5	5.8	90.7	Al alloy
Spectrum 4	52.5	32.3	15.2	spinel
Spectrum 5	53.6	22.4	24.0	spinel
Spectrum 6	54.5	19.3	26.2	spinel
Spectrum 7	59.5	0.1	40.4	Al_2O_3
Spectrum 8	2.7	6.2	91.2	Al alloy
Spectrum 9	53.2	19.7	27.1	spinel
Spectrum 10	53.0	22.0	25.0	spinel
Spectrum 11	58.2	0.1	41.6	Al_2O_3
Spectrum 12	2.4	5.8	91.8	Al alloy
Spectrum 13	6.0	5.6	88.5	Al alloy
Spectrum 14	56.0	23.6	20.4	spinel
Spectrum 15	62.2	0.0	37.8	Al_2O_3
Spectrum 16	55.8	18.6	25.6	spinel
Spectrum 17	55.0	15.3	29.7	spinel
Spectrum 18	47.2	24.6	28.2	spinel
Spectrum 19	50.6	10.7	38.7	spinel
Spectrum 20	2.7	5.5	91.9	Al alloy
Spectrum 21	59.2	0.1	40.7	Al_2O_3
Spectrum 22	51.0	24.2	24.8	spinel
Spectrum 23	43.2	22.3	34.5	spinel
Spectrum 24	40.9	15.3	43.8	spinel
Spectrum 25	2.5	5.7	91.8	Al alloy
Spectrum 26	57.5	0.0	42.4	Al_2O_3